NBSIR 85-3025

MATERIALS STUDIES FOR MAGNETIC FUSION ENERGY APPLICATIONS AT LOW TEMPERATURES - VIII

To

Department of Energy
Office of Fusion Energy
Washington, D.C. 20545

Prepared by

NBSIR 85-3025

UC 20b, c

TECHNICAL REPORTS

MATERIALS STUDIES FOR MAGNETIC FUSION ENERGY APPLICATIONS AT LOW TEMPERATURES - VIII

Edited by

**R.P. Reed
Fracture and Deformation Division
National Bureau of Standards
Boulder, Colorado 80303**

May 1985

Sponsored by

**Department of Energy
Office of Fusion Energy
Washington, D.C.   20545**

U.S. DEPARTMENT OF COMMERCE, Malcolm Baldrige, Secretary

NATIONAL BUREAU OF STANDARDS, Ernest Ambler, Director

CONTENTS

CONTENTS (continued)

STRUCTURAL ALLOYS (continued)

iv

SUMMARY

This report contains results of a research program to produce material property data that will facilitate design and development of cryogenic structures for the superconducting magnets of magnetic fusion energy power plants and prototypes. The program was developed jointly by the staffs of the National Bureau of Standards and the Office of Fusion Energy of the Department of Energy; it is managed by NBS and sponsored by DOE. Research is conducted at NBS and at various other laboratories through subcontracts with NBS.

Research results for 1984 are summarized in an initial "Highlights of Results" section and reported in detail in the technical papers that form the main body of this report. The technical papers are presented under four headings reflecting the main program areas: Welding, Nonmetallics, Structural Alloys, and Technology Transfer. Objectives, approaches, and achievements are summarized in an introduction to each program area.

A new welding laboratory has been developed. This facility, equipped for precise control of gas metal arc, gas tungsten arc, and shielded metal arc welding processes, is already assisting in the careful, controlled preparation of weldments for low temperature study. Our finite-element modeling experience has been used to study damage effects in glass/epoxy laminates (G-10CR, G-11CR) at low temperatures. The stress-strain characteristics were correlated with the sequence and types of damage accumulation. This study should contribute to our longer range objective of establishing mechanical property criteria for safe design of low temperature composite structures. A new alloy development criterion, the quality index, has been proposed to take into account both strength and toughness considerations. This quality index has been applied to consider the amount of nickel and nitrogen additions necessary to achieve specific low temperature strength and toughness objectives in austenitic stainless steels. The development of test equipment has been completed that measures, with computer assistance and control, the fatigue threshold stress-intensity levels. Measurement data at 4 K are presented for selected austenitic steels. New low temperature strength and toughness data for nitrogen-strengthened Fe-Cr-Ni-Mn austenitic stainless steels are given. Correlations of fracture toughness with associated fracture morphology have led to the discovery of faceted areas that have been associated with {111} face-centered cubic planes in high-nitrogen alloys. The effect of carbon and nitrogen on stacking fault energies in austenitic stainless steels has been measured. Previous estimates of the contribution from interstitial alloying elements to the stacking fault energy had been widely divergent. New elastic property data on high-manganese austenitic stainless steels are reported.

ORGANIZATIONAL CONTACTS

The people responsible for the various major aspects of the program are listed below so that specific technical questions may be directed to them.

Department of Energy, Office of Fusion Energy, Washington, D.C. 20545

Program Monitor	V. K. Der	(301) 353-5736
		(FTS) 233-5736

National Bureau of Standards, Boulder, Colorado 80303

Program Manager	R. P. Reed	(303) 497-3870
		(FTS) 320-3870
Welding	H. I. McHenry	(303) 497-3268
	T. A. Siewert	(303) 497-3523
	D. P. Vigliotti	(303) 497-3222
Nonmetallics	M. W. Austin	(303) 497-3504
	M. B. Kasen	(303) 497-3558
	R. D. Kriz	(303) 497-3547
	H. M. Ledbetter	(303) 497-3443
Structural Alloys	J. M. Arvidson	(303) 497-3424
	Y. W. Cheng	(303) 497-5545
	H. M. Ledbetter	(303) 497-3443
	H. I. McHenry	(303) 497-3268
	P. T. Purtscher	(303) 497-5789
	D. T. Read	(303) 497-3853
	R. P. Reed	(303) 497-3870
	R. L. Tobler	(303) 497-3421
Technology Transfer	N. J. Simon	(303) 497-3687

PROGRAM DESCRIPTION

The overall objective of the program is to assist in the design, construction, and safe operation of low-temperature magnetic fusion energy (MFE) systems, especially superconducting magnets, through effective materials research and materials technology transfer. The specific steps taken to achieve this objective are: (1) evaluation of low-temperature materials research needs specific to MFE devices; (2) development and monitoring of a research program to acquire the necessary data; and (3) rapid dissemination of the data to potential users through personal contacts, publications, and workshops.

Efforts directed at the first specific objective began with the publication of the "Survey of Low Temperature Materials for Magnetic Fusion Energy" in March 1977. A recent publication updating part of this survey, "Structural Alloys for Superconducting Magnets in Fusion Energy Systems," was included in volume IV (1981) of this series. In volume VI (1983), reviews of the properties of austenitic stainless steels and of austenitic-steel elastic constants also contributed to this objective. Through interactions with low-temperature design, construction, and measurement programs, such as the Large Coil Project and MFTF-B, we are aware of new problems as they arise. This year's contribution to the second objective is described in Table 1 in the form of an outline of the research projects. The results appear later in this report. Again this year, increased emphasis has been placed upon research oriented toward the establishment of test standards. The third objective is satisfied, in part, by these annual reports and by the series of NBS-DOE Workshops on Materials at Low Temperatures, which are held in Vail, Colorado. Since 1982, handbook pages presenting the available data for specific materials have been distributed to those members of the magnetic fusion energy community involved with low-temperature materials.

Table 1. Outline of the NBS-DOE Program on Material Studies for Magnetic Fusion Energy Applications at Low Temperatures.

Program Area	Organization	Program Description
A. Welding		
1. Austenitic-steel welds	NBS	Evaluation of the strength and toughness properties of weldments at 4 K. Continuation of studies to understand the mechanisms by which residual delta ferrite, Mn, and interstitial elements affect the deformation and fracture of stainless-steel welds.
B. Nonmetallics for Magnet Structures		
1. Standardization	NBS	Continued cooperation with industry to refine cryogenic-grade specification for commercial, nonmetallic, bulk-insulating laminates.
2. Controlled test-specimen development	NBS	Development of methods for rapidly and inexpensively producing highly characterized, small specimens for use in screening the significant parameters influencing cryogenic radiation resistance of nonmetallic composite insulators.
3. International cooperation	NBS, Rutherford Laboratory, Osaka University	Agreement to cooperate in development of specimens, material selection, and test procedures in developing radiation-resistant insulating materials.
4. Influence of damage	NBS, Swiss Federal Laboratories	Determination of the influence of microcracks on design properties, such as stiffness and strength.

Table 1 (continued)

Program Area	Organization	Program Description

C. Structural Alloys

1. Strong, tough alloys	NBS	Assessment of low-temperature properties of selected austenitic alloys containing varying concentrations of C, N, and Mn with an Fe-Cr-Ni base. Assessment of Japanese austenitic alloys with an Fe-Mn base.
2. Strong, fatigue-resistant alloys	NBS	Study of fatigue and fatigue crack-growth rates of candidate structural alloys, including 300 series stainless steels, Fe-Mn base austenitic alloys, and age-hardened alloys.
3. Low-temperature codes and standards	NBS	Research to establish low-temperature mechanical test standards, now emphasizing tensile, fracture toughness, and fatigue.
4. Physical properties	NBS	Measurement of properties, such as elastic constants, thermal expansion, and volume; especially, alloying effects.

D. Technology Transfer

1. NBS-DOE Workshop	NBS	Presentation of research results to the fusion community, discussion of new problems, and interaction between magnet designers, material specialists, and other interested people during a workshop.
2. Handbook	NBS	Analysis of mechanical properties of AISI 304 high-nitrogen content stainless steels with respect to temperature and interstitial content (1984). Distribution (1985) of pages of the data handbook for AISI 304 (N, LN, HN, LHN) stainless steels and for AISI 316L and 304 weldments. Preliminary work on aluminum alloy 2219 data.

HIGHLIGHTS OF RESULTS

HIGHLIGHTS OF RESULTS

WELDING

A welding laboratory was established for detailed study of the welding arc and preparation of highly characterized welds for cryogenic mechanical property evaluations. The laboratory contains an adaptive control GMA welding system that controls the weave width and contact-to-tip distance by sensing the arc voltage. By means of an on-board computer using prepro- grammed algorithms, the unit continuously controls heat input and travel speed. A transistorized current regulator permits interference-free power for careful study of the welding arc. The laboratory contains power supplies for GTA, GMA, and SMA weldings, gas mixing systems, and other support equipment.

A fully austenitic weldment produced by a filler metal manufacturer was evaluated at 4 K. The undiluted weld metal had a composition of Fe-15Mn-8Ni- 1Mo-0.7C and was produced by submerged arc welding a 21-mm plate using a butt joint configuraiton. The yield strength (1115 MPa) and toughness ($K_{Ic} \cong 194$ MPa$\sqrt{m}$) combination compares favorably with existing base metal properties for AISI-304 type alloys.

A linear equation based on previously published data was developed to predict the 76-K CVN toughness for shielded metal arc deposit compositions. This study proposed a simpler and more accurate predictive equation to help select improved compositions for future applications. Analysis of 79 weld deposits revealed that calculated FN was the most significant term for predicting the CVN toughness. This term, when allowed to be negative, was also an excellent predictor of toughness for the fully austenitic composi- tions and the AISI type 316 compositions, although no mechanism was proposed.

NONMETALLICS

Standardization

We continue to work with representatives of the United States laminating industry to provide magnet builders with commercial sources of standardized, reliable, nonmetallic insulating materials. We have ongoing consultation with users and manufacturers about the adequacy of specifications.

Controlled Test-Specimen Development

Recognizing the unique demands put on specimens to be used in radiation research, we have developed new methods to produce specimens that combine the attributes of low cost, a high degree of characterization, small size, and flexibility in component selection and treatment. We refined the system for producing uniaxially reinforced, 3- to 4-mm-diameter rod specimens and now can produce specimens of excellent quality from liquid-mix epoxy-resin systems. We are modifying the technique for hot-melt epoxy and polyimide

resin systems. These specimens will be subjected to radiation in the NLTNIF reactor at ORNL and then evaluated for radiation degradation by means of short-beam shear and torsional shear tests.

International Cooperation

A cooperative program with laboratories in Japan and England has resulted in the production and testing of specimens with identical configuration. All members of the Japanese group (headed by Prof. T. Okada at Osaka University and including individuals at Kyoto University, the University of Osaka Prefecture, and the Hoxan Corporation) have successfully produced specimens containing glass, graphite, and silicon-carbide fibers by using the NBS method. Performance has been evaluated in three-point flexure. Similar success was achieved by Dr. D. Evans of the Rutherford Laboratory in England. An effective exchange of information is continuing. We plan to exchange specimens and report our results jointly in 1985.

Property Determination and Modeling

1. Measurements on the influence of damage at 76 K on the mechanical performance of woven composites at low strains. We predicted and measured the influence of crack formation on the mechanical performance of standard glass epoxy laminates (G-10CR, G-11CR) at low strains and low temperatures. Damage was modeled by finite elements as microcracks confined to fiber bundles that were oriented transverse to the tensile load direction. From experiments we studied the formation of damage as a collection of fiber breaks and transverse fiber bundle cracks. We discovered that the sequence and types of damage, at strains well below ultimate, control the discontinuities (knees) in the load-deformation (stress-strain) diagrams. However, between knees, the material remains linear elastic at low temperatures. We found that G-11CR has two knees and three distinct moduli, whereas G-10CR has only two moduli and a single knee at a lower strain than G-11CR. A decrease in moduli measured near the first knee compares well with predictions of finite-element theory.

2. Elastic representation surfaces of unidirectional graphite/epoxy composites. From our studies on fiber-reinforced materials, we found several new properties by examining the elastic representation surfaces. In particular, unidirectional graphite/epoxy exhibits a high elastic anisotropy and unusual geometrical features in its elastic-property polar diagrams. From a five-point component (hexagonal symmetry) elastic stiffness tensor, we computed and displayed representation surfaces where large variations in Young's modulus, Poisson's ratio, torsional modulus, and linear compressibility are due to peculiar geometries: large negative Poisson's ratios result from changes in fiber volume fraction and tilt angles away from symmetry planes. On the basis of Christoffel equation solutions, we described some unusual elastic-wave-surface topological features. Some new, unexpected results include: a shear-wave velocity that exceeds a longitudinal-wave velocity in the plane transverse to the fiber and a wave that changes polarization character from longitudinal to transverse as the propagation direction sweeps from the fiber axis to the transverse plane.

4

STRUCTURAL ALLOYS

Strong, Tough Alloys

Major accomplishments for the year include the following:

The tensile strength and fracture toughness at 4 K were studied as a function of nickel (6 to 15 wt.%) and nitrogen (0.09 to 0.28 wt.%) contents for eight austenitic stainless steels. Results indicate that nitrogen increases the tensile yield strength and decreases the fracture toughness, $K_{Ic}(J)$. Nickel has little significant effect on tensile yield strength but increases the fracture toughness. A new parameter, called the quality index, is presented and defined as the product $\sigma_y \cdot K_{Ic}(J)$. This index relates to the capacity of the alloy to achieve greater strength or toughness, but not at the expense of the other parameter. Nickel alloying is shown to increase the quality index; nitrogen has little effect.

Thirty-two alloys were included in a study of conventional notch tensile testing as a method of fracture toughness characterization for austenitic stainless steels at liquid helium temperature, 4 K. For the same austenitic stainless steels, tensile and J-integral fracture toughnesses [$K_{Ic}(J)$] were also measured. For these materials, the notch tensile strength (σ_{NTS}) generally increases with yield strength (σ_y), and the σ_{NTS}/σ_y ratios are typically much greater than 1.0. Correlations among σ_{NTS}, $K_{Ic}(J)$, and σ_y were assessed. The best correlation was found between the ratio $\sigma_{NTS}/K_{Ic}(J)$ and the toughness, $K_{Ic}(J)$.

Strong, Fatigue-Resistant Alloys

A new facility is in use that facilitates the difficult and time-consuming measurement of threshold fatigue. It is capable of measuring fatigue-crack growth rates as low as one angstrom (less than one lattice spacing) per load cycle in the temperature range 295 to 4 K. Near-threshold fatigue-crack growth rates and threshold stress intensity factors are especially important data because they are used to determine the stress limits below which existing cracks cease to grow.

This new fatigue-testing apparatus is completely and automatically controlled by a computer. It consists of a servo-hydraulic test machine, a vacuum-insulated cryostat, a minicomputer, and temperature-control system. The computer systematically decreases the test loads until the threshold for crack growth is reached. The fatigue-crack growth rate measurements extend over four orders of magnitude, from 10^{-6} to 10^{-10} m/cycle. A typical test cycles 6.4-mm-thick specimens at a frequency of 40 Hz for 4 days, 24 hours a day--a total of 13 million fatigue cycles.

Preliminary data have been reported on alloys 304L, 304LN, and 316. The threshold stress intensity factors vary from 7.4 to 8.5 MPa√m for these alloys at 4 K.

Physical Properties

The physical properties provided at least three types of information: material characterization, key design parameters, and tests for anomalous behavior.

1.   Anomalous low-temperature elastic-constant behavior was identified in two austenitic alloys. Near 54 K, the alloy Fe-20Cr-16Ni-6Mn undergoes a magnetic transition. The bulk modulus begins to soften at a higher temperature, near 150 K. Near 191 K, all elastic constants of the alloy Fe-18Cr-3Ni-12Mn exhibit anomalous behavior arising from a paramagnetic-to-antiferromagnetic spin-glass transition.

2.   The effect of interstitial carbon and nitrogen on low-temperature sound velocities in 304-type stainless steels was studied. Nine alloys containing between 9.3 and 1.3 atomic percent carbon and nitrogen show low-temperature physical-property anomalies associated with a magnetic transition. Contrary to existing reports, the magnetic transition temperature decreases sharply with increasing interstitial content.

3.   New measurements were made of the monocrystal Voigt elastic-stiffness constants (C_{11}, C_{12}, and C_{44}) for Fe-19Cr-10Ni. By means of seven models, these are related to the measured polycrystal elastic constants.

Codes and Standards

Cooperation has been established between NBS, industry, and other government laboratories within a Metal Properties Council (MPC) Low Temperature Task Group to develop this program. The task group prepared a proposal to provide the information needed to extend tensile test standards to very low temperatures. The program considers the effects of strain rate on specimen heating (and, therefore, flow strength) and grain size (to establish minimum specimen sizes). Potential research contractors have submitted responses to this proposal. The final contractor will be selected soon, and MPC is now soliciting organizations to obtain the necessary funds to support this program.

TECHNOLOGY TRANSFER

An NBS-DOE Workshop on Materials at Low Temperatures was held in Vail, Colorado on October 14-17, 1984. The workshop brought together material specialists and magnet designers to report recent research and to identify and discuss structural materials problems in superconducting magnet design and construction for fusion energy systems. In addition to the formal presentation sessions, there were discussion meetings to formulate research objectives in structural alloys, welding, and nonmetallics. The proceedings of this informal workshop were not published; however, a copy of the program and an informal summary of the proceedings may be found in the Technology Transfer section of this report.

Handbook and supporting documentation pages have been prepared for AISI 304 (N, LN, HN, LHN) stainless steels and will be distributed in preliminary draft format. Properties covered include: tensile strength, yield strength, elongation, reduction of area, stress-strain curves, elastic constants, impact energy, fracture toughness, stress- and strain-controlled fatigue life, and fatigue crack growth rate. The scope of the handbook has been expanded to include analysis and correlation of AISI 304 properties with respect to interstitial carbon and nitrogen content. The AISI 304 pages will be submitted to the advisory task group of the "Materials Handbook for Fusion Energy Systems" for their review process. Handbook pages on AISI 316 alloys and Fe-21Cr-6Mn-9Ni are being reviewed. Preliminary work on handbook pages covering AISI 304 electromagnetic and thermal properties and AISI 304 and 316L welds is in progress.

The Japan Atomic Energy Research Institute initiated a program in 1982 to develop cryogenic steels for use in the large superconducting magnets planned for their Fusion Experimental Reactor. The target properties for the cryogenic steels are a yield strength of 1200 MPa and a fracture toughness of 200 MPa√m at 4 K. Five Japanese steel companies have developed candidate alloys that met or nearly met the property goals. Progress on developing these steels was reviewed at a U.S./Japan workshop in December 1984 and is summarized in this report.

WELDING

WELDING PROGRAM

LEADER: T. A. Siewert, NBS
STAFF: H. I. McHenry, D. P. Vigliotti, NBS

OBJECTIVES:

1. Investigation of the metallurgical factors that affect the mechanical
    properties of stainless-steel weldments at cryogenic temperatures.
2. Contributions to the development of improved filler metals for welding
    stainless steels for liquid-helium service.
3. Evaluation of the mechanical properties of weldments at 4 K.
4. Development of methods of detecting defects and evaluation of their
    significance in stainless-steel weldments.

RESEARCH PAST YEAR (1984):

1. A welding laboratory was established for detailed study of the welding
    arc and highly characterized weld for mechanical property studies.
2. The tensile properties and fracture behavior of a Fe-15Mn-8Ni-1Mo-0.7C
    fully austenitic weldment were evaluated at 4 K.
3. Improved predictive equations for 76-K Charpy V-notch tests were devel-
    oped.
4. Mechanical properties testing at 4 K in support of superconducting
    magnet design and construction continued.

RESEARCH THIS YEAR (1985)

1. The effect of various interstitial elements will be evaluated in type
    316L GMA weldments at 76 and 4 K.
2. A series of weldments based on a type 308 composition and with varying
    alloy additions will be used to clarify the effects of manganese and
    nitrogen in SMA weldments for cryogenic service.
3. The tensile properties and fracture toughness of an electron beam weld
    in 75-mm-thick 304LN will be measured at 4 K.
4. Mechanical property testing at 4 K in support of superconducting magnet
    design and construction will continue.

Summary of Mechanical Property Measurements of Welds [*]

Filler Metal, Process, Base Metal	Country of Supplier	Tensile 295, 76, 4 K	Elastic 295 4 K	Fracture Toughness 295, 76, 4 K	Fatigue Crack Growth Rate 295, 76, 4 K	Charpy Impact 76 K
Austenitic Steels						
308, (SMA), 21/6/9	U.S.	1978		1978		1978
E308L-15, (SMA), 316LN	U.S.	1979		1979		1979
308L, (SMA)	U.S.	1980		1980	1980	
308L, (FCMA)	U.S.	1980		1980	1980	
308L, (GMA)	U.S.	1980		1980	1980	
308L(0.6N),(FCMA)	U.S.	1981		1981	1981	
308L(0.8N), (FCMA)	U.S.	1981		1981	1981	
E316L-15 (N=0.044), (SMA), 316LN	U.S.	1979		1979		1979
E316L-15 (N=0.071), (SMA), 316LN	U.S.	1979		1979		1979
E316L, (SMA), (316)	U.S.	1979		1979		1979
E316, (SMA), (316)	U.S.	1979		1979		1979
316L, (SMA)	U.S.	1981		1981	1981	
316L, (ES)	U.S.	1981		1981	1981	
316L, (GTA)(GMA)(SA), 304L	U.S.	1981		1981		1981
316L, (SAW)	U.S.	1982		1982	1982	
316L(mod.), (SMAW)	U.S.			1982	1982	
E316L (SMA), 316	U.S.		1982, 1983			
316L, (SA)	U.S.	1980		1980	1980	
316L, (SMA)	U.S.	1980		1980	1980	
316L, (GTA), 304L	U.S.	1980				1980
316L, (GMA), 304L	U.S.	1980				1980
316L, (SA), 304L	U.S.	1980				1980
320LR, (SMA)	U.S.	1984		1984		
AWS 330 (mod.), 304L	U.S.	1978		1979		1978
15Mn-8Ni-1Mo-0.7C	U.S.	1984		1984		
6.5Cr-25Mn-2.8Ni-1.4Mo,(SMA), 5Cr-25Mn-1Ni	Japan	1982		1982	1982	
13Cr-20Ni-9Mn, (SMA), 21/6/9	U.S.	1978				1978
15Cr-12Ni-10Mn (SMA)	Germany	1981				1981
16Cr-16Ni-2Mo, (FCMA)	U.S.	1980		1980	1980	
16Cr-16Ni-4Mo, (FCMA)	U.S.	1981		1981		
17Cr-16Ni-4Mo, (SMA)	U.S.	1981		1981		
18Cr-16Ni-9Mn, (SMA), 21/6/9	U.S.	1978		1981		1978
18Cr-16Ni-9Mn, (GMA)	U.S.	1980		1980	1980	
18Cr-20Ni-6Nb, (GMA)		1981		1981		1981
18Cr-20Ni-5Mn, (GMA)		1981				1981
18Cr-20Ni-6Ti, (GMA)		1981				1981
18Cr-20Ni-9Mn, (GMA)		1981		1981		1981
18Cr-18Ni-5Mn (SMA)	Sweden	1981		1981		1981
18Cr-16Ni-9Mn (SMA)	U.S.S.R.	1981				1981
19Cr-16Ni-7Mn (GMA)		1981				1981
20Cr-10Ni-9Mn, (SMA), 21/6/9	U.S.	1978				1978
20Cr-16Ni-7Mo, (SAW)		1981				
Nitronic 40W, (SMA), 21/6/9	U.S.	1978		1981		1978
Aluminum Alloys						
5556, (GMA), 5083-0	U.S.	1980		1981	1981	
5183, (GMA), 5083-0	U.S.	1980		1981	1981	

*Properties listed by year in this table may be located in "Materials Studies for Magnetic Fusion Energy Applications at Low Temperatures" as follows: 1978, Vol. I, NBSIR 78-884; 1979, Vol. II, NBSIR 79-1609; 1980, Vol. III, NBSIR 80-1627; 1981, Vol. IV, NBSIR 81-1645; 1982, Vol. V, NBSIR 82-1667; 1983, Vol. VI, NBSIR 83-1690; 1984, Vol. VII, NBSIR 84-3000.

STAINLESS STEEL WELDING PROGRAM

T. A. Siewert

Fracture and Deformation Division
National Bureau of Standards
Boulder, Colorado 80303

This past year has been one of transition in the NBS welding program as the Fracture and Deformation Division has developed the capability to prepare specialized weldments and is planning to take a more active role in welding research for cryogenic applications.

NBS Welding Laboratory

The capability to prepare specialized weldments was achieved through the formation of a welding laboratory. This laboratory was designed to be self-sufficient and versatile. It has the necessary equipment to perform all tasks in the production of weldments from plate preparation to the final inspection. Three welding processes are being used [gas metal arc (GMA), gas tungsten arc (GTA), and shielded metal arc (SMA)], and three classes of material are being welded (stainless steel, aluminum, and low alloy steel). The laboratory is equipped with an adaptive controlled GMA welding system, a GMA weld weaving system, various power supplies, a multicomponent shielding gas mixing system, a rotating weld table, an oxyacetylene cutting table, and other support equipment. This equipment has been installed in a large bay, which contains an overhead crane (2-t capacity). This bay also contains new wiring to the power supplies and piping for distributing the shielding gas to the various weld stations.

The welding laboratory serves two major functions: One is to advance the science of welding through clarifying the interactions of the welding electrode with the arc, the shielding gas or slag system, and the molten weld pool. The second function is to produce highly characterized test specimens for evaluation by the NDE and mechanical property groups. Not only can these specimens be produced much more rapidly than previously, but the unique capabilities of welding might be used to fabricate novel test specimens for better evaluation of material behavior.

Goals

The welding program has received further direction from a discussion session entitled "Research Objectives in Welding" at the NBS-DOE Workshop on Materials at Low Temperatures held October 14-17, 1984 (see page 299). The 4-K property goals for welds in cryogenic structures are:

Interim	Yield Strength	1000 MPa
	Fracture Toughness	150 MPa√m
Eventual	Yield Strength	1000 MPa
	Fracture Toughness	200 MPa√m

We are encouraging industry participation in the development of consumables and procedures that will meet these goals by assisting in some of the cryogenic testing. Since these cryogenic tests are difficult to perform and testing facilities are not widely available, a screening program has been established to evaluate the candidate welds. The sequential steps include a 76-K Charpy V-Notch (CVN) test of the weldment by the producer. Welds with an absorbed energy above 54 J will be forwarded to the NBS Fracture and Deformation Division for tensile testing at 76 K and comparison with a screening goal of 750 MPa. Further toughness and strength tests at 4 K will be conducted at NBS if the properties meet the screening goals.

Current Projects

Several electrode manufacturers and fabricators have expressed interest in the screening program established to meet the goals of the NBS-DOE Workshop. Several SMA weldments are anticipated during the year, and a fabricator is intending to furnish an electron beam weld in 50-mm AISI type 304LN plate.

The effect of interstitial elements (in stainless steel welds) on the cryogenic mechanical properties are being studied. In previous programs, nitrogen and carbon have been studied in plate materials. However, the predictive equations for strength and toughness are not valid for welds of similar compositions. Mechanical properties and microstructures of welds with various interstitial elements will be evaluated to determine which interstitials can increase the weld strength with the least degradation of the toughness.

Another program involves the study of the interaction of manganese and nitrogen in stainless steel weld metal. Previous studies have either varied the manganese level while holding the nitrogen level virtually constant or kept their ratio nearly constant. In this program, the two elements will be varied independently, using test design matrices with both fixed and varying ferrite number (FN), to assess their individual and combined effects on strength and toughness. We will also assess the effect of molybdenum and boron addition on the properties of these stainless steel welds.

Completed Projects

A fully austenitic weldment produced by a filler metal manufacturer was evaluated at 4 K. The undiluted weld metal had a composition of Fe-15Mn-8Ni-1Mo-0.7C and was produced by submerged arc welding a 21-mm plate using a butt joint configuration. The yield strength (1115 MPa) and toughness ($K_{Ic} \cong 194$ MPa$\sqrt{m}$) combination compares favorably with existing base metal properties for AISI 304 type alloys.

A linear equation based on previously published data was developed to predict the 76-K CVN toughness for shielded metal arc deposit compositions. This study proposed a simpler and more accurate predictive equation to help select improved compositions for future applications. Analysis of 79 weld deposits revealed that calculated FN was the most significant term for predicting the CVN toughness. This term, when allowed to be negative, was also an excellent predictor of toughness for the fully austenitic compositions and the AISI type 316 compositions, although no mechanism was proposed.

Tensile and Fracture Properties of an Fe-14Mn-8Ni-1Mo-0.7C Fully Austenitic Weld Metal at 4 K^{+}

R. L. Tobler, R. E. Trevisan[*] and R. P. Reed

Fracture and Deformation Division
National Bureau of Standards
Boulder, Colorado

A fully austenitic steel butt weld 21 mm thick was produced by submerged arc welding using an experimental filler metal composition: Fe-14Mn-8Ni-1Mo-0.7C. The tensile and fracture properties of this weld were measured in liquid helium to evaluate its candidacy for applications at 4 K. The yield strength (1115 MPa) and toughness ($K_{Ic} \cong 192$ MPa·m^2) combination of this material compares favorably with existing base metal properties for AISI 304 type alloys. A conventional ductile fracture consisting of void formation and coalescence was evidenced in both tensile fracture toughness specimens.

Key Words: austenitic steel; cryogenic testing; fracture toughness; low temperature tests; mechanical properties; microstructure; tensile properties; weldments.

INTRODUCTION

This paper describes the 4 K tensile and fracture toughness properties of a newly developed, fully austenitic Fe-14Mn-8Ni-1Mo-0.7C weld metal. Austenitic welds usually contain a small amount of second phase δ-ferrite to prevent hot cracking on cooling to room temperature. The δ-ferrite, however, is undesirable for extreme cryogenic service since δ-ferrite is embrittled at low temperatures. A study of the fully austenitic Fe-14Mn-8Ni-1Mo-0.7C composition is therefore of interest for the development of fully austenitic welds for cryogenic service.

To exclude the formation of δ-ferrite and achieve a fully austenitic weld, an appropriate chemical composition must be selected according to the Delong diagram. Elmer, McHenry, and Whipple [1] tested several fully austenitic stainless steel compositions in the form of as-welded plates. They concluded that, while additional research is necessary to identify the optimum chemical composition and weld process variables, it is possible to obtain microfissure-free austenitic welds that have attractive strength/toughness properties at 4 K. In this paper we consider an Fe-14Mn-8Ni-1Mo-0.7C filler metal composition, describe its mechanical behavior at 4 K, and compare its performance with stainless steel welds and AISI 304 type base metals.

MATERIAL

The material tested was a submerged-arc butt weld produced using two sections of 21-mm-thick mild steel plate and Fe-14Mn-8Ni-1Mo-0.7C electrode. The steel plates were each coated with 2 layers of weld metal to minimize dilution in the actual weld. Welding was performed in the flat position using 3.175-mm tubular wire at 450 A, 30 V, and 5.9 to 6.8 mm/s travel speed with neutral

flux and a 38.1 mm electrical stickout. The chemical composition of the weld
is given in Table 1. Radiography indicated that this weldment met the
requirements of AWS A5.23.

Microstructures viewed normal to the longitudinal direction of the weld
are shown in Figs. 1 and 2. Figure 1A is representative of the dendritic aus-
tenite phase revealed by etching with 1% nital solution. No δ-ferrite is pre-
sent, as verified by electrolytic etching with KOH. Examination of a total
cross-sectional area of 200 mm^2 revealed only one interdendritic microfissure,
which is shown in Fig. 1B. Also present was a homogeneous distribution of MnS
and FeS inclusions, which is a common feature in welded steels, as shown in
Fig. 2.

EXPERIMENTAL PROCEDURES

Tests at 4 K were performed in a cryogenic apparatus [2] with material in
the as-welded condition using tensile and compact specimens with the orienta-
tions shown in Fig. 3.

The tensile properties in the longitudinal weld direction were determined
by testing two specimens at a strain rate of 4.2×10^{-4} s^{-1}. The specimens
were 6.35 mm in diameter and 44.3 mm in gage length. Uncertainties in strength
measurements are less than ±3%. Three compact specimens were also prepared.
These were 20 mm thick (B) and 50.8 mm wide (W), with W/B = 2.5 [3]. The
planar dimensions were those of a standard 25.4-mm-thick K_{Ic} test specimen
with W/B = 2.0, but the notch was modified to allow loadline deflection measure-
ments [2,3].

Two compact specimens failed to provide useful results: the first, with
a relatively short crack length (a/W $\cong$ 0.50), failed by cleavage in the mild
steel at the loading pin holes; the second developed an irregular crack front.

A third specimen (a/W $\cong$ 0.69) was tested successfully and analyzed using linear-elastic and elastic-plastic methodologies [3,4]. Uncertainites in K_{Ic} determinations are estimated at about 10%. Also, the 4 K fracture surface was examined with a magnetic torsion balance device and by scanning electron microscopy.

RESULTS

The 4 K tensile properties of the Fe-14Mn-8Ni-1Mo-0.7C weld metal are listed in Table 2, and the tensile fracture surface is shown in Fig. 4. A conventional cup-and-cone fracture is manifested but the final cross-sectional area is slightly elliptic, owing to the anisotropy of plastic deformation. Higher magnifications of the flat fracture (center) and shear fracture (circumferential) zones are shown in Figs. 5 and 6. The flat fracture zone shows circular dimples and pores which evidence a conventional ductile failure mechanism consisting of void coalescence (Fig. 5). The shear fracture zone shows elliptic dimples and some porosity (Fig. 6). There is no evidence of brittle failure mechanisms.

The 4 K fracture test results are summarized in Figs. 7 and 8. The K_Q value according to the ASTM E 399-83 procedure is 144 MPa·m$^{\frac{1}{2}}$ while the K_{Ic} estimate according to J-integral calculations is 192 MPa·m$^{\frac{1}{2}}$. However, neither value can be considered a valid measurement of K_{Ic} for reasons given below.

The K_Q value calculated from the curve of Fig. 7 is invalid because of failure to satisfy the specimen thickness requirement (section 9.1.3, ASTM E 399-83) and also because the P_{max}/P_Q ratio, 1.15, exceeds the allowable limit of 1.10 (section 9.1.2, ASTM E 399-83). The actual specimen thickness is 20.2 mm, whereas 42 mm may be required for valid results, according to the K_{Ic} test standard.

J-integral calculations were performed using the same test record (Fig. 7) used to obtain K_Q. Valid J-resistance curves could not be obtained, however, because load-point instabilities occurred, followed by arrests, giving the displacement-controlled test record the serrated appearance shown in Fig. 7. The occurrence of such instabilities represents unloading at the crack tip which is unacceptable according to the ASTM E 813-81 test procedure.

From the practical side, serrations limit the number of J-Δa data points that can be obtained in single specimen tests, since unloading compliance measurements can only be performed at points of crack arrest. As a result, we obtain the pseudo-resistance curve shown in Fig. 8. Since the Δa increments associated with serrations are uncontrollable, only two data points fall in the prescribed Δa interval defined by the 0.15 to 1.5 mm offset limits of E 813-81. Failure to obtain four data points within the specified interval invalidates the results according to sections 3.1 (note 2) and 9.3.2 of ASTM E 813-81. Nevertheless, an estimate of K_{Ic} was calculated from the apparent J_{Ic} from Fig. 8 as follows [4]:

$$K_{Ic}(J) = [E \cdot J_{Ic}]^{\frac{1}{2}} = [207 \text{ GPa} \cdot 178 \text{ kJ/m}^2]^{\frac{1}{2}} = 192 \text{ MPa} \cdot \text{m}^{\frac{1}{2}}$$

Figure 9 shows the fracture surface at the center of the compact specimen after testing at 4 K. The fracture surface is 100% dimpled. In addition, examination of the 4 K tensile and fracture specimen surfaces with a magnetic torsion balance indicated that no α' (body-centered cubic) martensite had formed during the loading to fracture at 4 K. The sensitivity of the balance is 0.2%. Therefore this fully austenitic steel appears ductile and fully stable against martensitic phase transformation during deformation to fracture at 4 K.

DISCUSSION

Fracture mechanics data for weldments at 4 K are rare because of the experimental complexities of testing at cryogenic temperatures. However, fracture toughness data for seven fully austenitic steel weldments are reported in the work of Elmer, McHenry, and Whipple [1], and their data are compared with ours in Fig. 10. These data represent similar specimen orientations and data reduction procedures, although other factors such as grain size, weld process, and manufacturing variables were uncontrolled.

As seen in Fig. 10, the performance of the Fe-14Mn-8Ni-1Mo-0.7C weld containing no chromium compares well with the data for fully austenitic stainless steel weld compositions. In general, the weld metal data demonstrate an inverse trend between toughness and strength which is analogous to the trend for AISI 304 type base metals, although the scatter is larger for welds. It is also evident that some of the fully austenitic weld metal compositions, including Fe-14Mn-8Ni-1Mo-0.7C, nearly match the properties of the unwelded base metals.

Note that the above comparison is based on TL orientations [3] for the base metal and welds. Since welds are highly anisotropic, comparisons based on other fracture plane orientations could give different results.

Although serrations affect the interpretation and calculation of fracture test results, the consequences of their occurrence in 4 K test records has never been properly studied. Previously, several base metals of relatively high strength displayed similar serrations and invalid J_R curves [5]. Also, as discussed in a study of AISI 310 steel, serrations at 4 K are common even in very ductile materials [6]. In the ductile materials, there is probably a correspondence between the occurrence of serrations in fracture tests and discontinuous yielding in tensile tests owing to adiabatic heating [6]. So far,

the approach to characterizing the fracture toughness of these materials has been to calculate J_{Ic} as if the serrations were absent, and on this basis the comparisons of Fig. 10 were made.

Finally, it must be noted that during specimen fabrication the weld metal was found to be extremely difficult to machine, and carbide tools were necessary. The Fe-14Mn-8Ni-1Mo-0.7C weld metal is a close relative of the Hadfield manganese steels which have high work-hardening capacities. Poor machinability is therefore a significant disadvantage of this weld metal composition.

REFERENCES

1. J. W. Elmer, H. I. McHenry, and T. A. Whipple, Strength and Toughness of Fully Austenitic Stainless Steel Filler Metals at 4 K, in NBSIR 81-1645, Materials Studies For Magnetic Fusion Energy Applications At Low Temperatures - IV (1981) 289-302.

2. D. T. Read and R. L. Tobler, Mechanical Property Measurements at Low Temperatures, in: Advances in Cryogenic Engineering, Vol. 28, Plenum Press, New York (1982) 17-28.

3. Standard Test Method for Plane Strain Fracture Toughness of Metallic Materials, ASTM Designation E 399-83, 1984 Annual Book of ASTM standards, Amer. Soc. Test. Mater., Philadelphia (1984) 519-554.

4. Standard Test Method for J_{Ic}, A Measure of Fracture Toughness, ASTM Designation E 813-81, 1984 Annual Book of ASTM Standards, Amer. Soc. Test. Mater., Philadelphia (1984) 763-781.

5. R. L. Tobler, D. T. Read, and R. P. Reed, Strength/Toughness Relationship for Interstitially Strengthened AISI 304 Stainless Steels at 4 K Temperature, in Fracture Mechanics: Thirteenth Conference, ASTM STP 743, R. Roberts, Ed., Amer. Soc. Test. Mater., Philadelphia (1981) 250-268.

6. R. L. Tobler, Ductile Fracture with Serrations in AISI 310S Stainless Steel at Liquid Helium Temperature, in: Elastic-Plastic Fracture: Second Symposium, Volume II-Fracture Resistance Curves and Engineering Applications, ASTM STP 803, C. F. Shih and J. P. Gudas, Eds., Amer. Soc. Test. Mater., Philadelphia (1983) 763-776.

Table 1. Chemical composition of the weld deposit (wt. %).

Fe	Mn	Ni	Mo	C	P	S	Si
balance	14.41	8.05	1.08	0.704	0.013	0.009	0.41

Table 2. Tensile properties of Fe-14Mn-8Ni-1Mo-0.7C weld metal at 4 K.

Specimen No.	Yield strength, σ_y, MPa (ksi)	Ultimate strength, σ_u, MPa (ksi)	Elongation in 44 mm gage length, %	Reduction of area, %
1	1180 (171)	1390 (202)	20.3	23
2	1050 (152)	1140 (165)	14.7	15
Avg	1115 (162)	1265 (184)	17.5	19
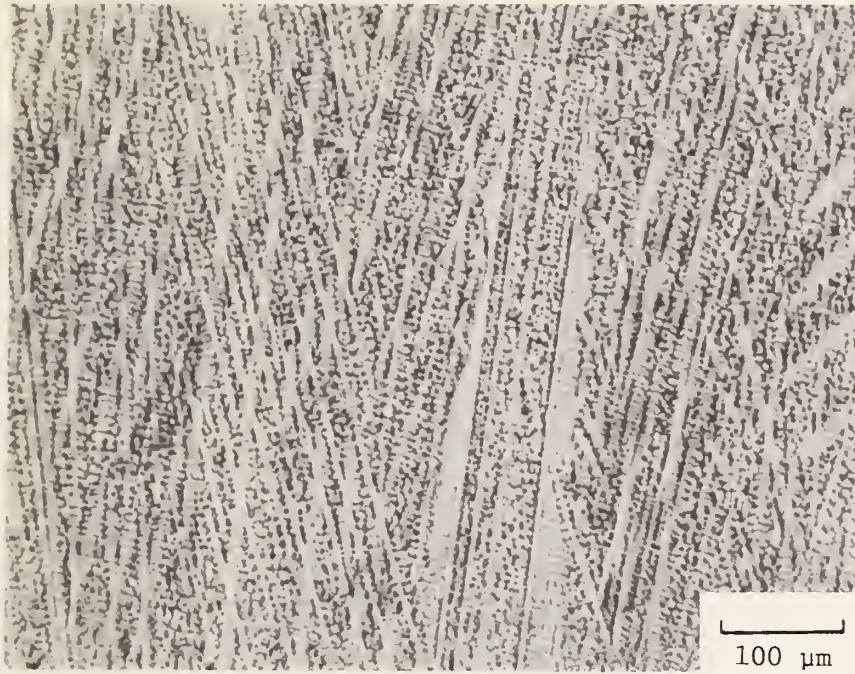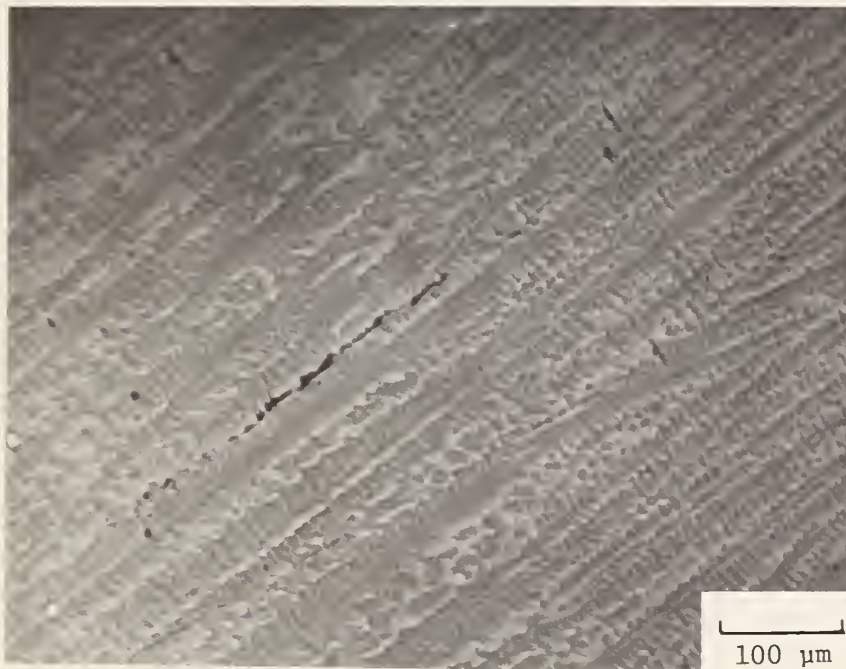
Figure 1. Etched microstructures of the weld fusion zone.

23
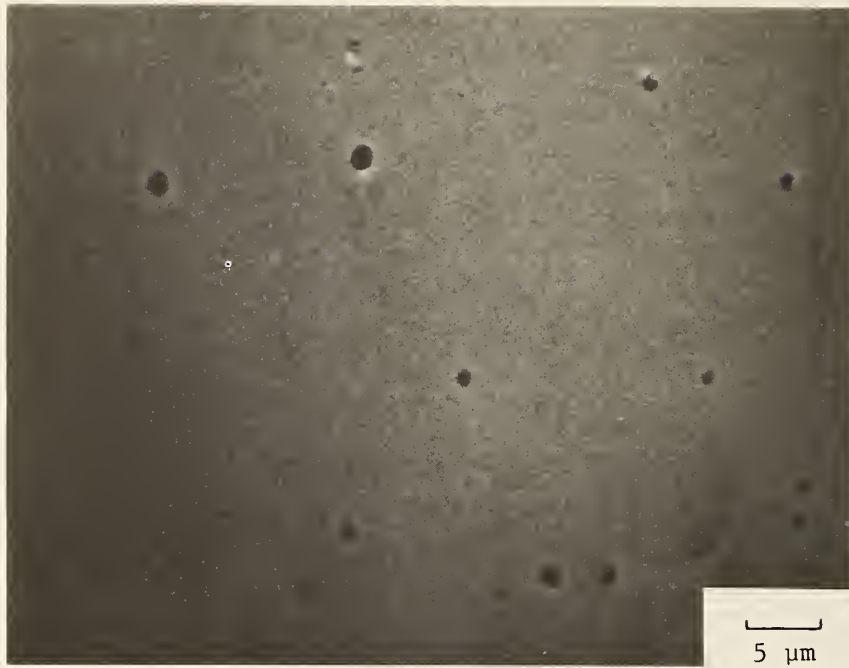
Figure 2. Unetched microstructure of the weld fusion zone.
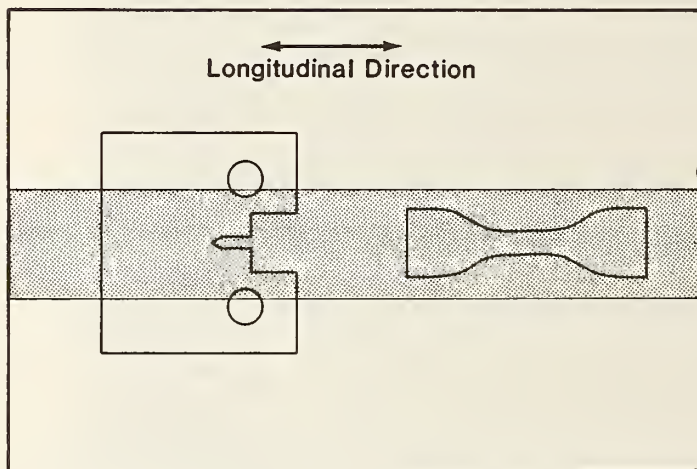
Overall weldment dimensions:

22x100x533

All dimensions in mm.
(not to scale)

Figure 3. Orientation of the tensile and compact specimens in the weldment.

Figure 4.   Cup-and-cone fracture morphology of 4 K tensile specimen.
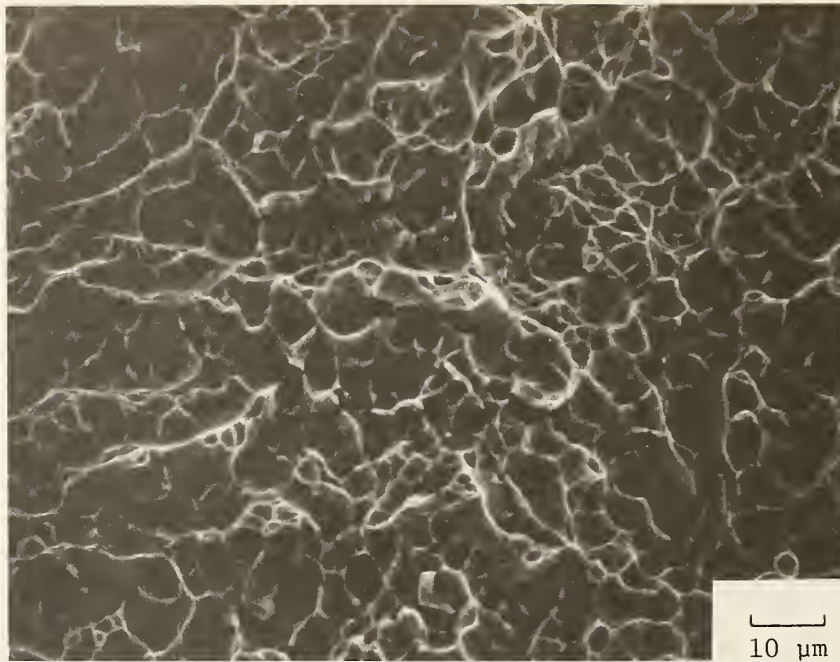
Figure 5.   Scanning electron microscope view of flat fracture
(center) section of 4 K tensile specimen.
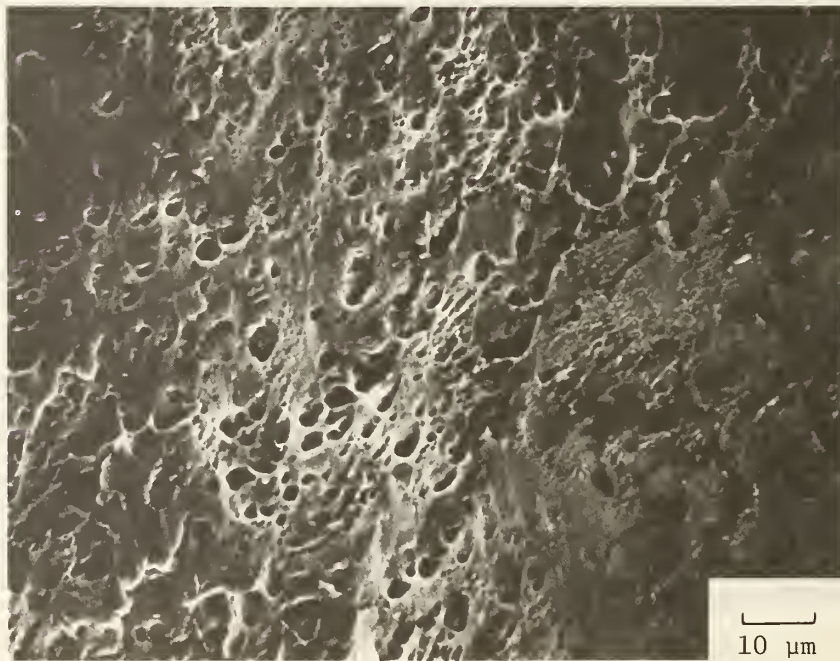
Figure 6.   Scanning electron microscope view of shear fracture
(edge) section of 4 K tensile specimen.
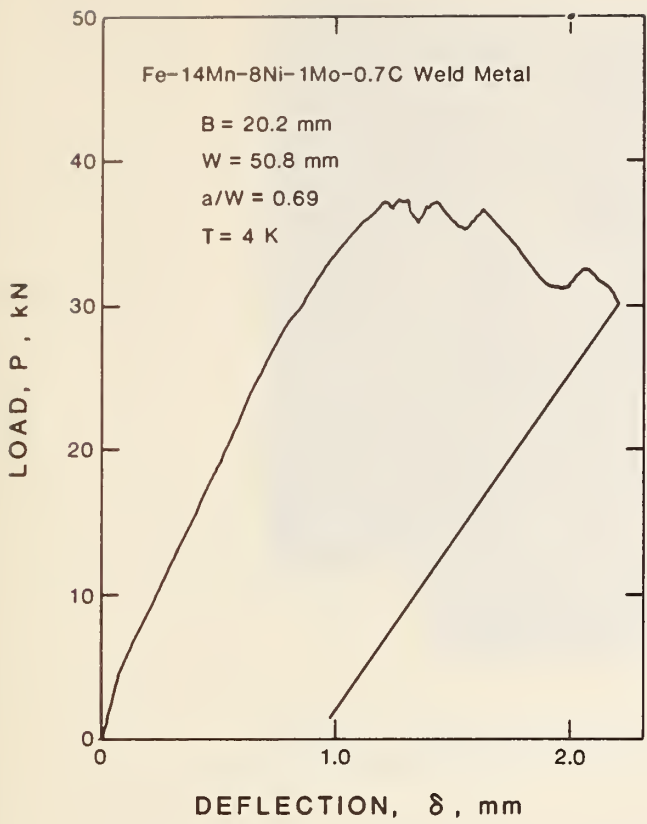
Figure 7.   Load-deflection test record
for a precracked compact
fracture specimen at 4 K.
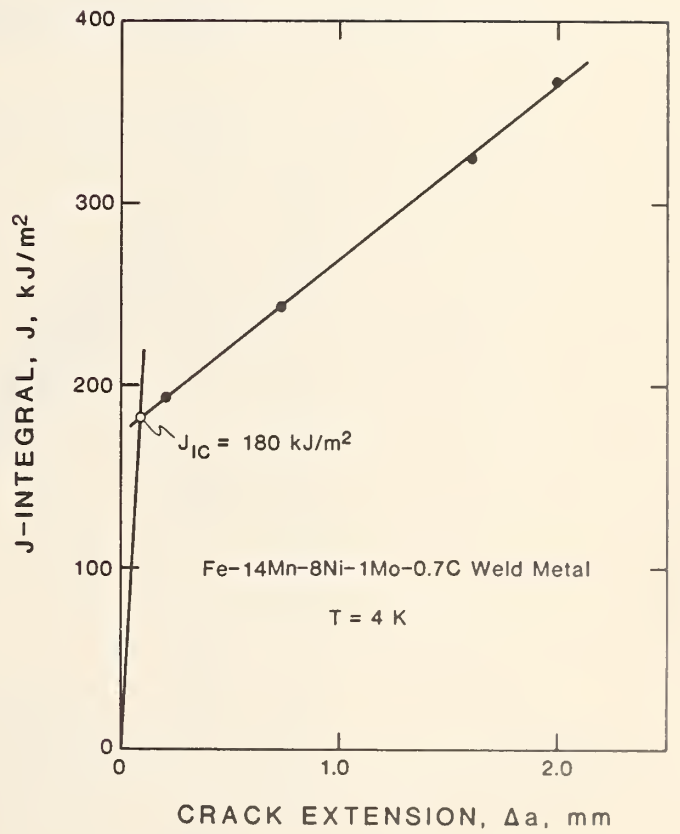
Figure 8.   J-resistance curve at 4 K.

27
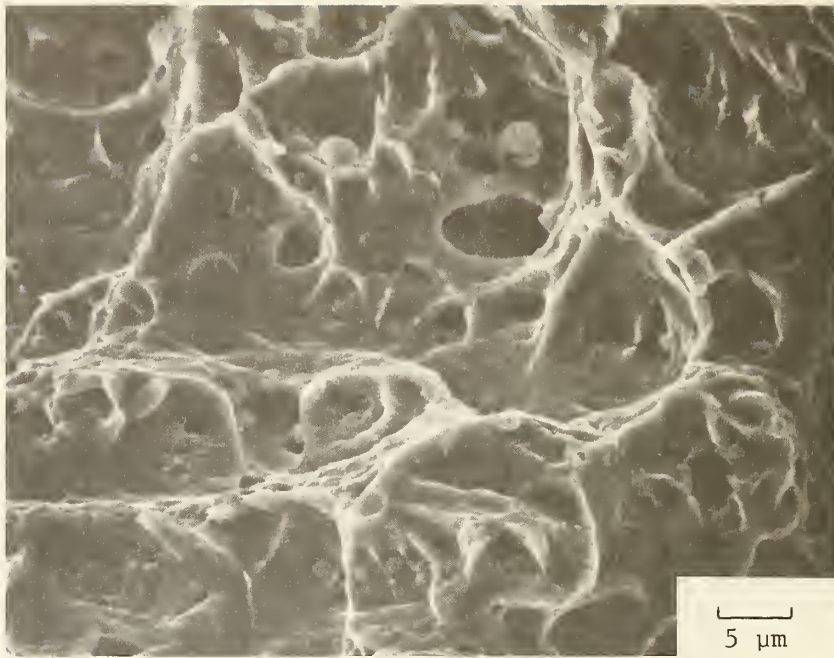
Figure 9. Scanning electron microscope view of the 4 K
fracture topography of the compact specimen.
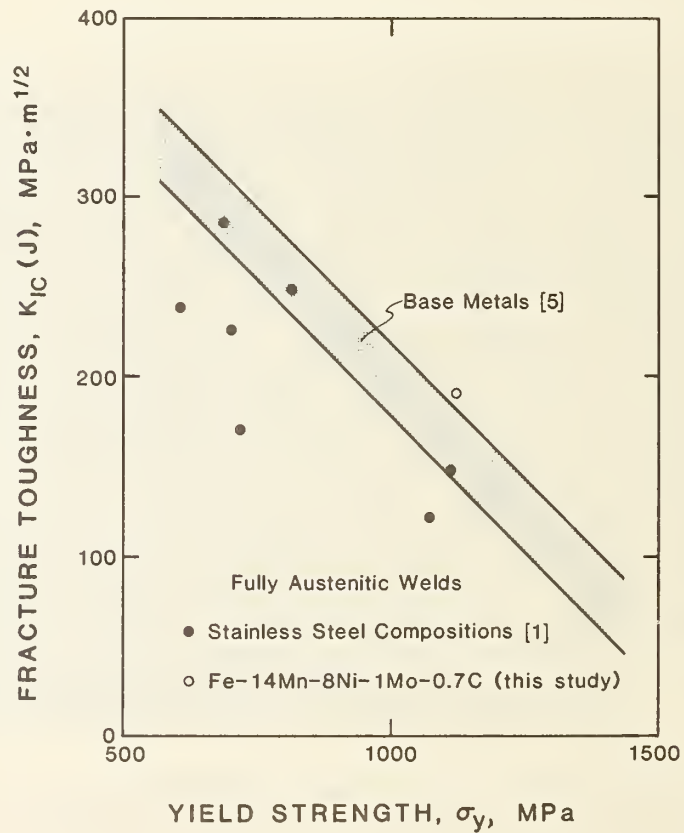
Figure 10. Compilation of strength-versus-toughness data
for fully austenitic welds at 4 K, including
comparison with AISI 304 type base metals at 4 K.

28

Predicting the Toughness of SMA
Austenitic Stainless Steel Welds at 77 K[*][+]

Thomas A. Siewert
Fracture and Deformation Division
National Bureau of Standards
Boulder, Colorado

Austenitic stainless steels often provide the best combination of strength and toughness for cryogenic applications: however, the weld toughness is frequently much lower than that of the base metal. This study proposes a more accurate and simpler model for developing improved filler metal compositions.

Several previous studies of the weld toughness were analyzed separately and in combination using a stepwise regression method and an expanded variable list. The total data base consisted of chemical composition, ferrite number (FN), and the Charpy V-notch (CVN) toughness at 77 K of 79 austenitic stainless steel welds deposited by the shielded metal arc process. Analysis of the complete data base revealed that the FN calculated from the Schaeffler diagram was the most significant variable for predicting the CVN toughness. The predictive equation produced a better correlation between the measured and predicted values of weld toughness than the previously published predictive equations.

The group of 36 fully austenitic welds and the group of 21 type 316 welds in the data base were analyzed by the same procedure. In both cases the ferrite number was found to be the most significant predictor of toughness.

1.0 Introduction

Austenitic stainless steels are often chosen for support structures in cryogenic service because of their high toughness. Unfortunately, the weld toughness can be considerably lower than that of the plate material, especially for shielded metal arc welds.[1] Previous studies have correlated stainless steel weld composition and toughness at 77 K.[2-4] This paper, using a stepwise regression technique, reexamines these data and develops improved correlations between the composition and toughness. Four improved predictive equations are compared to the previously developed equations.

Siewert[2] and Szumachowski and Reid[3,4] statistically correlated the Charpy V-Notch (CVN) toughness at 77 K to the composition, for a wide variety of stainless steel welds produced by the SMA process. These studies developed equations for quantitative prediction of the weld toughness based on the weld's chemical composition. However, these studies used a six- or seven-variable model with the variables chosen from a very limited data set.

Siewert reported the predictive equation

$$\text{CVN (ft·lbf)} = 62 - 60\ C - 7\ Mn - 2.5\ Cr + 2.9\ (Ni-Mo) - 0.75\ FN \quad (1a)$$

which, when converted into SI units by multiplying the ft·lbf units by 1.36 to obtain joules, becomes

$$\text{CVN (J)} = 84 - 82\ C - 10\ Mn - 3.4\ Cr + 3.9\ (Ni-Mo) - FN \quad (1b)$$

where the elements are in weight percent and FN (ferrite number) is the measured value from the weld. The R^2 value (a correlation of the measured value with the predicted value) was 0.61.

Szumachowski and Reid reported the predictive equation

$$\text{CVN (ft·lbf)} = 82.9 - 175.8\ C + 0.42\ Mn - 0.90\ Cr + 2.16\ Ni - 0.80\ Mo$$
$$- 111.3\ N - 3.45\ (\text{coating}) \quad (2a)$$

which, when converted to SI units, becomes

$$\text{CVN (J)} = 113 - 239\ C + 0.57\ Mn - 1.22\ Cr + 2.94\ Ni - 1.09\ Mo$$
$$- 151\ N - 4.69\ (\text{coating}) \quad (2b)$$

where the elements are in weight percent. The value of either 15 or 16 should be inserted for coating to distinguish between the lime (-15) and rutile (-16) slag system designations when evaluating their effect on the toughness. In this case the R^2 value was 0.69.

This paper uses a broader data base than the earlier study,[2] analyzes the effects of additional elements, includes interactive terms such as compounds and various mathematical representations of delta ferrite, and then selects

the variables from the combined data bases by a stepwise regression technique. This process provides a clearer ranking of the factors that control the 77-K weld-metal toughness and so provides more detailed guidance for future improvements in electrodes.

2.0   Procedure

The data bases of Siewert[2] and Szumachowski and Reid[3,4] were combined because they had similar ranges of compositions, welding procedures, and CVN testing procedures. But, because a systematic error due to slight differencs in the slag system or weld procedure for the two bases could exist, a term distinguishing the two bases was included in the analysis.

Siewert's data base was expanded by the addition of a number of elements, which had been measured but not included in the data analysis. Percentages by weight for these elements--O, Ti, V, Co, and Cu--were added to the base (Table 1). Szumachowski and Reid's data were used as originally published and are not listed here.[3,4]

Additional variables were generated by forming products between various elements to determine if these interactions might be significant. The variables FNCD, FNCS, FNCH, and FNCB are mathematical representations of the various constitution diagrams used to predict the FN (the third letter of each variable emphasizes that they were calculated, and the last letter of each term refers to DeLong, Schaeffer, Hall, and Babcock and Wilcox, respectively).[5] These constitution diagrams, developed to predict FN from the composition, were reduced to equation form and listed in this Welding Research Council publication. Table 2 defines the variables, both elements and combinations, that were used in the analysis of Table 1. Table 3 defines the variables that were common to both data sets and so used for the various analyses of the combined sets.

A multiple linear regression model was used. A stepwise regression technique was used to select variables to be included in the model. This procedure computes the correlations between all the variables and the dependent variable, CVN. It then selects the variable most highly correlated with CVN and enters it into the model. Using partial correlation coefficients as before, it next selects the variable whose partial correlation with CVN is the highest. This process is repeated until none of the variables selected can meet the selection criterion, based on an F-statistic. In this study, an F value of 4.0 was chosen as the critical value in the stepwise regression technique. (F is defined as the square of the quantity-regression coefficient divided by the standard error. F can also be expressed roughly as a 95 percent confidence level or a ratio of best parameter estimate to standard error, of 4.0.)

3.0   Results and Discussion

3.1   Analysis of Table 1 (18 welds)

This table (the expanded Siewert data base) contained variables that were not in the Szumachowski and Reid data base: O, Ti, V, Co, Cu, and their interactive terms. The predictive equation computed from these data is

$$\text{CVN (J)} = 38 - 0.68 \text{ FNCD} - 1.67 \text{ FN} \tag{3}$$

where FNCD and FN are defined in Table 2. The results are summarized in Table 4.

The R^2 value of 0.94 indicates this model fits the data better than the previous model did (Equation 1), even though the new model has only two variables (the measured ferrite number) and FNCD (a representation of the ferrite number). FNCD is listed in Table 2 as a mathematical equation with many terms, but its physical significance is that of one variable, the potential to form ferrite or, when negative, the relative reluctance to form ferrite. FNCD was the first variable selected by the stepwise technique, indicating it was the most significant variable in predicting the CVN toughness. It was slightly more significant (21 percent) than FNCS but substantially more significant (200 percent) than Ni, the variable of third highest significance.

The second iteration resulted in the addition of FN to the model. None of the other variables met the requirements of an F value of 4.0 (corresponding to a 95 percent confidence level). The choice of FN (the measured ferrite number and so always positive) in this iteration indicates a slight difference in the effect of ferrite in the positive and negative potential regions. Changes in FN in the positive (measured) region have a greater effect on toughness than changes of ferrite potential in the negative region.

The list of variables not in the equation (Table 4) should also be reviewed because variables with an F value greater than 2.0 came close to meeting the selection criterion. Both C and Cr had negative coefficients, which agree with the negative coefficients previously reported (Equations 1 and 2). The negative coefficient for Co is of questionable significance because of the limited range of values. The negative coefficients for CMn, CCr, and CN might indicate some interactions are occurring.

Since none of the variables unique to Table 1 were found to be significant, the two data bases were combined to improve the accuracy of the model. The larger base clarified the slight indication of some correlation of these other terms.

3.2 Analysis of the Combined Data Base (79 Welds)

The predictive equation computed from the data is

$$\text{CVN (J)} = 19 - 1.4 \text{ FNCS} - 890 \ C^2 + 1.4 \text{ Ni} \tag{4}$$

where FNCS and C^2 are defined in Table 3. The results are presented in Table 5. The R^2 value of 0.73 indicates a poorer fit than that of Table 4. However, with just three terms, the model has a better fit than that of reference 2 with 6 terms (Equation 1) or reference 4 with 7 terms (Equation 2).

This time FNCS was the variable first selected by the stepwise technique. Its F value of 149 indicated substantially greater significance than the F value of 110 for FNCD, the F value of 108 for FNCH and FNCB, and the F value

of 97 for Ni. Clearly, negative ferrite potential, in general, and FNCS, here in particular, is the most significant variable in predicting the cryogenic toughness. The variable FNCS differs from FNCD in several characteristics. Two of these are considered to have a significant effect on the program's choice of the best term.

1. The term FNCS is based on the Schaeffler constitution diagram that covers a wide range of compositions and many different phase regions (Fig. 1).[6] For this reason, it is expected to be accurate for the ranges in compositions included in the data bases. In the Schaeffler diagram, the constant ferrite lines pivot around an axis with a varying angular orientation. The negative ferrite isopleths (constant ferrite lines) were also chosen to vary with a variable spacing, unlike the parallel and equally spaced negative ferrite lines used by Szumachowski and Reid.[3] The variable FNCD is based on the DeLong constitution diagram, which covers of a small region of the Schaeffler diagram that was refined specifically for the ferrite-containing austenitic stainless steels.[7] The type 330 compositions in the data base fall far outside the intended bounds of applicability.

2. The variable FNCD includes nitrogen. Nitrogen has the two opposing effects of reducing the FN (which improves the toughness according to equations 3 and 4 and reference 7) while degrading the toughness, at constant FN.[4] Apparently it is hard to resolve these conflicting effects since the program chose the term without nitrogen (FNCS).

To clarify these two effects, another variable FNCSN was produced, incorporating the nitrogen factor from FNCD into the FNCS equation. Its F value of 134 seems to indicate that both nitrogen and the narrower intended range of the DeLong diagram reduce the statistical significance of FNCD for the combined bases, with range of the diagram having the larger effect.

In the second iteration of the stepwise technique, C^2 was added to the model. Its F value was approximately double that of C, the second largest value. This variable indicates the deleterious effect of carbon, substantially increasing in its effect at higher concentrations. This is quite surprising, as the type 330 stainless steel compositions had both the best toughness and the greatest carbon concentrations. This model suggests a type 330L might produce substantial improvements in toughness.

In the third and last iteration, Ni was chosen. The addition of this variable emphasizes the beneficial effect of nickel on the toughness, even beyond its effect in the term FNCS.

The list of the variables not in the equation yields further clues to the effects of the variables that do not quite meet the significance standards but could indicate a trend. Those with an F value above 1 are now considered since this is the largest data base, and possible trends can be investigated in the following analyses of certain regions of applicability. The variable C is positively correlated and seems to indicate that C^2 slightly overestimates the negative effect of C. The variable S is positively correlated, because the type 330 compositions tend to have the highest sulfur levels while producing the best toughness. The variable CMo is negatively correlated, giving an indication of a possible interaction. The term base gives a

slight indication of differences between the two data bases. Six nitrogen-containing variables--N, MnN, CrN, FNCD, FNCH and FNCB--have negative correlations. This is a good indication that nitrogen is having a deleterious effect, but its effect is not significant over the entire range of compositions. Although Szumachowski and Reid[4] indicated a number of compositions where nitrogen seemed to have a clearly detrimental effect, there might be other compositions where the effect is less pronounced. These other compositions would be of interest since nitrogen could be added to increase the strength without degrading the toughness, similar to what has been accomplished with the plate material.[8]

A search was made for other variables (especially higher order effects) that would improve the model. After the model was fitted, all the observed values, predicted values, and residuals from the statistical computations were plotted against all the variables in Table 3. No trends were observed. Therefore, the model seems to be the best that can be obtained for the entire data base. For a better understanding of the applicable range of the model, selected portions of the data base were examined in more detail.

3.3 Analysis of 36 Fully Austenitic Welds

The fully austenitic compositions were selected by choosing FNCS to be less than or equal to zero. The results are presented in Table 6. The predictive equation is

$$CVN \ (J) = 5 - 2.3 \ FNCS - 1000 \ C^2 + 82 \ Si \tag{5}$$

where FNCS, C^2, and Si are defined in Table 3.

In general, the model is a confirmation of that obtained for the combined data bases (Table 5). The slightly higher coefficient for FNCS offsets the effect of Ni in the other model. The choice of Si with a positive coefficient is surprising. Silicon is generally considered to reduce the toughness. Its choice is probably due to the high silicon levels in some of the high toughness compositions, similar to the choice of C^2 in the previous model.

The list of variables not in the equation gives some guidance as to possible trends that did not meet the significance requirements. Since this analysis considers only a portion of the entire data base, the value of 2.6 for base indicates a slight difference between the two data bases that had been combined in this study. This is probably due to slight differences in the manganese content in the type 330 compositions. The variables Cr, CCr, and FNCD indicate some positive correlation while N, CMn, and MnN indicate some negative correlation. Less significance is attributed, in general, to the list of variables not in the equation since the data set is smaller.

3.4 Analysis of Type 316 Welds

As indicated, type 316 stainless steel, primarily the low-carbon grade 316L, has been used for the majority of recent cryogenic construction. It has produced good toughness while resisting the microfissuring associated with the fully austenitic compositions. Results of the 21 type 316 compositions are summarized in Table 7. The predictive equation is

$$CVN\ (J) = 49 - 2.7\ FNCS - 95\ MnN - 2\ FN \tag{6}$$

where FNCS, MnN, and FN are defined in Table 3.

Once again, FNCS was determined to be the most significant predictor of cryogenic toughness. The previously observed[4] detrimental effect of nitrogen in this grade is indicated best by the variable MnN. The variable FN is again an indicator that the presence of ferrite is more detrimental than the increase in ferrite potential in the negative region. None of the variables that had not been included in the equation had F values greater than 2.

4.0 Conclusions

Based on a statistical correlation between SMA weld compositions and their Charpy V-Notch toughness, the following conclusions are drawn:

1. Ferrite number, calculated by the Schaeffler diagram and allowed to be negative, is consistently the most significant predictor of CVN toughness in welds at 77 K. The importance of this variable was not recognized in previous studies.

2. Other variables, such as measured FN, Ni, Si, ferrite number calculated by the DeLong diagram (FNCD) and C^2, can be significant, depending on the range of compositions considered.

3. Over the entire range of austenitic stainless steel weld compositions considered, the best predictive equation at 77 K is:

$$CVN\ (J) = 19 - 1.4\ FNCS - 890\ C^2 + 1.4\ Ni \tag{4}$$

where the variables are defined in Table 3.

4. Further improvements in the toughness of electrodes for cryogenic service can best be obtained by decreasing the ferrite potential. Such fully austenitic compositions will require further study of the microfissuring tendency.

5.0 Acknowledgment

6.0 References

1. "Low Temperature Materials Workshop for Magnetic Fusion Energy - An Informal Summary," in Materials Studies for Magnetic Fusion Energy Applications at Low Temperatures - VIII, R. P. Reed, ed., NBSIR 85-3025, National Bureau of Standards, Boulder, Colorado, p. 305.

2. Siewert, T. A., "How to Predict Impact Energy from Stainless Steel Composition," Weld. Des. Fabr., June 1978, p. 88.

3. Szumachowski, E. R., and Reid, H. F., "Cryogenic Toughness of SMA Austenitic Stainless Steel Weld Metals: Part I - Role of Ferrite," Weld. J., Nov. 1978, p. 325-S.

4. Szumachowski, E. R., and Reid, H. F., "Cryogenic Toughness of SMA Austenitic Stainless Steel Weld Metals: Part II - Role of Nitrogen," Weld. J., February 1979, p. 34-S.

5. "H_2 Embrittlement of Austenitic Stainless Steel with Special Consideration Given to Sigma Phase," Weld. Res. Bull. 240, Aug. 1978.

6. Schaeffler, A., "Constitution Diagram for Stainless Steel Weld Metal," Met. Prog., 56, 1946, p. 680.

7. DeLong, W. T., "Ferrite in Austenitic Stainless Steel Weld Metal," Weld. J., July 1974, p. 173-S.

8. Read, D. T., McHenry, H. I., Steinmeyer, P. A., and Thomas, R. D., Jr., "Metallurgical Factors Affecting the Toughness of 316L SMA Weldments at Cryogenic Temperatures," in Materials Studies for Magnetic Fusion Energy Applications at Low Temperatures - II, NBSIR-79-1609, R. P. Reed, ed., National Bureau of Standards, Boulder, Colorado, 1979, p. 315.

TABLE 1

WELD DEPOSIT COMPOSITIONS - BASIS FOR REFERENCE 7, WITH ADDED VARIABLES
(Elements in Weight Percent)

TYPE	C	Mn	Si	P	S	Cr	Ni	Mo	N	O	Ti	Co	V	Cu	FN (Measured)	CVN (J)
316 -16	0.043	1.92	0.52	0.025	0.014	19.2	13.2	2.20	0.056	0.086	0.035	0.08	0.09	0.13	4	24
310 -16	0.127	2.15	0.54	0.018	0.012	26.4	20.5	0.22	0.060	0.095	0.051	0.18	0.06	0.14	0	46
308 -15	0.056	1.95	0.59	0.018	0.020	19.8	9.5	0.09	0.044	0.073	0.009	0.14	0.05	0.10	8	16
308L-15	0.033	1.81	0.50	0.019	0.020	19.2	9.5	0.15	0.066	0.067	0.007	0.15	0.06	0.08	6	29
308L-16	0.027	1.68	0.42	0.019	0.014	19.4	9.5	0.13	0.090	0.084	0.025	0.14	0.06	0.10	4	22
308 -16	0.043	1.73	0.49	0.026	0.017	20.0	9.9	0.12	0.074	0.086	0.029	0.12	0.05	0.16	6	22
308L-15	0.035	1.99	0.64	0.027	0.020	19.9	9.7	0.43	0.056	0.075	0.007	0.20	0.05	0.16	6	26
308L-15	0.040	2.14	0.31	0.033	0.018	19.6	9.7	0.44	0.064	0.080	0.009	0.18	0.05	0.18	6	27
308L-15	0.045	2.63	0.23	0.033	0.016	19.9	9.8	0.44	0.050	0.088	0.009	0.18	0.05	0.18	6	22
308 -15	0.050	1.78	0.58	0.023	0.023	19.8	9.6	0.11	0.074	0.082	0.010	0.32	0.05	0.11	6	16
308L-15	0.030	1.52	0.49	0.025	0.020	18.9	9.7	0.15	0.085	0.074	0.005	0.03	0.05	0.09	4	34
310 -15	0.200	1.83	0.49	0.015	0.013	25.9	20.4	0.21	0.068	0.073	0.018	0.17	0.05	0.14	0	42
310Mo-15	0.105	1.62	0.86	0.018	0.008	25.1	19.7	2.60	0.050	0.063	0.019	0.09	0.06	0.08	5	19
316 -15	0.050	1.56	0.51	0.035	0.020	18.0	13.3	2.20	0.082	0.073	0.003	0.11	0.05	0.14	0	42
316L-15	0.030	1.57	0.54	0.027	0.015	17.9	13.5	2.20	0.050	0.067	0.003	0.05	0.05	0.11	0	45
330 -15	0.200	1.63	0.45	0.024	0.011	15.1	33.5	0.72	0.036	0.043	0.025	0.19	0.07	0.19	0	91
308 -15	0.060	1.93	0.47	0.018	0.013	19.9	9.7	0.13	0.064	0.054	0.019	0.06	0.05	0.15	6	24
308L-16	0.029	0.90	0.71	0.018	0.015	20.4	10.0	0.02	0.086	0.091	0.029	0.05	0.06	0.04	12	16

TABLE 2

VARIABLES USED IN THE ANALYSIS OF TABLE 1

VARIABLE	DEFINITION
C	–
Mn	–
Si	–
P	–
S	–
Cr	–
Ni	–
Mo	–
FN	Measured on weld;
Coating	5 is entered for a
	–15 coating and 6 for
	a –16 coating
O	–
Ti	–
Co	–
V	–
Cu	–
C^2	C · C
Mn^2	Mn · Mn
CMn	C · Mn
CCr	C · Cr
CN	C · N
MnO	Mn · O
SiO	Si · O
MnN	Mn · N
CrN	Cr · N
TiN	Ti · N
TiO	Ti · O
FNCD	$-30.65 + 3.49 \ (Cr + Mo + 1.5 \ Si)$ $- \ 2.5 \ [Ni + 30 \ (C + N) + 0.5 \ Mn]$
FNCS	$-39.1 + 43.5 \ (Cr + Mo + 1.5 \ Si + 0.5 \ Cb -$ $- \ 5.8)/ \ (Ni + 30 \ C + 0.5 \ Mn + 2)$
FNCH	$-13.77 + 2.88 \ (Cr + 1.21 \ Mo + 0.48 \ Si)$ $- \ 3.125 \ (Ni + 0.11 \ Mn + 0.0086 \ Mn^2$ $+ \ 24.5 \ C + 18.6 \ N)$
FNCB	$-15.35 + 3(Cr + 1.21 \ Mo + 0.48 \ Si)$ $- \ 3.18 \ (Ni + 0.11 \ Mn + .0.0086 \ Mn^2$ $+ \ 24.5 \ C + 18.6 \ N)$

TABLE 3

VARIABLES USED IN THE ANALYSIS OF THE COMBINED DATA BASES

VARIABLE	DEFINITION
C	–
Mn	–
Si	–
P	–
S	–
Cr	–
Ni	–
Mo	–
FN	Measured on weld;
Coating	5 is entered for a -15 coating and 6 for a -16 coating
Base	Term to distinguish the 2 data bases
C^2	C · C
Mn^2	Mn · Mn
CMn	C · Mn
CCr	C · Cr
CN	C · N
MnN	Mn · N
CrN	Cr · N
CrNi	Cr · Ni
FNCD	$-30.65 + 3.49 \ (Cr + Mo + 1.5 \ Si)$ $- 2.5 \ [Ni + 30 \ (C + N) + 0.5 \ Mn]$
FNCS	$-39.1 + 43.5 \ (Cr + Mo + 1.5 \ Si + 0.5 \ Cb$ $- 5.8)/ \ (Ni + 30 \ C + 0.5 \ Mn + 2)$
FNCH	$-13.77 + 2.88 \ (Cr + 1.21 \ Mo + 0.48 \ Si)$ $-3.125 \ (Ni + 0.11 \ Mn + 0.0086 \ Mn^2$ $+ 24.5 \ C + 18.6 \ N)$
FNCB	$-15.35 + 3 \ (Cr + 1.21 \ Mo + 0.48 \ Si)$ $- 3.18 \ (Ni + 0.11 \ Mn + 0.0086 \ Mn^2$ $+ 24.5 \ C + 18.6 \ N)$

TABLE 4

PREDICTIVE EQUATION BASED ON TABLE 1

Variable	Coefficient	Std. Error of Coefficient	F*
(y intercept)	38		
FNCD	-0.68	0.07	102
FN	-1.67	0.41	·17

$R^2 = 0.94$ Compositions Analyzed = 18

Variables Not in Equation

Variable	Partial Correlation	F*
C	-0.42	3.0
Mn	-0.26	1.0
Si	-0.07	0.06
P	0.32	1.6
S	0.24	0.9
Cr	-0.36	2.1
Ni	-0.29	1.3
Mo	0.002	0.0
N	0.07	0.08
Coating	-0.21	0.7
O	-0.18	0.5
Ti	-0.35	2.0
Co	-0.45	3.5
V	-0.25	0.9
Cu	-0.05	0.04
C^2	-0.33	1.8
Mn^2	-0.22	0.7
CMn	-0.42	3.0
CCr	-0.38	2.4
CN	-0.36	2.1
MnO	-0.31	1.5
SiO	-0.11	0.2
MnN	-0.23	0.8
CrN	-0.11	0.2
TiN	-0.30	1.4
TiO	-0.30	1.3
FNCS	0.30	1.4
FNCH	0.35	1.9
FNCB	0.35	1.9

*A value of 4 is necessary to enter the equation.

40

TABLE 5

PREDICTIVE EQUATION BASED ON COMBINED DATA BASES

Variable	Coefficient	Std. Error of Coefficient	F*
(y intercept)	19		
FNCS	-1.4	0.26	26
C^2	-890	193	21
Ni	1.4	0.45	10

$R^2 = 0.73$ Compositions Analyzed = 79

Variables Not in Equation

Variable	Partial Correlation	F*
C	0.13	1.3
Mn	-0.09	0.6
Si	0.11	0.8
P	-0.02	0.02
S	0.18	2.6
Cr	-0.12	1.1
Mo	-0.04	0.2
N	-0.16	2.2
FN	0.02	0.02
Coating	-0.07	0.4
Base	-0.13	1.3
Mn^2	-0.08	0.5
CMn	-0.08	0.5
CN	-0.02	0.02
CCr	0.08	0.5
CMo	-0.17	2.1
MnN	-0.21	3.4
CrN	-0.17	2.2
CrNi	-0.05	0.2
FNCD	-0.12	1.0
FNCH	-0.14	1.4
FNCB	-0.14	1.4

*A value of 4 is necessary to enter the equation.

TABLE 6

PREDICTIVE EQUATION BASED ON THE FULLY AUSTENITIC COMPOSITIONS

Variable	Coefficient	Std. Error of Coefficient	F*
(y intercept)	5		
FNCS	-2.3	0.31	54
C^2	-1000	200	24
Si	82	20	16

$R^2 = 0.76$ Compositions Analyzed = 36

Variables Not in Equation

Variable	Partial Correlation	F*
C	0.16	0.8
Mn	-0.19	1.2
P	0.23	1.7
S	-0.15	0.7
Cr	0.29	2.8
Mo	-0.02	0.01
N	-0.24	2.0
FN	-0.16	0.8
Coating	-0.23	1.8
Base	-0.28	2.6
Mn^2	0.20	1.4
CMn	-0.29	3.0
CN	0.09	0.2
CCr	0.27	2.5
CMo	-0.20	1.3
MnN	-0.29	2.9
CrN	-0.09	0.2
FNCD	0.31	3.3
FNCH	0.11	0.4
FNCB	0.12	0.5

*A value of 4 is necessary to enter the equation.

TABLE 7

PREDICTIVE EQUATION BASED ON THE TYPE 316 COMPOSITIONS

Variable	Coefficient	Std. Error of Coefficient	F*
(y intercept)	49		
FNCS	-2.7	0.49	31
MnN	-95	26	14
FN	-2	0.78	7

R^2 = 0.87   Compositions Analyzed = 21

Variables Not in Equation

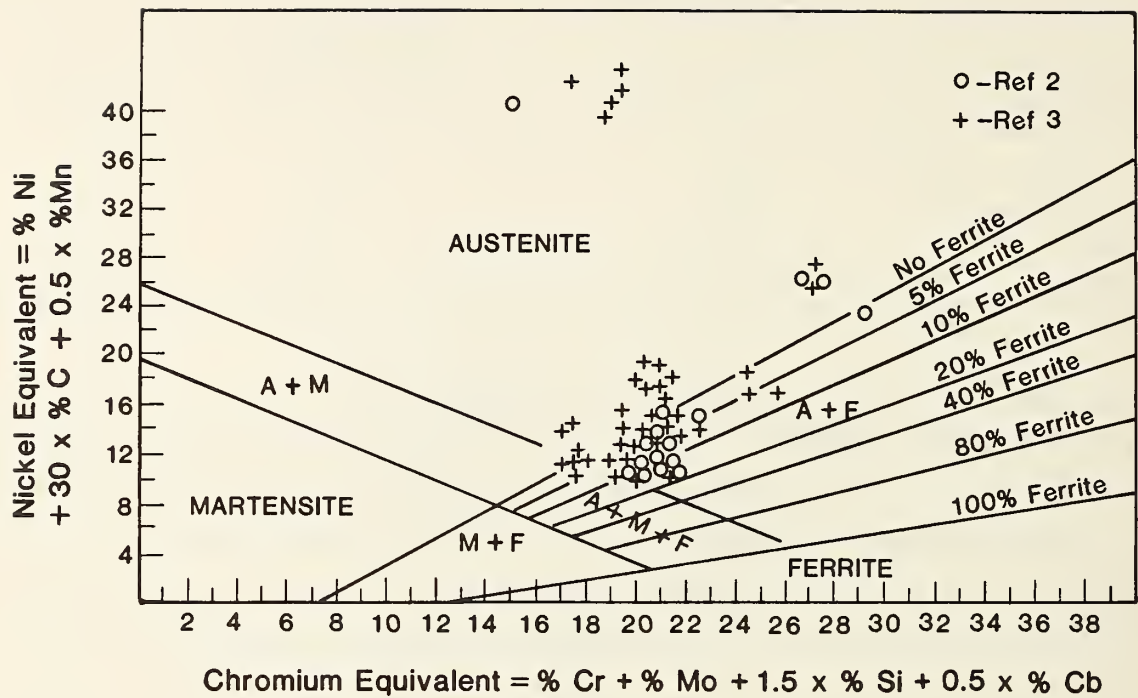| Variable	Partial Correlation	F*
C	0.28	1.4
Mn	-0.15	0.4
Si	0.20	0.7
P	0.28	1.4
S	0.12	0.25
Cr	0.10	0.16
Ni	0.10	0.43
Mo	0.16	0.15
N	0.15	0.39
Coating	-0.05	0.04
Base	-0.05	0.04
C^2	0.25	1.0
Mn^2	-0.16	0.41
CMn	0.25	1.05
CN	0.24	0.98
CCr	0.28	1.34
CMo	0.29	1.42
CrN	0.18	0.52
CrNi	0.09	0.14
FNCD	0.25	1.0
FNCH	0.25	1.0
FNCB	0.24	1.0

*A value of 4 is necessary to enter the equation.

43

Figure 1. Schaeffler Diagram, illustrating the distribution of the weld compositions.

NONMETALLICS

NONMETALLICS PROGRAM

LEADERS: M. B. Kasen, H. M. Ledbetter, NBS
STAFF: M. W. Austin, R. D. Kriz, NBS

OBJECTIVES:

1.   Measurement, modeling, and understanding of the properties of composites
     that enter essentially into the conception, design, construction,
     operation, and performance of magnetic-fusion-energy equipment.
2.   In cooperation with industry, the establishment and refinement of
     cryogenic-grade specifications for insulating laminates and test methods
     for materials selection.

RESEARCH PAST YEAR (1984):

1.   Comparison of theory and experiment on the influence of damage in woven
     composites at low temperatures on load-deformation behavior at low
     strains.
2.   Study of elastic representation surfaces of unidirectional composites.
3.   Development of radiation-resistant insulators for magnetic fusion energy
     systems that utilize superconducting magnetic confinement at low tempera-
     tures.

RESEARCH THIS YEAR (1985):

1.   Study of the relationship between damage and load-deformation behavior
     of woven composites at low temperatures for cyclic mechanical and
     thermal loads.
2.   Development of improved test methods for new polymer materials subject
     to neutron irradiation at low temperatures.
3.   Development of a computer program to calculate the load-deformation
     behavior of metallic-nonmetallic laminates structures at low tempera-
     tures.

MECHANICAL-DAMAGE EFFECTS
IN WOVEN LAMINATES AT LOW TEMPERATURES

Ronald D. Kriz
Fracture and Deformation Division
Center for Materials Science
National Bureau of Standard
Boulder, Colorado 80303

Walter J. Muster
Metals Division
Swiss Federal Laboratories for Materials
Testing and Research (EMPA)
Dubendorf, Switzerland

Large quantities of nonmetallic woven composites will be used in magnetic fusion energy structures at low temperatures. We predicted and measured the influence of crack formation on the mechanical performance of standard glass/epoxy laminates (G-10CR, G-11CR) at low temperatures. Mechanics of the load-deformation response of a unit cell of weave was predicted by a finite element model that assumes generalized plane strain. Damage was modeled as macrocracks confined to individual fiber bundles that were oriented transverse to the tensile load direction. From experiments with tension loads, we studied the formation of damage as a collection of fiber breaks, fiber bundle cracks, and delaminations between adjacent fiber bundles. Earlier experiments had shown that the strain to failure of the laminate increased when the components became brittle at low temperatures. We explain this behavior from results of our studies on the formation of damage in three-layer laminates of G-10CR and G-11CR at 76 K and 295 K: we

measured fiber bundle cracks in the laminate interior and individual fiber fractures at the laminate edges by a replication technique. We discovered that the sequence and types of damage, at strains well below ultimate, control the discontinuities (knees) in the load-deformation (stress-strain) diagrams. However, between the knees, the material remains linear elastic at lower temperatures. We found that G-11CR has two knees and three distinct moduli; G-10CR has only two moduli and a single knee at a lower strain than G-11CR. Decrease in moduli measured near the knees compared well with predictions from the finite element model.

Introduction

Magnetic-fusion-energy (MFE) power plants may use large quantities of nonmetallic composites [1]. There are a variety of applications where woven glass/epoxy laminates can provide thermal insulation, electrical insulation, and structural support. For instance, in the structural design of superconducting magnets at 4 K, nonmetallics are used primarily as electrical insulation where only small mechanical loads occur. However, when cooled to liquid helium temperature (4 K), large internal stresses can occur within these structures because of large differential thermal contractions between metals and nonmetals. When these thermally induced stresses are combined with stresses induced by small mechanical loads (magnetic loads), microcracks may initiate at applied loads well below the yield strength. The formation of large numbers of microcracks could limit the electrical, thermal, and mechanical usefulness of these materials for MFE applications. The coalescence of microcracks and voids could also limit their usefulness as barriers for containment of cryogenic liquids and gas.

In anticipation of these MFE applications, standardization of G-10CR and G-11CR woven glass/epoxy high pressure industrial laminates* was established for low temperatures in cooperation with the National Bureau of Standards [2,3]. Standardization of these materials for low temperature applications minimized the variability in electrical, thermal, and mechanical properties that concern the MFE designer.

In this study, we measured the variability in mechanical performance caused by the formation of damage in a unit cell of plain weave (see Fig. 1). The concept of a unit cell was introduced by Ishikawa [4]. Previous studies by Kriz [5] on the unit cell predicted the influence of damage on Young's modulus and the redistribution of internal stresses. Variations in moduli and internal stresses were calculated by a finite-element model (FEM). Some details of the FEM and the idealized damage are repeated here for comparison with the formation of actual damage observed from experiment. This FEM provides only a limited explanation of the relationship between damage and the peculiar nonlinearities (knees), see Ref. 6, in the load-deformation diagrams.

Since theory failed to provide a complete explanation of these nonlinearities, we reported the correlation between nonlinearities and individual damage events at predetermined loads. From these observations we determined which type of damage had the most influence. To date, only fiber breaks and transverse cracks in the resin of the fill fiber bundles (fill resin cracks) were recorded for thin laminates loaded in tension.

---

*The primary difference between G-11CR and G-10CR is that G-11CR contains an aromatic amine component in the epoxy-resin to improve radiation resistance.

Theory

The unit cell of a woven structure was defined by Ishikawa [4] as the smallest repeating structural unit. The plain-weave unit cell shown in Fig. 1 can be further characterized by four identical geometries in planes A, B, C, and D. In each of these planes we assumed generalized plane strain. Hence, the FEM [5] allowed out-of-plane nodal displacements. With these idealizations we approximated the three-dimensional load-deformation behavior with a two-dimensional grid.

Figure 2 is a schematic representation of the weave geometry of the four planes in Fig. 1. For simplicity in calculations, we approximated a constant fiber curvature, θ, for all elements in the warp region of Fig. 2. The boundary conditions shown in Fig. 2 simulated the idealized symmetrical structure of a laminate with two woven layers (see Fig. 3a). The curvature, θ, shown in Fig. 2 is equivalent to the maximum curvature shown in Fig. 3a. This model is limited to transverse cracks in the resin of the internal fill fiber bundles (see Fig. 3a). Hence, only 50 percent of all possible fill resin cracks were modeled. To study the significance of fill resin cracks with weave geometry, we varied θ (Fig. 3a) from 0° to 45°. For a woven laminate, it is physically impossible to require $\theta = 0°$. Hence, the condition of $\theta = 0°$ in Fig. 3b represents a special limiting case for the woven laminate, where the fill resin crack can be compared with the ply crack in a 0°/90° laminate.

The finite element grid of Fig. 2 contained 1004 elements and 543 nodes. Each element had three nodes with three degrees of freedom per node. Out-of-plane displacements allowed the calculation of the three-dimensional strain state. Exact details of this element formulation are given in Refs. 5 and 7.

Components of the element stiffness matrix, which has been modified for θ are given in Appendix A.

Because of the many simplifications in this model, we can only approximate the behavior of the unit cell. From these approximate calculations, we chose not to emphasize absolute values but rather changes in the behavior that are caused by variations in weave curvature, temperature, and formation of fill cracks. Another approximation in this model occurs near the crack tip at point "d" of Fig. 2 where the dimension of the smallest element was restricted to the size of one glass fiber diameter (100 μm). Although stresses closer to the crack tip can be approximated by smaller elements, this method assumes material homogeneity, which is violated when the element size approaches the size of heterogeneity (100 μm). For metals with small grain size this is not a problem, but for fiber-reinforced materials, predictions of stress singularities should be confined to within one fiber diameter of the crack tip.

The applied in-plane and out-of-plane strains, ε_x and ε_y, are calculated from thin-laminate-plate theory [8], which assumes zero stress through the thickness:

$$\varepsilon_x = A_{yy}N_x/(A_{xx}A_{yy} - A_{xy}^2) \qquad (1)$$
$$\varepsilon_y = -A_{xy}N_x/(A_{xx}A_{yy} - A_{xy}^2) \qquad (2)$$

where A_{xx}, A_{yy}, and A_{xy} are laminate midplane stiffness [9] that are calculated from elastic properties listed in Table 1. The fiber and matrix properties were calculated from experimental results of Dahlerup-Peterson and Perot [10], and from these results composite properties were calculated using

53

equations of Hashin [11]. From experiment, the laminate load, N_x = 175 N/mm, near the knee was used to calculate the strains ε_x = 0.011 and ε_y = 0.0017. Young's moduli in the damaged and undamaged state were calculated using these strains, and the resulting stress was obtained by summation of nodal forces along the surface x = 0 with a unit depth. A worst-case thermal load of ΔT = -318 K was chosen for the operating temperature of 76 K, and a strain-free state was assumed at 395 K. Under these load conditions we predicted the influence of weave curvature and fill-crack damage on the elastic behavior of a unit cell at 76 K. Results of these calculations are compared with experiment in the following section.

Experiment

A total of thirteen G-10CR and fourteen G-11CR tensile specimens were cut by shear from panels of cryogenic grade laminates [2]. For all specimens, the warp fiber bundles were aligned with the load axis. Both panels were 0.5-mm thick with three layers of a plain weave. All specimens were 5.0-cm long and 1.77-cm wide. The edges of six specimens of each material were polished so that edge damage could be recorded by the replication technique described in Ref. 12. There are four test groups shown in Table 2; specimens of each type were tested at 295 K (room temperature) and 76 K (liquid nitrogen).

The cryogenic test fixture is shown in Fig. 4. The fixture was designed to allow free access to the polished edge for replication of damage. The extensometer, shown in Fig. 5, was mounted from the side opposite the polished edge. All specimens were quasi-statistically loaded in tension at 20 N/s. The first three specimens from each group listed in Table 2 were

loaded in tension to ultimate fracture strength. From these results one
specimen with a polished edge from each group was loaded to 80 percent ulti-
mate and impregnated with an x-ray dye penetrant of zinc iodide solution
while under a static load of 1000 N. A second specimen with a polished edge
was loaded in increments of 200 N. Damage at the edge of these specimens was
recorded by replication at room temperature after each load increment. For
76-K tests, a warm-up period was required before replication of edge damage
at room temperature.

From these preliminary tests, we observed peculiar nonlinear behavior at
76 K that required additional tests. Additional specimens of G-10CR and
G-11CR were loaded in tension at predetermined loads to determine a possible
correlation between these nonlinearities and cracks in the fill fiber bun-
dles. Densities of fill cracks were determined by observation through the
thicknesses of the semitransparent thin laminates. Fill crack densities
observed in the interior of the laminate were compared with fill cracks
observed on replicas that were taken from the same specimen.

Results and Discussion

A summary of present and previous experimental results are given in
Table 3. Our results compare well with the previous studies [2, 13], except
we report two additional Young's moduli (E_2, E_3) and a strain (ε_T^1) that
locates the first knee in the stress-strain diagram. A second knee was
observed for G-11CR, but is only reported here as a change in modulus between
E_2^{11} and E_3^{11}. These new parameters are defined geometrically at 76 K in
Fig. 6 for G-10CR and in Fig. 7 for G-11CR. At room temperature (295 K)
bimodulus behavior does not exist (see Fig. 8). Other studies [5, 14,]

55

reported similar bimodulus results at low temperatures but no explanations are given for this behavior. In this study, we examine relationships between damage accumulation and these nonlinearities.

The stress-strain response of a bisphenol A epoxy resin, representative of resin used in G-10CR and G-11CR, is included in Figs. 6, 7, and 8 for comparison. The failure strain of the resin at 295 K is larger than those of G-10CR and G-11CR. At 76 K, the opposite is true: we observed that the epoxy failure strain, ε_{resin}, was much lower than laminate fracture strains. We also observed that ε_T^1 is slightly lower than ε_{resin}. This observation implies that the first knee at 76 K could be related to a resin failure in the laminate. Because the resin is constrained in the fiber-reinforced laminate, we predict that the resin will fail at a lower strain ($\varepsilon_T^1 < \varepsilon_{resin}$). This prediction requires experimental verification of epoxy failures that correspond with knees in the stress-strain diagrams.

From experimental observations we correlated individual damage events to nonlinear behavior in the stress-strain diagrams (see Figs. 9-16). At 76 K we observed several epoxy failures in the fill fiber bundles of G-10CR and G-11CR prior to the knee (see Figs. 12 and 16). In all cases prior to fracture we observed only cracks in the resin of the fill fiber bundles (fill resin cracks) and individual fiber fractures in the warp fiber bundles. There was no evidence of large delamination events either prior to or after laminate fracture. Hence, in Table 4 only the initiation of fill resin cracks and fractures of warp fibers are correlated with laminate load. For both materials, larger loads were required to initiate damage at lower temperatures.

After the initiation of damage we measured the growth of this damage with increasing load. To correlate damage events with stress-strain non-

linearities, we inverted the conventional stress-strain format and superposed the damage growth on the same diagrams with load as the common abscissa (see Figs. 9, 11, 13, 15). In all cases damage increased exponentially with increasing load. The nonlinearities shown in Figs. 9 and 11 correlated well with the growth of fill résin cracks in G-10CR at 76 K and 295 K, but the growth of warp fiber fractures at much lower loads had no influence on these nonlinearities. From these experiments we conclude that fiber fractures do not contribute to changes in Young's modulus. For all types of damage we drew a continuous curve through a limited set of experimental measurements. Here we assumed that there are no discontinuities in the growth rate of damage. More accurate measurements would be required to measure the presence of growth rate discontinuites, which may be partly responsible for the second knee in Fig. 15.

The bimodulus behavior of G-10CR at 76 K is compared in Fig. 17 with the change in modulus predicted by FEM where only 50 percent of fill fiber bundles were modeled with resin cracks. From experiment we observed resin cracks in all fill fiber bundles (100 percent). Hence, the decrease in modulus for G-10CR in Fig. 17 is larger than that predicted by the FEM. The thin-slice approximation for FEM appears to be a serious oversimplification, which models only a portion of the woven structure. A complete three-dimensional model would provide a more accurate prediction, but the two-dimensional model sufficiently predicts the correct trend, which is a drop in modulus caused by the accumulation of one resin crack in each fill fiber bundle.

For G11-CR at 76 K we observed several resin cracks in the fill fiber bundles (see Fig. 16) and consequently measured a much larger drop in modulus

at the first knee than that in G-10CR (Table 3). At the same load in Figs. 11 and 15 we observed more than twice the number of fill resin cracks in G-11CR than in G-10CR, but the moduli of G-11CR and G-10CR are similar at 3000 N because of an increase in modulus for G-11CR from E_2^{11} to E_3^{11}. This increase in modulus at the second knee in Fig. 7 could be caused by straightening of warp fiber bundles after multiple resin cracks in the fill fiber bundles. Unfortunately, there is no evidence of warp bundle straightening at 76 K, because replicas were taken at reduced loads after warm-up to prevent formation of new damage. For thicker laminates multiple cracking will still occur, but straightening of warp bundles may be suppressed because of the constraint through the thickness. Hence, the second knee for G-11CR may be a result of the thin specimen geometry.

The fill resin cracks observed at the edge with replicas did not match with interior fill resin cracks. Because of the semitransparent property of the thin laminate, we observed the formation of all interior fill resin cracks by light transmission through the thickness. Fill resin cracks originated at the interior and grew towards the edge. Not all interior fill resin cracks extend to the laminated edge. Hence, for woven laminates edge damage is not representative of interior damage. The opposite is true for nonwoven laminates, where transverse ply cracks originate at the edge and extend the full width of the specimen [11].

Fiber fractures observed at the edge are also not representative of fiber fractures in the laminate interior. For nonwoven graphite/epoxy laminates, Schulte et al. [15,16] demonstrated that at the laminate edges, fibers failed at lower loads because of the reduced cross-sectional area of sectioned fibers and flaws induced by polishing. Consequently, at the

laminate edges there are typically large numbers of fiber fractures that occur randomly. When the plane of the laminate edge intersected the thickest portion of a warp fiber bundle, we observed large numbers of random fiber fractures. For G-11CR we observed large number of random fiber fractures at 295 K and fewer fiber fractures at 76 K (see Figs. 14 and 16). A high density of fiber fractures always occurred near the fill resin crack tip at 76 K. This observation is consistent with stresses predicted by FEM in the warp region near the fill crack tip (see Fig. 18): when the temperature decreases we predict an increase in σ_x when $\theta = 0$ and only a small decrease in σ_x for larger angles of θ. For G-10CR we did not observe this trend where fill cracks did not dominate fractures of warp fibers (see Figs. 10 and 12). Again, these discrepancies may be caused by edge effects discussed by Schulte; we recommend a closer examination of warp fiber fractures in the laminate interior.

Although fiber fractures do not influence the modulus, the accumulation of fiber fractures in warp bundles influences ultimate strength because the warp fiber bundles carry the largest portion of the tension load. If more fiber fractures occur at the laminate edge, then we may be observing the damage state that initiates ultimate fracture. The edge damage state of G-10CR at 295 K in Fig. 13 revealed unusually large displacements between broken fiber ends only within the fractured region. Also, there were observed fewer fiber fractures on the edge of G-11CR than in G-10CR at 76 K, which may account for the higher laminate fracture strength of G-11CR.

For both G-10CR and G-11CR only small delaminations were observed after fracture. Prior to fracture no delaminations occurred at either 295 K or 76 K. Previous studies [17] for nonwoven laminates showed that delaminations

can originate from the tips of transverse ply cracks at the interlayer inter-face. For woven laminates with θ = 45° we predicted (see Fig. 19) by the FEM a decrease delamination stresses when the fill resin crack occurs and when the temperature decreases to 76 K. Hence, in this study we predicted and experimentally verified that delaminations are prevented for moderate to large weave curvatures by the formation of fill resin cracks at low tempera-tures.

Soft x-rays of damaged specimens impregnated with zinc-iodide solution (see Ref. 16) could not detect the presence of fill resin cracks. The zinc-iodide dye-penetrant works well with graphite/epoxy materials; but it is inadequate for detecting damage in glass/epoxy materials. A variety of voltages, currents, and exposure times revealed only the woven structure of laminates that were known to have extensive damage. The exact nature of internal damage remains unknown for these laminates.

Summary

From experiments of 76 K and 295 K we observed that damage in specimens of G-10CR and G-11CR accumulated as resin cracks in fill-fiber bundles and individual fiber fractures in warp-fiber bundles. Only small regions of delamination were observed between warp and fill fiber bundles after laminate fracture. For both materials, larger loads were required to initiate damage at 76 K. Except for G-11CR at 76 K, warp fibers always fractured before the formation of fill resin cracks. In general, fiber fractures were observed as random events that were not related to fill resin cracks. In G-11CR at 76 K, fiber fractures always occurred within a region of stress concentration near the tip of the resin crack.

From a finite-element analysis we predicted a decrease in Young's modulus, which was modeled by formation of resin cracks in 50 percent of the fill fiber bundles. In G-10CR and G-11CR at 76 K, a high density of fill resin cracks was observed at a strain similar to the failure strain of the neat resin. From theory we predicted that a high density of fill resin cracks would result in a reduced modulus, or a knee, in the stress-strain diagram. For both materials at 295 K we observed a nonlinear stress-strain diagram with no knees. At 76 K we observed two knees and three moduli for G-11CR where the third modulus increased in value (see Fig. 15). For G-10CR at 76 K, we observed only one knee at a strain lower than the first knee of G-11CR. The second knee for G-11CR may represent a rapid growth of fill resin cracks, $E_2^{11} < E_1^{11}$, followed by a straightening in warp fibers and an increase in modulus $E_3^{11} > E_2^{11}$. Fractographic evidence of multiple fill resin cracks in G-11CR supports this explanation. Before laminate fracture, Young's moduli for both materials were approximately equal. Between knees, the stress-strain response in tension was linear for both materials. Most of the accumulated damage and nonlinearities in the stress-strain diagrams occurred at strains well below fracture. This is an important consideration for design applications where these materials are only loaded to small strains.

Fiber fractures had no influence on the appearance of the stress-strain diagrams. For G-10CR at 295 K, large numbers of fiber fractures occurred randomly and large crack opening displacements (CODs) were observed in the region of laminate fracture. At a lower temperature we observed fewer fiber fractures and measured a higher laminate fracture strength. If the temperature is decreased, we predicted by FEM a decrease in stress in the warp region where fiber fractures occur. This prediction implies a higher

strength at lower temperatures. From FEM we also predict a decrease in
delamination stresses with a decrease in temperature when fill cracks are
present. Experiments verified minimal delaminations.

From both theory and experiment, we conclude that the weave geometry is
beneficial at lower temperatures: when fill resin cracks occur delaminations
are prevented at the fill-warp interface.

Acknowledgments

References

1. M. B. Kasen, Composite laminate applications in magnetic fusion energy
    superconducting magnet systems, Proceedings of the 1978 International
    Conference on Composite Materials, Toronto, Canada (1978).

2. M. B. Kasen, G. R. MacDonald, D. H. Beekman Jr., and R. E. Schramm,
    Mechanical, electrical and thermal characterization of G-10CR and G-11CR
    glass/epoxy laminates between room temperature and 4 K, Advances in
    Cryogenic Engineering, Vol. 26, Plenum Press, New York, pp. 235-244
    (1980).

3. M. B. Kasen and R. E. Schramm, Current status of standardized
    nonmetallic cryogenic laminates, Advances in Cryogenic Engineering,
    Vol. 28, Plenum Press, New York, pp. 171-177 (1981).

4. T. Ishikawa, Anti-symmetric elastic properties of composite plates of
    satin weave cloth, Fiber Sci. Technol., Vol. 15, pp. 127-145 (1981).

5. R. D. Kriz, Influence of damage on mechanical properties of woven com-
    posites at low temperatures, Compos. Technol. Rev., in press.

6. H. Benz, I. Horvath, K. Kwasnitza, R. K. Maix, and G. Meyer, Worldwide
    cryogenics - Switzerland Cryogenics at BBC Brown, Boveri & Co., Ltd.,
    Cryogenics, Vol. 19, pp. 3-15 (1979).

7. A. P. Nagarkar and C. T. Herakovich, "Nonlinear temperature dependent
    failure analysis of finite width composite laminates," VPI-E-79-36,
    Virginia Polytechnic Institute and State University, Blacksburg,
    Virginia (1979).

8. R. Y. Kim and H. T. Hahn, Effect of curing stresses on first ply fail in composite laminates, J. Compos. Mater., Vol. 13, pp. 2-16 (1979).

9. R. M. Jones, Mechanics of Composite Materials, McGraw-Hill, New York, pp. 147-173 (1975).

10. K. Dahlerup-Peterson and A. Perrot, "Properties of Organic Composite Materials at Cryogenic Temperatures," CERN; ISR-BOM/79-39, Geneva, Switzerland (1979).

11. Z. Hashin, "Theory of Fiber Reinforced Materials," NASA-CR-1974, NASA Langley Res. Cent., Hampton, Virginia (1972).

12. D. O. Stalnaker and W. W. Stinchcomb, in Composite Materials: Testing and Design (Fifth Conference), ASTM STP 674, American Society for Testing and Materials, Philadelphia, pp. 620-641 (1979).

13. H. M. Ledbetter, Dynamic elastic modulus and internal friction in G-10CR and G-11CR fiberglass-cloth-epoxy composites, Cryogenics, Vol. 20, pp. 637-640 (1980).

14. M. B. Kasen, Mechanical and thermal properties of filamentary-reinforced structural composites at cryogenic temperatures 1: Glass-reinforced composites, Cryogenics, Vol. 15, pp. 327-349 (1975).

15. K. Schulte and W. W. Stinchcomb, Damage development near the edge of a composite specimen during quasi-static and fatigue loading, Compos. Techol. Rev., Vol. 6, pp. 3-9 (1984).

16. R. D. Jamison, K. Schulte, K. L. Reifsnider, and W. W. Stinchcomb, "Characterization and analysis of damage mechanisms in tension-tension fatigue of graphite/epoxy laminates," Effects of Defects in Composite Materials, ASTM STP 836, American Society for Testing and Materials, Philadelphia, pp. 21-55 (1984).

17. A. L. Highsmith, W. W. Stinchcomb, and K. L. Reifsnider, "Effect of fatigue-induced defects on the residual response of composite laminates," Effects of Defects in Composite Materials, ASTM STP 836, American Society for Testing and Materials, Philadelphia, pp. 194-216 (1984).

Appendix A

The elemental stiffness matrix that is commonly used for laminated plate analysis has been changed to include rotations of the fiber orientations within the x-z plane of Fig. 2. In Ref. 6 an elemental stiffness matrix was constructed for a three-node generalized plane strain simple element that allowed for arbitrary rotations in the y-z plane. Here we reconstruct a similar element with the same symbolic notation as in Ref. 6, but only rotations in the x-z plane are included in the calculations.

For an arbitrary rotation in the x-z plane, we have rewritten the orthorhombic material stiffness matrix in contracted notation, where the subscripts (1,2,3) correspond to the (y,x,z) coordinates in Fig. 2.

Tensor transformation:
$$\overline{C}_{ijkl} = a_{ir}a_{js}a_{kt}a_{lu}C_{rstu} \tag{A1}$$

Transformation array:

a_{ij}	1	2	3
$\overline{1}$	1	0	0
$\overline{2}$	0	$\cos\theta$	$\sin\theta$
$\overline{3}$	0	$-\sin\theta$	$\cos\theta$

(A2)

Constitutive relation:
$$\{\sigma\} = [\overline{C}]\{\varepsilon\} \tag{A3}$$

$$
\begin{Bmatrix} \sigma_1 \\ \sigma_2 \\ \sigma_3 \\ \tau_{23} \\ \tau_{13} \\ \tau_{12} \end{Bmatrix}
=
\begin{bmatrix}
\overline{C}_{11} & \overline{C}_{12} & \overline{C}_{13} & \overline{C}_{14} & 0 & 0 \\
\overline{C}_{12} & \overline{C}_{22} & \overline{C}_{23} & \overline{C}_{24} & 0 & 0 \\
\overline{C}_{13} & \overline{C}_{23} & \overline{C}_{33} & \overline{C}_{34} & 0 & 0 \\
\overline{C}_{14} & \overline{C}_{24} & \overline{C}_{34} & \overline{C}_{44} & 0 & 0 \\
0 & 0 & 0 & 0 & \overline{C}_{55} & \overline{C}_{56} \\
0 & 0 & 0 & 0 & \overline{C}_{56} & \overline{C}_{66}
\end{bmatrix}
\begin{Bmatrix} \varepsilon_1 \\ \varepsilon_2 \\ \varepsilon_3 \\ \gamma_{23} \\ \gamma_{13} \\ \gamma_{12} \end{Bmatrix}
\tag{A4}
$$

where σ and τ are normal stresses and shear stresses, ε and γ are normal strains and engineering shear strains, and $\overline{C}_{ij}$ are imansformed material stiffnesses written below as functions of the warp angle θ defined in Fig. 2.

$$\overline{C}_{11} = C_{11}$$

$$\overline{C}_{22} = m^4 C_{22} + n^4 C_{33} + 2m^2 n^2 (C_{23} + 2C_{44})$$

$$\overline{C}_{33} = n^2 C_{22} + m^4 C_{33} + 2m^2 n^2 (C_{23} + 2C_{44})$$

$$\overline{C}_{44} = n^2 m^2 (C_{22} + C_{33}) + (m^2 - n^2)^2 C_{44} - 2n^2 m^2 C_{23}$$

$$\overline{C}_{55} = m^2 C_{55} + n^2 C_{66}$$

$$\overline{C}_{66} = n^2 C_{55} + m^2 C_{66}$$

$$\overline{C}_{12} = m^2 C_{12} + n^2 C_{13}$$

$$\overline{C}_{13} = n^2 C_{12} + m^2 C_{13} \tag{A5}$$

$$\overline{C}_{14} = nm\,(C_{13} - C_{12})$$

$$\overline{C}_{56} = nm\,(C_{55} - C_{66})$$

$$\overline{C}_{23} = n^2 m^2 (C_{22} + C_{33}) + (m^4 + n^4) C_{23} - 4n^2 m^2 C_{44}$$

$$\overline{C}_{24} = -nm^3\,C_{22} + mn^3 C_{33} + nm(m^2 - n^2)(C_{23} + 2C_{44})$$

$$\overline{C}_{34} = -n^3 m C_{22} + m^2 n\,C_{33} + nm(n^2 - m^2)(C_{23} + 2C_{44})$$

where $n = \sin\theta$ and $m = \cos\theta$.

In Ref. 6 the elemental stiffness matrix $[K]$ is calculated by pre-multiplying the material stiffness matrix $[\overline{C}]$ by the transpose of the connectivity array $[B]^T$ and postmultiplying the result by the connectivity array $[B]$:

$$[K] = [B]^T\,[\overline{C}]\,[B] \tag{A6}$$

where the connectivity array $[B]$ relates the out-of-plane strain ξ_1 and nodal

displacements (u_i, v_i, w_i); i = 1,2,3 to the strains [ε].

$$[\varepsilon] = [B] \{\xi_1, u_i, v_i, w_i\}, \quad i = 1,2,3 \tag{A7}$$

$$[B] = \begin{bmatrix} A_k & 0 & 0 & 0 & 0 & 0 & 0 & 0 & 0 & 0 \\ 0 & 0 & 0 & 0 & a & c & e & 0 & 0 & 0 \\ 0 & 0 & 0 & 0 & 0 & 0 & 0 & b & d & g \\ 0 & 0 & 0 & 0 & b & d & g & a & c & e \\ 0 & b & d & g & 0 & 0 & 0 & 0 & 0 & 0 \\ 0 & a & c & e & 0 & 0 & 0 & 0 & 0 & 0 \end{bmatrix} \tag{A8}$$

where A_k is the element area and a, b, c, d, e, are other geometric
parameters for the element defined in Ref. 6.

When we perform the operations in Eq. A6, we obtain the symmetrical

components $K_{ij} = K_{ji}$ for the element stiffness array [K]. When the out-of-

plane strain is a known quantity (applied strain), then the first row of [K]

is irrelevant and the first column of [K] becomes a known quantity, which is

added to the known load vector [F]. The components of the remaining [9 x 9]

element stiffness array are:

$$K_{11} = [b^2\overline{C}_{55} + 2ab\overline{C}_{56} + a^2\overline{C}_{66}]/A_k$$

$$K_{12} = [bd^2\overline{C}_{55} + (cb + ad)\overline{C}_{56} + ac\overline{C}_{66}]/A_k$$

$$K_{13} = [bg\overline{C}_{55} + (be + ag)\overline{C}_{56} + ae\overline{C}_{66}]/A_k$$

$$K_{22} = [d^2\overline{C}_{55} + 2cd\overline{C}_{56} + c^2\overline{C}_{66}]/A_k \tag{A9}$$

$$K_{23} = [dg\overline{C}_{55} + (ed + cg)\overline{C}_{56} + ce\overline{C}_{66}]/A_k$$

$$K_{33} = [g^2\overline{C}_{55} + 2eg\overline{C}_{56} + e^2\overline{C}_{66}]/A_k$$

$$K_{44} = [a^2\overline{C}_{22} + 2ab\overline{C}_{24} + b^2\overline{C}_{44}]/A_k$$

$$K_{45} = [ac\overline{C}_{22} + (ad + bc)\overline{C}_{24} + bd\overline{C}_{44}]/A_k$$

$$K_{46} = [ae\bar{C}_{22} + (ag + be)\bar{C}_{24} + bg\bar{C}_{44}]/A_k$$

$$K_{47} = [a^2\bar{C}_{24} + ab(\bar{C}_{23} + \bar{C}_{44}) + b^2\bar{C}_{34}]/A_k$$

$$K_{48} = [d(a\bar{C}_{23} + b\bar{C}_{34}) + c(a\bar{C}_{24} + b\bar{C}_{44})]/A_k$$

$$K_{49} = [g(a\bar{C}_{23} + b\bar{C}_{34}) + e(a\bar{C}_{24} + b\bar{C}_{44})]/A_k$$

$$K_{55} = [c^2\bar{C}_{22} + 2cd\bar{C}_{24} + d^2\bar{C}_{44}]/A_k$$

$$K_{56} = [ce\bar{C}_{22} + (cg + de)\bar{C}_{24} + dg\bar{C}_{44}]/A_k$$

$$K_{57} = [b(c\bar{C}_{23} + d\bar{C}_{34}) + a(c\bar{C}_{24} + d\bar{C}_{44})]/A_k$$

$$K_{58} = [cd(\bar{C}_{23} + \bar{C}_{44}) + c^2\bar{C}_{24} + d^2\bar{C}_{34})]/A_k$$

$$K_{59} = [g(c\bar{C}_{23} + d\bar{C}_{34}) + e(c\bar{C}_{24} + d\bar{C}_{44})]/A_k$$

$$K_{66} = [e\bar{C}_{22} + 2eg\bar{C}_{24} + g^2\bar{C}_{44})]/A_k$$

$$K_{67} = [e(b\bar{C}_{23} + a\bar{C}_{24}) + g(b\bar{C}_{34} + a\bar{C}_{44})]/A_k$$

$$K_{68} = [d(e\bar{C}_{23} + g\bar{C}_{34}) + c(e\bar{C}_{24} + g\bar{C}_{44})]/A_k$$

$$K_{69} = [g^2\bar{C}_{34} + ge(\bar{C}_{23} + \bar{C}_{44}) + e^2\bar{C}_{24}]/A_k$$

$$K_{77} = [b^2\bar{C}_{33} + 2abc\bar{C}_{34} + a^2\bar{C}_{44}]/A_k$$

$$K_{78} = [db\bar{C}_{33} + (da + cb)\bar{C}_{34} + ca\bar{C}_{44}]/A_k$$

$$K_{79} = [bg\bar{C}_{33} + (ag + eb)\bar{C}_{34} + ea\bar{C}_{44}]/A_k$$

$$K_{88} = [d^2\bar{C}_{33} + 2dc\bar{C}_{34} + c^2\bar{C}_{44}]/A_k$$

$$K_{89} = [dg\bar{C}_{33} + (gc + ed)\bar{C}_{34} + ce\bar{C}_{44}]/A_k$$

$$K_{99} = [g^2\bar{C}_{33} + 2ge\bar{C}_{34} + e^2\bar{C}_{44}]/A_k$$

(A9)

from the first column of the [K] array we add the following terms to the load
vector:

$$F(4) = -(a\bar{C}_{12} + b\bar{C}_{14})\xi_1$$

$$F(5) = -(c\bar{C}_{12} + d\bar{C}_{14})\xi_1$$

$$F(6) = -(e\bar{C}_{12} + g\bar{C}_{14})\xi_1$$

$$F(7) = -(b\bar{C}_{13} + a\bar{C}_{14})\xi_1$$

$$F(8) = -(d\bar{C}_{13} + c\bar{C}_{14})\xi_1$$

$$F(9) = -(g\bar{C}_{13} + e\bar{C}_{14})\xi_1$$

(A10)

All remaining F_i and K_{ij} are set equal to zero.

When a thermal load is induced by a temperature change, free thermal strains $\{\epsilon_1^T, \; \epsilon_2^T, \; \epsilon_3^T, \; \gamma_{23}^T\}$ are subtracted from the left side of Eq. A7, and ξ_1 becomes an unknown quantity. Hence, we now have a [10 x 10] element stiffness array where the arrays are arranged to include these additional terms in the tenth row and column of [K]:

$$
\begin{aligned}
K_{4,10} &= a\overline{C}_{12} + b\overline{C}_{14} \\
K_{5,10} &= c\overline{C}_{12} + d\overline{C}_{14} \\
K_{6,10} &= e\overline{C}_{12} + g\overline{C}_{14} \\
K_{7,10} &= b\overline{C}_{13} + a\overline{C}_{14} \\
K_{8,10} &= d\overline{C}_{12} + c\overline{C}_{14} \\
K_{9,10} &= g\overline{C}_{12} + e\overline{C}_{14} \\
K_{10,10} &= \overline{C}_{11}A_K
\end{aligned}
\qquad (A11)
$$

Additional terms, F_i, are added to the load vector:

$$
\begin{aligned}
F(1) &= F(2) = F(3) = 0 \\
F(4) &= aQ + bR \\
F(5) &= cQ + dR \\
F(6) &= eQ + gR \\
F(7) &= bS + aR \\
F(8) &= dS + cR \\
F(9) &= gS + eR
\end{aligned}
\qquad (A12)
$$

where
$$
\begin{aligned}
Q &= \overline{C}_{12}\epsilon_1^T + \overline{C}_{22}\epsilon_2^T + \overline{C}_{23}\epsilon_3^T + \overline{C}_{24}\gamma_{23}^T \\
R &= \overline{C}_{14}\epsilon_1^T + \overline{C}_{24}\epsilon_2^T + \overline{C}_{34}\epsilon_3^T + \overline{C}_{44}\gamma_{23}^T \\
S &= \overline{C}_{13}\epsilon_1^T + \overline{C}_{23}\epsilon_2^T + \overline{C}_{33}\epsilon_3^T + \overline{C}_{34}\gamma_{23}^T
\end{aligned}
$$

$$F(10) = \bar{C}_{11}\epsilon_1^T + \bar{C}_{12}\epsilon_2^T + \bar{C}_{13}\epsilon_3^T + \bar{C}_{14}\gamma_{23}^T$$

Although the material is linear elastic, superposition of [K] matrices for (ξ_1, known) and (ξ_1, unknown) is not possible because the arrays and their solutions are unique. Superposition of results is only possible after the solution of unknown displacement vector for each case.

$$F(10) = \bar{C}_{11}\epsilon_1^T + \bar{C}_{12}\epsilon_2^T + \bar{C}_{13}\epsilon_3^T + \bar{C}_{14}\gamma_{23}^T$$

Table 1. Elastic-thermal properties

| PROPERTY | ISOTROPIC CONSTITUENTS* | | TRANSVERSELY ISOTROPIC COMPOSITE † |
	BISPHENOL EPOXY	E GLASS FIBER	GLASS/EPOXY ($V_f = 0.50$)
Young's modulus, GPa	$E = 7.16$	$E = 82.22$	$E_\ell = 44.69$ $E_t = 17.88$
Shear modulus, GPa	$G = 2.77$	$G = 32.55$	$G_{\ell t} = 6.801$ $G_{tt} = 6.888$
Poisson's ratio	$\nu = 0.293$	$\nu = 0.263$	$\nu_{\ell t} = 0.278$ $\nu_{\ell t} = 0.298$
Coefficient of thermal expansion, $10^{-6}K^{-1}$ *	--	--	$\alpha_\ell = 5.963$ $\alpha_t = 23.39$

*Properties from Ref. 9.
†Elastic properties from Ref. 10.
 V_f = volume fraction of glass fibers.
 Subscript ℓ indicates fiber direction; subscript t indicates transverse plane.

Table 2. Specimens tested

TEMPERATURE	G-10CR	G-11CR
76 K	3 for static fracture 1* for x-ray damage 1* for replica damage 3* for fill resin crack count	3 for static fracture 1* for x-ray damage 1* for replica damage 4* for fill resin crack count
295 K	3 for static fracture 1* for x-ray damage 1* for replica damage	3 for static fracture 1* for x-ray damage 1* for replica damage

*Indicates specimens with polished edges for damage replication.

Table 3. Summary and comparison of experimental results

	G-10CR						G-11CR					
	295 K			76 K			295 K			76K		
Moduli	REF. 2	REF. 13	PRESENT WORK	REF. 2	REF. 13	PRESENT WORK	REF. 2	REF. 13	PRESENT WORK	REF. 2	REF. 13	PRESENT WORK
E_1* (GPa)	27.9 28.5 24.0 26.8	29.4 ± 1.0	27.0 26.5 27.1 26.9	31.4 34.1 28.9 31.5	34.4	30.7 33.6 32.8 32.4	30.2 33.1 35.0 32.8	31.4 ± 0.4	31.6 30.2 28.0 29.9	34.7 37.3 40.7 37.5	37.6	34.7 33.5 34.8 34.3
E_2* (GPa)						19.9 18.5 19.8 19.4						17.4 18.2 17.4 17.7
E_3* (GPa)												19.5 20.6 21.2 20.4
Strains												
ϵ_T^1 (%)						1.20 1.10 1.15 1.15						0.95 0.85 0.95 0.91
ϵUTS† (%)	1.89 1.62 1.63 1.72		1.80 1.80 1.60 1.73	3.54 3.21 2.86 3.20		3.10 3.45 3.45 3.33	1.86 1.66 1.63 1.72		2.00 1.95 2.40 2.10	3.51 3.47 3.12 3.37		3.90 3.90 4.05 3.95
Strength												
UTS†(MPa)	429 358 419 402		449 427 376 417	878 877 657 803		747 813 843 809	463 486 477 475		480 467 487 478	932 975 982 963		885 917 953 918

* Subscripted values are defined in Figs. 6, 7, and 8.
† UTS indicates ultimate strength.

71

Table 4. Comparison of loads for initiating damage
          [warp fiber fracture load (N)/fill resin fracture load (N)].

TEMPERATURE	G-10CR	G-11CR
295 K	[500/800]	[500/500]
76 K	[600/1800]	[1500*/1300]

* Warp fiber fractures coincided with fill resin fractures.
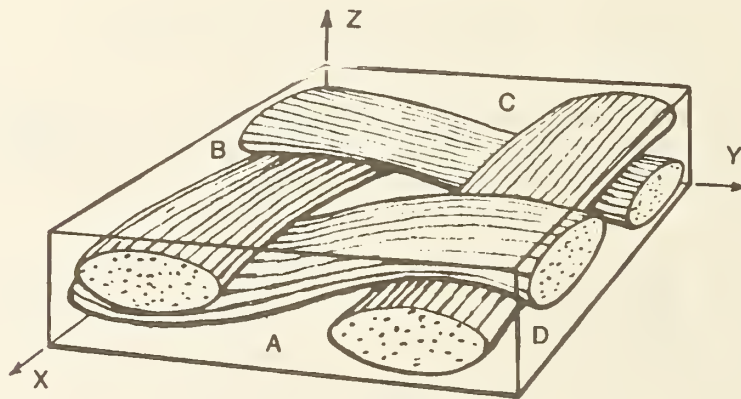
Figure 1.   Unit of cell of woven-fabric composite.
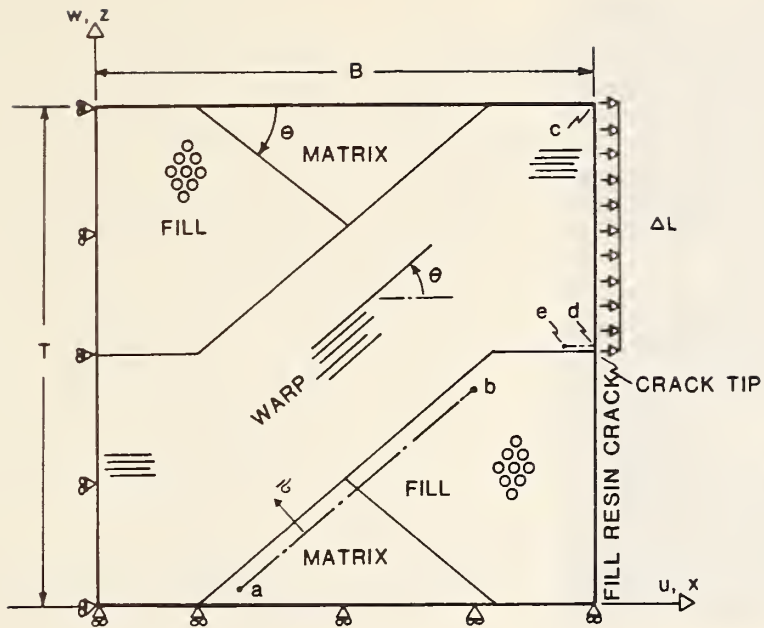
Figure 2.   Thin slice of unit cell.   Theta, θ, denotes angle between warp-
fiber orientation and the x direction.
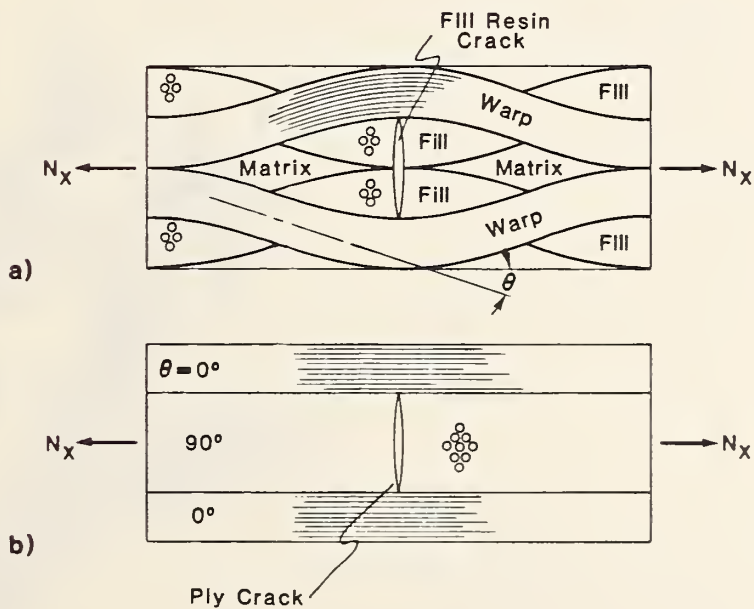
Figure 3a.   Two-layer woven laminate with an interior fill resin crack.
    3b.   0°/90° laminate with 90° ply crack.

73
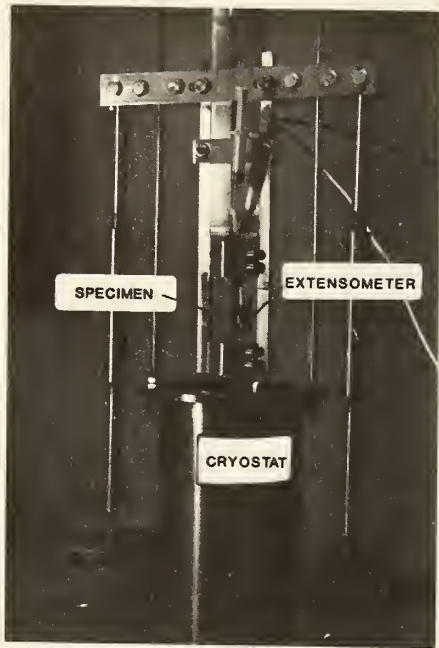
Figure 4.   Cryogenic fixture for replicating
            edge damage.
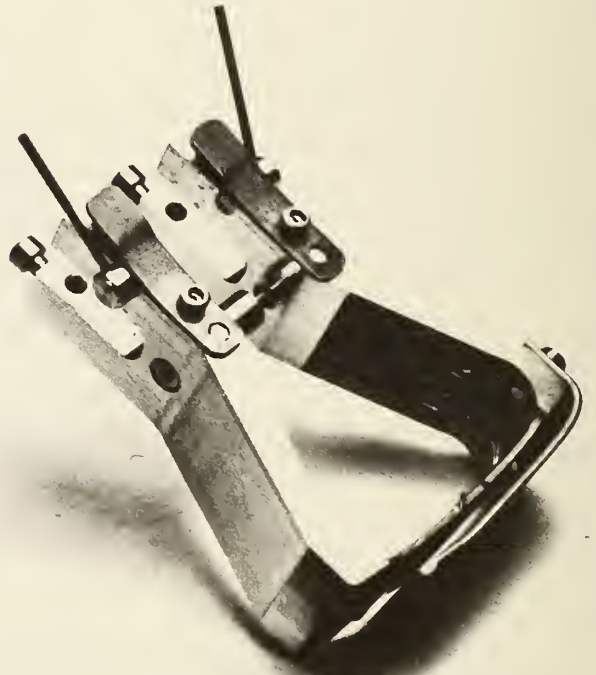
Figure 5.   Cryogenic extensometer.
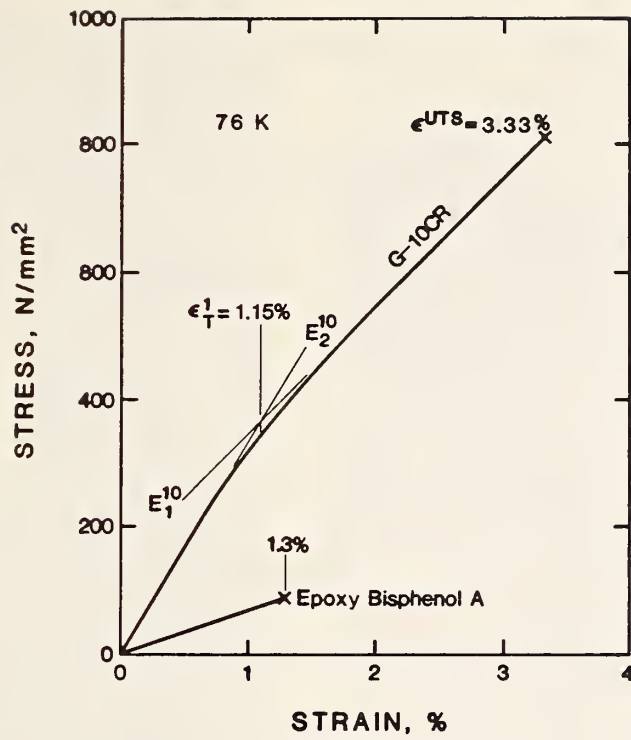
Figure 6. Geometric characteristics defined for the stress-strain response of G-10CR in tension of 76 K with neat resin.
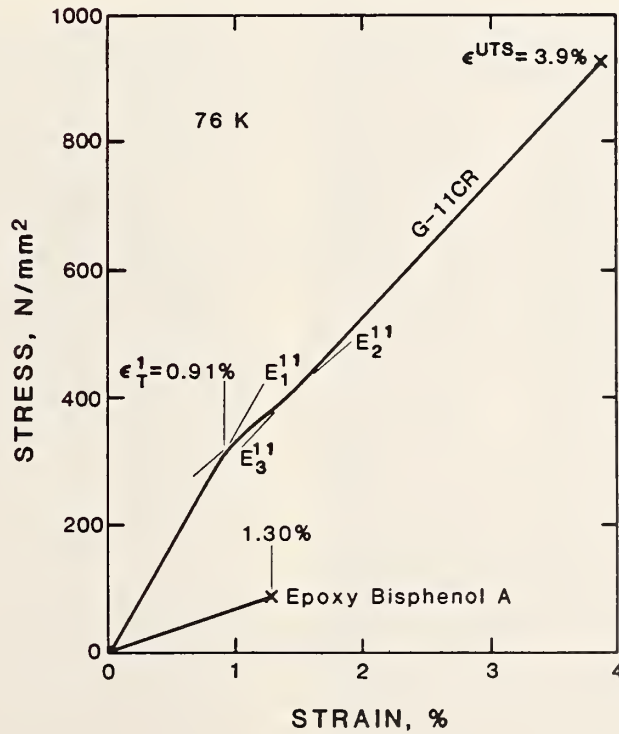
Figure 7. Geometric characteristics defined for the stress-strain response of G-11CR in tension at 76 K with neat resin.
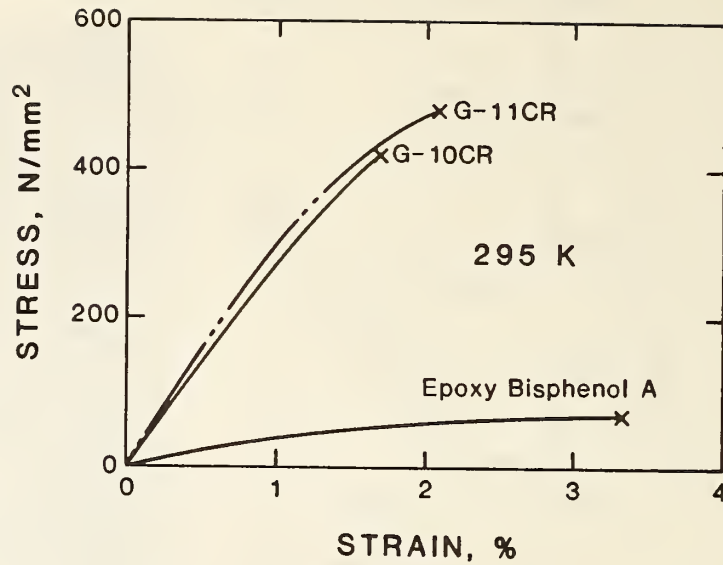
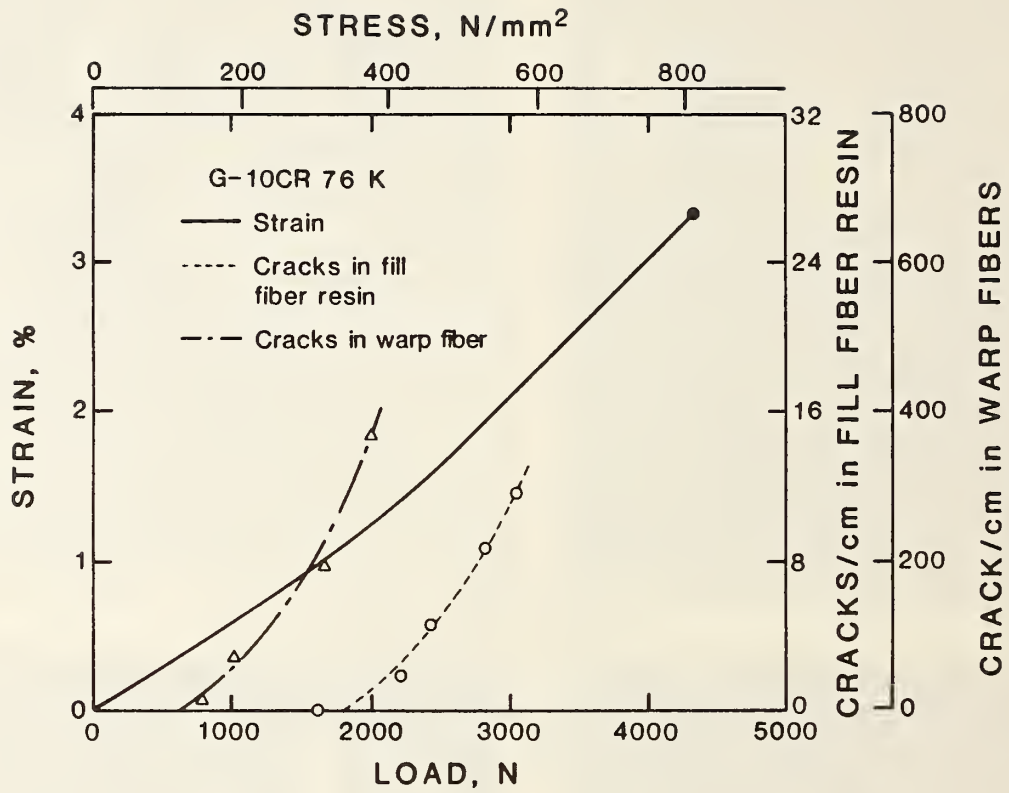Figure 8.   The stress-strain response of G-10CR and G-11CR at 295 K with neat resin.
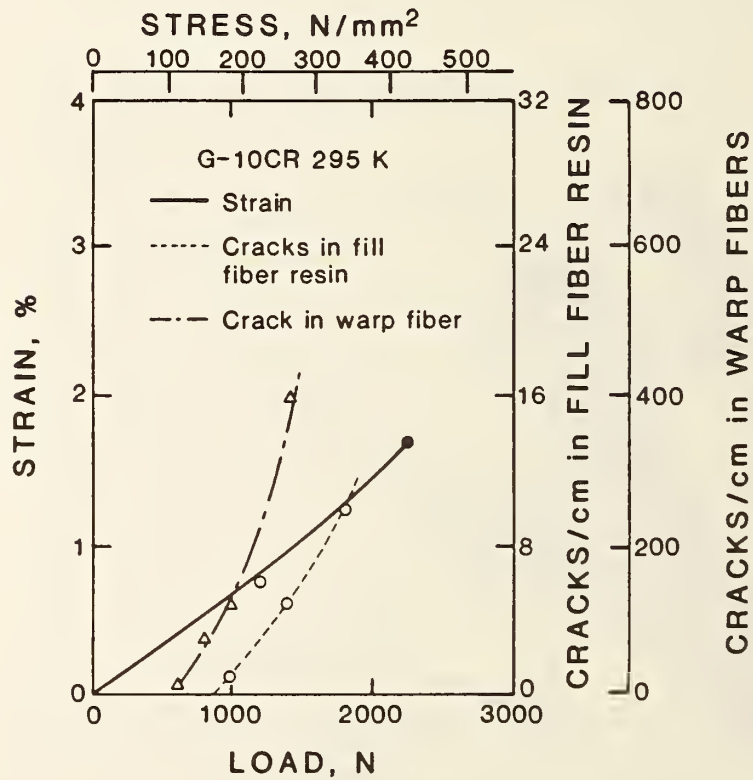
Figure 9.   Correlation between damage formation and stress-strain response of G-10CR in tension at 295 K.

G-10 CR   295 K

TENSION →

100 μm

Warp Fiber Fractures

Fill Resin Cracks

1800 N
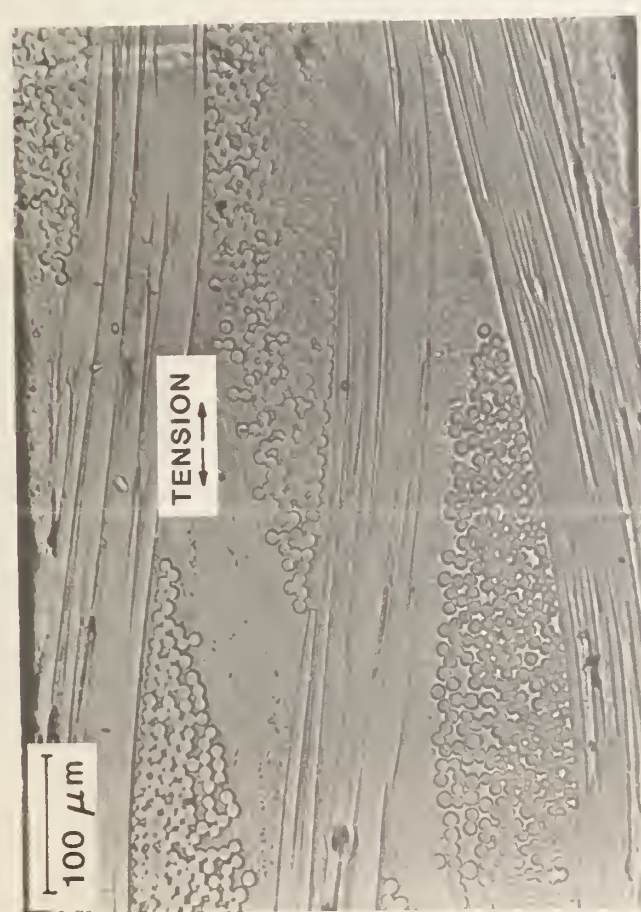
1850 N (fracture)
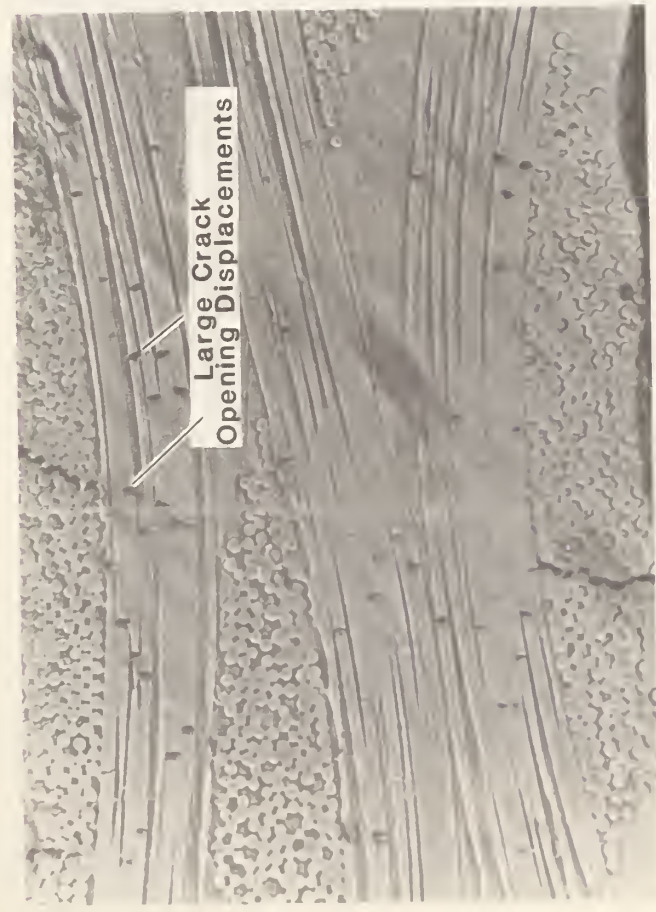
800 N

Large Crack Opening Displacements
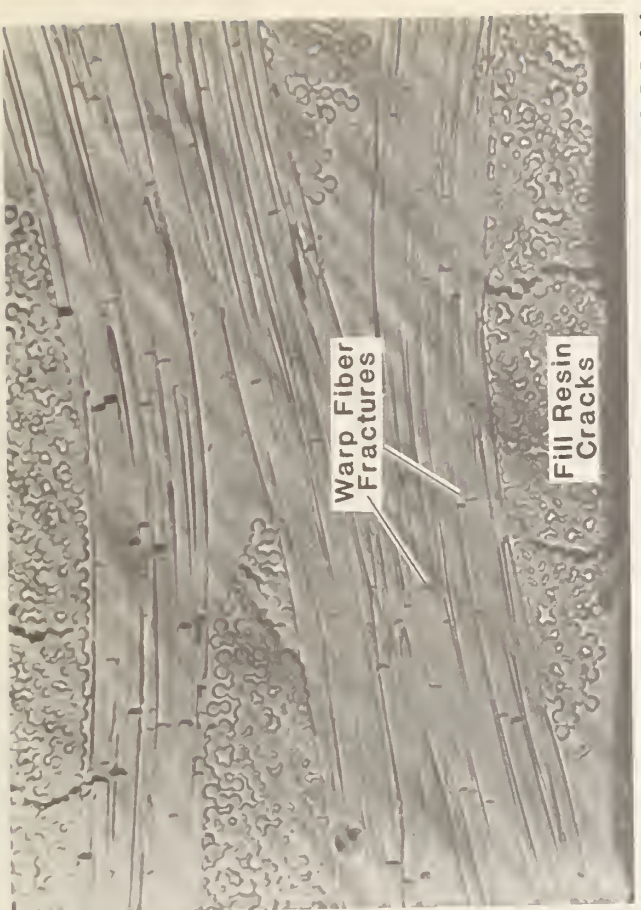
1850 N

Figure 10.   Edge damage corresponding to loads of Fig. 9. Note large crack opening displacements between broken fiber ends at 1850 N in the region of final fracture.

77

Figure 11. Correlation between damage formation and stress-strain response
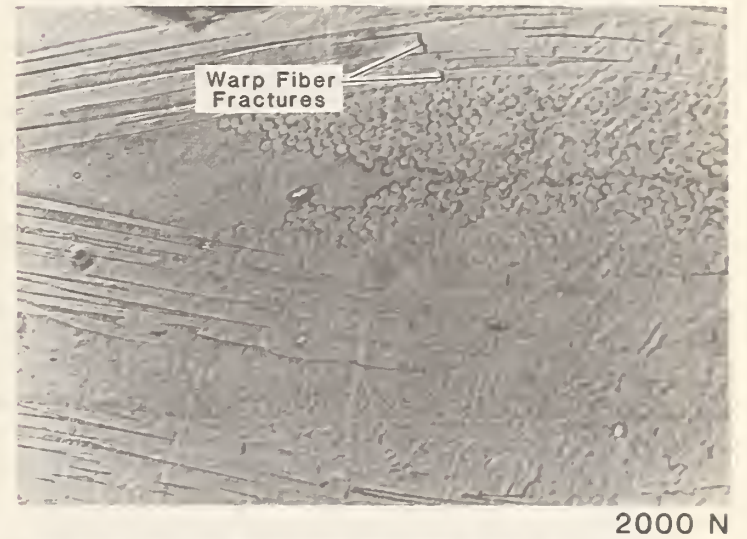of G-10CR in tension at 76 K.

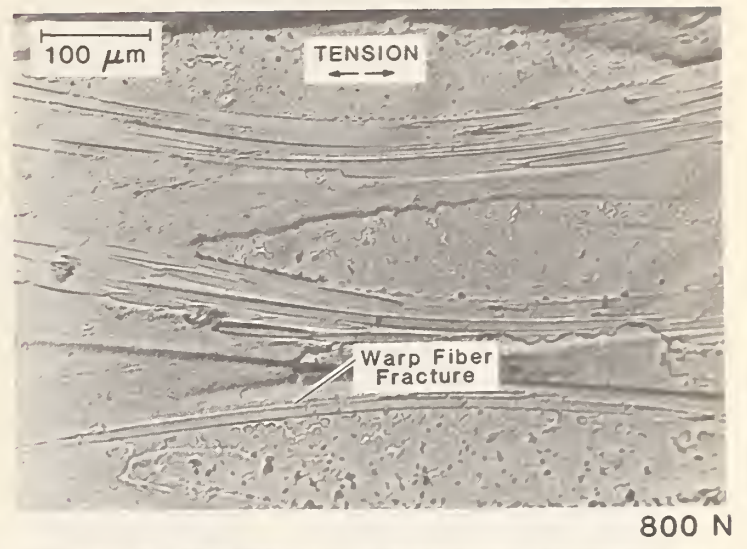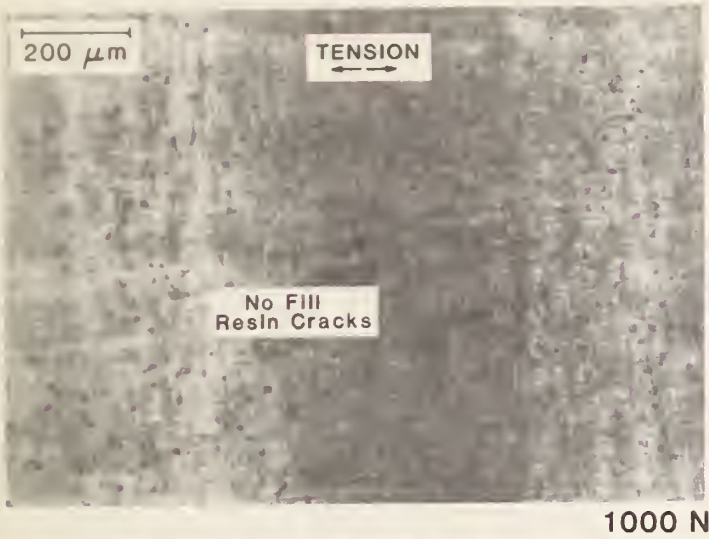Top View   Side View
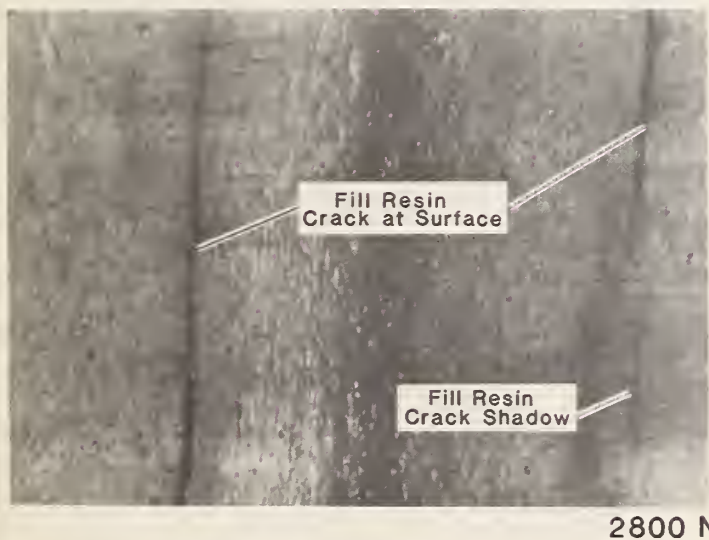
Figure 12. Top and edge views of damage corresponding to loads of Fig. 11.
Damage in top views are fill resin cracks often observed as
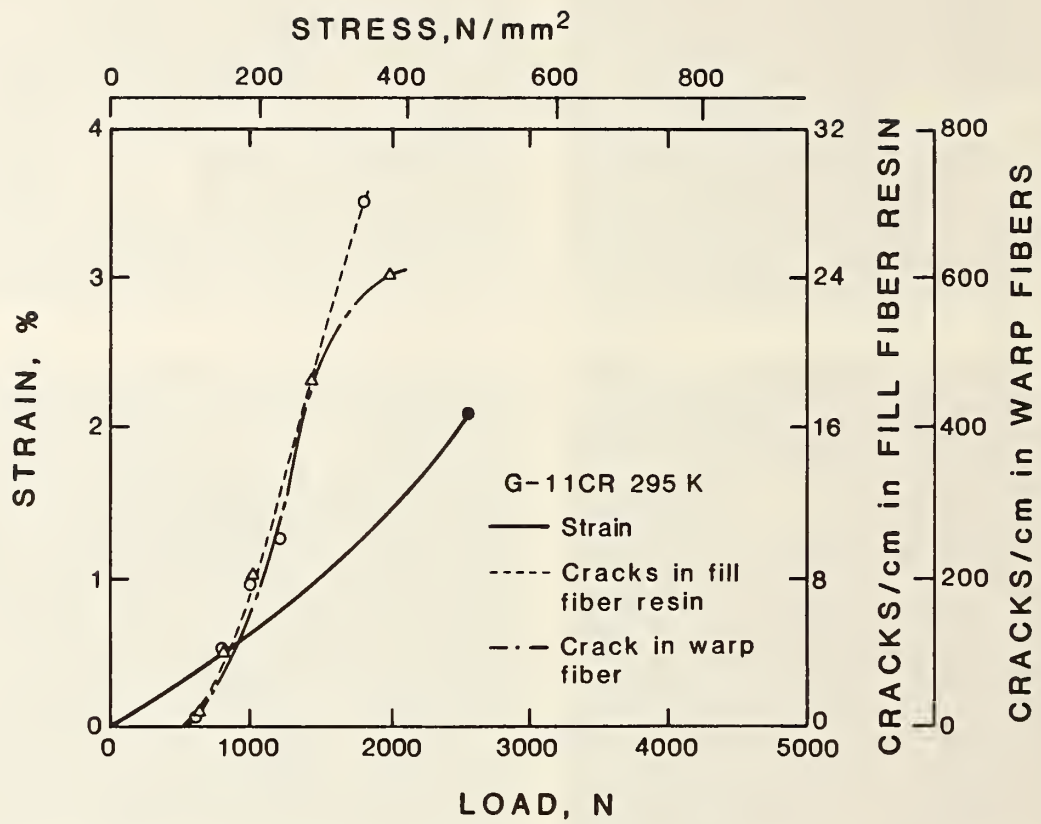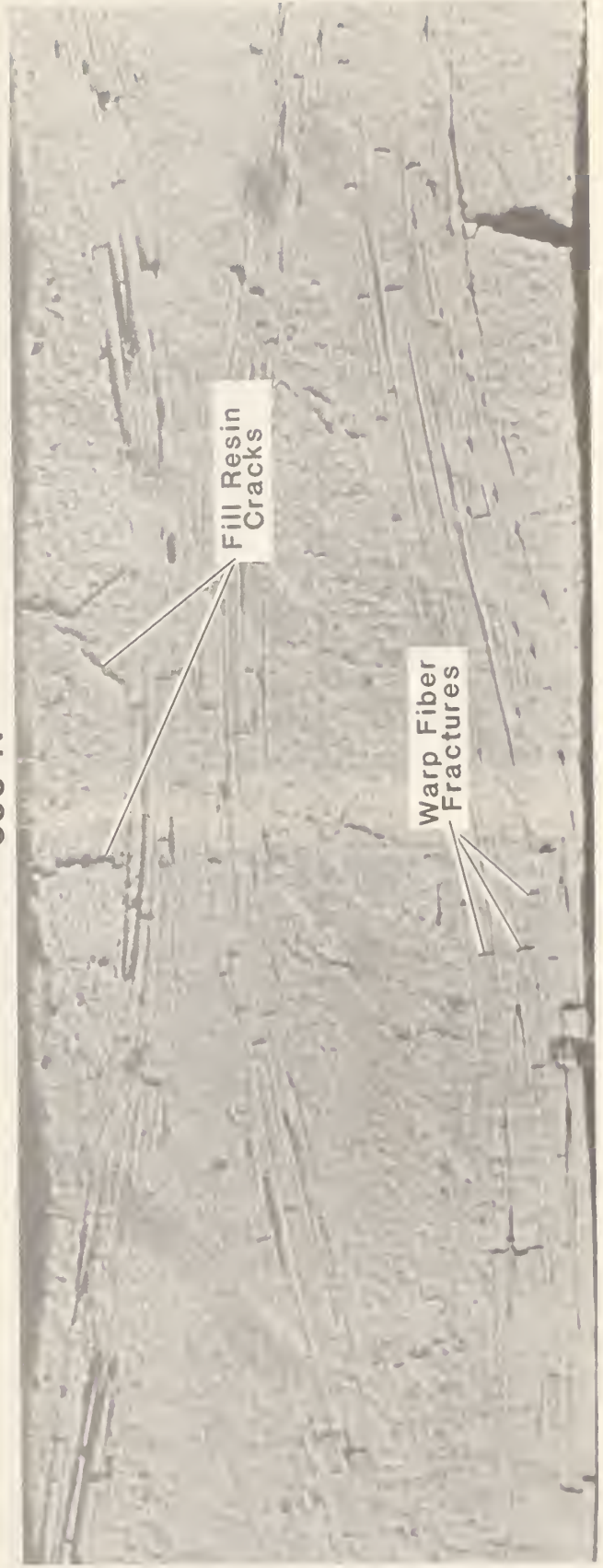shadows below the surface.

Figure 13. Correlation between damage formation and stress-strain response of G-11CR in tension at 295 K.

G-11 CR   295 K

TENSION

500 N

100 μm

Fill Resin
Cracks

Warp Fiber
Fractures
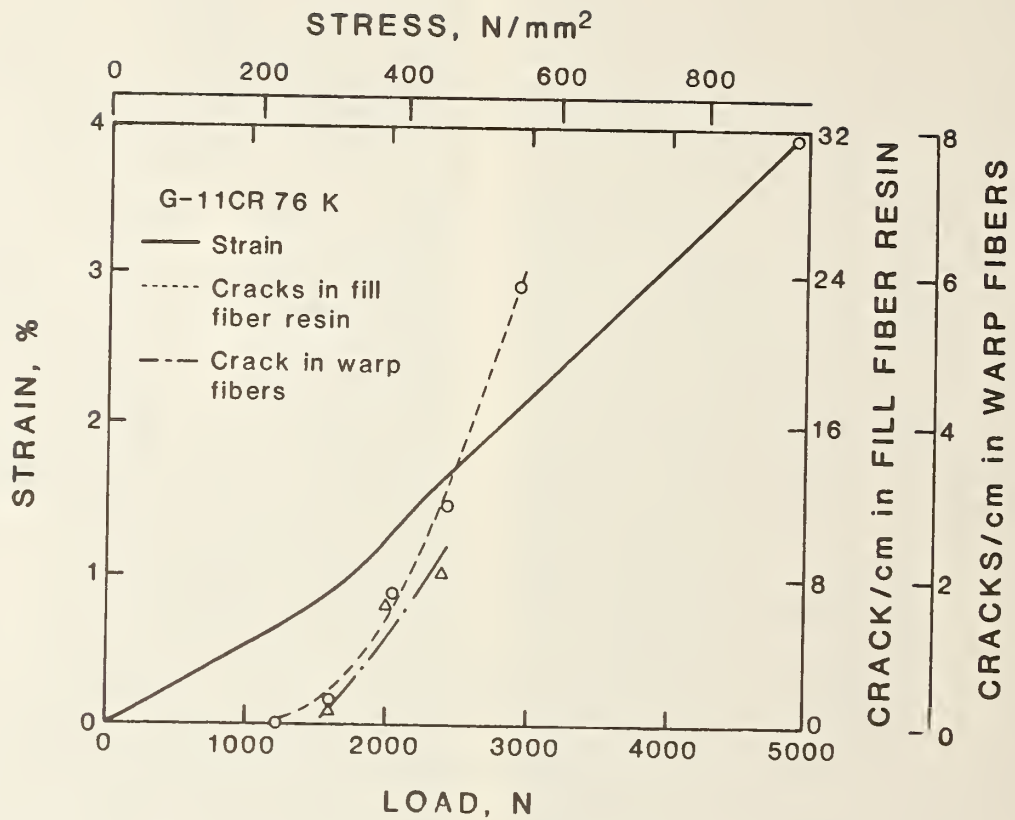
2000 N

Figure 14. Edge damage corresponding to loads of Fig. 13.

81

Figure 15. Correlation between damage formation and stress-strain response of G-11CR in tension at 76 K.

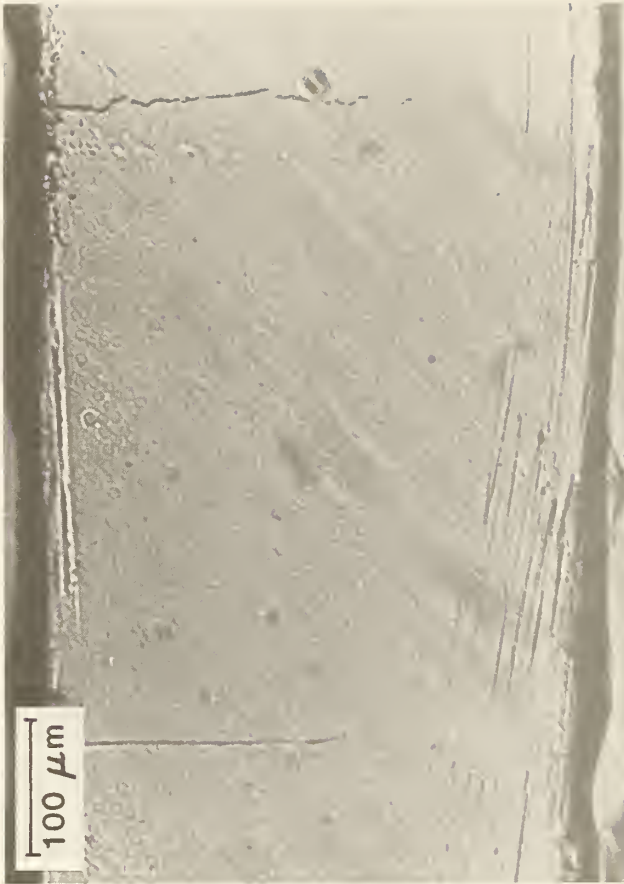Figure 16a. Top and edge views of damage corresponding to loads of Fig. 15.

G-11 CR   76 K

Side View

TENSION

100 μm

1200 N

1600 N

Fill Resin Crack

Top View

TENSION

200 μm

1200 N

1800 N

Resin Cracks in Warp and Fill Bundles

83

G-11 CR   76 K

Top View   Side View

2000 N   2000 N

3000 N   3200 N

100 μm

200 μm

Fill Resin Cracks
and Warp Fiber
Fractures Coincide

Multiple Resin
Cracks

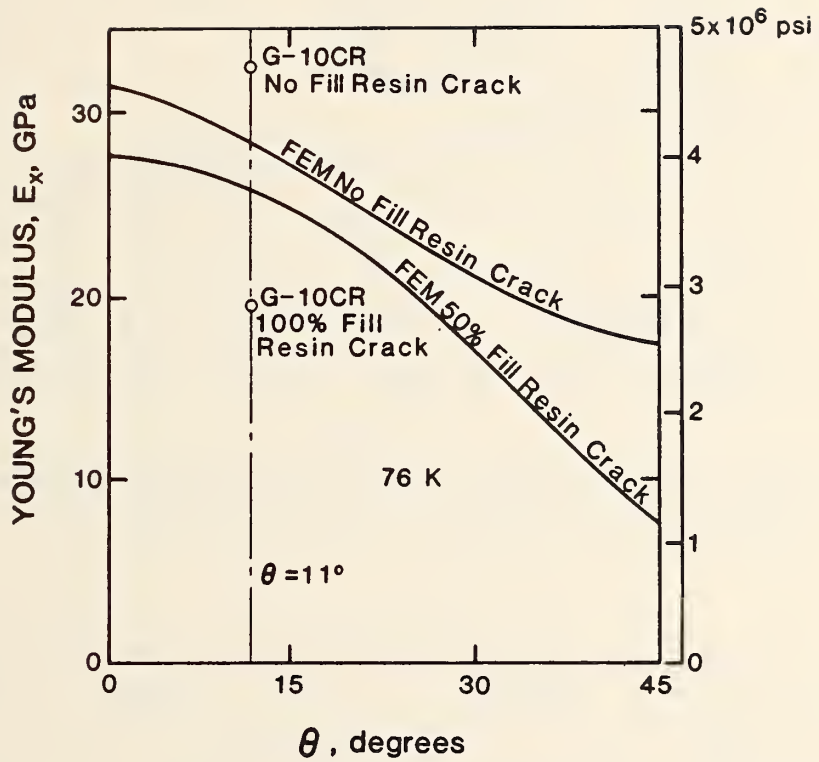Figure 16b. Top and edge views of damage corresponding to loads of Fig. 15.

84

Figure 17. Influence of internal fill cracks on woven unit cell Young's modulus:
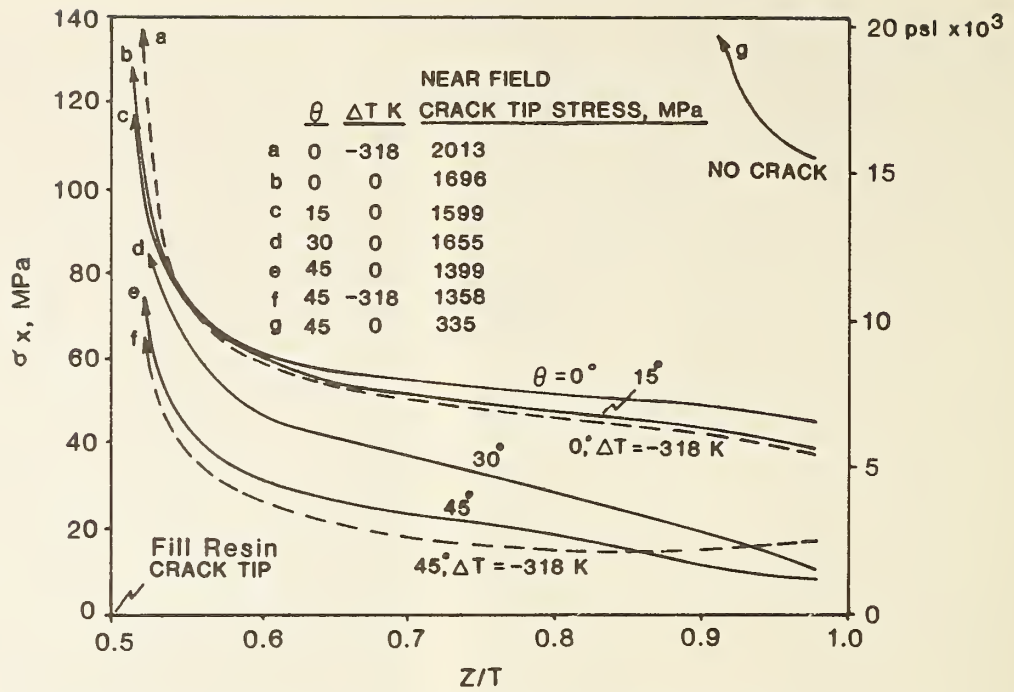a comparison between FEM and experiments for G-10CR.

Figure 18. Stress concentrations in warp fiber bundle above fill resin crack
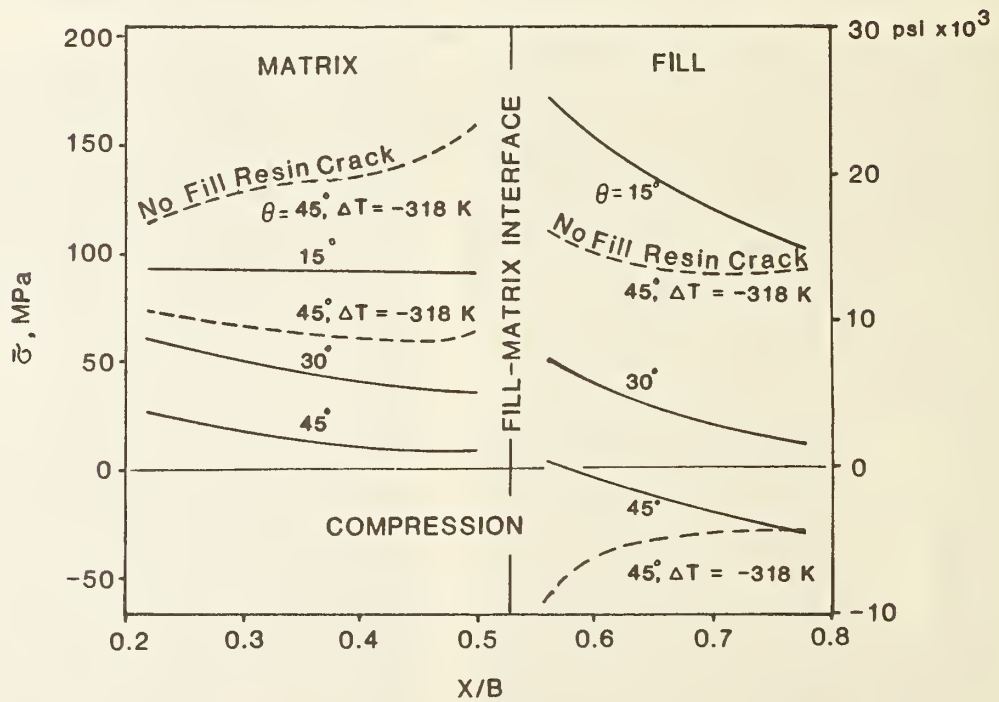along line a-b in Fig. 2: results from Ref. 5.

Figure 19. Stress concentrations in warp fiber bundle above fill resin crack
along line c-d in Fig. 2: results from Ref. 5.

NONMETALLIC MATERIAL STANDARDIZATION -

MATERIALS AND TEST METHODS[*+]

M. B. Kasen
Fracture and Deformation Division
National Bureau of Standards
Boulder, Colorado

The system for producing uniaxially reinforced, 3-4 mm diameter rod specimens described in the Sixth Annual Progress Report[1] has been refined and validated by production of excellent quality specimens using liquid-mix epoxy resin systems. The methodology is undergoing further modification to permit use of hot-melt epoxy and polyimide resin systems as will be required for the experimental program to be conducted in the NLTNIF reactor at ORNL. Preliminary studies indicate that short beam and torsional shear test methods will be useful in evaluating radiation degradation. Development of these and other applicable test methods are continuing. A cooperative program established with laboratories in Japan and in England has resulted in the production and testing of specimens having an identical configuration. An effective interchange of laboratory data is continuing.

OBJECTIVES

To provide, in cooperation with ORNL and LANL, specimens required for studies to develop organic insulators having the cryogenic neutron irradiation resistance required for MFE systems utilizing superconducting magnetic confinement. To develop test methods and analytical procedures for assessing radiation damage. To stimulate and participate in international cooperation directed toward accomplishing these objectives.

PROGRESS AND STATUS

We have demonstrated that specimens containing up to 58 volume percent glass fiber can be produced without macroscopically visible defects using epoxy resin systems that have a workable viscosity at room temperature. We

are presently experimenting with a resin system similar to that used in manu-
facturing the G-11 type of industrial laminate and with several polyimide
(bismaleimide) systems. These systems must be worked in the hot condition.
We are therefore investigating various methods of introducing heating into
the production apparatus. Many resins of interest must be blended with a
solid cure agent. We have therefore installed a 900 watt ultrasonic system
to facilitate blending without the use of solvents. It has been successfully
used to blend the G-11 resin system.

We have demonstrated that specimens 19 mm long can be successfully
tested in short beam shear. We have also demonstrated that such specimens
can be successfully tested in the torsional shear mode. These test modes are
of importance in evaluating radiation degradation of the fiber-matrix
interface.

A Japanese group, headed by Prof. T. Okada, ISIR, Osaka University and
including individuals at Kyoto University, The University of Osaka Prefecture,
and the Hoxan Corporation, has successfully produced specimens containing
glass, graphite, and silicon carbide fibers using the NBS method. Performance
has been evaluated in three-point flexure. A similar effort has been under-
taken by Dr. D. Evans of the Rutherford Laboratory in England. An effective
exchange of information is continuing, and plans are being made for exchange
specimens and for joint reporting of results during 1985.

SPECIMEN DEVELOPMENT

Specimen Quality

Our initial objective was to develop techniques for producing specimens
free of macroscopic defects. We initially selected a resin system composed of
a low viscosity bisphenol A epoxy resin cured with a low viscosity liquid
polyamide. This produced an almost transparent specimen, facilitating the
quality evaluation. We later introduced a system based on a standard
undiluted bisphenol A epoxy resin cured with a liquid aromatic amine, modi-
fied with polyoxypropylenediamine. This system was suggested by Dr. Evans as
a candidate radiation resistant impregnation or potting resin. These systems
have a workable viscosity at or slightly above room temperature, simplifying
the production process. Figure 1 illustrates that the quality objective was
attained.

The following procedure was established:

Step 1: Resin Mixing

Components are weighed out in a 100 ml beaker to produce a mix of
about 80 ml. Components are manually stirred.

Step 2: Resin Degassing

As recommended by Dr. Evans, the resin is vacuum degassed while
being stirred to break up the surface tension. This is accomplished by a
wire frame connected to a shaft penetrating a rotating vacuum seal. Stirring

speed is 60-70 rpm. Vacuum is provided by a mechanical forepump. A bleed valve controls the pressure level to prevent overflow of the resin during the initial stages of degassification. A typical degassing operation requires 40-60 minutes. The vacuum chamber consists of a glass bell jar, permitting infrared heating of the resin to reduce its viscosity and to increase the rate of degassing.

Step 3:   Preparing the Fiber Reinforcement

The basic reinforcing element is a glass fiber tow 600 mm long, folded in the center to provide a doubled tow 300 mm long. The volume fraction of glass obtained from introducing various multiples of the basic element into the tube mold is calculated from knowledge of the weight of this element, the density of the glass, and the volume of the tube. For the type of glass used in these experiments, incorporation of 4, 5, 6, and 7 doubled tows produces calculated glass volume fractions of 33%, 41%, 49% and 58%, respectively, in a 3 mm i.d. tube mold. The doubled tows are tied in the center with a nylon monofilament line to facilitate pulling into the tube mold.

Step 4:   Vacuum Impregnation

Impregnation is performed in the apparatus illustrated in Figure 2. Degassed resin is allowed to rise to the level of the pinchclamp, which is then closed to permit evacuation of the air in the glass strands. The pinchclamp is then opened and the resin is allowed to rise to just above the level of the glass fibers. With proper degassing, this can be accomplished without excessive bubble formation. Admitting atmospheric pressure into the system accomplishes the fiber impregnation.

Step 5:   Drawing into the Mold

The drawing procedure is illustrated in Figure 3. The nylon line is passed up the tube mold bore and the mold end is inserted under the resin in the impregnation tube. The glass tows are manually started up the tube mold while maintaining a head of resin, after which the pulling rate is controlled at about 2 cm/min by a variable speed motor. When the mold is filled, the end is capped to prevent loss of resin during the cure cycle. The NBS process uses commercially available PTFE tubing, 3 mm i.d., 7 mm o.d., 300 mm long, as the specimen molds. The tubing is selected to have a smooth interior. Specimens may also be made in glass tube coated with a release agent. However, PTFE is preferred, as it reduces the possibility of contaminating the resin during the cure cycle.

The vacuum system used in this process contains a cold trap that can be activated to prevent contamination of the glass fibers by back streaming of the pump oil.

Step 6: Specimen Cure

The PTFE tube mold is held in a tight fitting glass tube during cure to maintain specimen straightness. Curing takes place in a pressure vessel constructed from copper pipe. A pressure cure has been found necessary to prevent formation of surface defects. Approximately 5 kg/cm^2 (70 psi) of nitrogen has been found to produce excellent results.

Neat resin specimens are produced by vacuum drawing of the degassed resin into the tube molds followed by pressure curing.

Step 7: Specimen Removal

Specimens may be either pushed or pulled from the PTFE molds, which may then be reused.

As shown in Table 1, the coefficients of variability in diameter among rods produced with a given mold are on the order of 0.1% to 0.3%, indicating excellent dimensional reproducibility. Dimensional differences between the molds reflect differing lots of PTFE tubing. A total of 22 rods were dimensioned in this experiment.

Many systems of interest to this program require heating to above room temperature to achieve a workable viscosity. For example, a typical resin of the type used in the G-11 industrial laminate is quite viscous below about 60-65° C. The bismaleimide types of polyimide resin, which are of great interest to this program because of excellent radiation resistance, require processing temperatures on the order of 150° C. Modifications are currently being made to the production apparatus to accommodate these requirements.

Many of these resin systems require blending of a liquid resin with a solid cure agent. In commercial practice, solvents are frequently added to reduce the melting temperature. However, this cannot be done with the NBS method, as evolution of such solvents during the cure cycle would cause porosity. Hodges and St. Clair[2] have recently demonstrated that ultrasonic energy may be used to blend many such systems without the use of solvents. Figure 4 illustrates results obtained at NBS on the G-11 type of resin using a 900 W, 20 kHz, self-tuning ultrasonic system.

Fiscal Year 1985 Plans

Our current objective is to produce fiber-reinforced and neat-resin specimens of the following types for use in initial radiation studies in the NLTNIF reactor:

1) G-11CR system approximation

2) Polyimides

    a) PG-11CR approximation
    b) Developmental bismaleimide

90

3) Rutherford epoxy potting resin

The G-11CR specimens are intended to provide a baseline of performance reflecting current material usage. The PG-11CR specimens are intended to simulate the current polyimide variant of the CR laminate grades. The developmental bismaleimide system is representative of the latest polyimide resin development technology. The potting resin is included in response to a recommendation made by participants at the 1984 NBS/DOE Vail Workshop (see the workshop summary on page 299). Additional resin systems may be included upon recommendation of the program participants.

Additionally, procedures will be developed for producing specimens having silane glass finishes containing systematically increasing hydrogen contents. These will be useful in evaluating the influence of finish chemistry on interfacial degradation. Consideration will also be given to producing specimens reinforced with boron-free E glass and with glass of higher intrinsic strength.

TEST METHOD DEVELOPMENT

Mechanical Tests

Since the fiber-matrix interface is expected to be a prime location for damage accumulation during irradiation, shear properties are expected to be an important test parameter. We have therefore investigated the feasibility of performing flexural shear tests on the rod specimens. The fixture illustrated in Figure 5 is similar to a conventional 3-point fixture for conducting apparent interlaminar shear strength tests, differing primarily in contouring of the supports and of the loading nose to accommodate round specimens. Required specimen length is only 15 mm for a 3 mm diameter specimen tested at a span/depth ratio of 3.0. This makes it very economical of material and minimizes the volume required during irradiation.

An initial series of tests was conducted with this fixture at 295 K and 76 K. Five specimens each from two rods manufactured with the bisphenol A/polyamide resin system and containing either 50 or 60 v/o type E glass reinforcement were tested at each temperature. As illustrated on Figure 6, a series of distinct load drops appeared on the load-time curves of specimens tested at 76 K, indicating onset of consecutive shear failures with increasing stress. Continuous bending over of the 295 K curve is attributed to the exceptional room temperature ductility of the selected resin system. This precludes failure by the shear mode.

A typical 76 K shear failure is illustrated in Figure 7. Narrow shear bands initially progressed into the specimen in an inverted V configuration from the point of contact with the loading nose. These bands subsequently acted as nuclei for massive shear failures that propagated along the specimen length, giving rise to the observed load drops.

The 76 K test data, summarized in Table 2, reflect the stress required to initiate the first massive longitudinal shear failure (first load drop). The low coefficients of variability suggest that this may be a viable test mode at

cryogenic temperatures. The small influence of fiber volume fraction on shear strength was not unexpected because shear strength is known to pass through a maximum in the vicinity of 50-60 v/o fiber content.

While the flexural shear test method appears potentially useful, the complexity introduced by the continuously changing stress state makes it difficult to quantify the results. An alternative would be to conduct shear tests in torsion. Exploratory tests conducted at 76 K showed that it was possible to induce longitudinal shear in this manner. It was further found that the required torsional stress could be introduced by means of copper tube end caps frozen onto the specimen ends. The ability to grip specimens in this manner might prove useful in evaluating damage accumulation as a function of applied stress using the dynamic resonance technique. The presence of bulky end caps could interfere with the sensitivity of such measurements.

Fiscal Year 1985 Plans

The following test methodology objectives must be met to prepare for the initial irradiation series to be conducted at the NTLNIF facility:

1) Development of apparatus and techniques for comparing mechanical performance of specimens before irradiation and after warming to room temperature following irradiation.

2) Development of procedures for relating changes in failure mode to changes in mechanical performance and to the molecular level damage introduced by the irradiation.

Additionally, consideration will be given to the following objectives which must be met in preparation for future test programs:

1) Development of approaches to assessing mechanical performance of specimens after irradiation without warmup.

2) Development of methodology for assessing damage accumulation during warmup after irradiation.

3) Development of methods for mechanical testing while under irradiation.

INTERNATIONAL COOPERATION

Rutherford Appleton Laboratories (England)

Dr. David Evans has communicated his initial experience in preparing specimens using the NBS technique and has described the initial test results obtained during room temperature testing in three-point flexure. While promising, excessive variability indicated a need to improve both the quality

of the specimen and to refine the testing technique. Dr. Evans is presently investigating a process for direct vacuum impregnation of the specimens at final size.

Dr. Evans has developed a prototype fixture permitting sequential flexural testing of a series of specimens at 4 K without requiring intermediate warmup. He has also been very helpful in suggesting candidate resin systems for inclusion in the initial test series.

ISIR, Osaka University (Japan)

Professor Toichi Okada has organized a cooperative effort between ISIR, KURRI (Kyoto University), The University of Osaka Prefecture, and the Cryogenic Technology and Development Center, Hoxan Corporation, to investigate the feasibility of standardizing the fabrication and testing of composite specimens using the NBS technique. Specimens fabricated with two types of epoxy matrix and reinforced with glass, graphite, silicon carbide, and alumina were fabricated by Hoxan and tested in three-point flexure at 295 K and at 76 K by the other three participants. Results of this study were reported at the 1984 ICMC Conference on Nonmetallic Materials and Composites at Low Temperatures in Heidelberg, West Germany.[3] They concluded that the production method was simple and effective. However, they also experienced excessive variability in flexural test data. They are presently investigating a four-point testing procedure that they hope will produce more consistent results.

Fiscal Year 1985 Plans

We have tentatively agreed that each laboratory should attempt to produce identical specimens to validate the concept of standardization. A commonly agreed upon type of resin and type and quantity of glass reinforcement would be used. The specimens would be exchanged between laboratories for comparative evaluation. An assessment of specimen uniformity will also be made by an independent laboratory.

We have also tentatively agreed to a joint reporting of results at the 1985 ICMC Conference or at the NBS/DOE Vail Workshop.

REFERENCES

1.   M. B. Kasen, "Materials and Test Methods," pp. 48-52 in Special Purpose Materials Annual Progress Report for Period Ending October 1, 1983, DOE/ER-0113/3, U.S. Department of Energy, May 1984.

2.   W. T. Hodges and T. L. St. Clair, "Ultrasonic Mixing of Epoxy Curing Agents," NASA Technical Memorandum 85643, National Aeronautics and Space Administration, Langley Research Center, Hampton, Virginia, 1983.

3. T. Okada, S. Nishijima, H. Yamaoka, K. Miyata, Y. Tsuchida, K. Mizobuchi, Y. Kuraoka, and S. Namba, "Mechanical Properties of Unidirectionally Reinforced Materials," presented at ICMC Conference on Materials and Composites at Low Temperatures, Heidelberg, West Germany (1984). To be published in Nonmetallic Materials and Composites at Low Temperatures 3, Plenum Press, New York.

Table 1. Variability in diameter (mm) among rods produced by PTFE tube molds.

Tube No.	Avg.	St. Dev.	CV
1	3.0793	0.00732	0.0024
2	2.9727	0.00881	0.0030
3	2.9580	0.00316	0.0011

Table 2. Flexural shear data at 76 K.

Volume Fraction	Rod No.	Strength (MPa)	Std. Dev.	CV
50	1	23.6	1.0	0.042
	2	23.0	2.0	0.087
		23.3	1.5	0.064
60	1	23.3	1.1	0.047
	2	23.6	0.3	0.013
		23.5	0.8	0.034

Figure 1. Transparency of a 3 mm diameter specimen containing 58 v/o glass indicates excellent fiber wetting and absence of porosity.

A   B

Figure 2. Impregnation is performed by evacuating the glass tows in a 12.7 mm (0.5 in) diameter inner tube (A). The resin is transferred into the tube, and atmospheric pressure is admitted to complete the impregnation (B).
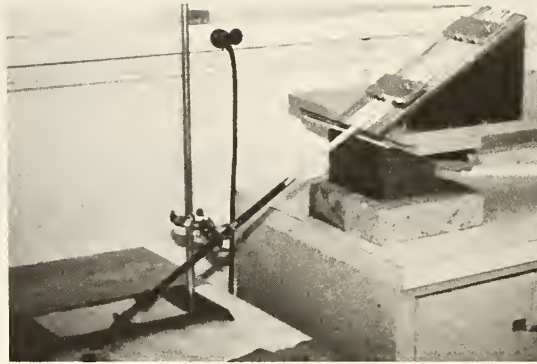
Figure 3. The impregnated glass tows are pulled into the 3 mm diameter PTFE tube mold while maintaining a head of resin to prevent entrainment of air. The unused resin may be recovered.

Figure 4. G-11 resin system as hand mixed (A) and after three minutes of ultrasonic blending (B).
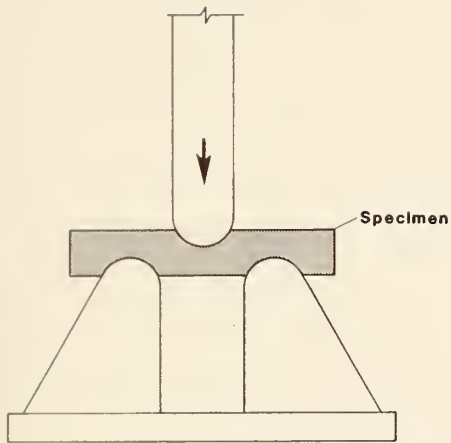
Figure 5. Sketch of fixture for testing 3 mm diameter specimens in flexural shear. Specimen is 15 mm long.
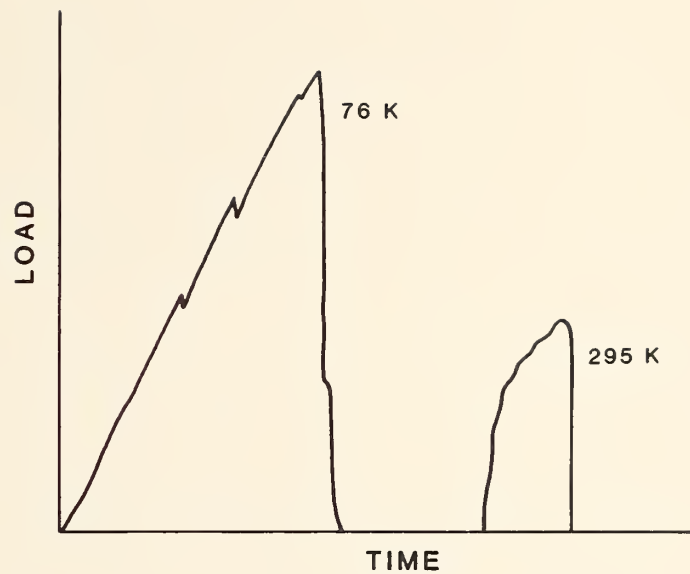

Figure 6. Typical load-time curves obtained during flexural shear tests. Serrations at 76 K indicate onset of longitudinal shear.
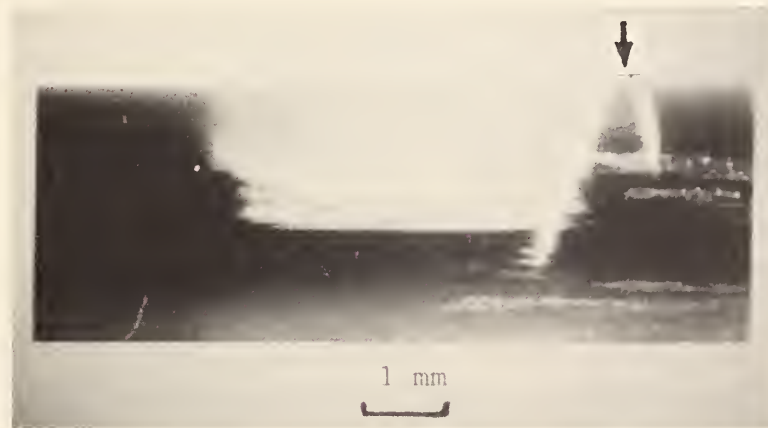

Figure 7. Typical longitudinal shear failure at 76 K. Arrow indicates the point of contact of the loading nose. Shear bands have propagated into the specimen, forming an inverted V and acting as the nucleating point for massive longitudinal shear failure.

Elastic Representation Surfaces of Unidirectional
Graphite/Epoxy Composites[*]

R. D. Kriz and H. M. Ledbetter

Fracture and Deformation Division
National Bureau of Standards
Boulder, Colorado 80303 USA

Unidirectional graphite/epoxy composites exhibit high elastic anisotropy and unusual geometrical features in their elastic-property polar diagrams. From the five-component transverse-isotropic elastic-stiffness tensor we compute and display representation surfaces for Young's modulus, torsional modulus, linear compressibility, and Poisson's ratios. Based on Christoffel-equation solutions, we describe some unusual elastic-wave-surface topological features. Musgrave considered in detail the differences between phase-velocity and group-velocity surfaces arising from high elastic anisotropy. For these composites, we find effects similar to, but more dramatic than, Musgrave's. Some new, unexpected results for graphite/epoxy include: a shear-wave velocity that exceeds a longitudinal velocity in the plane transverse to the fiber; a wave that changes polarization character from longitudinal to transverse as the propagation direction sweeps from the fiber axis to the perpendicular axis.

Key Words: graphite/epoxy; acoustic properties; elastic properties; energy flux deviation; group velocity; mode conversion

---

INTRODUCTION

Graphite/epoxy composites with unidirectional fiber reinforcement exhibit transverse-isotropic elastic symmetry; thus, five independent elastic constants. In matrix form, one can represent the elastic-stiffness tensor as

$$[C_{ij}] = \begin{bmatrix} C_{11} & C_{12} & C_{13} & 0 & 0 & 0 \\ & C_{11} & C_{13} & 0 & 0 & 0 \\ & & C_{33} & 0 & 0 & 0 \\ & & & C_{44} & 0 & 0 \\ & & & & C_{44} & 0 \\ & & & & & (C_{11}-C_{12})/2 \end{bmatrix} \qquad (1)$$

which is symmetrical, that is $C_{ji} = C_{ij}$. The elastic compliances, S_{ij}, relate inversely to the C_{ij}:

$$[S_{ij}] = [C_{ij}]^{-1} \qquad (2)$$

In form, the S_{ij} matrix looks identical to the C_{ij} matrix except that $S_{66} = 2(S_{11}-S_{12})$.

While Eq. 1 displays all the elastic-constant information as an "irreducible set," it displays directly very little of the wealth of practical information and interesting geometrical properties contained in C_{ij}.

For uniaxial graphite/epoxy, the present study considers many geometrical features of the elastic-constant tensor. For example: representation surfaces of Young's modulus, torsional modulus, linear compressibility, and Poisson's ratio. Following Musgrave [1], who studied materials such as zinc, we consider the velocity and slowness surfaces and find some remarkable features

concerning the acoustic-energy flux. Following Ledbetter and Kriz [2], who focused on orthotropic materials, we find some peculiarities also in graphite/epoxy. First, a shear velocity exceeds the longitudinal velocity in the plane perpendicular to the fibers. Second, a wave changes polarization character from longitudinal to transverse as the wave direction sweeps from the fiber axis to the perpendicular axis.

CALCULATIONS

Elastic representation surfaces

Representation of elastic properties by geometrical surfaces has obvious utility, as described by Nye [3]. Following a procedure outlined by Lekhnitskii [4], representation surfaces can be derived via the general elastic-compliance fourth-rank-tensor transformation:

$$S'_{ijkl} = a_{im} a_{jn} a_{kr} a_{ls} S_{mnrs} \tag{3}$$

Here we choose the x_3 axis parallel to the fibers of a unidirectional fiber-reinforced composite. We assume isotropy in the x_1-x_2 plane, transverse to the fibers. For hexagonal (transverse-isotropic) symmetry, transformations for all elastic constants are axially symmetric about x_3. Thus, elastic constants depend only on rotations, $+\theta$, away from x_3 toward the x_1-x_2 plane. Transformation equations for Young's modulus, $E_3(\theta)$, torsional modulus, $T_3(\theta)$, shear modulus, $G_{23}(\theta)$, linear compressibility, $K_3(\theta)$, and Poisson's ratio, $\nu_{32}(\theta)$, are in Voigt notation:

$$E_3^{-1}(\theta) \equiv S'_{33}(\theta) = S_{11} + x(2S_{13} + S_{44} - 2S_{11})$$
$$+ x^2(S_{11} + S_{33} - 2S_{13} - S_{44}) \tag{4}$$

$$T_3^{-1}(\theta) \equiv [S_{44}'(\theta) + S_{55}'(\theta)]/2 = S_{44} + (1 - x)(S_{11} - S_{12} - S_{44}/2)$$
$$+ 2x(1 - x)(S_{11} + S_{33} - 2S_{13} - S_{44}) \qquad (5)$$

$$G_{23}^{-1}(\theta) \equiv S_{44}'(\theta) = S_{44} + 4x(1 - x)(S_{11} + S_{33} - 2S_{13} - S_{44}/2) \qquad (6)$$

$$K_3(\theta) = S_{11} + S_{12} + S_{13} - x(S_{11} - S_{33} + S_{12} - S_{13}) \qquad (7)$$

$$\nu_{32}(\theta) \equiv -S_{23}'(\theta)/S_{33}'(\theta) = E_3(\theta)[S_{13} + x(1 - x)(S_{11} + S_{33} - 2S_{13} - S_{44})] \qquad (8)$$

where $x = \cos^2\theta$. We also consider the transformation of ν_{13} as shown in Fig. 1 where there are two rotations: α around x_2 followed by β around x'_1. Given the tilt angle α, we calculated ν_{13} in the x_2-x_3 plane. For this double rotation we find:

$$\nu_{13}(\alpha,\beta) \equiv -S_{13}''(\alpha,\beta)/S_{11}'(\alpha) = -\{(S_{11} + S_{33} - S_{44})\cos^2\alpha \, \sin^2\alpha \, \cos^2\beta$$
$$+ S_{12}\cos^2\alpha \, \sin^2\beta + S_{13}[\cos^2\beta(\cos^4\alpha + \sin^4\alpha) + \sin^2\alpha \, \sin^2\beta]\}/S_{11}'(\alpha) \qquad (9)$$

where
$$S_{11}'(\alpha) = S_{33}'(90 - \alpha) = E_3^{-1}(90 - \alpha) \qquad (10)$$

When the tilt angle is zero β equals θ and Eq. 9 reduces to

$$\nu_{13}(\theta) = -[S_{12}\sin^2\theta + S_{13}\cos^2\theta]/S_{11}'(\alpha) \qquad (11)$$

Based on Eqs. 4-11, we give polar diagrams, Figs. 2-8, that represent the unusual anisotropy of various elastic constants of unidirectional graphite/epoxy.

102

Acoustic representation surfaces

The influence of elastic constants, calculated from Eqs. 4-11, on stress-wave propagation is represented by polar diagrams of the eigenvalue solutions to Christoffel's equations [1]:

$$(C_{ijkl}\, n_j n_k - \rho v^2 \delta_{il})\, p_i = 0 \qquad (12)$$

where C_{ijkl} is the fourth-rank elastic-stiffness tensor, n_i are the direction cosines of the wave vector measured from the principal material axes x_i, ρ is the mass density, δ_{il} is the Kronecker delta, v is the phase velocity that propagates along n_i, and p_i are the particle-displacement direction cosines. Solution of Eq. 12 yields three eigenvalues, ρv^2, and the corresponding eigenvector, p_i, for each phase velocity. The orientation of the particle displacement with respect to the wave vector is denoted by subscripts (t, qt, ql) on the phase velocities: t means that p_i is transverse to n_i ($n_i p_i = 0$); qt (quasi-transverse) means that the largest component of p_i is transverse to n_i ($0 < n_i p_i < 1\sqrt{2}$); and ql (quasi-longitudinal) means that the largest component of p_i is parallel to n_i ($1/\sqrt{2} < n_i p_i < 1$). Along principal material axes, pure transverse waves and pure longitudinal waves must exist for all wave phase velocities. The eigenvalue solutions, ρv^2, are the roots of the characteristic equation, written as the determinant of Eq. 12:

$$\begin{vmatrix} (C_{11}n_1^2 + C_{66}n_2^2 + C_{44}n_3^2) - \rho v^2 & (C_{12} + C_{66})n_1 n_2 & (C_{13} + C_{44})n_2 n_3 \\[2mm] (C_{12} + C_{66})n_1 n_2 & (C_{66}n_1^2 + C_{11}n_2^2 + C_{44}n_3^2) - \rho v^2 & (C_{13} + C_{44})n_2 n_3 \\[2mm] (C_{13} + C_{44})n_2 n_3 & (C_{13} + C_{44})\, n_2 n_3 & (C_{44}n_1^2 + C_{44}n_2^2 + C_{33}n_3^2) - \rho v^2 \end{vmatrix} = 0 \qquad (13)$$

Velocity surfaces are calculated from Eq. 13 by considering all possible wave vector orientations. Because of hexagonal elastic symmetry, the velocity surfaces are also axially symmetrical around x_3. Thus, solutions to Eq. 13 are calculated as functions of $+\theta$ from x_3:

$$v_t(\theta) = [(C_{44}\cos^2\theta + C_{66}\sin^2\theta)/\rho]^{1/2} \tag{14}$$

$$v_{qt}(\theta) = [(C_{44} + C_{11}\sin^2\theta + C_{33}\cos^2\theta - \sqrt{C})/2\rho]^{1/2} \tag{15}$$

$$v_{qt}(\theta) = [(C_{44} + C_{11}\sin^2\theta + C_{33}\cos^2\theta + \sqrt{C})/2\rho]^{1/2} \tag{16}$$

where
$$C = [(C_{11}-C_{44})\sin^2\theta + (C_{44}-C_{33})\cos^2\theta]^2 + (C_{13} + C_{44})^2\sin^2 2\theta$$

One should note that subscripts t, qt, and qℓ represent only labels. In special cases, displacements t, qt, qℓ, and ℓ may coexist on the same phase-velocity surface [2]. Thus, rarely, Eqs. 15 and 16 yield polarizations different from the designated qt and qℓ subscripts. Equation 14 represents an exception where v_t is always a pure-transverse wave for all orientations.

Intersections of these velocity surfaces with the isotropic x_1-x_2 plane yield three concentric circles with pure-longitudinal or pure-transverse modes. Unlike isotropic materials, the two pure-transverse velocities calculated from Eqs. 14 and 15 do not coincide in the isotropic x_1-x_2 plane where:

$$v_t(90) = (C_{66}/\rho)^{1/2} \; ; \; v_{qt}(90) = (C_{44}/\rho)^{1/2} \tag{17}$$

The eigenvector solutions to Eq. 12 are the particle displacements, $\{p_1:p_2:p_3\}$:

$$p_1 = [n_1^2 (C_{11} + C_{12})/2]^{1/2}/[\rho v^2-(C_{11}-C_{12})/2-C_{44}n_3^2] \tag{18}$$

$$p_2 = [n_2^2(C_{11} + C_{12})/2]^{1/2}/[\rho v^2+(n_2^2-n_1^2)C_{11}/2+C_{12}/2-n_3^2 C_{44}] \tag{19}$$

$$p_3= [2n_3^2(C_{13}+C_{44})^2/(C_{11}+C_{12})]^{1/2}/\{\rho v^2+(n_2^2-n_1^2)C_{44}+n_3^2[2(C_{23}+C_{44})^2/(C_{11}+C_{12})+C_{33}]\} \tag{20}$$

The acoustic energy may propagate in a direction different from the wave vector. This direction of propagation is the energy-flux vector and the corresponding velocity of propagation is the group velocity, v_g. For homogeneous plane waves, the energy-flux vector and v_g coincide [5]. For isotropic materials, energy-flux vector and group velocity coincide with the wave vector and with phase velocity. For anisotropic materials the energy-flux vector deviates from the wave vector by an angle, Δ. For plane homogeneous waves, the same deviation angle exists between phase and group velocities:

$$v_g(\Theta,\Delta) = v(\Theta)/\cos \Delta \tag{21}$$

Polar diagrams of group velocities can be calculated from Eq. 21. We follow Musgrave [6] and plot v_g as a function of $\Theta' = \Theta + \Delta$. Due to the deviation of energy-flux, group-velocity surfaces appear distorted when compared with phase-velocity surfaces. Hence, polar diagrams of v_g are also called energy surfaces.

One calculates the deviation angle, Δ, from the direction cosines (n_i, L_i) of the wave vector and energy-flux vector, respectively:

$$\Delta = \cos^{-1} n_i L_i \qquad (22)$$

For orthorhombic symmetry, Kriz [7] gave the direction cosines, L_i, of the energy-flux vector. For hexagonal symmetry, with transformations in the x_2-x_3 plane ($n_1 = 0$), these become:

$$L_1 = C_{66} p_1 p_2 n_2 + C_{44} p_1 p_3 n_3 \qquad (23)$$

$$L_2 = C_{66} p_1^2 n_2 + C_{22} p_2^2 n_2 + C_{23} p_2 p_3 n_3 + C_{44}(p_2 p_3 n_3 + p_3^2 n_2) \qquad (24)$$

$$L_3 = C_{22} p_3^2 n_3 + C_{33} p_2 p_3 n_2 + C_{44}(p_1^2 n_3 + p_2 p_3 n_2) \qquad (25)$$

Effects of fiber volume fraction on the effective C_{ij} were calculated using relationships derived by Datta, Ledbetter, and Kriz [8].

RESULTS AND DISCUSSION

Polar diagrams shown in Figs. 2-8 were calculated using the elastic constants in Table 1. Matrix and graphite-fiber elastic constants were obtained from Ref. 9. For comparison, Table 1 includes elastic constants for other polyacrylonitrile (PAN) graphite fibers.

The peculiar elastic behavior caused by the elastic anisotropy of the graphite fibers is shown in Figs. 2-8 at various fiber volume fractions. At zero volume fraction ($V_f = 0.0$) the matrix is isotropic and spherical representation surfaces (circular cross sections) are observed for all elastic constants. The largest orientational variations in elastic constants occur at $V_f = 1.0$. At intermediate V_f, we see that Poisson's ratios, linear compressibility, and Young's modulus are more affected by small changes in V_f.

Torsional and shear modulus are affected less. Both Poisson's ratios (ν_{32} and ν_{13}) exhibit large negative values. For ν_{32} this is caused by variations in V_f and for ν_{13} this is caused by variations in tilt angle, α. In all cases, the Poisson's ratios satisfy the bounds derived by Christensen [12]:

$$-1 < \nu_{12} < +1; \quad \nu_{13} < (E_1/E_3)^{1/2} \tag{26}$$

Elastic anisotropy exerts similar influences on the acoustic representation surfaces. Figures 9 and 10 demonstrate the influence of fiber volume fraction on phase-velocity and group-velocity surfaces. Large changes in flux-deviation angles, shown in Fig. 11, occur at low V_f. Hence, the cusps observed on the group-velocity curves in Fig. 10 result from changes in flux deviations.

Figure 12 shows surprising behavior of the particle displacement orientations at $V_f = 1.0$. For the $v_{q\ell}$ surface the displacements in the x_2-x_3 plane undergo a transition from pure longitudinal along x_3 to pure shear along x_2. Consequently, in the x_1-x_2 plane one observes a shear wave moving faster than a longitudinal wave. While peculiar, similar properties were reported by Ledbetter and Kriz [2] for orthorhombic crystals. In orthorhombic crystals, this rare occurrence of $v_t > v_\ell$ leads to the interconnection of $v_{q\ell}$ and v_{qt} surfaces into a single surface (also see Musgrave [13]). For hexagonal symmetry we observe $C_{44} = C_{22}$ when $V_f \cong 0.96$ and consequently $v_t = v_\ell$ in the x_1-x_2 plane. At volume fractions higher than 0.96 one observes a mode transition without the $v_{q\ell}$ and v_{qt} surfaces interconnecting into a single surface.

This mode transition can be observed in Fig. 13. There the displacement deviations, $\delta = \cos^{-1} n_i p_i$, from the wave vector are shown versus Θ. In Fig.

13 one observes that fiber volume fraction effects a smooth mode transition. The mode transition starts at $V_f = 0.3$ where $v_{q\ell}$ transitions into v_{qt} at $\Theta = 56°$. This transition does not continue into v_t; v_{qt} transitions back to $v_{q\ell}$. From $\Theta = 56°$ to $\Theta = 62°$ one observes a partial mode transition $(v_{qt} > v_{q\ell})$. As V_f increases, this mode transition continues predictably; for $V_f > 0.96$, v_{qt} transitions into v_t. Thus, ℓ, $q\ell$, qt, and t particle displacements are observed along a single surface.

While Hashin's composite-cylinder-assemblage model [14] can predict elastic constants for systems approaching $V_f = 1.0$, the geometric limit for hexagonal-packed circular fibers is $V_f = \pi/(2\sqrt{3})$ or 0.907, which is less than the volume fraction required for mode transition.

Such mode transitions can occur in composites at $V_f < 0.907$ when fiber constant $C_{44} \gg C_{22}$. Such a change in fiber elastic anisotropy could result from changing the fiber texture; but for fibers studied to date C_{44} exceeds C_{22} by only 5 to 20 percent.

The peculiar elastic anisotropy discussed above depends strongly on the fiber-elastic-constant values. The elastic constants for PAN graphite fibers shown in Figs. 2-8 at $V_f = 1.0$ were extrapolated by Kriz and Stinchcomb [9] using Hashin's composite-cylinder-assemblage model [14]. The correction $\beta_2 = K_{FTT}/(K_{FTT} + 2 G_{FTT})$, noted by Hashin [15], changes the elastic constants predicted in Ref. 9 less than one percent over the full range of fiber volume fractions. Thus, the fiber elastic constants in Table 1 are accurate and compare well with constants evaluated independently by Dean and Turner [10] and by Smith [11]. The well-developed radial structure of PAN graphite fibers observed by Diefendorf et al. [16] is consistent with the transverse-isotropic symmetry reported by Kriz and Stinchcomb [9]. Fiber constants

listed in Table 1 satisfy mechanical-stability conditions, that is Eq. 1 must be positive-definite. The fiber Poisson's ratios also satisfy the bounds of Eq. 26.

CONCLUSIONS

At low fiber volume fractions, Young's modulus E_3, linear compressibility K_3, and Poisson's ratios ν_{32} and ν_{13} are influenced most by the graphite-fiber anisotropy. Shear modulus G_{23} and torsional modulus T_3 are less affected by fiber anisotropy. Large negative values were observed for Poisson's ratios ν_{13} and ν_{32}, which were also influenced by fiber anisotropy. Poisson's ratio ν_{32} is sensitive to small variations in fiber volume fraction. Poisson's ratio ν_{13} is sensitive to rotations around the x_2 axis. Graphite-fiber anisotropy also affects both phase and group velocities, particularly the latter. In the x_1-x_2 plane the fiber constants $C_{44} > C_{22}$ cause a shear-wave speed to exceed a longitudinal-wave speed; consequently the longitudinal wave along x_3 transitions into a pure shear wave in the x_1-x_2 plane. This mode transition depends on fiber volume fraction.

ACKNOWLEDGMENT

REFERENCES

1. Musgrave, M.J.P., _Crystal Acoustics_, Holden-Day, San Francisco, 1970, p. 83.

2. Ledbetter, H. M. and Kriz, R. D., "Elastic-Wave Surfaces in Solids," Physica Status Solidi (b), Vol. 11, 1982, pp. 475-480.

3. Nye, J. F., _Physical Properties of Crystals_, Oxford U. P., London, 1957, pp. 143-148.

4. Lekhnitskii, S. G., _Theory of Elasticity of an Anisotropic Body_, Holden-Day, San Francisco, 1963, p. 51.

5. Hayes, M. and Musgrave, M.J.P., "On Energy Flux and Group Velocity," Wave Motion, Vol. 1, 1979, pp. 75-82.

6. Musgrave, M. J. P., "On the Propagation of Elastic Waves in Aeolotropic Media II. Media of Hexagonal Symmetry." Proceedings of the Royal Society of London, Vol. 226, 1954, pp. 356-366.

7. Kriz, R. D., "Mechanical Properties for Thick Fiber Reinforced Composite Materials Having Transversely Isotropic Fibers," Masters Thesis, College of Engineering, Virginia Polytechnic Institute and State University, Blacksburg, Virginia, 1976.

8. Datta, S. K., Ledbetter, H. M., and Kriz, R. D., "Calculated Elastic Constants of Composites Containing Anisotropic Fibers," International Journal of Solids and Structures, Vol. 20, 1984, pp. 429-438.

9. Kriz, R. D. and Stinchcomb, W. W., "Elastic Moduli of Transversely Isotropic Fibers and Their Composites," Experimental Mechanics, Vol. 19, 1979, pp. 41-49.

10. Dean, G. D. and Turner, P., "The Elastic Properties of Carbon Fibers and Their Composites," Compoistes, Vol. 4, 1973, pp. 174-180.

11. Smith, R. E., "Ultrasonic Elastic Constants of Carbon Fibers and Their Composites," Journal of Applied Physics, Vol. 43, 1972, pp. 2555-2561.

12. Christensen, R. M., _Mechanics of Composite Materials_, John Wiley and Sons, 1979, p. 79.

13. Musgrave, J. J. P., "On an Elastodynamic Classification of Orthorhombic Media," Proceedings of the Royal Society of London (A), Vol. 374, 1981, pp. 401-429.

14. Hashin, Z., "On Elastic Behavior of Fiber Reinforced Materials of Arbitrary Transverse Phase Geometry," Journal of Mechanics and Physics of Solids, Vol. 13, 1965, pp. 119-134.

15. Hashin, Z., "Analysis of Properties of Fiber Composites with Anisotropic Constituents," Journal of Applied Mechanics, Vol. 46, 1979, pp. 543-550.

16. Diefendorf, R. J., Riggs, D. M., and Sorensen, I. W., "The Relationships of Structure to Properties in Graphite Fibers," Technical Report No. AFML-TR-72-133, p. 65, Air Force Materials Laboratory, Wright-Patterson Air Force Base, Ohio.

Table 1. Matrix and graphite fiber elastic properties in units of GPa, except ν which is dimensionless

	C_{33}	C_{11}	C_{12}	C_{13}	C_{44}	ν_{32}	ν_{12}
Matrix[1] Ref. 9	8.63	8.63	4.73	4.73	1.95	0.354	0.354
Fiber[2] Ref. 9	235	20.0	9.98	6.45	24.0	0.279	0.490
Ref. 10	240	20.4	9.40[3]	10.5	24.0	0.35	0.497
Ref. 11	221	19.4	6.60[3]	5.8	20.3	0.23	0.32
Composite[4] (V_f=0.6)	144	13.6	7.0	5.47	6.01	0.284	0.497

1. Epoxy matrix composition is tetraglycidyl 4,4' diaminodiphenyl methane cured with diaminodiphenyl sulphone (TGDDM-DDS).

2. Graphite fibers are pyrolized from polyacrylonitrile fibers.

3. C_{12} is calculated from $C_{66} = (C_{11}-C_{12})/2$.

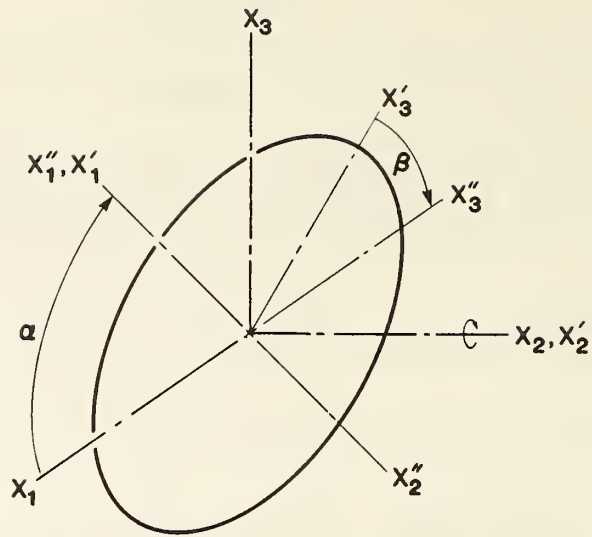4. Composite properties are calculated from equations derived in Ref. 8.

111

Fig. 1 Coordinate transformations for ν_{13} $(\alpha,\ \beta)$.
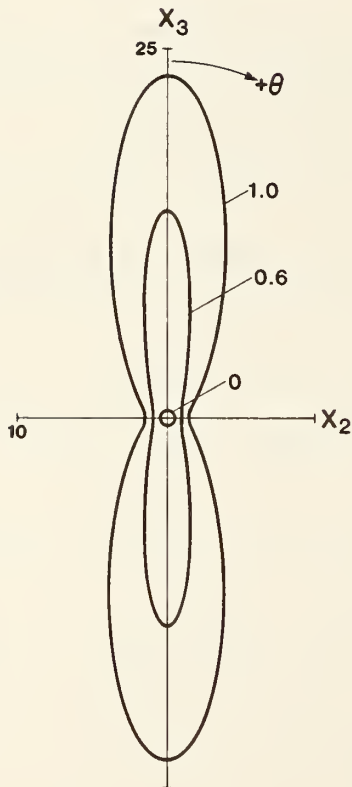Uniaxial load along $x_1'' = x_1'$.

Fig. 2 Polar diagram of Young's
modulus E_3 for various fiber
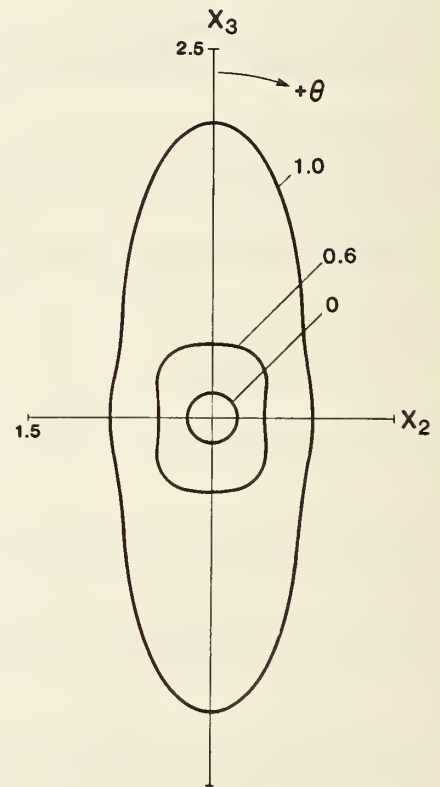volume fractions, in GPa.

Fig. 3 Polar diagram of torsional
modulus T_3 for various fiber
volume fractions in GPa.

112
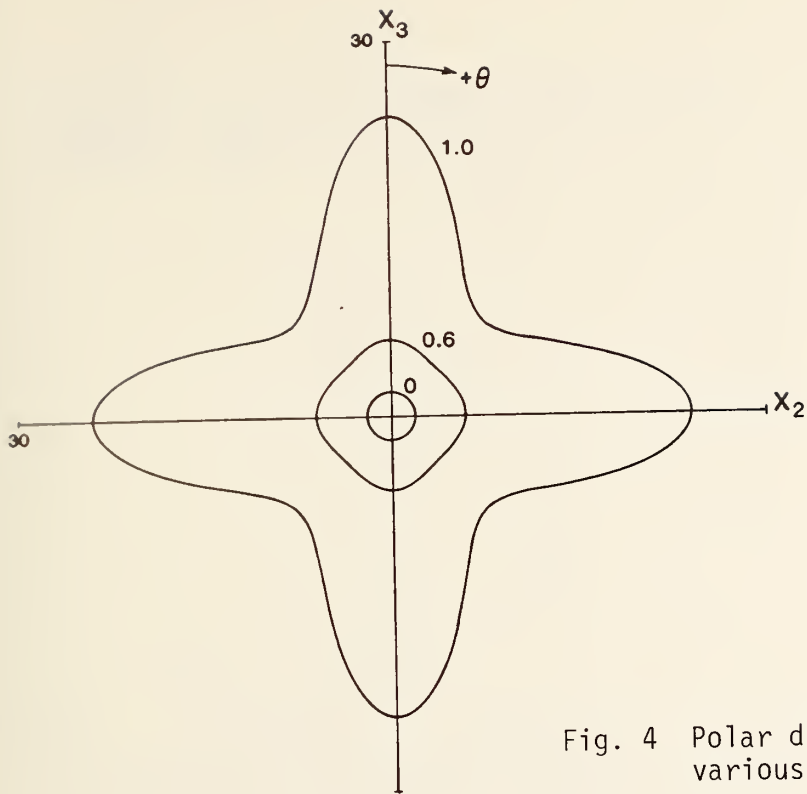
Fig. 4 Polar diagram of shear modulus G_{23} for
various fiber volume fractions, in GPa.
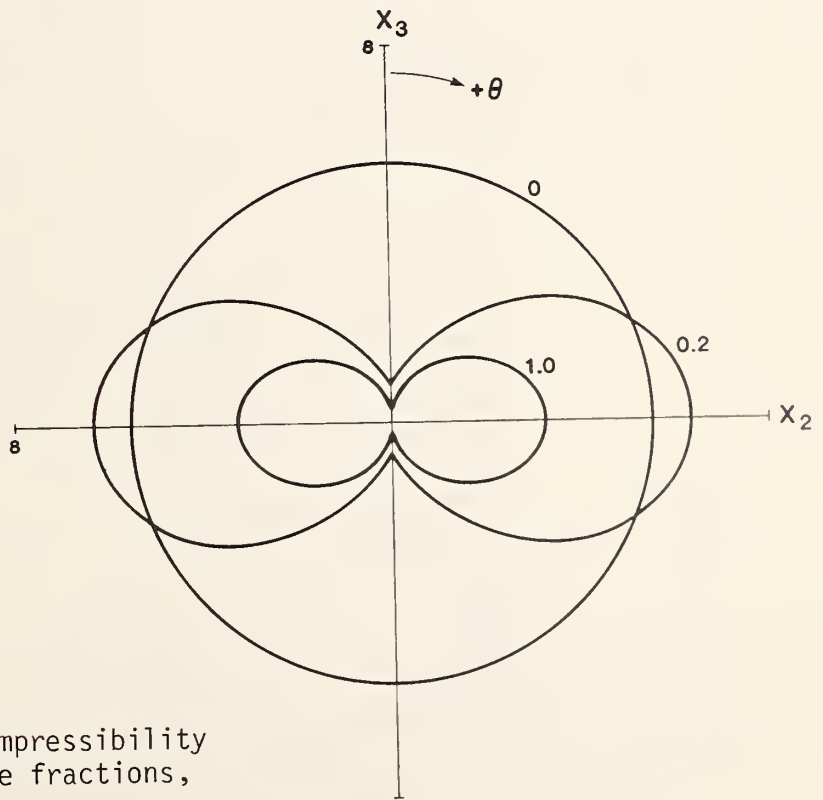
Fig. 5 Polar diagram of linear compressibility
K_3 for various fiber volume fractions,
in GPa.

113
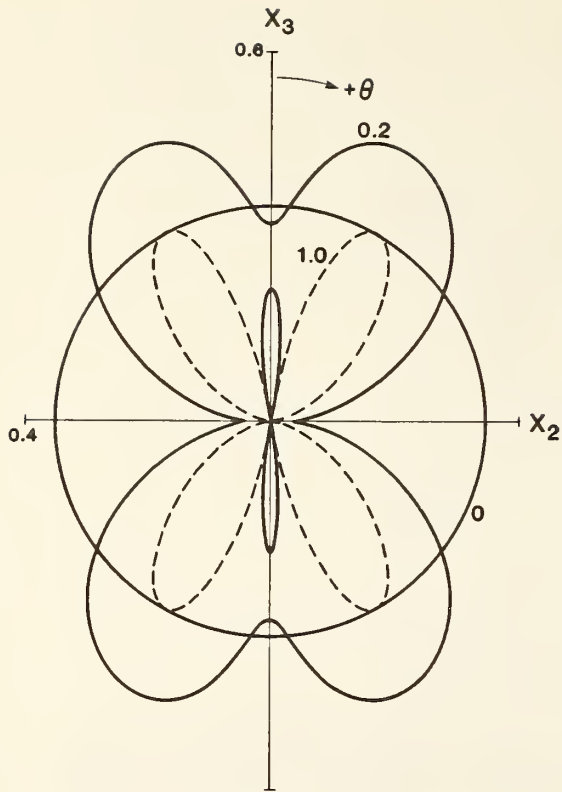
Fig. 6 Polar diagram of Poisson's ratio v_{32} for various fiber volume fractions.
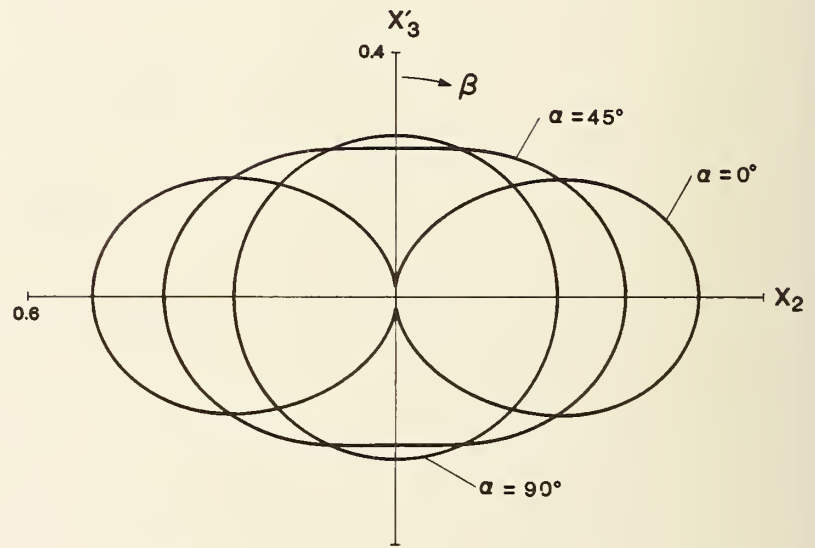
Fig. 7 Polar diagram of Poisson's ratio v_{13} for various tilt angles, α (see Fig. 1), at a fiber volume fraction of 0.6.
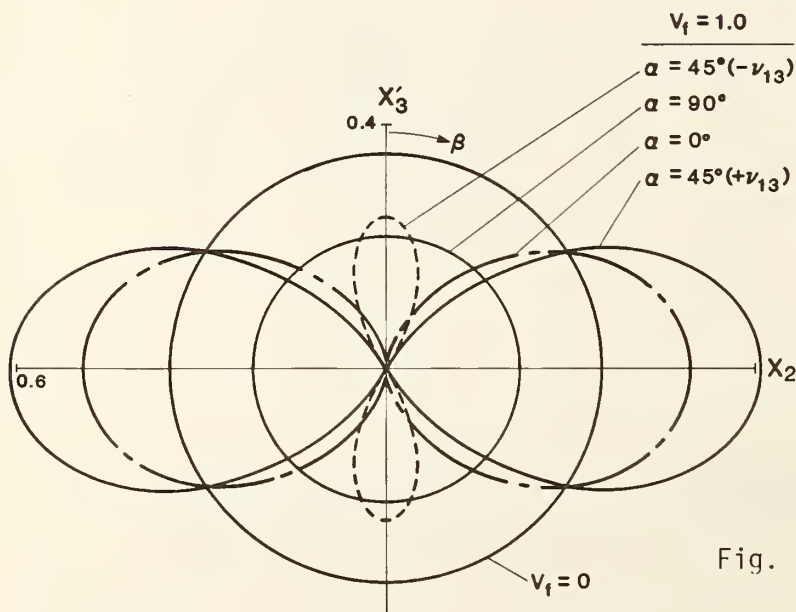
Fig. 8 Polar diagram of Poisson's ratio v_{13}. Same as Fig. 7 with fiber volume fractions of 0.0 and 1.0.

114
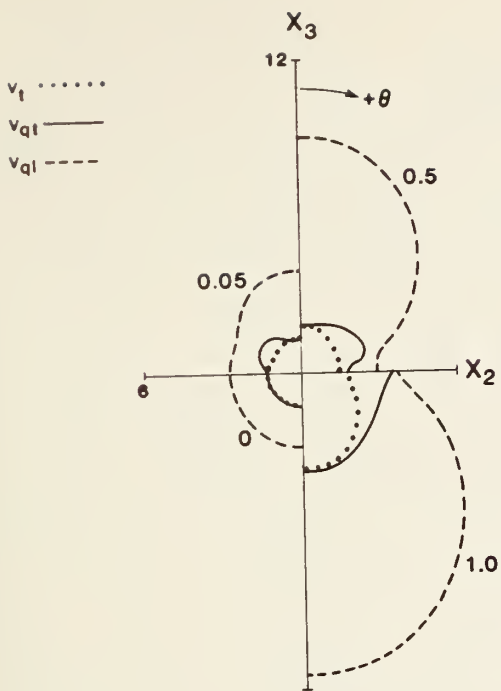
Fig. 9 Phase-velocity polar diagram for four volume fractions.
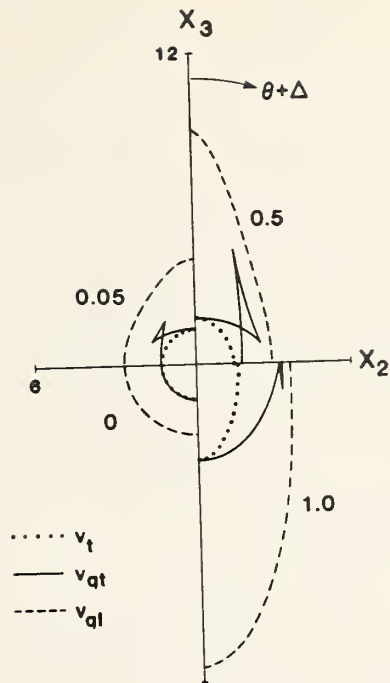
Fig. 10 Group-velocity polar diagram corresponding to Fig. 9.
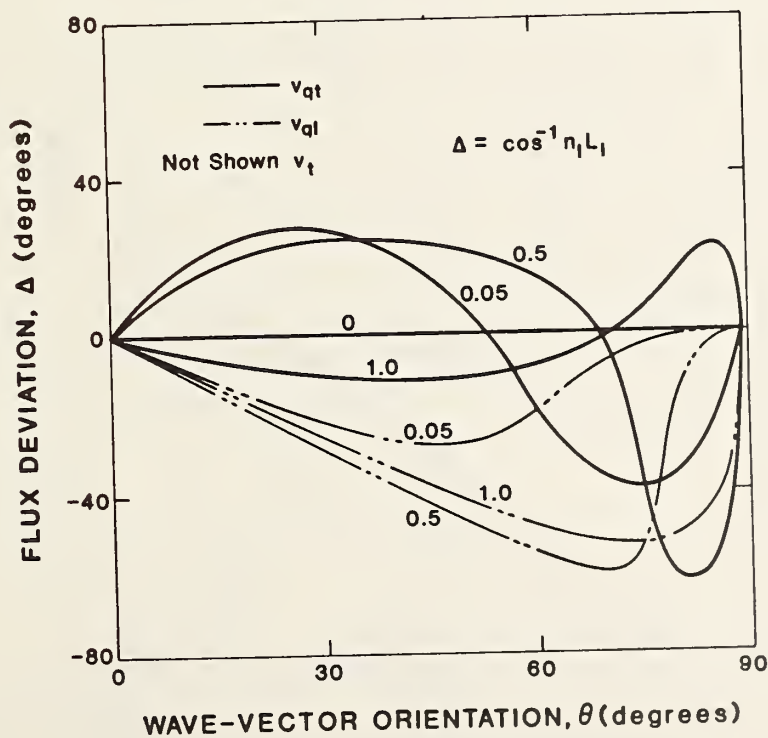
Fig. 11 Flux-deviation directions for various fiber volume fractions. For clarity, v_t curves are omitted.
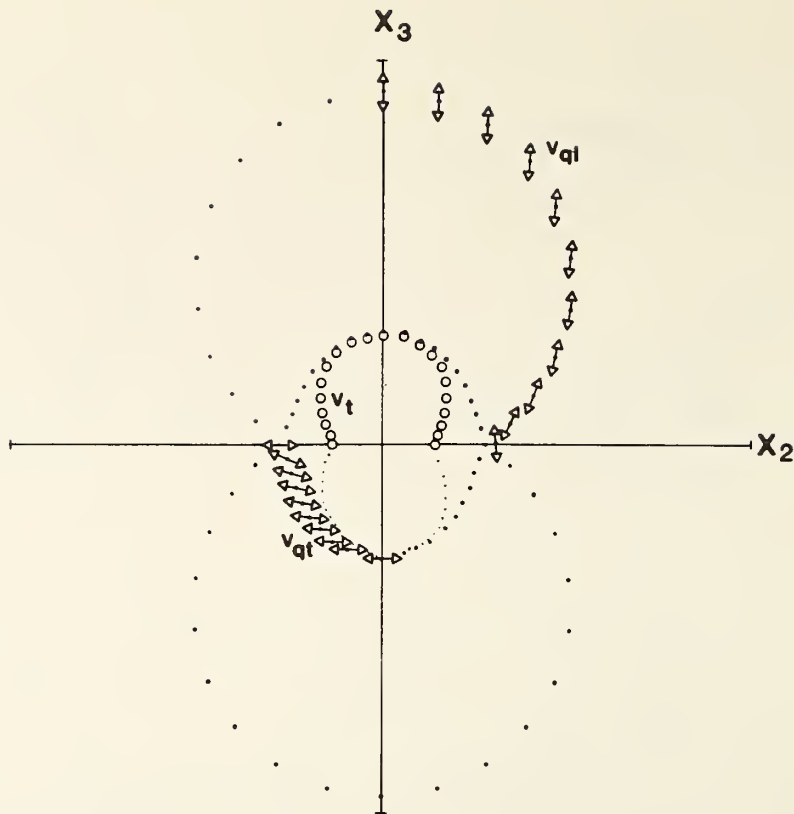
Fig. 12   Polar diagram of displacement directions superimposed on the phase-velocity
surfaces at V_f = 1.0.   For clarity, only one quadrant is shown.
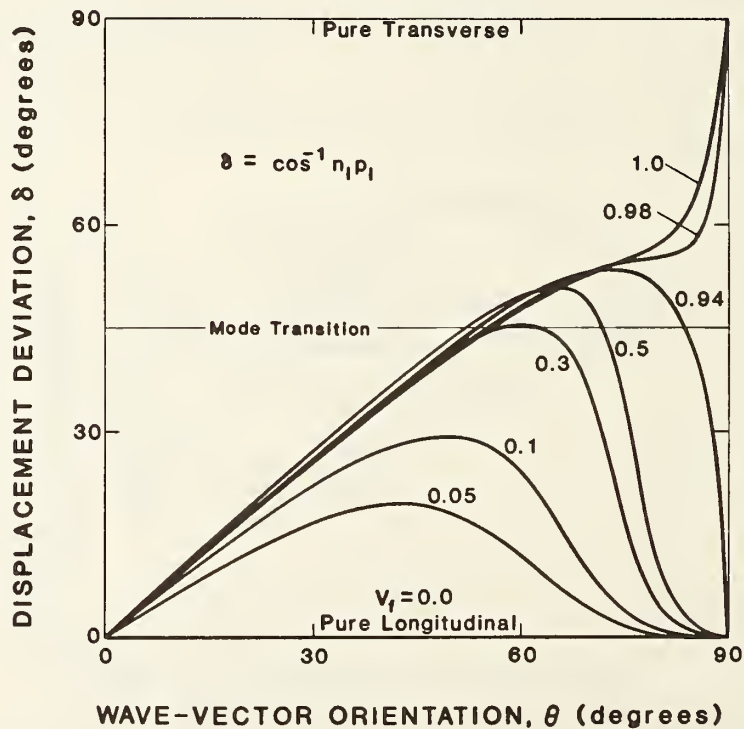
Fig. 13   Displacement-direction deviations for $v_{q\ell}$.   For higher
fiber volume fractions, a mode transition occurs.

STRUCTURAL ALLOYS

STRUCTURAL ALLOYS PROGRAM

LEADER: R. P. Reed, NBS
STAFF: J. M. Arvidson, Y. W. Cheng, H. M. Ledbetter, H. I. McHenry,
         P. T. Purtscher, D. T. Read, R. L. Tobler, NBS

OBJECTIVES:

1. Development of strong, tough structural alloys for use at 4 K in super-
    conducting magnets.
2. Development of strong, fatigue-resistant structural alloys for use at
    4 K in pulsed superconducting magnets.
3. Development of effective codes and standards related to low-temperature
    property measurements and structural design.

RESEARCH PAST YEAR (1984):

1. Characterization of Japanese high-manganese and austenitic stainless
    steels.
2. Assessment of the use of the notch tensile test to replace the J-inte-
    gral fracture toughness test for routine testing at 4 K.
3. Measurement of temperature dependence of flow strength of OFHC copper
    and 1100 aluminum.
4. Initiation of a cooperative program with industry to develop a lower
    cost alloy than 304LN, with equivalent strength and toughness at 4 K.
5. Threshold fatigue testing of 304, 316, and 310 steels at 4, 76, and
    295 K.
6. Studies on low-temperature elastic properties of austenitic steels.
7. Initiation of a program to measure the stacking-fault energy of high-
    manganese austenitic steels.
8. Continuation of efforts to establish a program to develop low-tempera-
    ture mechanical-property test standards.

RESEARCH THIS YEAR (1985)

1. Characterization of 316 LN alloys obtained from Japan and Germany.
2. Study of thermally activated deformation processes in austenitic steels.
3. Low-temperature creep measurements on 304, 316, and 310 alloys.
4. Threshold fatigue measurements to study effects of R ratio and frequency
    on 4-K measurements.
5. Measurement of stacking-fault energy of Fe-18Cr-8Ni base alloys with
    varying nitrogen and manganese concentrations.
6. Measurement of low-temperature elastic properties of selected austenitic
    steels.
7. Continuation of interaction with Metal Properties council to develop
    low-temperature mechanical-property test standards.
8. Cooperative studies with industry to study 316-type alloys and replace-
    ment of nitrogen with manganese.

SUMMARY OF MECHANICAL PROPERTY MEASUREMENTS OF STRUCTURAL ALLOYS

Alloy (Designation)	Country of Supplier	Tensile 295,4 K	Elastic 295-4 K	Fracture Toughness 295,76,4 K	Fatigue Crack Growth Rate 295,76,4 K	Fatigue S-N 4 K	Report Volume* (page)
AUSTENITIC STEELS							
Fe-19Cr-9Ni (304)	U.S.	I,II,III IV,VI,VII	I,II,III IV,VI,VII	I,II,III, IV	II,III,IV	I	I(15,71,213),II(79,149, 175),III(15,91,105, 117),IV(37,101,203,215, 227),V(71),VI(73),VII (13),VII(47),VII(75), VII(157)
Fe-19Cr-9Ni (304L)	U.S.	II,III, IV	I,II,IV	III,IV	III,IV		I(213),II(79,123,175), III(15),IV(37,101,131, 302,215)
Fe-19Cr-9Ni-N (304N)	U.S.	I,III, IV	IV	I,III,IV	I,III,IV		I(93),III(15),IV(37, 101,203,215)
Fe-19Cr-9Ni-N (304LN)	U.S.	II,III, IV,V,VI	IV	II,III,IV	II,III,IV	II	II(35,79),III(15),IV (37,101,203),V(29),VI (113)
Fe-19Cr-9Ni- 1 to 8Mn (304LN)	U.S.	IV,V	V	IV,V			IV(77),V(15,59,189)
Fe-17Cr-9Ni-8Mn	U.S.		III				III(91)
Fe-17Cr-13Ni-2Mo (316)	U.S.	I,II,III, IV,VI	VI	I,II	II	I	I(15,71),II(79),III(49, 105,117),IV(147),V(185), VI(87),VI(157)
Fe-17Cr-13Ni-2Mo (316LN)	U.S.	II		II	II		II(79)
Fe-25Cr-21Ni (310)	U.S.	V,VI,VII	III,VI	V			III(105,117),V(71,145), VI(73),VII(65)
Fe-18Cr-3Ni-13Mn	U.S.	I,VI	III	I	I,VI,VII		I(93),III(91),VI(53), VII(85)
Fe-21Cr-6Ni-9Mn (21/6/9)	U.S.	I	III,VI	I		I	I(15,71),III(91), VI(157)
Fe-21Cr-12Ni-5Mn	U.S.	I,II	III	I,II	I,II		I(93),II(79),III(91)
Fe-17Cr-18Mn-0.5N	U.S.	VII					VII(65)
Fe-13Cr-19Mn	USSR		III		VI		III(79),VI(41)
Fe-13Cr-22Mn-0.2N	Japan	VII					VII(65)
Fe-20Cr-16Ni-6Mn	USSR	V,VI	V				V(29,213),VI(113)
Fe-19Ni-9Co (200-300 grades)	U.S.		IV				IV(237)
Fe-5Cr-25Mn-0.2C	Japan	VII					VII(65)
Fe-5Cr-26Mn	Japan		VI				VI(181)
Many alloys		Review IV,V,VI	Review IV,V,VI	Review IV,V,VI	Review IV,V,VI, VII	Review IV,VI	IV(17,257),V(171), VI(11),VI(127),VI(157), VII(103)
ALUMINUM ALLOYS							
Al-4Mg (5083-0)	U.S.	IV				II	II(35),IV(185)
Al-6Cu-0.2Mn-0.1Fe (2219-T87)	U.S.		II	II	II	II	II(19)
SUPERCONDUCTORS							
Nb-45Ti	U.S.		III				III(133)

*Materials Studies for Magnetic Fusion Energy Applications at Low Temperatures: NBSIR 78-884 (I); NBSIR 79-1609 (II); NBSIR 80-1627 (III); NBSIR 81-1645 (IV); NBSIR 82-1667 (V); NBSIR 83-1690(VI); NBSIR 84-3000 (VII).

STRENGTH AND TOUGHNESS GOALS FOR CRYOGENIC STEELS

Harry I. McHenry
Fracture and Deformation Division
National Bureau of Standards
Boulder, Colorado

Superconducting magnets for future fusion devices will require cryogenic steels with improved combinations of strength, toughness, and weldability. To guide the development of these steels, possible research goals were discussed at the 1984 NBS-DOE Workshop (see page 299), and subsequently, goals for the strength and toughness of cryogenic steels were set as follows:

	Yield Strength, MPa at 4 K	Fracture Toughness, MPa√m at 4 K
Base Metal	1000	200
Weld		
One process	1000	200
Two processes	1000	150

The base metal properties are intended for plates and other product forms up to 100-mm thick. For alloys that meet these property goals, other factors will be evaluated, such as fatigue strength, physical properties, relative cost, and suitability for thickness greater than 100 mm.

There are two sets of property goals for welding. One process, presumably gas tungsten arc (GTA) welding, will be qualified to meet the same property goals as the base metal in all welding positions. This process could be used at any location in the magnet structure. A minimum of two other processes will be qualified for use in locations where the maximum stress is less than 75% of the maximum design stress. For these locations, the weld will match the base metal in yield strength and flaw tolerance. The latter will be achieved by requiring a weld metal toughness of 150 MPa√m, that is, 75% of the base metal toughness. The relaxed tolerance on weld toughness is intended to permit more efficient welding practices when the welds are located in low stress areas.

The base metal strength and toughness goals are based on two requirements: (1) the strength and toughness values must exceed the NBS strength-toughness trend line for austenitic stainless steels at 4 K and (2) the yield strength goal is the highest value on the trend line that has adequate toughness in 100-mm-thick plate. Adequate toughness is regarded as any toughness value that exceeds the ASTM validity requirement for plane strain fracture in 100-mm-thick plate with the specified yield strength.

The requirements are shown graphically in Figure 1. The NBS trend line shows that as yield strength increases there is a linear drop in fracture toughness. The ASTM validity requirement for 100-mm-thick plate shows that as yield strength increases, the fracture toughness measurement capability increases linearly. The two lines cross at a yield strength of 1000 MPa, where the level of toughness required to avoid plane strain fracture is 200 MPa√m. Thus, the requirements are yield strength greater than 1000 MPa and fracture toughness greater than 200 MPa√m.

These levels of strength and toughness are considered to be achievable using state-of-the-art manufacturing technology. However, to consistently meet these property requirements in heavy sections and in weld metals, improvements are required in stainless steel processing technology and in welding materials and procedures.
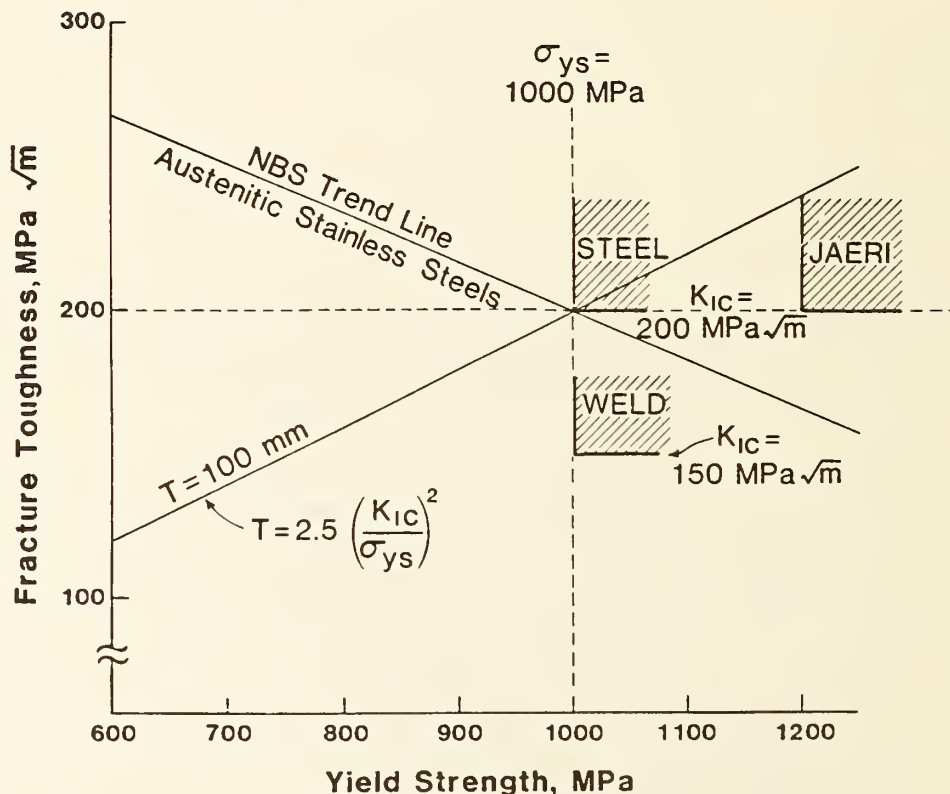
Fig. 1. Materials research goals for cryogenic steels at 4 K.

122

NICKEL AND NITROGEN ALLOYING EFFECTS ON THE STRENGTH AND TOUGHNESS OF AUSTENITIC STAINLESS STEELS AT 4 K[*][+]

P. T. Purtscher and R. P. Reed

Fracture and Deformation Division
National Bureau of Standards
Boulder, Colorado 80303

The tensile strength and fracture toughness at 4 K were studied as a function of Ni (6 to 15 wt.%) and N (0.09 to 0.28 wt.%) contents for eight austenitic stainless steels. Results indicate that N increases the tensile yield strength and decreases the fracture toughness, $K_{Ic}(J)$. Nickel has little significant effect on tensile yield strength but increases the fracture toughness. The temperature dependence of the yield strength, σ_y, follows the relationship $\sigma_y = \sigma_o e^{-AT}$ where σ_o is the yield strength at 0 K and A is the slope of $\ln \sigma_y$ vs. T. The parameter A is proportional to the stacking fault energy. Nickel increases stacking fault energy and austenite stability. Lower Ni alloys exhibited brittle facets on fracture surfaces examined using scanning electron microscopy. The brittle facets are {111} austenite planes and are related to slip-band faulting. A new parameter called the quality index is presented and defined as the product $\sigma_y \cdot K_{Ic}(J)$. This factor relates to the capacity of the alloy to achieve greater strength or toughness, but not at the expense of the other parameter. Nickel alloying is shown to increase the quality factor; N has little effect.

INTRODUCTION

To constrain magnetic forces developed in high-field superconducting magnets, structural alloys that are strong and tough at 4 K are required. It has been demonstrated that N is a potent solid-solution strengthening agent in austenitic stainless steels at 4 K.[1] However, the toughness of the high-N alloys decreases as the strength increases.[2] It is desirable to study the roles of Ni and Mn on toughness of high-N austenitic stainless steels. Perhaps by modest alloying changes, their low temperature toughness can be improved while maintaining high strength.

In this study Ni content was varied from 6 to 15 wt.% in austenitic stainless steel base alloys containing 19% Cr, 6% Mn, low C, and 0.09 to 0.28% N. Tensile strength and fracture toughness of the alloy series were measured in liquid helium and correlated with Ni and N contents.

EXPERIMENTAL PROCEDURE

The eight laboratory heats of steel included in this study (see Table 1) were supplied by E. O. Paton Institute of Electrowelding, Kiev, USSR. The chemical analyses were performed at the Colorado School of Mines, Golden, Colorado. All alloys were completely austenitic and in the form of 25-mm-thick plates. They were tested after solution treatment at 1060°C for 1 h and subsequent water quenching. The procedures and accuracies for tensile testing of round specimens and fracture toughness tests (J-integral) using compact-tension specimens have been discussed elsewhere.[2-4] All tests were conducted in liquid helium. Martensitic (body-centered cubic) transformation was monitored at room temperature, after testing at low temperature, using magnetic torsion balance equipment, which was previously calibrated to estimate volume percent. Scanning electron microscopy (SEM) and transmission electron microscopy (TEM) were used to study the associated fracture morphology and dislocation structures.

RESULTS

The average results of the tensile and fracture toughness tests at 4 K are listed in Table 2.

Typical engineering stress versus engineering strain curves at 4 K are shown in Fig. 1. The high-N alloys are characterized by high yield strengths and a lack of work hardening at large deformations. The lower N, less-stable alloys exhibit the characteristic three stages of stress-strain behavior identified earlier by Reed and Tobler;[5] note particularly alloy 739 (Fig. 1f). It is apparent that N increases σ_I (the elastic limit); N and Ni reduce and finally eliminate stage II [associated with hexagonal close-packed (ϵ) martensite and body-centered cubic (α') martensite at slip-band intersections] and stage III (associated with α'-induced work hardening). Discontinuous yielding occurred in all measurements, and the load drops near fracture ranged from about 25% for the stronger alloys to about 10% for the more ductile alloys.

The temperature dependence of the tensile yield strength, σ_y, was measured for three alloys from 4 to 295 K. The results are plotted in Fig. 2. There is a linear relationship between $\ln \sigma_y$ and temperature, similar to that of other austenitic steels.[3] The least stable alloy, 739, containing only about 8.7 wt.% Ni, exhibits little change of yield strength in the region between about 100 to 200 K. This region has been identified previously for metastable alloys[6] and is associated with the α' and ϵ martensitic transformations.[7]

The tensile yield strength is a strong function of the C and N content, as shown in Fig. 3. Here the function C + 2N is used. Reed and Simon[1] found this to be a representative function when they used regression analysis to describe all σ_y data on AISI 304 type alloys at 4 K. The data of this paper closely correspond to those from earlier research on Fe-19Cr-10Ni base alloys.[8] The σ_y at 4 K is strongly dependent on interstitial content. Strengthening from solid solution additions of Ni is small and insignificant.

The fracture toughness, $K_{Ic}(J)$, was estimated from J-integral measurements at 4 K and is plotted against σ_y in Fig. 4. Some data points fall within a band containing most of our earlier results[8] that primarily portray the effects of C and N alloying. But, there is not good conformance: alloy 416 has considerably better properties; alloys 413, 414, 520, and 739 have lower corresponding $K_{Ic}(J)$ to σ_y ratios.

The effect of Ni content on fracture toughness is shown in Fig. 5. Notice the clear trend of increasing toughness with increasing Ni in the 19Cr-4Mn-0.02C-(0.26-0.28)N alloys (413-416). From Table 2 it is clear that the alloys with lower N contents form no systematic series with respect to dependence of toughness on Ni content; presumably the N varies too much to permit comparison solely on the basis of Ni. Analyses of the data (Table 1) reveal that, at constant Ni content, toughness tends to be less at higher N content. This is also apparent from Fig. 1, considering that N content accounts for σ_y variation. Therefore, the values of $K_{Ic}(J)$ reported for the lower N content alloys (739, 740, 741) were adjusted to include consideration of N variability. From Fig. 4 a clear trend of decreasing $K_{Ic}(J)$ with increasing σ_y at 4 K has been found when C and N are systematically varied[8] and

$$K_{Ic}(J) = 500 - 0.3\sigma_y \qquad \text{(in MPa)} \qquad (1)$$

The average tensile yield strength at 4 K for the high-N content alloys (413-416, 520) is 1030 MPa. The corresponding $K_{Ic}(J)$, from Eq. 1, is 191 MPa$\sqrt{m}$. The fracture toughness of each low-N alloy was calculated, using Eq. 1, from their yield strength values. To normalize, these calculated values were subtracted from the measured $K_{Ic}(J)$.

The initial dislocation structures of alloys 413 and 416 were observed with TEM thin foils. Alloy 413 (low toughness, low Ni, high N) exhibited stacking faults in the annealed condition (Fig. 6); in alloy 416 (high toughness, high Ni, high N) no stacking faults were observed in the annealed dislocation structure.

The fracture appearances in the surface area associated with the critical J-integral measurements were characterized by SEM. The fracture surfaces of the high-N alloys (413-416) are shown in Fig. 7. As $K_{Ic}(J)$ increases, the fracture morphology becomes more dimpled (microvoid coalescence). Nonmetallic inclusions are associated with most dimples, as shown in Fig. 8. These large (3-4 μm) inclusions are Mn silicates, according to energy-dispersive x-ray analysis.

At low-Ni content [low $K_{Ic}(J)$], the fracture surfaces are faceted. There are small, step-like facets and large (size of grain) flat facets. The large facets, shown in Fig. 9, are apparently {111} planes of austenite. Linear traces on the faceted surfaces, such as those shown in Fig. 9b, correspond to other {111} traces, if we assume the surface is {111}. Their appearance is very similar to those recently identified as {111} by Tobler,[9] who used back-scattered Laue x-ray analysis and described them as regions of "slip-band decohesion."

---

*The highest temperature at which α' martensite forms at constant plastic deformation.

DISCUSSION

Strength

All alloys, except 416, partially transformed to body-centered cubic (α') martensite during plastic deformation. The average volume percent of α' that formed throughout the gage length, normalized by dividing by the percent elongation, correlates well with T_{md}* of Williams et al.[10] This is summarized in Table 3 and illustrated in Fig. 10. Williams et al. conducted regression analyses of various Cr, Ni, Mn, Si, C, N, and Mo chemistries after compressive deformation and used 45% elongation and 2 to 5% α' as a basis for T_{md}. Alloy 520 is outside the trend of the other alloys (see Fig. 10).

From earlier work,[3] the temperature dependence of the tensile yield stress is best portrayed as

$$(\sigma_y/G) = (\sigma_o/G_o)e^{-AT} \tag{2}$$

where σ_o is the yield strength at 0 K, G is the shear modulus, and G_o is the shear modulus at 0 K. Because we have not measured the shear modulus of most of the alloys in this series, the shear moduli are omitted in Fig. 2 and

$$\sigma_y = \sigma_o e^{-AT} \tag{3}$$

was used.

Since G changes only about 6% from 4 to 295 K, there is little difference between Eqs. 2 and 3.

Reed and Arvidson[3] pointed out that there may be a correlation between the temperature dependence of the tensile yield strength (constant A of Eq. 3) and the stacking fault energy; it is evident in Fig. 11.

The stacking fault energies (γ) of Fe-Cr-Ni austenitic stainless steels have been estimated.[11-13] On the basis of weak-beam electron microscopy data, Rhodes and Thompson[12] argue realistically that the regression analysis of other electron microscopy and x-ray data by Schramm and Reed[11] produced γ values that were too large. However, the Mn contribution suggested by Rhodes and Thompson is probably too large and results in very large values of γ in Fe-Cr-Ni-Mn austenitic steels. Brofman and Ansell[13] examined the contribution that C makes to the stacking fault energy of austenitic stainless steels and concluded that C additions raise γ, in a proportion similar to the contribution of C to T_{ms} [the martensite (α') start temperature].[7]

Currently in our laboratories the effects of both C and N are being studied and have been tentatively reported to increase γ.[14] For Fig. 11 we have chosen to use the Schramm-Reed analysis, compiled in Table 3, which produces admittedly high γ, but we think accurate relative values of γ in view of the major alloying elements Cr, Ni, and Mn.

The primary deformation mechanism in stage I (see Ref. 5) of polycrystalline austenitic steels at low temperatures may be associated with cross-slip. Schoeck and Seeger[15] predict a linear dependence of the $\ln \sigma$ vs. T for stage III single-crystal cross-slip as the rate-controlling deformation mechanism. More recently, Escaig[16] has developed a cross-slip model that predicts a linear dependence of flow strength on temperature. Clearly, we must continue studies to identify and characterize the rate controlling deformation mechanism in austenitic steels.

Toughness

There is strong dependence of fracture toughness on Ni content (Fig. 5) when the N content is held constant. SEM photomicrographs of the fracture surfaces at the initial fatigue-sharpened crack tip are shown in Fig. 7. It is apparent that as Ni content decreased, the corresponding fracture surfaces exhibit a transition from dimpled to faceted surfaces. These faceted surfaces, shown at higher magnification in Fig. 8, are cleavage-like in appearance but do not show the characteristic river patterns found on the cleavage facets of body-centered cubic alloys. The surface is probably a {111} austenite plane, considering the orientations of {111} slip-band traces (see Fig. 8) and the similarity to regions in another high-N austenitic stainless steel, which were identified as {111} austenite by Tobler.[9] Similar fracture features have been observed in austenitic stainless steels charged with H and fractured at room temperatures.[17,18] The study of Hannula et al.[17] shows a similar trend, in that brittleness increased with decreasing austenite stability.

Further study of the possible origin of apparently brittle {111} austenite was pursued with optical microscopy. The microstructure of the tougher alloy, 740, after several percent elongation is shown in Fig. 12, and that of the more brittle alloy 413 after similar elongation is shown in Fig. 13. The microstructure of alloy 740, containing 11.5% Ni, is characterized by lath-like α' martensite formation, contained within {111} austenite sheets and by lath-like α' martensite that formed at {111} slip-band intersections. The microstructure of alloy 413, containing only 5.6% Ni, is composed of many {111} slip-band traces. These slip-band traces are broader than those observed in alloy 740 and more distinctly etched. Less α' formation was noticed at slip-band intersections. Therefore, one may conclude that there is more extensive faulting in the lower Ni alloy. Other possible conclusions are: more extensive stacking-fault clusters exist, more hexagonal close-packed martensite is formed, or deformation twins are produced within the {111} slip-band packets. Obviously, very careful transmission electron microscopy must be performed to sort out distinctions among these three possible fault structures. In any case, the fault product or products within the slip-bands become more brittle at very low temperatures in higher N content austenitic stainless alloys, affecting the measured fracture toughness deleteriously and exhibiting regions of slip-band decohesion on the fracture surface.

THE QUALITY INDEX

Nickel and nitrogen contribute quite differently to the low temperature mechanical behavior of austenitic stainless steels. Nickel improves toughness and does not affect strength; nitrogen improves strength and reduces toughness. For most structural applications, both strength and toughness are required. It is useful, we believe, to consider both of these parameters together, as the product $\sigma_y \cdot K_{Ic}(J)$, and to examine the effects of alloying on this product, called the quality index. In Fig. 14, Ni content is plotted versus the quality index. Increasing Ni content increases this index. Stated another way, increasing Ni content leads to improved low temperature mechanical behavior, either increased toughness or increased strength or a combination of both.

The effect of C and N on the quality index is plotted in Fig. 15. Additions of C and N have little effect on the quality of mechanical behavior. Figure 3 shows that increased N content increases strength, and toughness is sacrificed.

SUMMARY

A series of eight austenitic stainless steels with varying Ni and N contents were measured at 4 K to determine tensile strength and fracture toughness. The results of the study are:

1. Nitrogen addition raises the tensile yield strength and reduces fracture toughness.

2. Nickel addition raises the fracture toughness and has little effect on strength.

3. The temperature dependence follows the relation $\sigma_y = \sigma_o e^{-AT}$. The parameter A is directly proportional to the stacking fault energy.

4. Factors that contribute to the cleavage-like facets on fracture facets (associated with low toughness) are high interstitial content, low stacking fault energy, and stress concentration. These surfaces have been associated with slip-band decohesion on {111} austenitic planes.

5. A quality index, defined as the product $\sigma_y \cdot K_{Ic}(J)$, has been proposed to suggest the quality of mechanical behavior. Nickel is shown to increase the quality index nitrogen has little effect.

ACKNOWLEDGMENTS

REFERENCES

1. R. P. Reed and N. J. Simon, in: "Advances in Cryogenic Engineering--
    Materials," vol. 30, Plenum Press, New York(1984), pp. 127-136.
2. R. L. Tobler, D. T. Read, and R. P. Reed, in: "Fracture Mechanics:
    Thirteenth Conference," ASTM STP 743, American Society for Testing and
    Materials, Philadelphia (1981), pp. 250-268.
3. R. P. Reed and J. M. Arvidson, in: "Advances in Cryogenic Engineering--
    Materials," vol. 30, Plenum Press, New York (1984), pp. 263-270.
4. D. T. Read and R. L. Tobler, in: "Advances in Cryogenic Engineering--
    Materials," vol. 28, Plenum Press, New York (1984), pp. 17-28.
5. R. P. Reed and R. L. Tobler, in: "Advances in Cryogenic Engineering--
    Materials," vol. 28, Plenum Press, New York (1982), pp. 49-56.
6. R. L. Tobler, R. P. Reed, and D. S. Burkholter, in: "Advances in
    Cryogenic Engineering--Materials," vol. 26, Plenum Press, New York
    (1980), pp. 107-119.
7. R. P. Reed, in: "Materials at Low Temperatures," American Society for
    Metals, Metals Park, Ohio (1983), pp. 295-341.
8. R. L. Tobler and R. P. Reed, in: "Materials Studies for Magnetic Fusion
    Energy Applications at Low Temperatures--III," NBSIR 80-1627, R. P.
    Reed, ed., National Bureau of Standards, Boulder, Colorado (1980), pp.
    17-48.
9. R. L. Tobler and D. Meyn in: "Materials Studies for Magnetic Fusion
    Energy Applications at Low Temperatures--VIII," NBSIR 85-3025, R. P.
    Reed, ed., National Bureau of Standards, Boulder, Colorado (1985), pp.
    167-179.
10. I. Williams, R. G. Williams, R. C. Capellaro, in: "Proceedings of Sixth
    International Cryogenic Engineering Conference," IPC Science and
    Technology Press, Guildford, Surrey, England (1976), pp. 337-341.
11. R. E. Schramm and R. P. Reed, Metall. Trans. 6A:1345-1351 (1975).
12. C. G. Rhodes and A. W. Thompson, Metall. Trans. 8A:1901-1906 (1977).
13. P. J. Brofman and G. S. Ansell, Metall. Trans. 9A:879-880 (1978).
14. H. M. Ledbetter and M. W. Austin, in: "Materials Studies for Magnetic
    Fusion Energy Applications at Low Temperatures--VIII," NBSIR85-x, R. P.
    Reed, ed., National Bureau of Standards, Boulder, Colorado (1985).
15. G. Schoeck and A. Seeger, in: "Defects in Crystalline Solids," The
    Physical Society, London (1955), pp. 340-346.
16. B. Escaig, J. Phys. 29:225-234 (1968).
17. S.-P. Hannula, H. Hanninen, and S. Tahtinen, Metall. Trans. 15A:2205-
    2211 (1984).
18. G. R. Caskey, in: "Fractography and Materials Science," ASTM STP 733,
    American Society for Testing and Materials, Philadelphia (1981), pp.
    86-97.

Table 1. Chemical Composition and Metallurgical Characterization

Alloy	Composition (wt.%)								Grain Size (μm)	Hardness (R_B)
	Cr	Ni	Mn	C	N	S	P	Si		
413	18.8	5.6	4.1	0.020	0.256	0.005	0.014	0.25	175	84
414	18.4	8.9	4.2	0.018	0.281	0.005	0.014	0.28	200	82
415	20.5	12.8	5.5	0.024	0.265	0.004	0.015	0.34	385	81
416	20.8	14.9	5.2	0.028	0.277	0.004	0.015	0.41	225	82
520	19.8	5.8	3.2	0.014	0.260	0.004	0.012	0.41	340	85
739	18.7	8.7	3.7	0.014	0.093	0.005	0.013	0.23	325	72
740	19.7	11.5	3.9	0.012	0.141	0.005	0.013	0.27	340	72
741	20.8	14.7	4.4	0.016	0.197	0.004	0.014	0.33	320	76

Table 2. Mechanical Property Results* at 4 K

Alloy	Tensile Strength			Fracture Toughness	Alloying Variables	
	σ_y (MPa)	σ_u (MPa)	Elongation (%)	$K_{Ic}(J)$ (MPa$\sqrt{m}$)	Ni (wt.%)	N (wt.%)
413	1075	1418	11	75	5.6	0.26
414	950	1650	42	143	8.9	0.28
415	1000	1580	32	204	12.8	0.27
416	1160	1630	22	239	14.9	0.28
520	960	1216	7	87	5.8	0.26
739	460	720	40	273	8.7	0.09
740	720	1370	42	244	11.5	0.14
741	870	1425	29	254	14.7	0.20

*Averages of 2 or 3 measurements.

Table 3. Tensile Characteristics

Alloy	Estimated Stacking Fault Energy (mJ/m^2)	Estimated T_{md} (K)	Slope of $\ln \sigma_y$ vs. T, A (10^{-3} MPa/K)	Average % Martensite ÷ Tensile Elongation
413	8	309		1.73
414	28	224		0.67
415	58	97		0.16
416	71	47	4.60	0
520	7	316		0.97
739	26	275	2.50	1.72
740	45	186	3.95	0.74
741	67	80		0.07
AISI 304	24		3.38	--
AISI 316	55		4.54	--
AISI 310	98		6.13	--
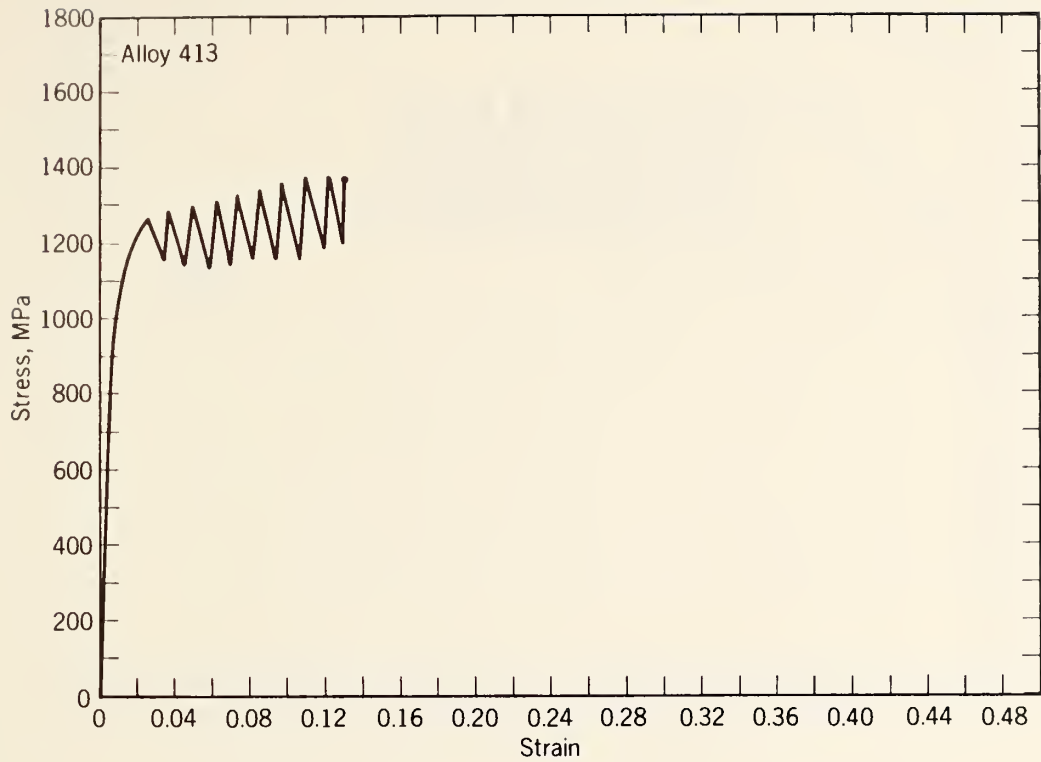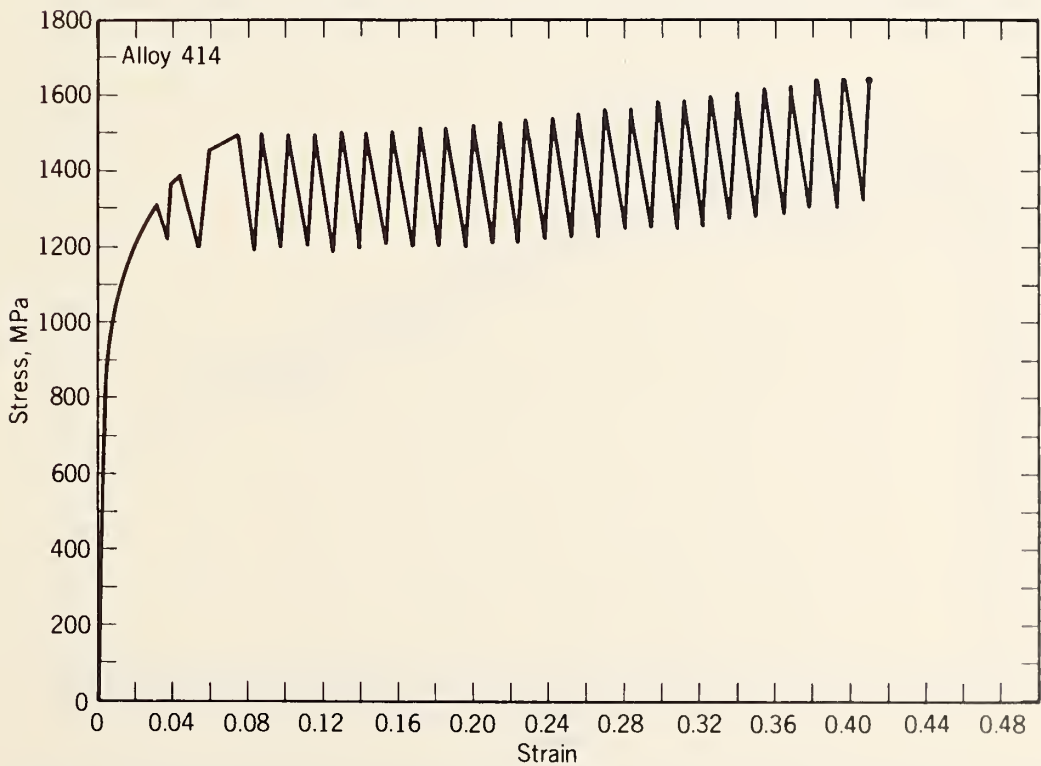
Fig. 1a and b.   Stress versus strain (engineering values) at 4 K
                 for alloys (a) 413 and (b) 414.

131
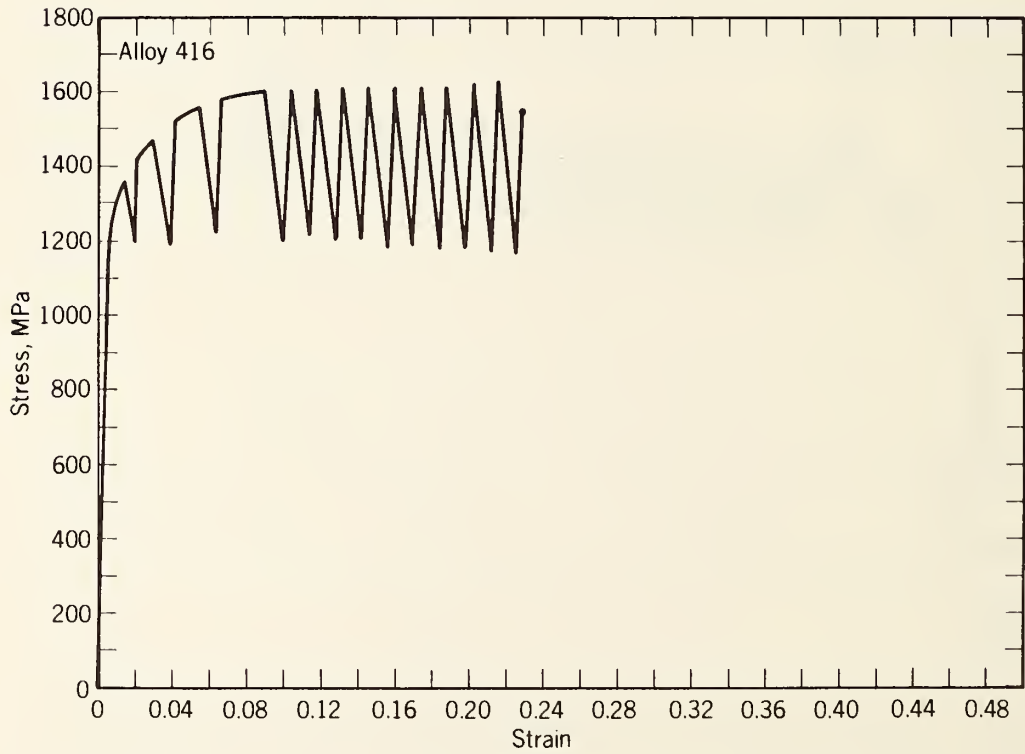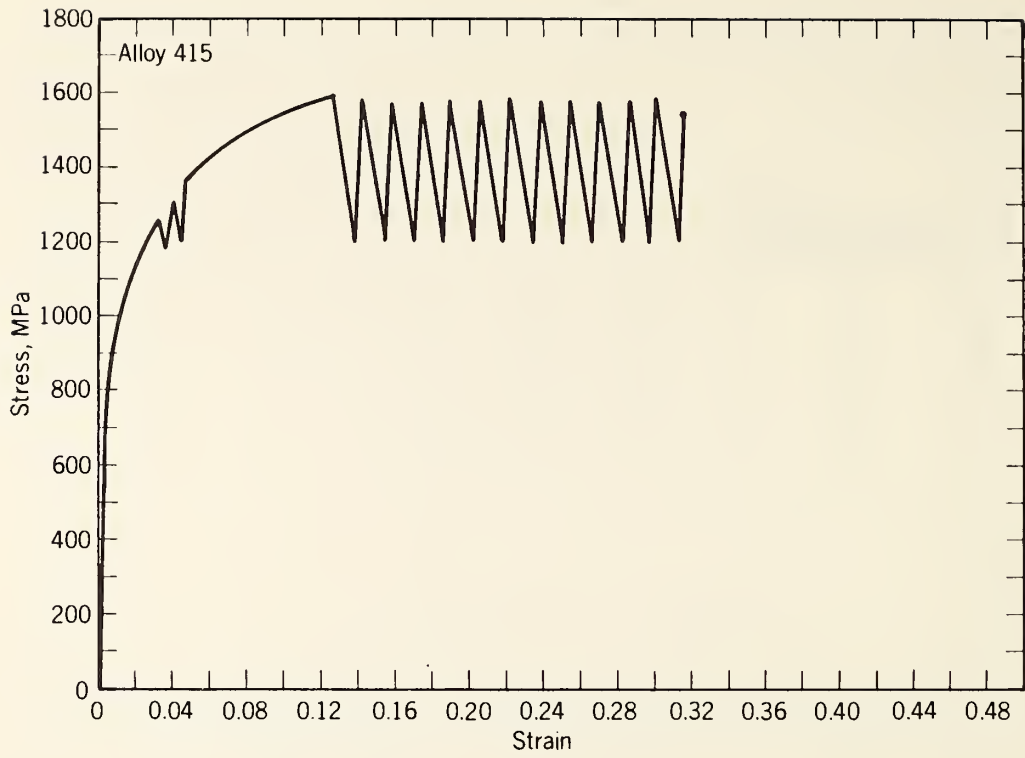
Fig. 1c and d. Stress versus strain (engineering values) at 4 K
for alloys (c) 415 and (d) 416.
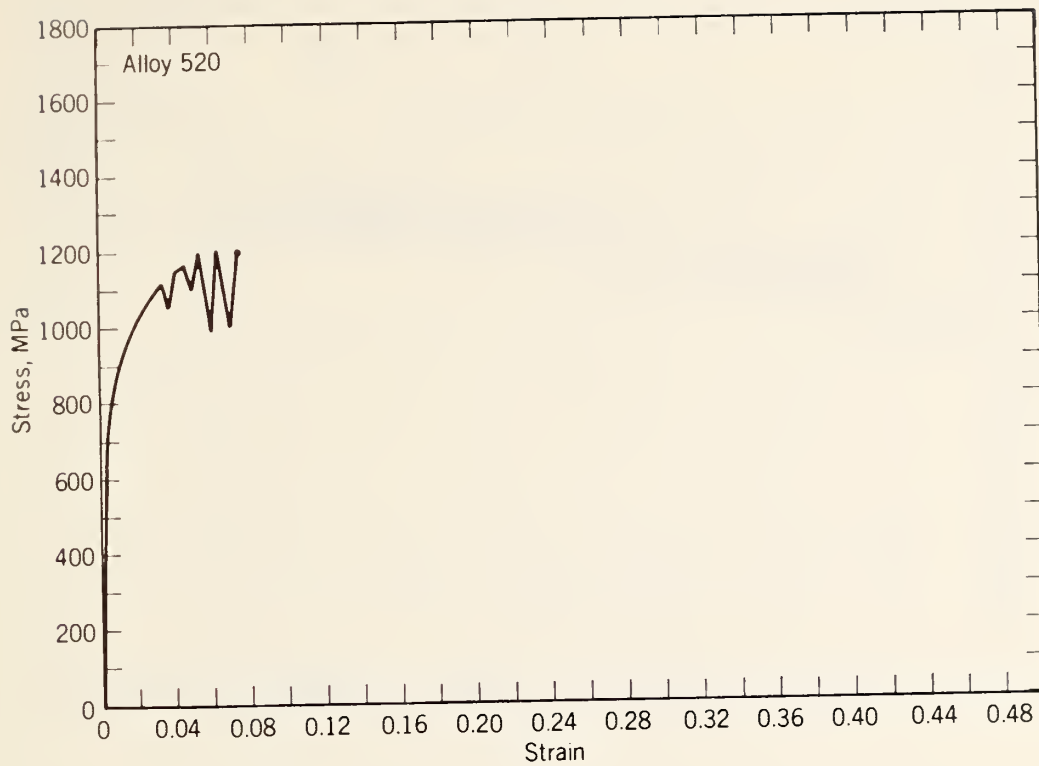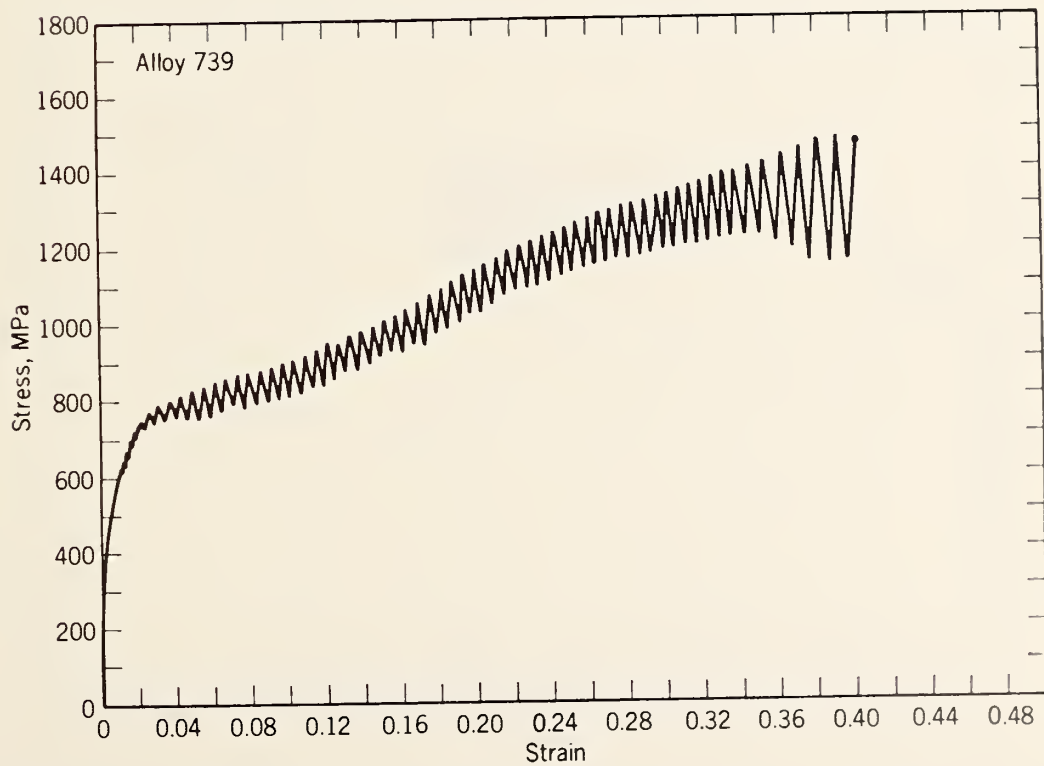
Fig. 1e and f. Stress versus strain (engineering values) at 4 K
for alloys (e) 520 and (f) 739.

133
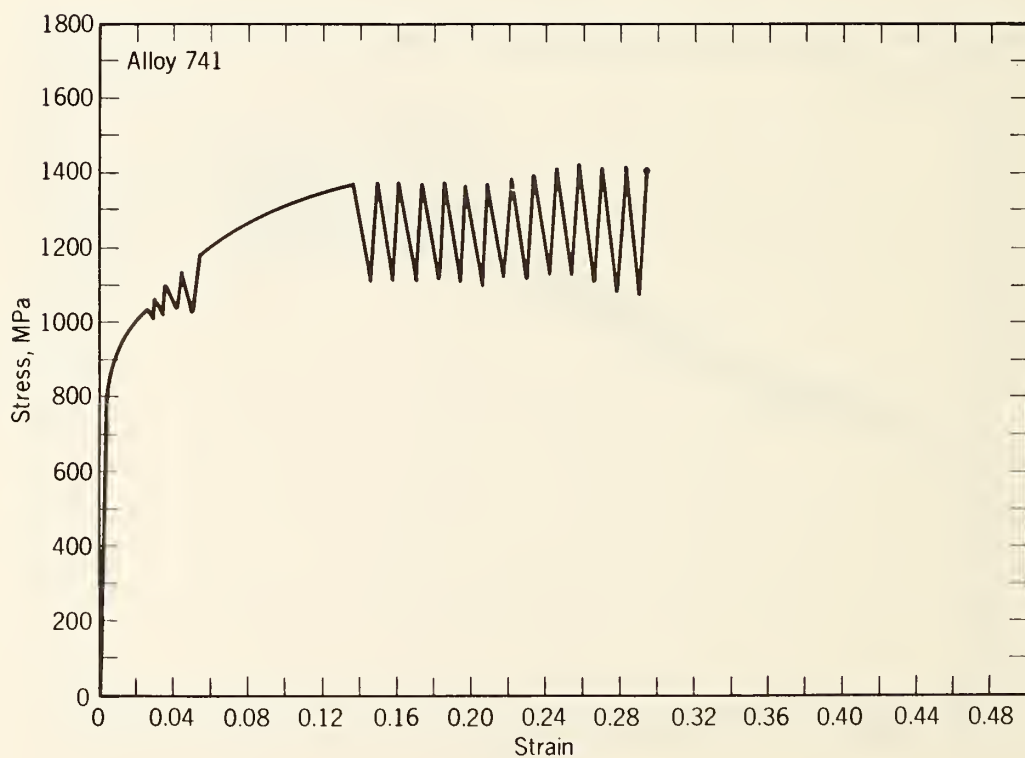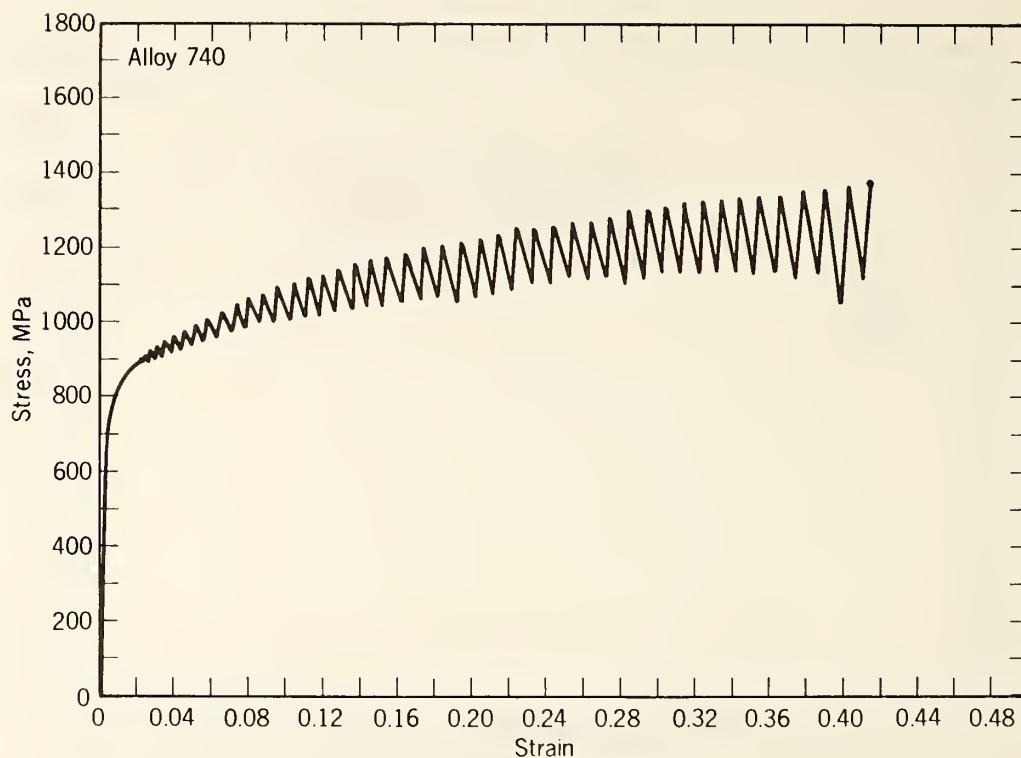
Fig. 1g and h. Stress versus strain (engineering values) at 4 K
for alloys (g) 740, and (h) 741.

134
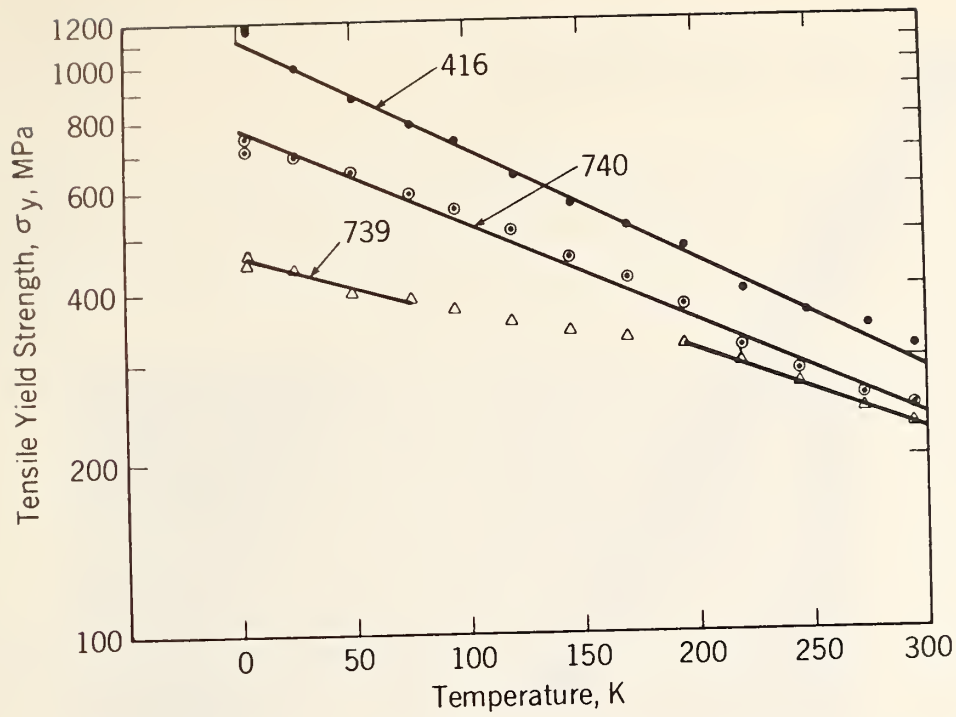
Fig. 2. Temperature dependence of the yield strength for 416, 739, and 740 alloys.
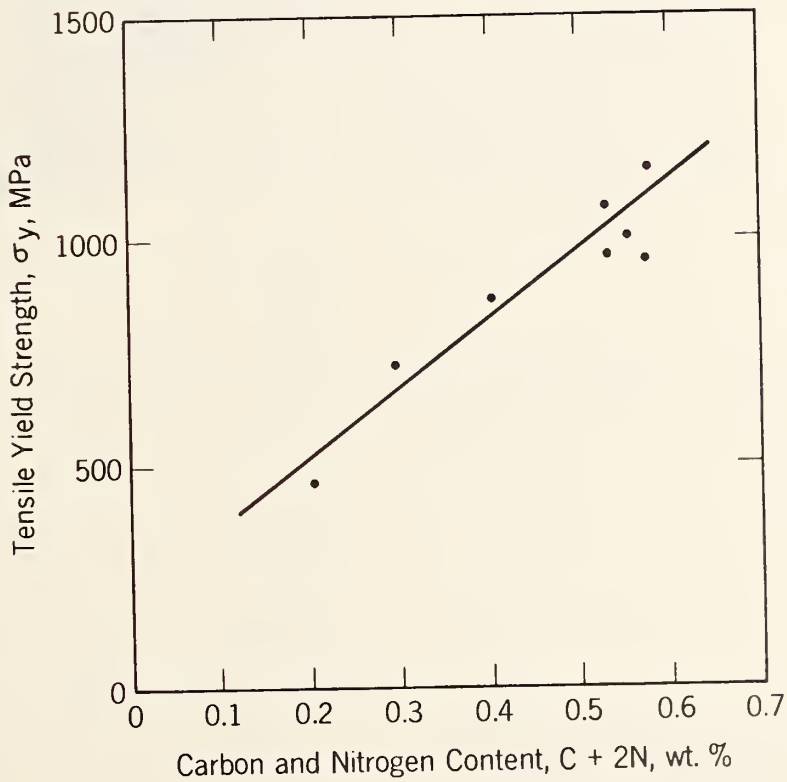
Fig. 3. Tensile yield strength at 4 K as a function of C and N content (C + 2N). Line indicates trend of a series of nine 19Cr-10Ni steels with varying C and N contents.[8]
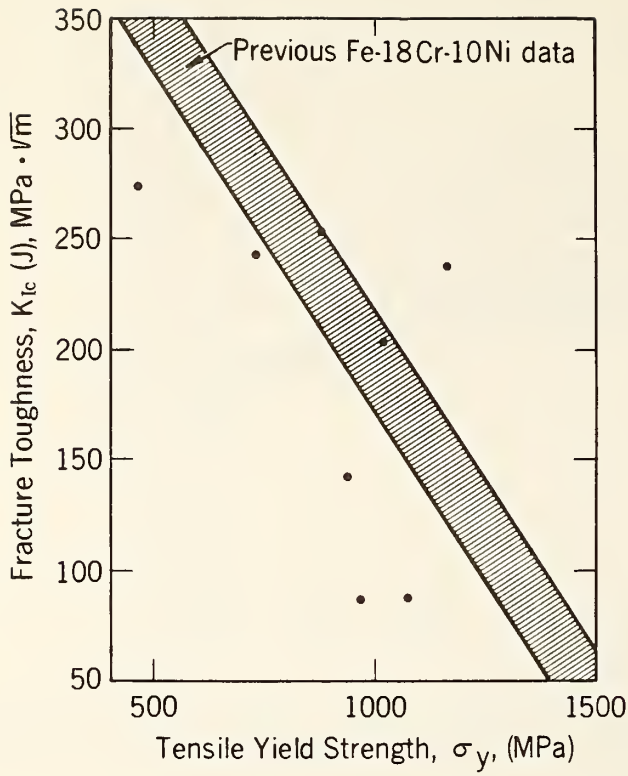
Fig. 4. Tensile yield strength versus
fracture toughness at 4 K.
Band represents previous data.[8]

Fig. 5. Fracture toughness at 4 K,
estimated from J-integral
measurements, versus Ni
content.

136
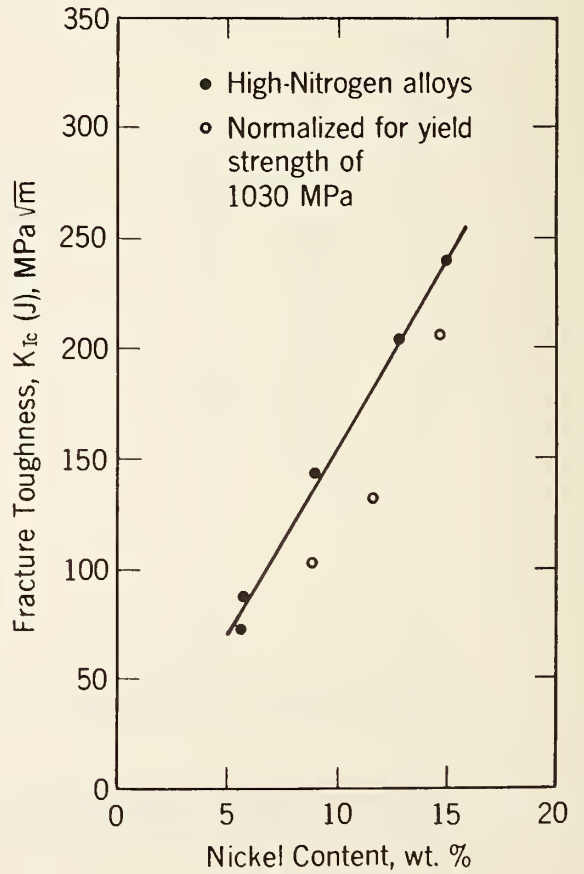
0.2 μm

Fig. 6. Transmission electron microscopy photographs of initial
structure of alloy 413. Arrows point out stacking faults.
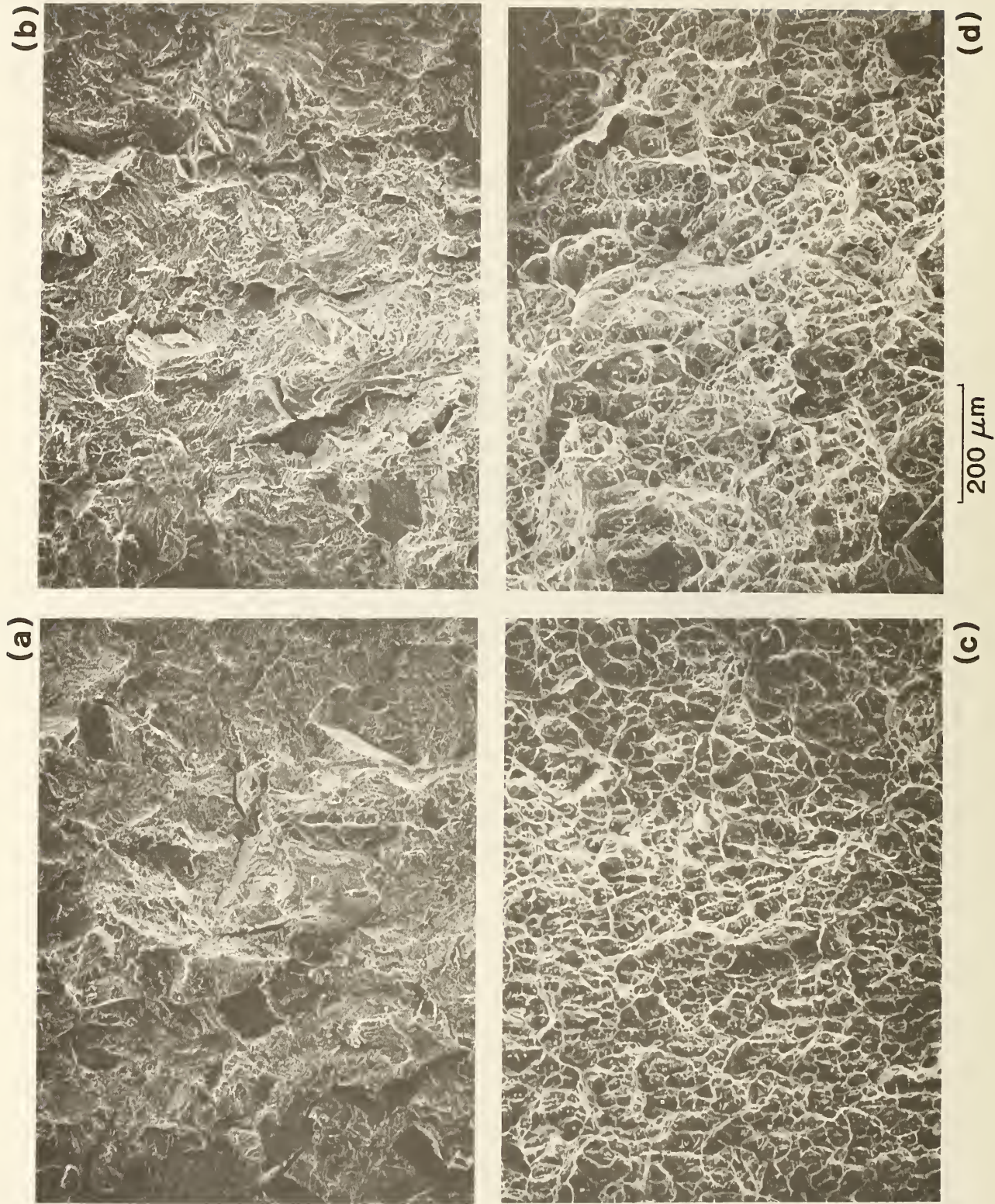
Fig. 7. Fracture surfaces at crack tip of alloys (a) 413, (b) 414, (c) 415, and 416 (SEM photomicrograph).

138

20 μm
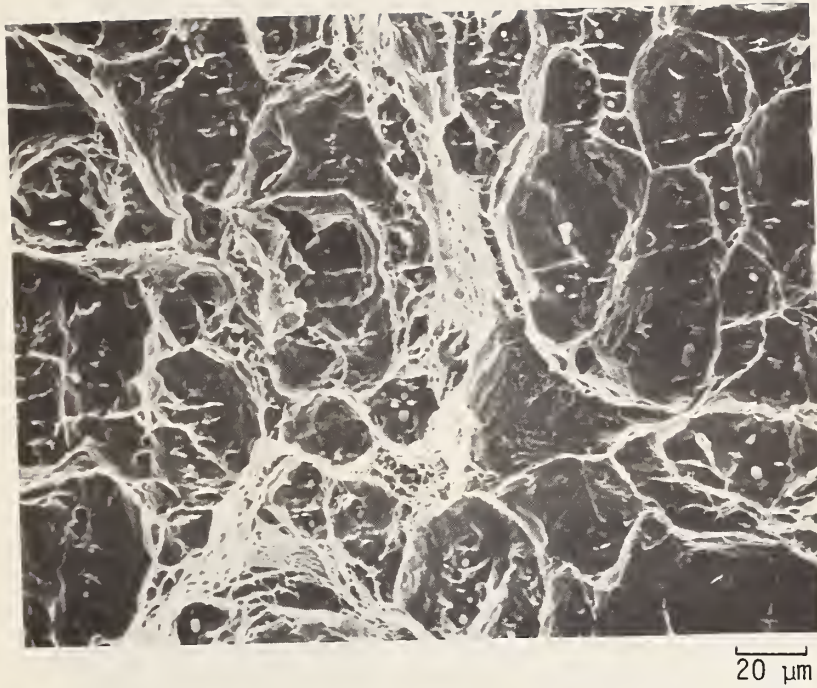
Fig. 8. Higher magnification SEM photograph of alloy 416.
Notice inclusions within most dimples.

(a)

20 μm

(b)
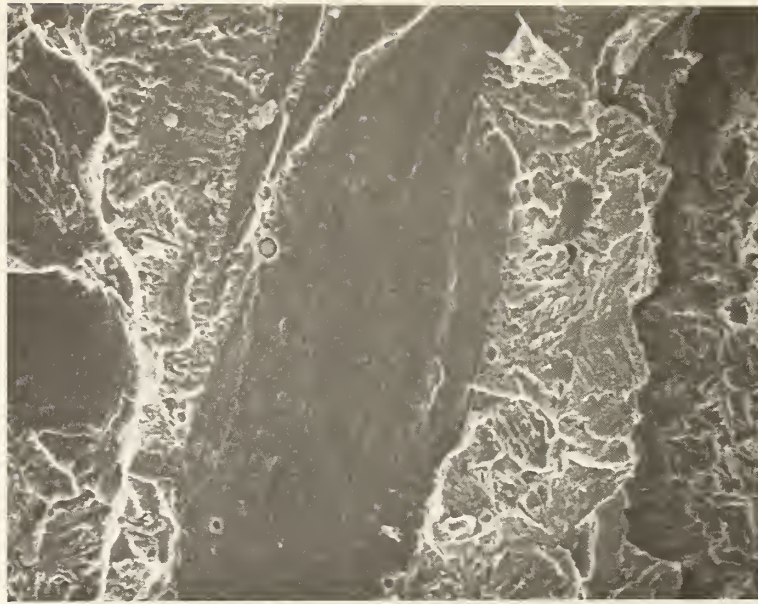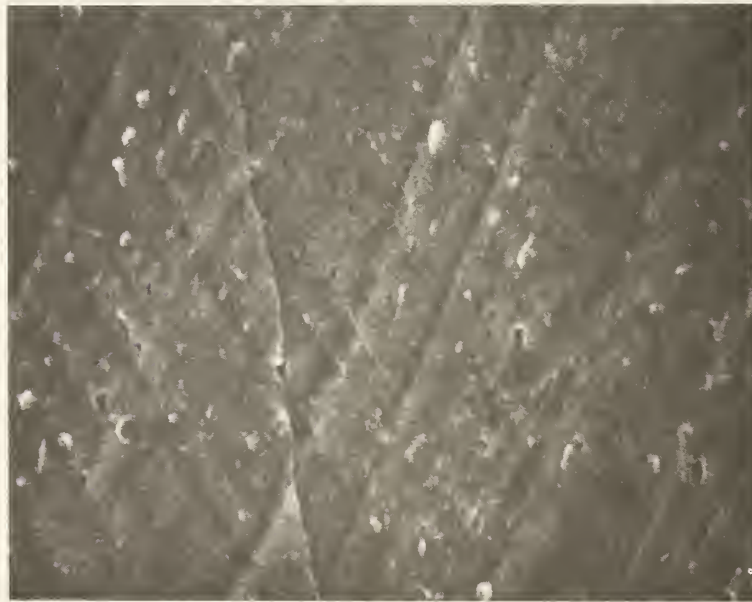
5 μm

Fig. 9. Cleavage-like areas that become apparent in the more brittle
alloys: (a) alloy 413, low magnification SEM photomicrograph;
(b) alloy 413, high magnification SEM photomicrograph.
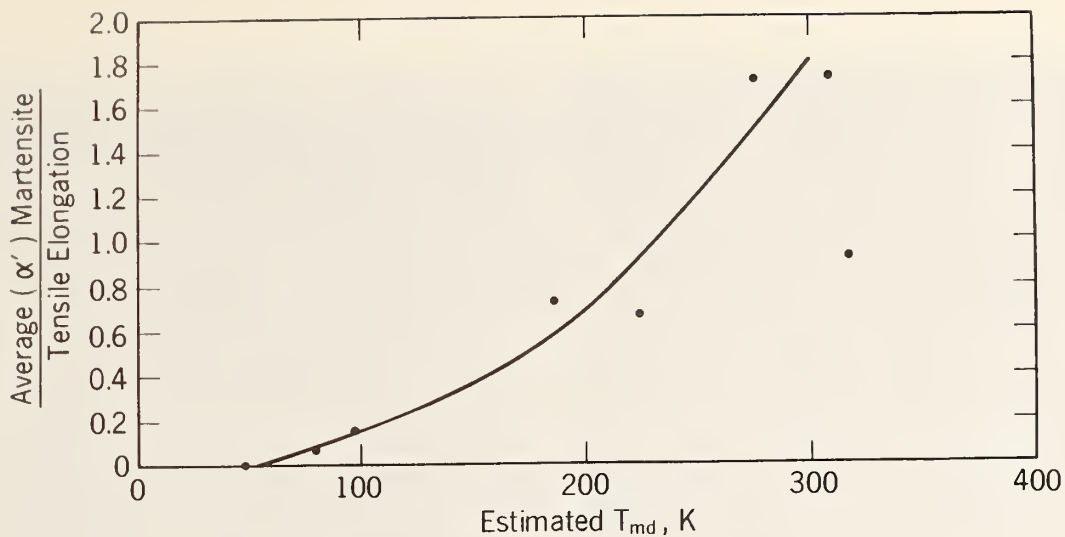
Fig. 10. The normalized average amount of α' martensite within the gage length of tensile specimens (after deforming at 4 K) plotted against the calculated md temperatures (based on chemical composition).
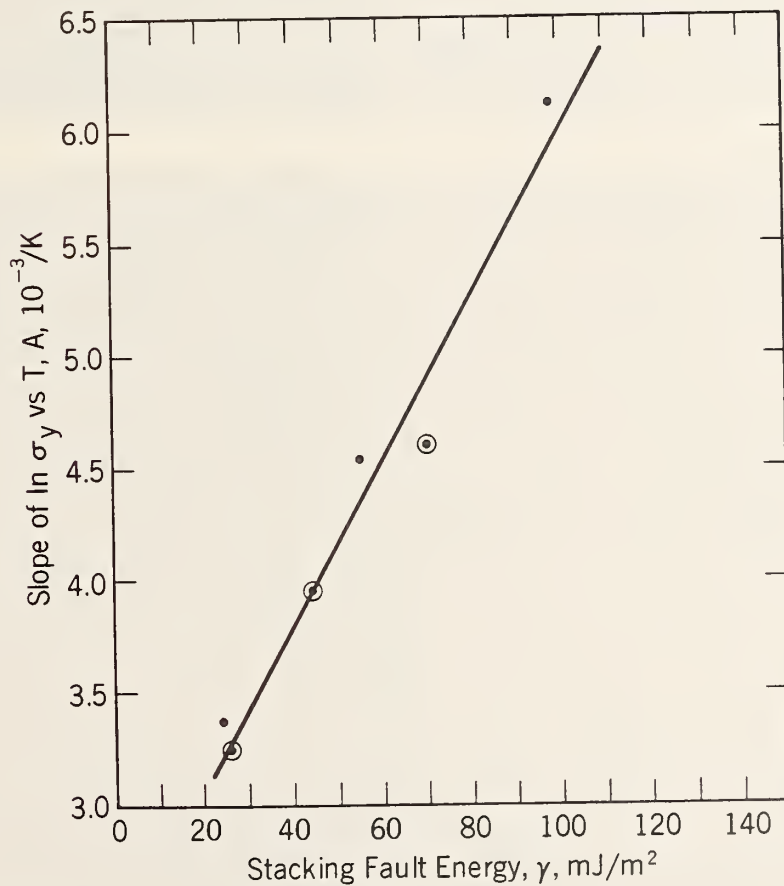
Fig. 11. Temperature dependence of yield strength (A of Eq. 2) versus estimated stacking fault energy, based on chemical composition. Three circled data points represent AISI 304, 316, and 310 alloys from a previous study.[3]
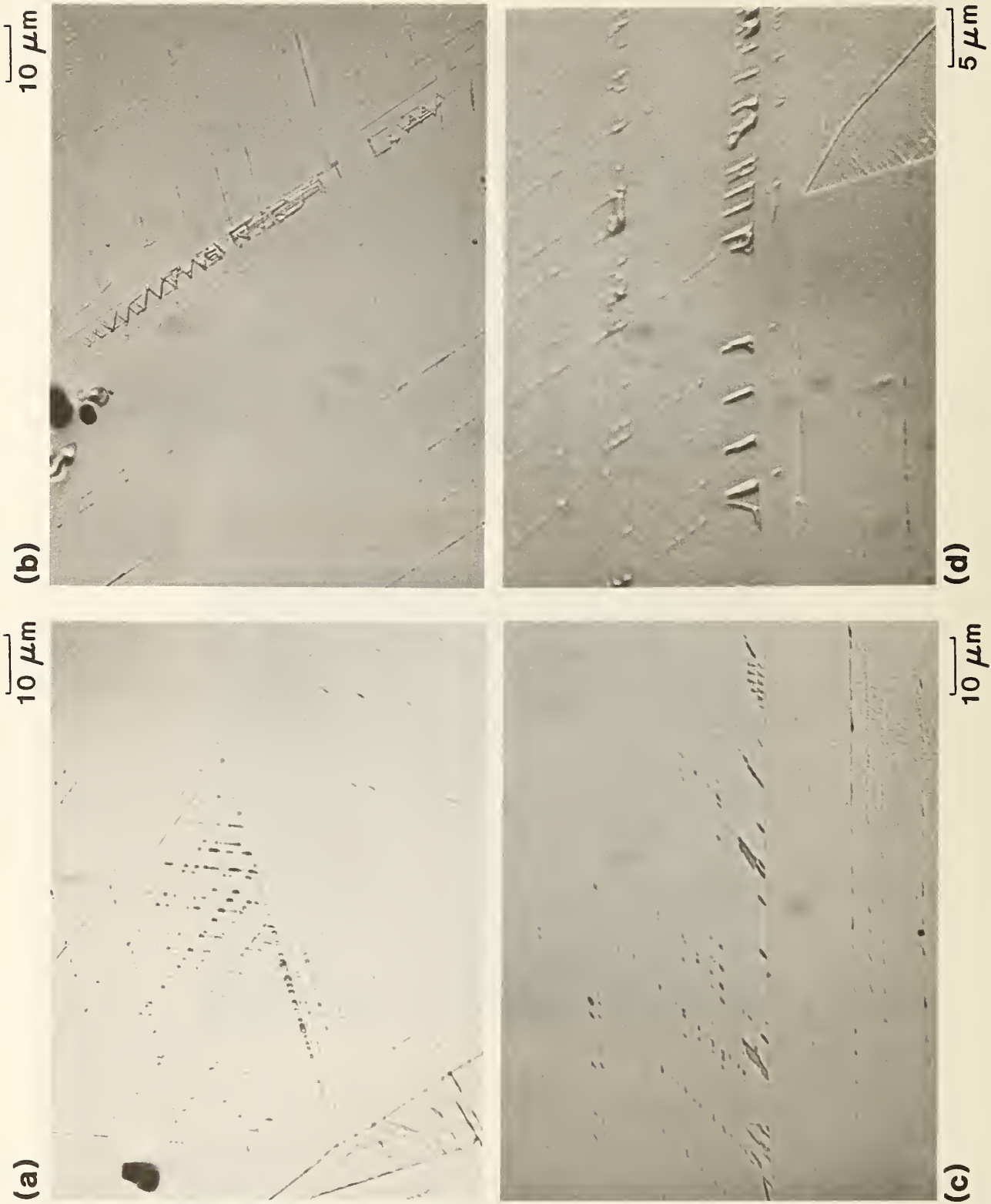
Fig. 12. Microstructure of alloy 740 after several percent elongation at 4 K. Parts a, b, and c are at 1000X; part d is at 2000X.

142
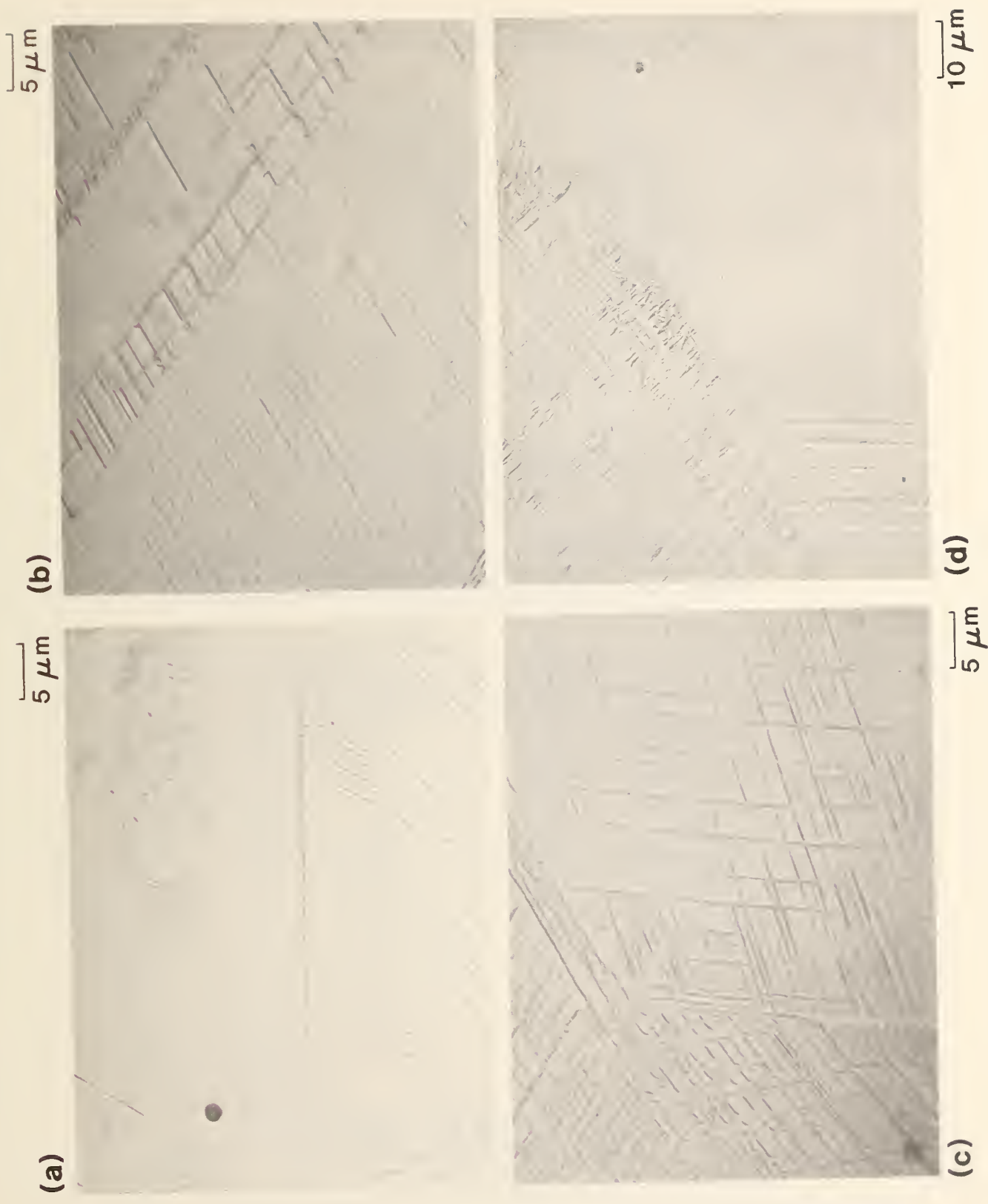
Fig. 13. Microstructure of alloy 413 after several percent elongation at 4 K. Parts a, b, and c are at 2000X; part d is at 1000X.

143
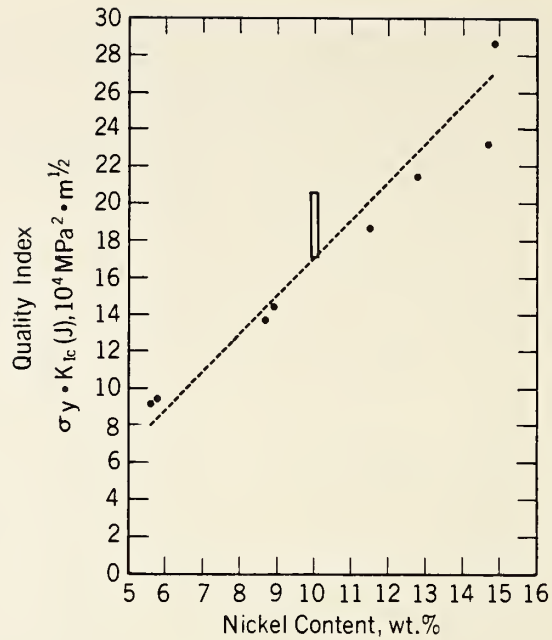
Fig. 14. The quality index $\sigma_y \cdot K_{Ic}(J)$ at 4 K plotted against
Ni content. Band of data includes a series of nine
19Cr-10Ni steels with varying C and N contents.[8]
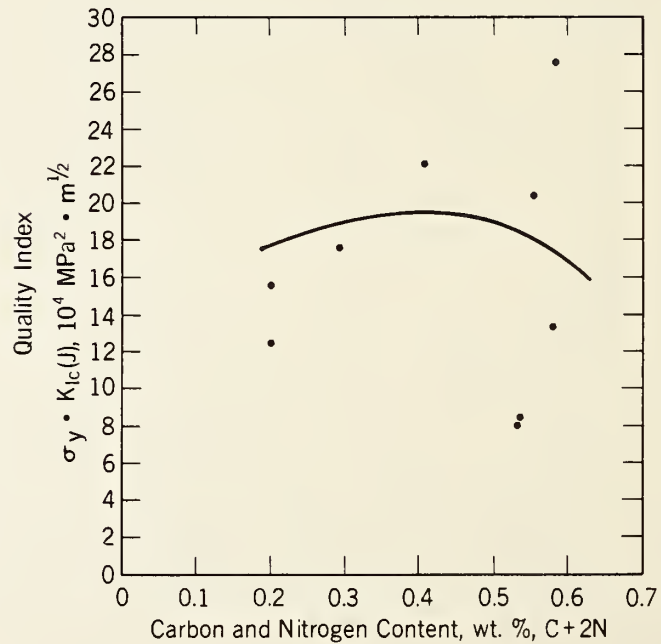
Fig. 15. The quality index $\sigma_y \cdot K_{Ic}(J)$ at 4 K plotted against C and
N content. Solid line represents data of a series of
nine 19Cr-10Ni steels with varying C and N contents.

144

LOW-TEMPERATURE SOUND VELOCITIES IN 304-TYPE
STAINLESS STEELS: EFFECT OF INTERSTITIAL C AND N

H. M. LEDBETTER

Fracture and Deformation Division, Center for Materials Science

National Bureau of Standards, Boulder, Colorado 80303, USA

Between T = 293 and 4 K, we measured the longitudinal ultrasonic velocity of
nine 304-type stainless steels with various C+N contents: 0.3 to 1.3
atomic percent. All alloys showed similar behavior: a regular increase in
velocity down to approximately 100 K; below this, an anomalous decrease caused
by a magnetic transition. The alloys varied in two ways: (1) contrary to
some reports, increasing C+N decreases the Néel temperature strongly,
approximately 13 K per atomic percent; (2) the magnitude of the
low-temperature elastic softening associated with the Néel transition
decreases slightly with increasing C+N content.

INTRODUCTION

Recently, Ledbetter and Austin[1] reported the effects of interstitial carbon
and nitrogen on the ambient-temperature elastic constants of 304-type stainless-
steel alloys. They found that all the elastic stiffnesses--Young modulus,
shear modulus, bulk modulus--decrease 0.5 to 0.9 percent per atomic percent
solute. The Poison ratio remains unchanged. Using Eshelby's model, they
related the elastic-stiffness decrease to volume increase. In another study
Ledbetter and Austin[2] used x-ray diffraction and Archimedes-method mass
density to determine the volume change due to interstitial C+N in an fcc
crystal structure. Both C and N increase volume. Despite its smaller size, N
is more effective. We attribute this to stronger interatomic bonding for C
atoms. For N, volume increases approximately 0.7 percent per atomic percent
interstitial.

The low-temperature properties of these alloys are of interest for two reasons.
First, because of their ductility and toughness, they see many low-temperature
applications where the elastic constants are key design parameters. Second,
at low temperatures these alloys undergo a magnetic transition that affects
the elastic constants. Conversely, elastic constants (or their companion
sound velocities) can be used to study the phase transition, which remains
only partially understood.

Reported here is a preliminary study of the low-temperature elastic properties of 304-type stainless steel with varying C+N content. Longitudinal velocity, v_ℓ, was measured nearly continuously between 293 and 4 K. This velocity gives the longitudinal modulus

$$C_\ell = \rho v_\ell^2 \qquad\qquad (1)$$

where ρ denotes mass density. This modulus contains both dilatational and shear modes, because

$$C_\ell = B + (4/3)G \qquad\qquad (2)$$

where B denotes bulk modulus and G shear modulus. Thus, changes in either dilatation resistance or in shear resistance appear in C_ℓ.

EXPERIMENT

Materials were described in detail previously[1]. For nine alloys the average weight-percentage chemical composition was 18.9Cr, 10.0Ni, 1.5Mn, balance Fe and trace elements. Table 1 gives the C+N contents. Rockwell B hardness increased continuously with C+N, from 73.4 to 88.5. Grain size ranged from 78 to 105 μm, averaging 88 μm.

Sound velocities were determined by a pulse-echo-overlap method at frequencies near 10 MHz by methods described previously[3].

RESULTS

Figure 1 shows the principal results: the variation of C_ℓ between 293 and 4 K for three alloys with different N contents. For clarity, results for the other six alloys, which vary C content, are omitted. They cluster around each of the three N-content curves. Table 1 also contains estimated T_N temperatures based on the midpoint temperature between C_ℓ(max) and C_ℓ(min). Figure 2 graphs these magnetic transition temperatures.

DISCUSSION

Qualitatively, all nine alloys behave similarly during cooling from 293 to 4 K. On average, C_ℓ increases 4.3 percent. This compares with 4.0 and 3.7 for copper and nickel, respectively. Higher C+N reduces T_N, that is stabilizes the fcc crystal structure against magnetic ordering. A simple interpretation here is that C+N dilates the fcc crystal structure, thus requiring lower temperatures to achieve the lower interatomic spacing required for direct magnetic-exchange interactions[4]. This finding contradicts that of Warnes and King[5] who, with respect to T_N, cite the "negligible influence of the interstitial solutes C and N". Figure 1 shows a nonnegligible effect: approximately 13 K per atomic percent interstitial. The measurement scatter precludes deciding whether C or N is more effective in lowering T_N. To settle this, we plan to measure magnetic susceptibility versus temperature.

The C_ℓ softening upon cooling through the magnetic transition is approximately the same for all nine alloys, -1.5 to -2.0%. This effect is quite large.

Using relationships developed by Eshelby[6] for point centers of dilatation, this softening implies a volume change at the magnetic transition of about +1.0%. No accurate dilatometric measurements exist to confirm this. But recently, Ehrhart et al.[7] studied γ-iron precipitates ($T_N \cong 70$ K) by x-ray diffraction and found a volume increase of 0.3% at the magnetic transition. The decreased elastic softening with increased C+N relates also to the dilation. Increased interatomic spacing causes a weaker magnetic interaction, a smaller volume change, and a smaller elastic-constant anomaly.

ACKNOWLEDGMENT

REFERENCES

1. Ledbetter, H. M. and Austin, M. W., to be published, available in report NBSIR 84-3000 (1984).

2. Ledbetter, H. M. and Austin, M. W., to be published, available in report NBSIR 84-3000 (1984).

3. Ledbetter, H. M., Frederick, N. V., and Austin, M. W., J. Appl. Phys. 51 (1980) 305.

4. Ledbetter, H. M., to be published, available in report NBSIR 84-3000 (1984).

5. Warnes, L. A. A. and King, H. W., Cryogenics 16 (1976) 659.

6. Eshelby, J. D., J. Appl. Phys. 25 (1954) 255.

7. Ehrhart, P. Schönfeld, B., Ettwig, H. H., and Pepperhoff, W., J. Mag. Mag. Mater. 22 (1983) 79.

Table 1

C	N	C+N	T_N
(at. pct.)	(at. pct.)	(at. pct.)	(K)
0.13	0.15	0.28	52
0.27	0.15	0.42	52
0.41	0.15	0.56	52
0.17	0.47	0.64	50
0.31	0.47	0.78	50
0.43	0.47	0.91	46
0.14	0.95	1.09	39
0.26	0.95	1.21	44
0.39	0.95	1.34	41
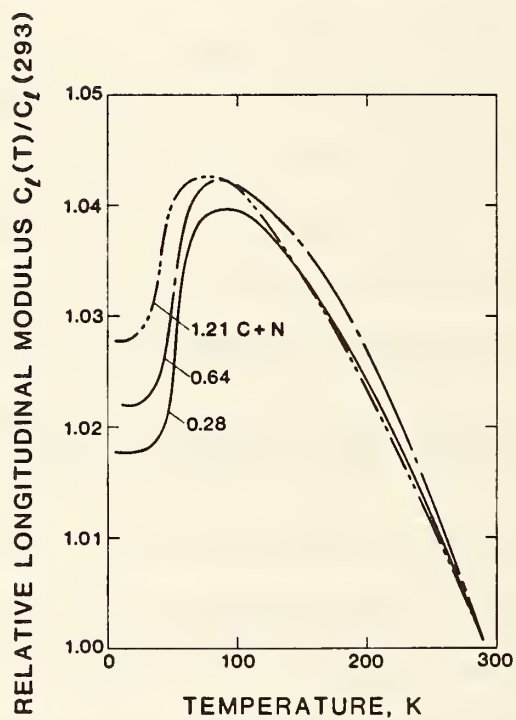
Fig. 1 Longitudinal modulus from T = 293 K to 4 K for three 304-type stainless steels with varying C+N content. Near 50 K, elastic softening occurs owing to a Néel transition (paramagnetic-antiferromagnetic).
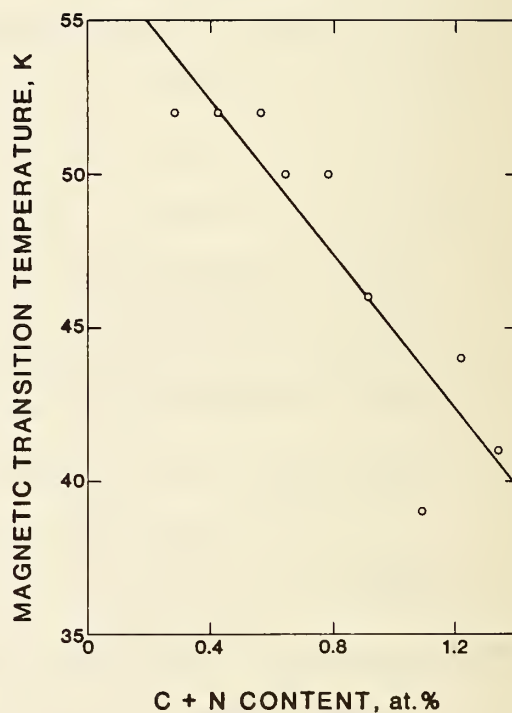
Fig. 2 Effect of interstitial C+N on the magnetic transition temperature.

LINEAR-ELASTIC FRACTURE OF HIGH-NITROGEN
AUSTENITIC STAINLESS STEELS AT LIQUID HELIUM TEMPERATURE*

R. L. Tobler, R. P. Reed, and P. T. Purtscher
Fracture and Deformation Division
National Bureau of Standards
Boulder, Colorado

Four Fe-Cr-Ni-Mn austenitic stainless steels containing 0.14, 0.26, 0.28, and 0.37 wt.% N were fractured in a liquid helium environment at 4 K, and valid measurements of the linear-elastic plane-strain stress-intensity factor, K_{Ic}, were obtained in most cases. Interstitial nitrogen significantly strengthens these steels at low temperatures so that relatively brittle fractures occur under plane-strain conditions at 4 K, despite the fact that these alloys are moderately ductile in uniaxial tension. The brittle failure mechanism at 4 K involves a form of cleavage or slip-band decohesion, as evidenced by the formation of transgranular facets on {111} crystallographic planes.

Key words: austenitic stainless steels; cryogenic properties of materials; fracture mechanisms; fracture toughness; mechanical properties; tensile properties; stainless steel alloys.

INTRODUCTION

The AISI 300 series austenitic stainless steels are traditional candidates for structural applications at cryogenic temperatures. With specified allowable nitrogen contents up to 0.16 wt.%, the yield strengths of these steels may reach 800 MPa at liquid helium temperature, 4 K. A practical means of achieving still higher strengths is to increase the manganese content so as to accommodate more nitrogen. To this end the Fe-Cr-Ni-Mn-N austenitic stainless steels were developed.

The Fe-Cr-Ni-Mn-N steels are stronger at 4 K than AISI 300 series steels, but less readily available and less well characterized with respect to mechanical properties, physical properties, and service experience. This paper presents fracture toughness data for four such steels containing 0.14, 0.26, 0.28, and 0.37% N. Owing to the relatively high strengths achieved at 4 K, linear-elastic plane strain fracture toughness (K_{Ic}) tests were possible with 25.4-mm-thick compact specimens following the ASTM E 399-83 method. Toughness measurements and fractographic observations are reported here, and comparisons are made with other nitrogen-strengthened Fe-Cr-Ni-Mn-N steels [1-5] and AISI 304 type steels [6] that are candidates for structural applications in fusion energy magnets operating under high stress fields in liquid helium.

MATERIALS

A description of the test materials, including composition, form, heat treatment, mechanical properties, and grain size, is given in Tables 1, 2, and 3. In Table 3, the properties at 295 K are quoted from the mill sheets, whereas the properties at 4 K were measured in the laboratory using 6.4-mm-diameter tensile specimens with 25.4-mm gage lengths (two tests per material). The materials are referred to by their nominal compositions and commerical designations as follows:

1) Fe-16Cr-8Ni-8Mn-0.14N (Nitronic 60*)
2) Fe-19Cr-7Ni-9Mn-0.26N (Nitronic 40*)
3) Fe-20Cr-8Ni-2Mn-0.28N (AISI 304 HN)
4) Fe-20Cr-7Ni-8Mn-0.37N (AISI 216)

The Fe-20Cr-7Ni-8Mn-0.37N steel was received in a hot and cold forged condition and was annealed in the laboratory prior to testing. The other three steels were received and tested in their annealed conditions. Also, the Fe-16Cr-8Ni-8Mn-0.14N steel contained one-half percent of a magnetic second phase at 295 K prior to testing, whereas the others were fully austenitic, as verified by examination with a magnetometer.

Because rectangular bars or plates of suitable thickness (25.4 mm) were not commercially available, cylindrical bars of Fe-16Cr-8Ni-8Mn-0.14N, Fe-20Cr-8Ni-2Mn-0.28N, and Fe-20Cr-7Ni-8Mn-0.37N steels were obtained. These

---

* Trade names are used here to describe the steels tested, and their use for this purpose in no way implies endorsement or recommendation by NBS.

bars were 76, 159, and 92 mm in diameter, respectively. Compact specimens were machined in RL orientations [7], and tensile specimens were extracted with the principal axes transverse to the longitudinal bar directions so that the fracture plane orientations in both specimens would be similar.

In the case of Fe-19Cr-7Ni-9Mn-0.26N steel, a rectangular bar was obtained and compact specimens of the TL orientation [7] were tested according to the usual practice.

PROCEDURES

Two K_{Ic} tests per steel were performed using 25.4-mm-thick (B) compact specimens. These specimens had a width (W) of 50.8 mm, a W/B ratio of 2, and standard planar proportions as per ASTM E 399-83 [7]. The notch was modified as shown in Figure 1, and a calibrated clip gage was positioned at the load-line in anticipation that J-integral measurements might be performed in some cases. (This modification proved unnecessary.)

Using the cryogenic apparatus described elsewhere [8,9], fatigue cracks of length a were introduced by computer-controlled sinusoidal loading at a stress ratio (R) of 0.1 and at a frequency of 14 Hz. The cracks were initiated at liquid nitrogen temperature (76 K), but the final 5 mm or more of crack growth was at liquid helium temperature (4 K). The ΔK value during fatigue was maintained constant at 30 MPa·m$^{1/2}$ by computer-controlled load reductions performed every 0.13-mm increment of crack growth. After fatigue cracking at 4 K, the fracture toughness tests were performed at a stroke rate of about 0.05 mm/s.

RESULTS AND DISCUSSION

Representative 4-K fracture test records for the steels of this study are shown in Figure 2. Type I load-displacement curves [7] were observed in each test. There was always a slight degree of nonlinearity during the terminal stages of loading, and sometimes a few small increments of unstable crack extension were observed prior to final fracture.

The calculated K_Q and K_{Ic} parameters are listed in Table 4, with pertinent specimen dimensions and validity criteria. As defined in ASTM E 399-83, K_Q is a conditional toughness measurement. To qualify as a valid K_{Ic} measurement, the relative crack length must be in the range:

$$0.45 \leq a/W \leq 0.55 \tag{1}$$

The following additional requirements must also be met:

$$P_{max}/P_Q \leq 1.10 \tag{2}$$

$$2.5(K_Q/\sigma_y)^2 \leq B, a \tag{3}$$

For most tests these criteria are satisfied, and valid K_{Ic} data are tabulated. But in the case of Fe-19Cr-7Ni-9Mn-0.26N steel, valid K_{Ic} data

were not obtained, owing to violations of Eqs. 2 and 3. J-integral tests of this steel were likewise invalid since fast-fracture prevented the development of a complete four-point resistance curve, as required according to the elastic-plastic test procedure, ASTM E 813-81 [10].

As a guide to rank the toughness of Fe-19Cr-7Ni-9Mn-0.26N relative to the other steels, the specimen strength ratios, R_{sc}, were calculated according to ASTM E 399-83 [7]. R_{sc} is the ratio of the maximum nominal net section stress to the material's yield strength. This parameter is a function of the maximum load the compact specimen can sustain; it is especially useful here because all specimens are the same size and shape. As shown in Figure 2 and Table 4, respectively, P_{max} and R_{sc} are highest for the Fe-19Cr-7Ni-9Mn-0.26N steel, a strong indication that its fracture toughness exceeds the values for the other steels in this study.

The fracture toughness results are plotted versus yield strength in Figure 3. In general, the Fe-20Cr-8Ni-2Mn-0.28N (AISI 304 HN) result of this study fits the trend for AISI 304 type steels [6], while the Fe-19Cr-7Ni-9Mn-0.26N and Fe-20Cr-7Ni-8Mn-0.37N steel results fit the trend for other previously tested Fe-Cr-Ni-Mn-N steels [3-5]. However, the Fe-16Cr-8Ni-8Mn-0.14N steel is highly deviant and demonstrates an exceptionally poor fracture toughness for its given value of yield strength.

Fractographic features of these steels are illustrated by scanning electron microscopy in Figures 4 through 6. All the 4-K fracture surfaces display areas of cleavage-like transgranular facets. On the macroscopic scale, the facets are smooth, flat, and highly refective. On the microscopic scale, there are obvious steps and visible slip line markings. Judging from the near 60° angles between the slip-line markings, the facets evidently form on {111} crystal planes. The {111} crystal plane indices were confirmed by x-ray diffraction in a study of a related steel, Fe-18Cr-3Ni-13Mn-0.37N [11]. Since the {111} planes are the active slip planes of the austenite phase, the failure process may be slip-plane decohesion.

In an on-going study of nitrogen-strengthened austenitic steels [12], the occurrence of facets on the fracture surface, concomitant with a degradation of toughness at 4 K, has been correlated with decreasing nickel content. Unpublished data indicate that manganese content is also an important variable [13]. Apparently chemical composition plays a significant role in the fracture process of these austenitic stainless steels at 4 K, but the mechanism by which chemical composition affects the fracture mode has not yet been identified.

With the unaided eye, a "woody" type of texture covers the surface of the Fe-16Cr-8Ni-8Mn-0.14N steel (Fig. 4), significantly different from the macroscopic appearance of the other three alloys (Figs. 5 and 6). The alloy with the woody-textured fracture surface has a lower toughness than expected for its respective yield strength. The same alloy contained one-half of one percent of a nonaustenitic phase (probably delta ferrite) prior to testing. The woody texture of the fracture surface and the presence of a second phase indicate that the material may not have been processed properly, which resulted in the relatively poor fracture toughness.

SUMMARY AND CONCLUSIONS

Austenitic stainless steels containing a high level of nitrogen are prone to brittle fracture at low temperatures despite their face-centered cubic crystal structures. In this study, 4-K fracture toughness tests were performed on 25.4-mm-thick compact specimens of Fe-Cr-Ni-Mn steels containing 0.14, 0.26, 0.28, and 0.37 wt.% N. Type I linear-elastic fracture test records were observed, and K_{Ic} and K_Q data ranging from 90 to 166 MPa·m$^{1/2}$ are reported. Brittle fracture under plane-strain conditions is associated with a cleavage-like failure mode consisting of transgranular facets that form along the {111} family of slip planes in the austenite lattice. Thus, the failure mechanism at 4 K may involve slip-plane decohesion, as documented for tests of a related Fe-18Cr-3Ni-13Mn-0.37N steel [11].

REFERENCES

1. A. Nyilas and L. Yan, Fracture Toughness Determination of 21Cr-6Ni-9Mn Stainless Steel at 4 K. Report 03-03-02P12C, Institut für Technische Physik, Kernforschungzentrum Karslruhe, Federal Republic of Germany (July 1984) 16.

2. J. M. Wells, R. Kossowsky, W. A. Logsdon, and M. R. Daniel, Structural Materials for Cryogenic Applications, Research Report 76-9D9-CRYMT-R1 Westinghouse Electric Corporation Research and Development Center, Pittsburgh, Pennsylvania, Final Technical Report (October 9, 1976) 181.

3. R. L. Tobler and R. P. Reed, Tensile and Fracture Behavior of a Nitrogen Strengthened Chronium-Nickel-Manganese Stainless Steel at Cryogenic Temperatures, in: Elastic-Plastic Fracture, ASTM STP 668, J. D. Landes, J. A. Begley, and G. A. Clark, Eds., American Society for Testing and Materials, Philadelphia, Pennsylvania (1979) 537-552.

4. D. T. Read and R. P. Reed, Toughness, Fatigue Crack Growth, and Tensile Properties of Three Nitrogen-Strengthened Stainless Steels at Cryogenic Temperatures, The Metal Science of Stainless Steels, Metallurgical Society of the AIME, New York (1979) 92-121.

5. D. T. Read and R. P. Reed, Fracture and Strength Properties of Selected Austenitic Stainless Steels at Cryogenic Temperatures, in: Materials Studies for Magnetic Fusion Energy Applications at Low Temperatures-II, NBSIR 79-1609, National Bureau of Standards, Boulder, Colorado (1979) 81-122.

6. R. L. Tobler, D. T. Read, and R. P. Reed, Strength/Toughness Relationship for Interstitially Strengthened AISI 304 Stainless Steels at 4 K Temperature, in: Fracture Mechanics: Thirteenth Conference, ASTM STP 743, Richard Roberts, Ed., American Society for Testing and Materials, Philadelphia, Pennsylvania (1981) 250-268.

7. Standard Test Method for Plane-Strain Fracture Toughness of Metallic Materials, ASTM Designation: E 399-83, 1984 Annual Book of ASTM Standards, Section 3, Metals Test Methods and Analytical Procedures, American Society Testing and Materials, Philadelphia, Pennsylvania (1984) 519-554.

8. D. T. Read and R. L. Tobler, Mechanical Property Measurements at Low Temperatures, in: Advances in Cryogenic Engineering, Vol. 28, R. P. Reed and A. F. Clark, Eds., Plenum Press, New York (1982) 17-28.

9. C. W. Fowlkes and R. L. Tobler, Fracture Testing and Results for a Ti-6Al-4V Alloy at Liquid Helium Temperature, Eng. Fract. Mech. 8:487-500 (1976).

10. Standard Test Method for J_{Ic}, A Measure of Fracture Toughness, ASTM Designation: E 813-81, 1984 Annual Book of ASTM Standards, Section 3, Metals Test Methods and Analytical Procedures, American Society Testing and Materials, Philadelphia, Pennsylvania (1984) 763-781.

11. R. L. Tobler and D. A. Meyn, Cleavage-like Fracture in Fe-18Cr-3Ni-13Mn-0.37N Austenitic Stainless Steel at Liquid Helium Temperature, in: Materials Studies for Magnetic Fusion Energy Applications at Low Temperatures--VIII, NBSIR 85-3025, R. P. Reed, Ed., National Bureau of Standards, Boulder, Colorado (1985) 167-179.

12. P. T. Purtscher and R. P. Reed, Nickel and Nitrogen Alloying Effects on the Strength and Toughness of Austenitic Stainless Steels at 4 K, in: Materials Studies for Magnetic Fusion Energy Applications at Low Temperatures--VIII, NBSIR 85-3025, R. P. Reed, Ed. National Bureau of Standards, Boulder, Colorado (1985) 123-144.

13. P. T. Purtscher and R. P. Reed, National Bureau of Standards, Boulder, Colorado, unpublished results.

Table 1. Mill chemical analyses (wt.%)

Material	Cr	Ni	Mn	N	C	Si	S	P	Cu	Mo	Co
Fe-16Cr-8Ni-8Mn-0.14N	16.49	8.23	8.04	0.140	0.068	4.14	0.005	0.027	0.44	0.26	--
Fe-19Cr-7Ni-9Mn-0.26N	19.44	6.67	9.34	0.263	0.040	0.37	0.001	0.013	--	--	--
Fe-20Cr-8Ni-2Mn-0.28N	20.21	8.44	1.83	0.280	0.059	0.50	0.021	0.025	0.60	0.59	0.16
Fe-20Cr-7Ni-8Mn-0.37N	19.82	6.93	8.45	0.370	0.060	0.47	0.009	0.030	--	2.51	--

Table 2. Material form and condition.

Material	Form	Condition Tested
Fe-16Cr-8Ni-8Mn-0.14N	76-mm-dia. round bar	Hot-rolled, annealed, and pickled: 1066°C, 1/2 h, water quench
Fe-19Cr-7Ni-9Mn-0.26N	25.4- x 254-mm rectangular bar	Hot-rolled, annealed, and pickled: 1093 to 1121°C, 1-3/4 h, water quench
Fe-20Cr-8Ni-2Mn-0.28N	159-mm-dia. round bar	Solution annealed: 1024°F, water quench
Fe-20Cr-7Ni-8Mn-0.37N	92-mm-dia. round bar	Hot and cold forged, and annealed: 1093°C, 3 h, water quench

Table 3. Mechanical properties and grain size of test materials. (Properties are for the as-recieved condition, except as noted.)

Material	Temperature (K)	Yield Strength, σ_y (MPa)	Ultimate Strength, σ_u (MPa)	Elongation (%)	Reduction of Area (%)	Rockwell Hardness (R_B)	Grain size (μm)
Fe-16Cr-8Ni-8Mn-0.14N	295 4	414 990	745 1346	56 5.7	72 12.3	88	40
Fe-19Cr-9Ni-7Mn-0.26N	295 4	372 1201	700 1657	52 11.2	75 26.9	94	76
Fe-20Cr-8Ni-2Mn-0.28N	295 4	441 1265	765 1727	47 7.8	73 22.2	92	46
Fe-20Cr-7Ni-8Mn-0.37N[a]	295 4	805 1398	969 1862	32 4.5	55 12.6	94	86

[a] Properties at 4 K are for the laboratory annealed condition.

158

Table 4. Fracture toughness test results at 4 K.

Material	Spec No.	Specimen Thickness, B (mm)	Specimen Width, W (mm)	Relative Crack Length, a/W	Load Ratio P_{max}/P_Q	Size Criterion, $2.5(K_Q/\sigma_y)^2$ (mm)	Yield Strength, σ_y (MPa)	Strength Ratio, R_{Sc}	K_Q (MPa·m$^{1/2}$)	K_{Ic} (MPa·m$^{1/2}$)
Fe-16Cr-8Ni-8Mn-0.14N	1	25.550	50.750	0.626	1.01	19.5	990	0.98	87[a]	--
	2	25.525	50.550	0.507	1.08	21.3		0.92	91	91
Fe-19Cr-7Ni-9Mn-0.26N	1	25.500	50.650	0.547	1.15	43.2	1201	1.28	158[b]	--
	2	25.500	50.650	0.592	1.16	47.5		1.54	166[b]	--
Fe-20Cr-8Ni-2Mn-0.28N	1	25.525	50.700	0.514	1.03	12.9	1265	0.68	91	91
	2	25.450	50.700	0.505	1.01	12.7		0.74	90	90
Fe-20Cr-7Ni-8Mn-0.37N	1	25.550	50.995	0.513	1.08	15.3	1398	0.74	109	109
	2	25.550	50.650	0.526	1.05	14.2		0.68	105	105

[a] $K_Q \neq K_{Ic}$ because a/W > 0.55 (section 7.3.2.1 of ASTM E 399-83).

[b] $K_Q \neq K_{Ic}$ because $P_{max}/P_Q > 1.1$ (section 9.1.2 of ASTM E 399-83).

and because $2.5 (K_Q/\sigma_y)^2 > B$ (section 9.1.3 of ASTM E 399-83).
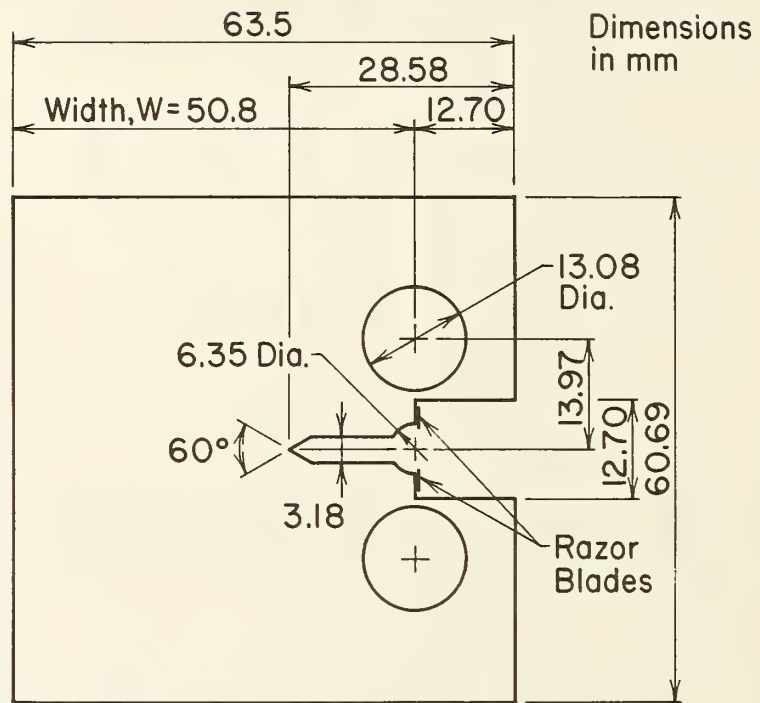
Figure 1. Compact specimen used in this study.
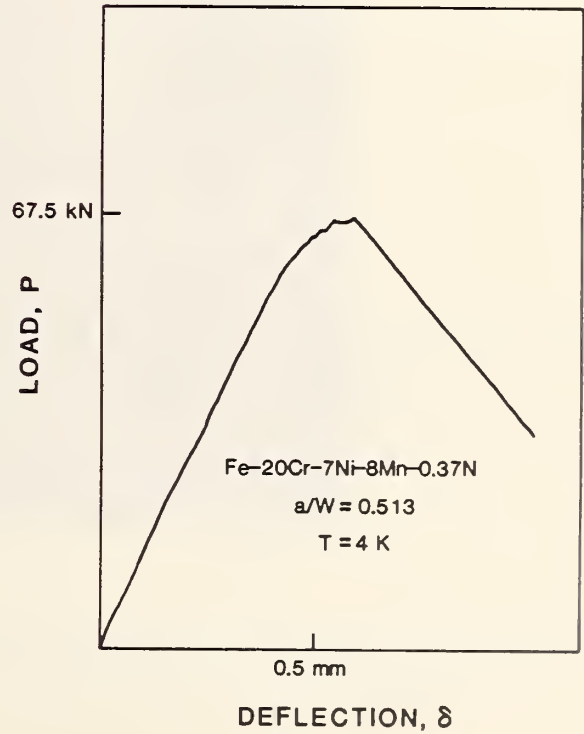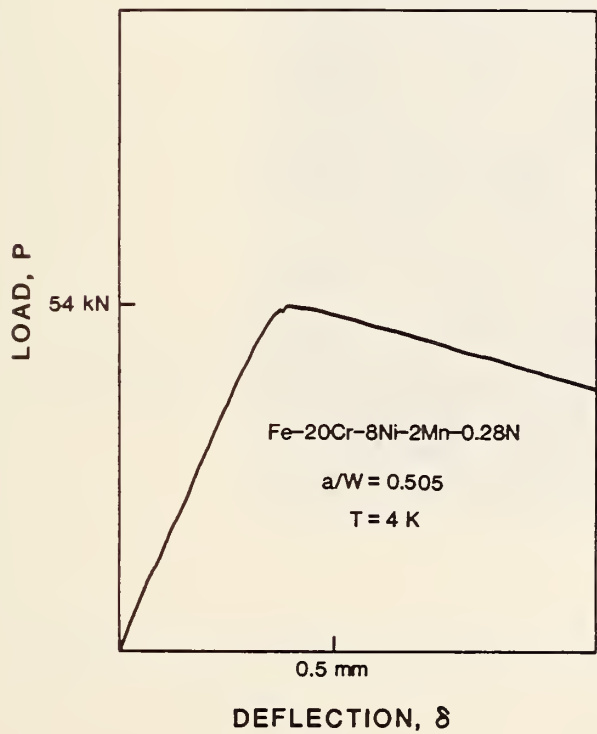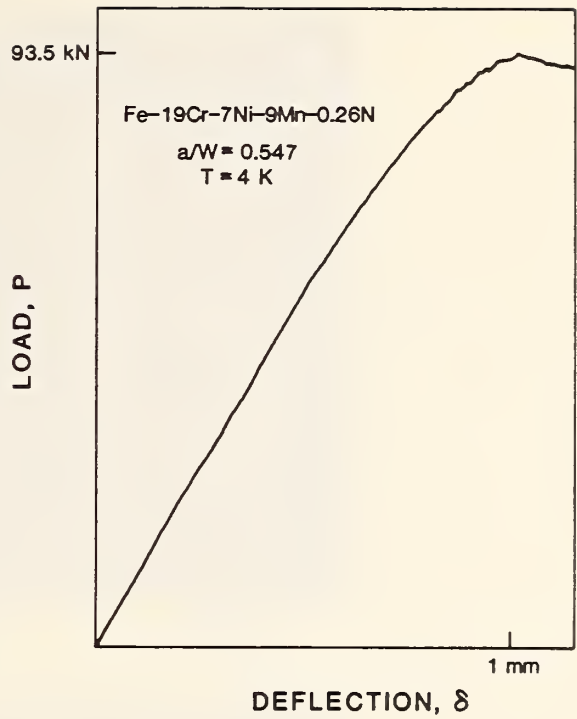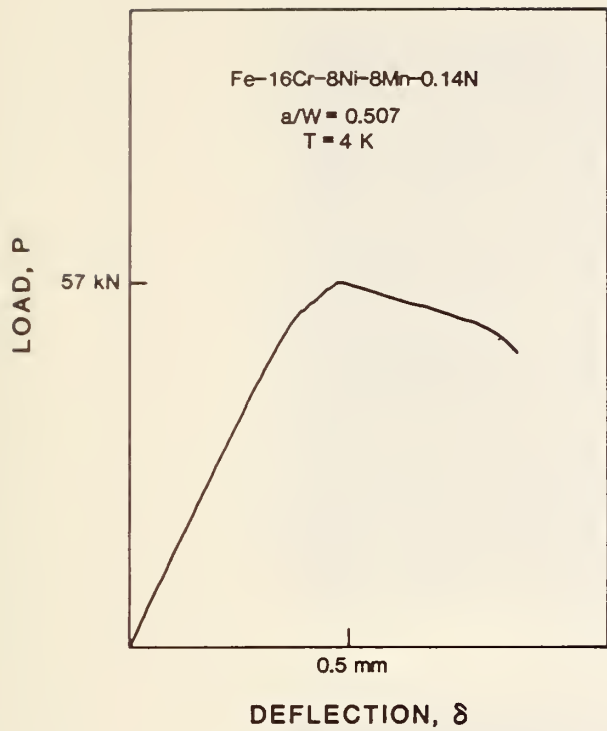
Figure 2. Representative 4-K fracture toughness test records for steels of this study.
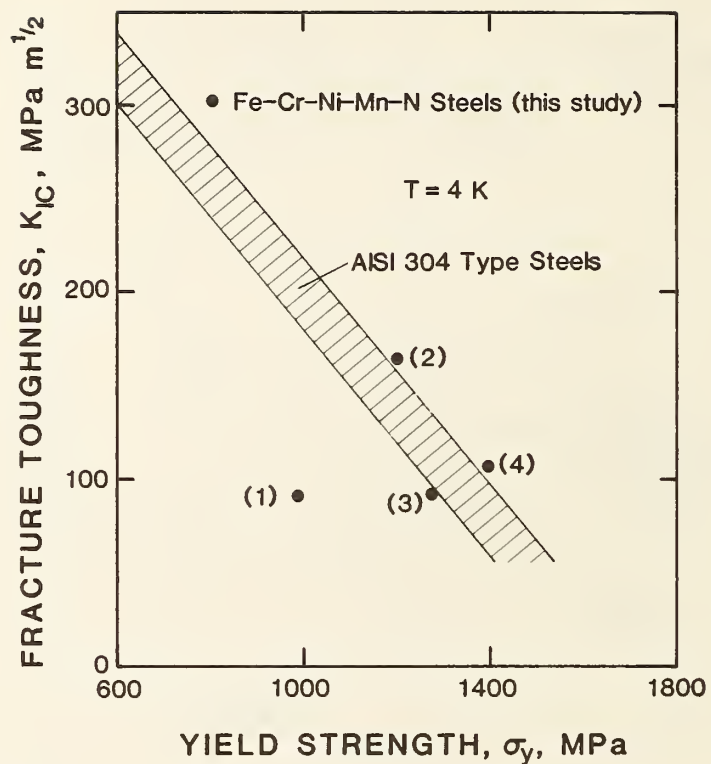
Figure 3. Fracture-toughness-versus-yield-strength trend at 4 K for steels of this study compared with previously tested austenitic stainless steels: (1) Fe-16Cr-8Ni-8Mn-0.14, (2) Fe-19Cr-7Ni-9Mn-0.26N, (3) Fe-20Cr-8Ni-2Mn-0.28N, (4) Fe-20Cr-7Ni-8Mn-0.37N.

A

200 μm

B
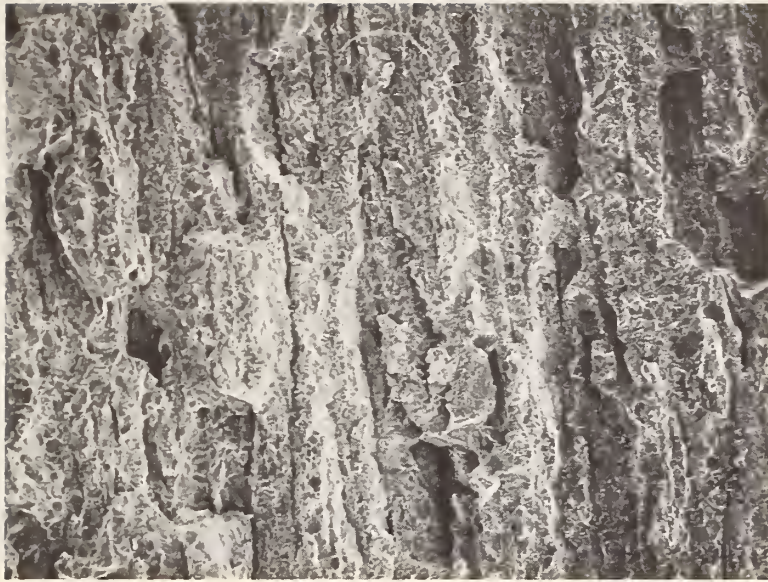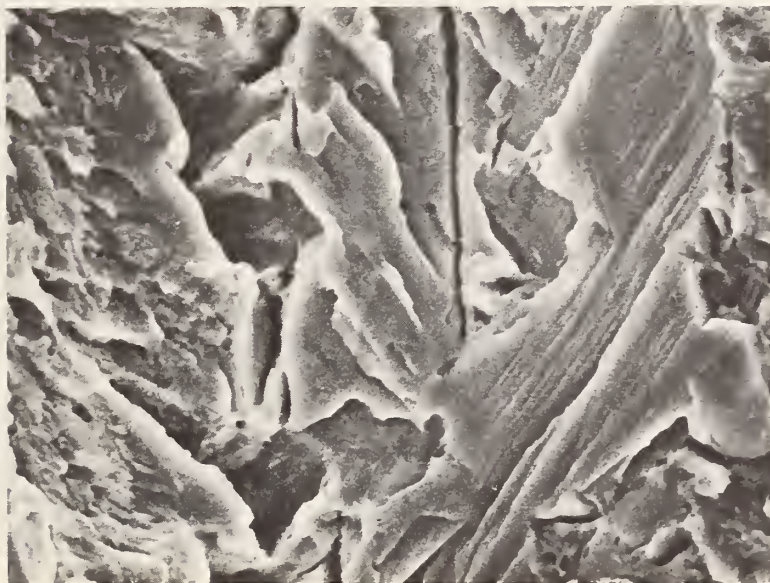
5 μm

Figure 4. Fractographic appearance of Fe-16Cr-8Ni-8Mn-0.14N steel fractured
at 4 K.
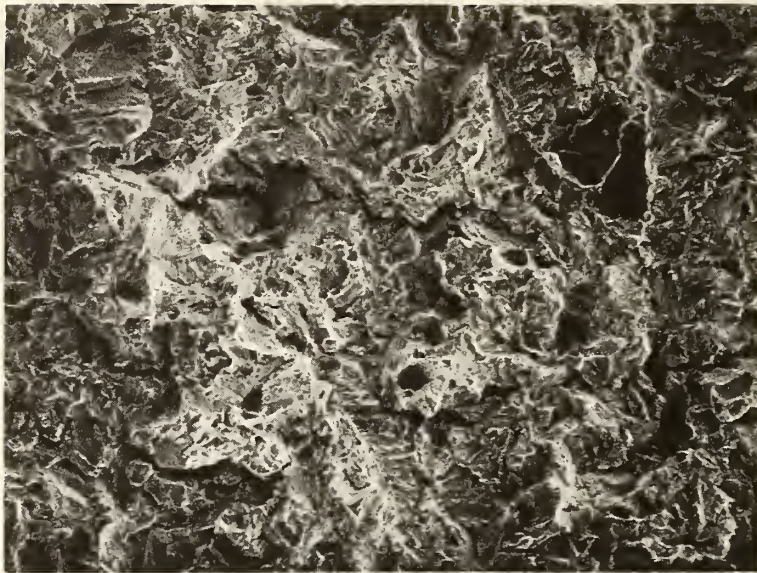
A

200 μm
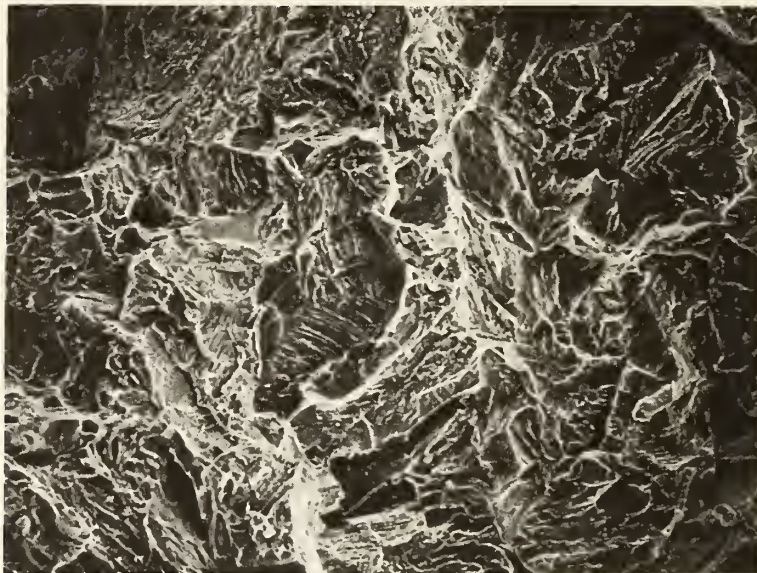
B

40 μm

Figure 5.   Fractographic appearance of Fe-19Cr-7Ni-9Mn-0.26N steel fractured
at 4 K.

164

20 μm
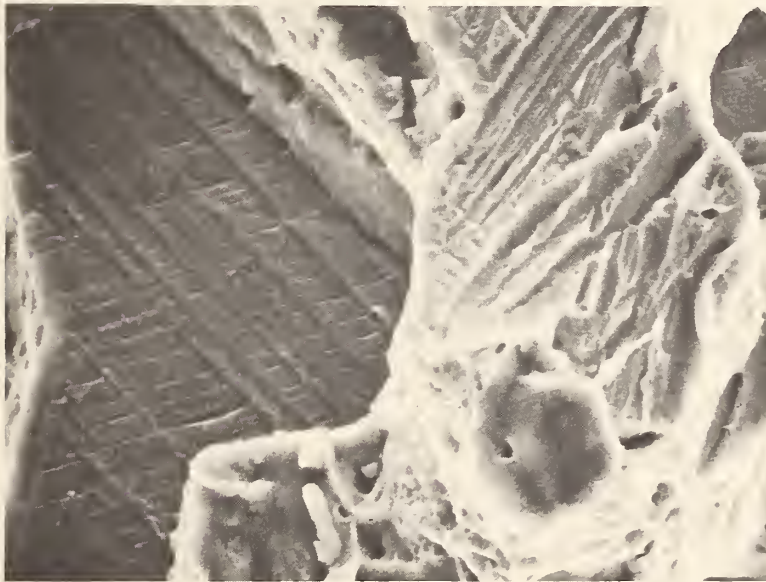
5 μm

Figure 6. Fractographic appearance of (A) Fe-20Cr-8Ni-2Mn-0.28N and
(B) Fe-20Cr-7Ni-8Mn-0.37N steels fractured at 4 K.

CLEAVAGE-LIKE FRACTURE IN
Fe-18Cr-3Ni-13Mn-0.37N AUSTENITIC STAINLESS STEEL AT LIQUID HELIUM TEMPERATURE[+]

R. L. Tobler
Fracture and Deformation Division
National Bureau of Standards
Boulder, Colorado 80303

and

D. Meyn
Materials Science and Technology Division
Naval Research Laboratory
Washington, DC 20375

Contrary to usual expectations for the face-centered cubic crystal structure, some nitrogen-alloyed austenitic stainless steels exhibit brittle fracture at temperatures approaching absolute zero. In this paper, plane strain fracture toughness and fractographic data are presented for an Fe-18Cr-3Ni-13Mn-0.37N steel tested at liquid helium temperature (4 K). Low toughness (K_{Ic} = 71 MPa$\cdot$m$^{1/2}$) and linear-elastic loading behavior was observed in 25-mm-thick compact specimens at this temperature, in association with a high tensile yield strength and a brittle failure mode consisting of transgranular facets. The transgranular facets produced in a coarse-grained sample of this steel at 4 K were identified by Laue x-ray diffraction and slip-line trace analysis as having formed on {111} austenite planes, which implies that slip-plane decohesion may be the brittle failure micromechanism.

Key words: austenitic steel; cleavage; cryogenic properties; face-centered cubic crystal structure; fractography; stainless steel alloy.

INTRODUCTION

According to traditional views, face-centered cubic (fcc) metals do not fracture by cleavage [1,2]. However, several exceptions have been cited recently in the literature [3-9]. For example, rhodium and iridium cleave in inert environments at room temperature [3,4]; nickel and Al-6Zn-3Mg cleave in liquid metals at various temperatures [5]; and high-strength nitrogen-alloyed austenitic (fcc) stainless steels cleave at liquid nitrogen temperature [6].

This note discusses brittle fracture in an austenitic stainless steel, Fe-18Cr-3Ni-13Mn-0.37N, tested in liquid helium at 4 K. Valid plane strain fracture toughness (K_{Ic}) data for this steel at 4 K are reported, a cleavage-like failure mechanism is described, and the crystal plane indices of the transgranular facets produced during fatigue and fracture are identified by x-ray diffraction and slip-line traces.

MATERIAL

The test material was a 25.4-mm-thick plate of Fe-18Cr-3Ni-13Mn-0.37N austenitic stainless steel in the commercially annealed condition: 1080°C for 1 h and water quenched. The mill chemical analysis in weight percent is: Fe-18.09Cr-3.26Ni-13.22Mn-0.37N-0.038C-0.12Mo-0.52Si-0.005S-0.028P. The material in the as-received condition has an average austenite grain diameter of 48 μm and a microstructure free of carbide precipitation. The mechanical properties are listed in Table 1.

PROCEDURE

Fracture toughness tests according to ASTM E 399-83 [11] were performed using compact specimens 25.4-mm thick (B) and 50.8-mm wide (W). Two specimens were machined from the as-received material, and one from laboratory annealed material. The laboratory anneal (1093° C, 37 h, water quenched) was applied to a sample of the Fe-18Cr-3Ni-13Mn-0.37N steel to enlarge its grains. Each specimen was fatigue cracked at stress-intensity factor ranges from 20 to 50 MPa·m$^{1/2}$ and then fractured at 4 K. The average grain diameter of the laboratory-annealed specimen was large enough (about 1 mm) to permit Laue x-ray microbeam analysis of individual crystal facets situated on the fracture surface of the polycrystalline aggregate.

RESULTS

A representative 4-K load-versus-deflection curve for the Fe-18Cr-3Ni-13Mn-0.37N steel in the as-received condition is shown in Figure 1. A type I [11] linear-elastic behavior is observed, with only slight nonlinearity prior to fast fracture.

The compact specimen fracture surface, shown in Figure 2, displays no shear lips. The fatigue and overload failure zones are both covered by smooth, highly reflective facets resembling the cleavage facets commonly seen in body-centered cubic (bcc) metals fractured at low temperatures. There is a relatively large degree of fatigue crack curvature, the edge crack lengths being

about 14 percent shorter than the three-point average crack lengths calculated according to ASTM E 399-83. Thus, the crack front curvature is sizable but does not exceed the 15 percent limitation set by section 8.2.2 of ASTM E 399-83 [11]. Magnetometer and x-ray examination of the 4 K fracture surface revealed no detectable bcc martensitic phase; the sensitivities were 0.2 and 3 percent, respectively.

The K_{IC} measurements for the as-received material are listed in Table 2. Also listed are specimen dimensions and test validity criteria as defined in the ASTM E 399-83 standard. The results for a chevron-notched and a straight-through notched specimen proved indistinguishable: The K_{IC} values are nearly equal, and crack front curvature is identical, which indicates that the type of crack-starter notch has no influence at all on the final crack front shape.

Figures 3 and 4 show facets produced in the coarse-grained specimen of Fe-18Cr-3Ni-13Mn-0.37N steel during fatigue and fracture at 4 K. The facet planes in both zones are oriented at angles from 90° to 53° with respect to the loading axis, or 0° to 37° from the macroscopic plane of fracture. As shown at higher magnification in Figs. 5 and 6, the facets display steps and slip-line markings, but no river patterns such as observed on classical cleavage facets for ferritic steels.

Three facets in the fatigue failure zone of this specimen were examined by Laue x-ray diffraction. All three facets were identified as {111} planes in an fcc structure, and the crystallographic directions in these {111} planes were apparently randomly oriented with respect to the crack propagation direction.

The overload zone facets for the coarse-grained specimen were also identified as {111} planes, on the basis of the 60° angle between the slip-line markings and between facet edges. Again, three facets in this zone were x-rayed. The planar indices could not be confirmed by x-ray diffraction because the diffraction technique produced no spot pattern, only general blackening due to the level of microplastic deformation induced at fracture. (The crystallographic directions for overload facets could not be determined, either). However, the fact that the overload zone facets are oriented like those in the fatigue zone indicates that they are also {111} planes.

DISCUSSION

According to a simple classical model, the occurrence of ductile or brittle fracture at a given test temperature depends on whether the yield strength (σ_y) or cleavage strength (σ_c) is reached first [1,2]. For metals, σ_c is relatively high and temperature insensitive. A critical factor, then, is the magnitude of σ_y and its rate of increase at low temperatures.

In most bcc metals and alloys, including ferritic steels, σ_y is strongly temperature dependent. As temperature is lowered, the lattice resistance to slip progressively increases until at some point σ_c is exceeded before slip can occur. As a result, cleavage is common in bcc materials at low temperatures [1]. For fcc metals and alloys, including austenitic stainless steels,

σ_y is typically low and not strongly temperature dependent. For many years, exceptions were unknown and there was a strong tendency to generalize that "slip occurs readily in fcc metals at all temperatures, their shear strengths are always lower than their cleavage strength, and they always fail in a ductile manner" [2].

Now, exceptional behavior has been discovered. Tensile loading of iridium in inert environments at room temperature, or of aluminum in liquid mercury, produces cleavage on {001} planes [3,5]. Corrosion fatigue cracking in aluminum alloys also produces cleavage on {001} planes [8]. Cleavage on {111} planes has also been observed in fcc metals under conditions of fatigue in alloys with coarse-grained structures and limited cross-slip [9].

For austenitic steels, cleavage was reported by Caskey [6] for an Fe-17.44Cr-15.31Mn-0.4/0.6N alloy in tensile tests at 78 K. The fracture surface displayed cleavage facets lying along coherent twin boundaries, transverse to the tensile axis. The fracture progressed by brittle micro-cracking across individual grains, followed by ductile fracture of the intervening material. The faceted failure mechanism was attributed to deformation faulting and to ε-phase formation. Similarly, a series of Fe-Cr-Mn-Ni steels was brittle at low temperatures [12-15]; this was attributed to several possible mechanisms, including the formation of brittle martensites and the high localization of strain arising from deformation faulting.

The Fe-18Cr-3Ni-13Mn-0.37N steel of this study is related to the Fe-Cr-Mn-Ni steels discussed above, all having been developed for the economical replacement of nickel by manganese and nitrogen. Manganese increases the solubility for nitrogen, which is the most potent austenite strengthening element at low temperatures. Thus, the steel of this study contains 0.37% nitrogen and σ_y more than triples between 295 and 4 K. Presumably, this strength increase promotes brittle fracture at 4 K, according to the classical model discussed above.

Various definitions of cleavage have been offered, leading to a problem of terminology. According to ASTM E 616-81 [16] standard terminology, cleavage is simply defined as "separation of a crystal along a plane of fixed orientation relative to the three-dimensional crystal structure within which the separation process occurs, with the separation process causing the newly formed surfaces to move away from one another in directions containing major components of motion perpendicular to the fixed plane." The facets on the Fe-18Cr-3Ni-13Mn-0.37N steel surfaces satisfy this definition of cleavage. Because the facets form along {111} planes (i.e, the active slip planes of the austenite), the failure mechanism might be defined as slip-plane decohesion or shear band cracking. However, all of the facets form at angles nearly parallel to the macroscopic fracture plane (i.e., high angles to the load axis), whereas shear band cracking is normally associated with 30 to 60° angles. The distinction between cleavage and slip-band decohesion in this steel is being investigated further.

The K_{Ic} measurements (70.2 and 71.0 MPa·m$^{1/2}$) agree well with the average K_Q value (71 MPa·m$^{1/2}$) reported by Read and Reed [10] for tests of the same heat of steel. Their K_Q values are reported as invalid because they failed to satisfy the crack front curvature requirements of ASTM E 399-74, the current standard at the time. Similar curvature occurred in the present study, but our measurements are valid because the curvature tolerances were relaxed in the updated ASTM E 399-83 standard. Although the fracture toughness of the Fe-18Cr-3Ni-13Mn-0.37N steel seems low for an austenitic alloy, in fact it meets expectations for steels of its strength level, on the basis of the known inverse trend of K_{Ic} versus σ_y [10].

SUMMARY AND CONCLUSIONS

The strength of Fe-18Cr-3Ni-13Mn-0.37N austenitic stainless steel increases dramatically at low temperatures, owing to high nitrogen content. At 4 K, where σ_y reaches 1540 MPa, linear-elastic fracture occurs in 25-mm-thick fatigue-cracked specimens subject to plane strain conditions. In this paper, valid K_{Ic} data (70.2 and 71.0 MPa·m$^{1/2}$) are reported at 4 K for the as-received steel of 48-μm grain size, and the brittle fracture mechanism involving cleavage-like transgranular facets was examined, using a coarse-grained specimen of the steel prepared for x-ray diffraction. After fracture in liquid helium, the transgranular facets were identified as {111} planes, and on this basis it is suggested that the microfailure mechanism of this steel at 4 K may involve slip-plane decohesion.

REFERENCES

1. A. S. Tetelman and A. J. McEvily, Jr., Fracture of Structural Materials, John Wiley and Sons, New York (1967) 212.

2. D. A. Wigley, Mechanical Properties of Materials at Low Temperatures, Plenum Press, New York (1971) 1-325.

3. S. S. Hecker, D. L. Rohr, and D. F. Stein, Brittle fracture in iridium, Metall. Trans. 9A (1978) 481-487.

4. C. Gandhi and M. F. Ashby, On fracture mechanisms of iridium and criteria for cleavage, Scr. Metall. 13 (1979) 371-379.

5. C. F. Old, Micromechanisms of crack growth in liquid metal environments, Met. Sci. Aug.-Sept. (1980) 433-440.

6. G. R. Caskey, Jr., Fracture of Fe-Cr-Mn austenitic steel, Report DP-MS-78-68, E.I. du Pont de Nemours and Co., Aiken, South Carolina (1978) 21.

7. S. P. Lynch, Cleavage in face-centered cubic metals, Met. Sci. 15 (1981) 463-467.

8. G. G. Garrett and J. F. Knott, Crystallographic fatigue crack growth in aluminum alloys, Acta Metall. 23 (1975) 841-848.

9. K. R. L. Thompson and J. V. Craig, Fatigue crack growth along cleavage planes in an aluminum alloy, Metall. Trans. 1 (1970) 1047-1049.

10. D. T. Read and R. P. Reed, Toughness, fatigue crack growth, and tensile properties of three nitrogen-strengthened stainless steels at cryogenic temperatures, in: The Metal Science of Stainless Steels, E. W. Collings and H. W. King, Eds., Metallurgical Society of the AIME, New York (1979) 92-121.

11. Standard Test Method for Plane-Strain Fracture Toughness of Metallic Materials, ASTM Designation E 399-83, 1984 Annual Book of ASTM Standards, Section 3, Vol. 03.01, American Society Testing and Materials, Philadelphia (1984) 519-554.

12. F. W. Schaller and V. F. Zackay, Low temperature embrittlement of austenitic Fe-Cr-Mn-Ni alloys, Trans. ASM, 51, (1959) 609.

13. C. M. Hsiao and E. J. Dulis, Effect of interstitial carbon plus nitrogen and precipitation reactions on the properties of austenitic Cr-Mn-C-N steels, Trans. ASM, 52 (1960) 855.

14. J. C. Shyne, F. W. Schaller, and V. F. Zackay, The tensile and yield strength of Cr-Mn-N steels at low temperatures, Trans. ASM, 52 (1960) 848.

15. J. D. Defilippi, K. G. Brickner, and E. M. Gilbert, Ductile to brittle transition in austenitic chromium-manganese-nitrogen stainless steel, Trans. Metall. Soc. AIME, 245 (1969) 2141.

16. Standard Terminology Relating to Fracture Testing, ASTM Designation E 616-82, 1984 Annual Book of ASTM Standards, Section 3, Vol. 03.01 American Society for Testing and Materials, Philadelphia (1984) 671-684.

Table 1. Mechanical properties of as-received Fe-18Cr-3Ni-13Mn-0.37N austenitic steel [10].

Temperature (K)	Yield stress (MPa)	Ultimate strength (MPa)	Elongation (%)	Reduction of Area (%)	Rockwell Hardness (R_B)
295	400	796	56	53	93
4	1540	1811	4	26	–

Table 2. Fracture toughness data for as-received Fe-18Cr-3Ni-13Mn-0.37N austenitic steel at 4 K.

Specimen number	Notch type	Specimen thickness, B (mm)	Specimen width, W (mm)	Average crack length, a (mm)	Relative crack length, a/W	Load Ratio, P_{max}/P_Q	Required thickness, $2.5(K_{Ic}/\sigma_y)^2$ (mm)	K_{Ic} (MPa·m$^{1/2}$)
1	chevron	25.400	50.725	25.975	0.512	1.05	5.2	70.2
2	straight-through	25.425	50.600	26.650	0.527	1.01	5.3	71.0

173
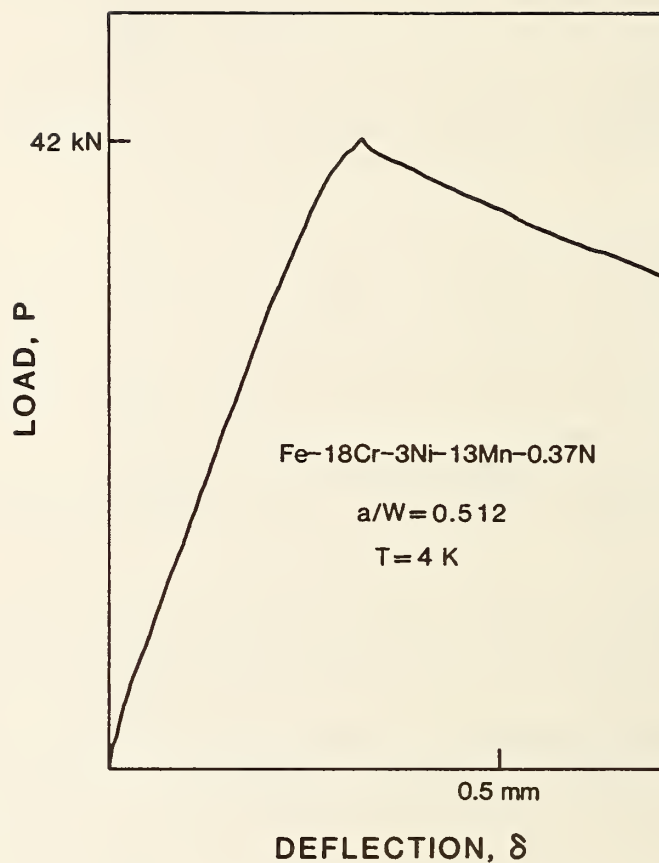
Figure 1. Load-versus-deflection test record at 4 K for chevron-notched
specimen of Fe-18Cr-3Ni-13Mn-0.37N steel in the as-received
condition.
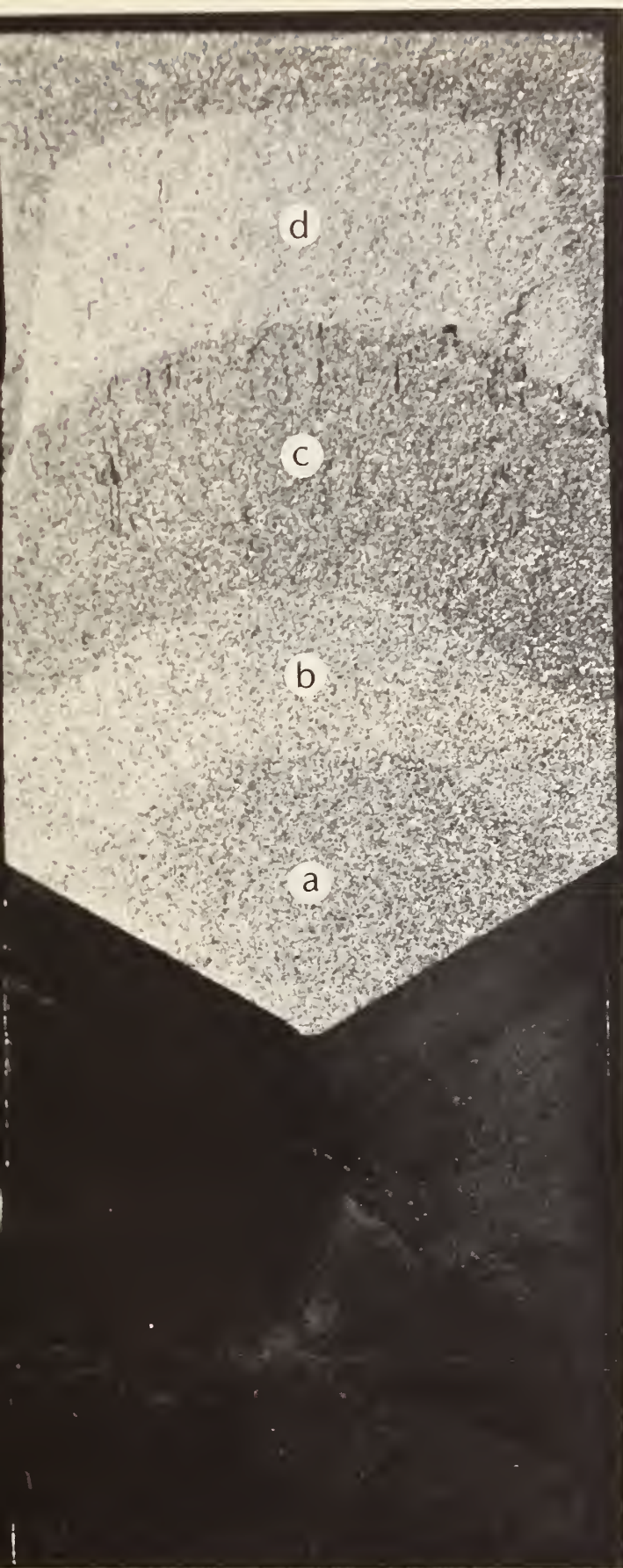
Figure 2. Macroscopic fracture surface
appearance of chevron-notched
Fe-18Cr-3Ni-13Mn-0.37N steel
after testing at 4 K:
a) fatigue zone, T = 76 K,
b) fatigue zone, T = 4 K,
c) overload failure zone,
   T = 4 K, and
d) final fracture after re-
   moval from the cryostat,
   T > 4 K.
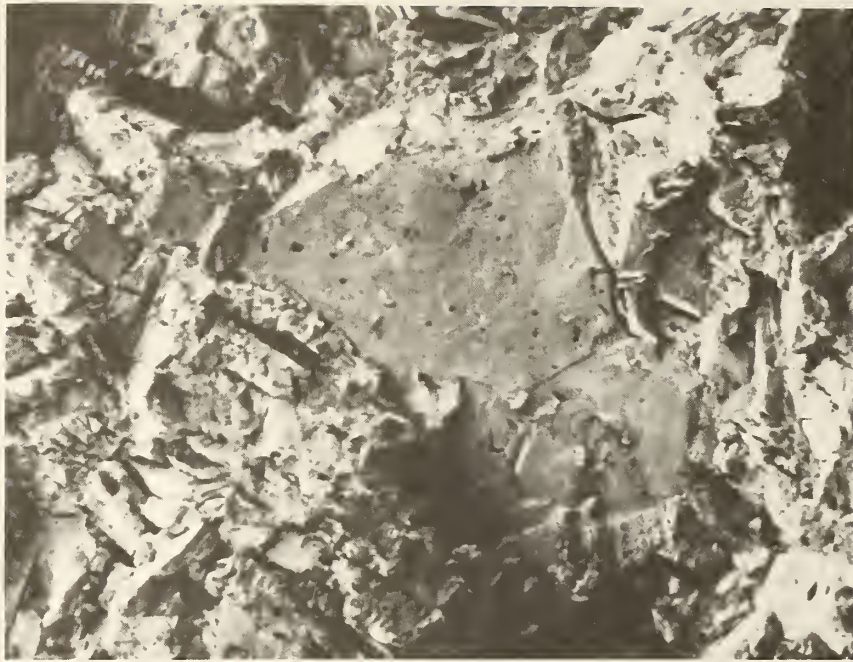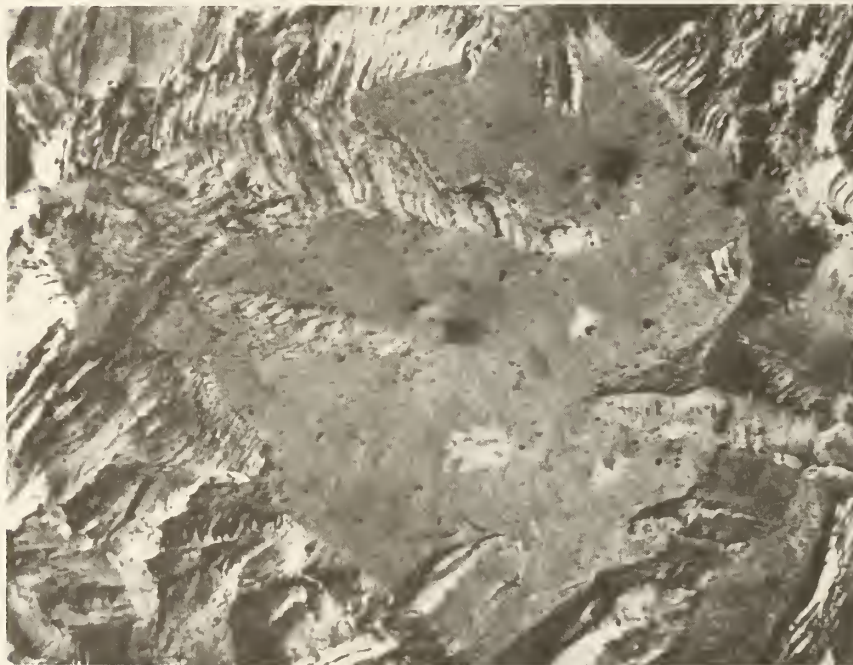
Figure 3. Crystallographic facets on the fatigue failure zone of coarse-grained Fe-18Cr-3Ni-13Mn-0.37N steel fractured at 4 K.

Figure 4. Crystallographic facets on the overload fracture zone of coarse-grained Fe-18Cr-3Ni-13Mn-0.37N steel fractured at 4 K.

177

Figure 5. Microscopic steps and fine slip-line traces
           on a fatigue zone facet (facet a of Fig. 3).
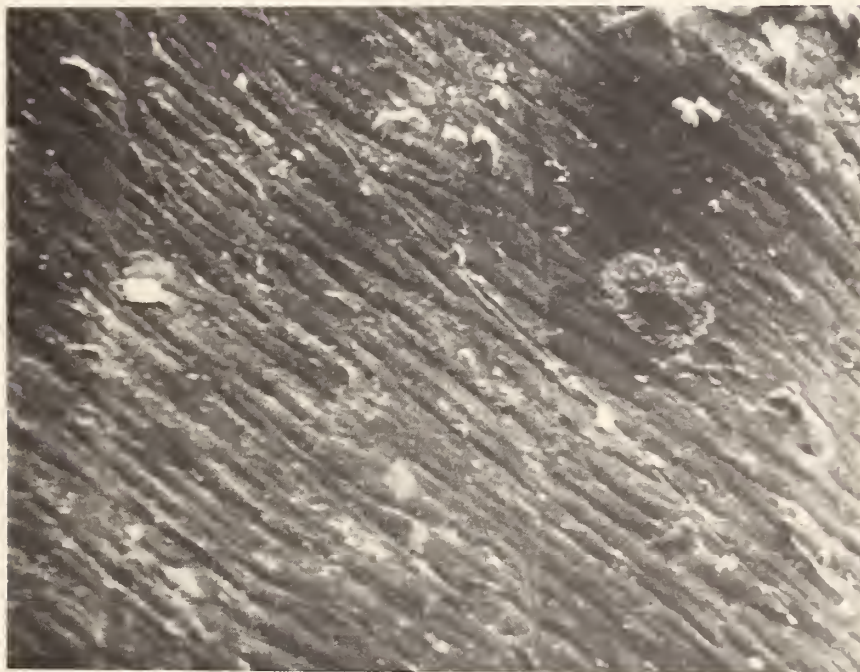
Figure 6. Slip-line traces on an overload zone facet (facet a of Fig. 4).

179

NOTCH TENSILE MEASUREMENTS AND FRACTURE TOUGHNESS
CORRELATIONS FOR AUSTENITIC STAINLESS STEELS*

R. P. Reed, R. L. Tobler, and D. T. Read

Fracture and Deformation Division
National Bureau of Standards
Boulder, Colorado 80303

Thirty-two alloys were included in a study of conventional notch tensile testing as a method of fracture toughness characterization for austenitic stainless steels at liquid helium temperature, 4 K. For the same austenitic stainless steels, tensile and J-integral fracture toughness [$K_{Ic}(J)$] measurements have also been conducted. For these materials the notch tensile strength (σ_{NTS}) generally increases with yield strength (σ_y), and the σ_{NTS}/σ_y ratios are typically much greater than 1.0. Correlations between σ_{NTS}, $K_{Ic}(J)$, and σ_y were assessed. The best data fit was found between the ratio, $\sigma_{NTS}/K_{Ic}(J)$, and the toughness, $K_{Ic}(J)$. Unfortunately, from this relation there is not uniqueness of K_{Ic} from σ_{NTS}. Therefore at this time it is not considered practical to obtain estimates of K_{Ic} from notch tensile tests for austenitic steels at 4 K. However, one may compare the J-integral fracture toughness and cylindrical bar notch tensile measurements. There are three regions: (1) linear elastic [σ_{NTS} increases as $K_{Ic}(J)$ increases]; (2) elastic-plastic [σ_{NTS} is essentially independent of $K_{Ic}(J)$]; (3) plastic [σ_{NTS} decreases as $K_{Ic}(J)$ increases]. The elastic-plastic (transition) region is associated with a plastic zone that extends completely through the notched cross-sectional area.

Key words: austenitic stainless steels; cryogenic properties of materials; fracture toughness; mechanical testing of materials; notch tensile tests.

INTRODUCTION

For austenitic stainless steels used in structural components of superconducting magnets, elastic-plastic fracture toughness evaluations at 4 K are usually required for qualification of base metals and welds. Two acceptable methods of quantitative fracture toughness measurement under elastic-plastic conditions are the J-integral and the crack-tip-opening displacement (CTOD) tests; both require large specimens with fatigue precracking to provide a sharp crack front. The complexity of measurement methodologies and difficulties in interpretation of test data prevent many laboratories from adopting these tests.

Impact tests are less expensive. Unfortunately, they provide only a qualitative measure of toughness and are unsuitable at 4 K because adiabatic heating occurs during straining prior to fracture. Adiabatic temperature rises of up to 150 K have occurred[1-3] and are possible because of the very low specific heat of metals at 4 K and the high strain rate from impact loading.

This paper assesses the use of the notch tensile test to estimate the elastic-plastic fracture toughness of austenitic stainless steels. Notch tensile tests were performed on austenitic steels at low temperatures[4-6] long before quantitative elastic-plastic fracture toughness methods became available. Subsequently, they have been used for direct measurement of the plane-strain fracture toughness of aluminum and steel alloys.[7-11] Specimen machining costs less than compact tensile specimens and the test methodology is simple, requiring no strain gages or displacement measurements.

The ratio of notch tensile strength (σ_{NTS}) to unnotched tensile yield strength (σ_y) is accepted as a qualitative indicator of fracture toughness: ratios greater than 1.0 indicate tough behavior (ability to deform plastically in the presence of stress concentration). A simplified stress concentration factor, K_t, is given by

$$K_t = (d/2r)^{1/2} \tag{1}$$

where d is the width between the notches and r is the notch radius. Typical K_t values used with cylindrical or flat specimens range from 4 to 7 for steels[4] and from 16 to 23 for aluminum alloys.[12]

Kaufman et al.[12] summarized an extensive room temperature notch tensile measurement program on aluminum cylindrical specimens. The alloys (age-hardened 2024, 2124, 7075, 7475) generally exhibited linear-elastic fracture behavior. The plane-strain fracture toughness (K_{Ic}) initially increased with increasing σ_{NTS}. However, at higher toughness levels, K_{Ic} tended to be less dependent on σ_{NTS}. They found that the ratio σ_{NTS}/σ_y was approximately linearly dependent on K_{Ic} at low ratios (~0.85 to 1.25). At higher values (~1.25 to 1.45), the ratio tends toward less dependency on K_{Ic}.

All previous notch tensile tests of alloys exhibiting elastic-plastic fracture behavior, such as austenitic steels at 4 K, have been used for qualitative toughness evaluation, and until now there appears to have been no attempt to correlate notch tensile measurements with K_{Ic} measurements. In this study, thirty-two austenitic stainless steels were tested at 4 K, and the relationships between σ_{NTS}, σ_y, and K_{Ic} were determined from the previously published 4-K tensile and J-integral fracture toughness data for these alloys.

EXPERIMENTAL PROCEDURES

The compositions and metallurgical variables for the alloys tested are given in other papers (see Table 1). These alloys include laboratory heats as well as mill heats. All alloys were completely austenitic (prior to

testing) and were tested in the annealed condition. The materials were supplied in the form of 25-mm-thick plates, except for the N-60 and AISI 216 steels, which were in the form of 76- and 92-mm-diameter bars, respectively.

The tensile, notch tensile, and compact-tension (fracture-toughness) specimen geometries are shown in Fig. 1. The tensile and notch tensile specimen axes were oriented transverse to the longitudinal bar or plate directions. The compact specimens were oriented with the notch plane normal to the transverse (plate) or radial (bar) directions, and crack propagation was along the longitudinal plate or bar directions. Thus, for each specimen type the fracture plane was similarly oriented with respect to microstructure.

Notch tensile tests were conducted at 4 K using a crosshead rate of 8.3×10^{-4} mm/s on two specimens per alloy. A 0.127-mm notch-tip radius was specified for each specimen. Notch radii, measured after grinding were varied from 0.125 to 0.135 mm. The stress concentration factor, K_t, from Eq. 1 is 4.3 to 4.5. During testing, plots of load versus time were recorded, and σ_{NTS} was calculated from the maximum load divided by the original notched cross-sectional area.

The tensile properties used in this paper for analysis were previously measured at a plastic strain rate of approximately 1.5×10^{-5}. At 4 K the yield and ultimate strength inaccuracies are about ± 2%, strain measurement inaccuracies are about ± 3%, and estimates of material variability for yield and ultimate strengths are about ± 5%. Notch tensile strength measurements reflect inaccuracies and material variabilities similar to those for the tensile strength measurements.

In most cases, the 4-K fracture-toughness data referred to in this paper represent K_{Ic} estimates based on J-integral tests. For several high-strength steels (N-50, 18/18, N-40, N-60, and AISI 216), the data represent direct measurements of K_{Ic}. The fracture test procedures are discussed extensively in references 18 and 20.

Specimen strain was initially monitored by using load-time chart traces and converting to crosshead travel, remembering to correct for load-train deflection. This procedure is thought to be sufficiently accurate except when load drops occur during plastic deformation at the notch tip prior to fracture. Most of the austenitic steels were tough enough for load drops to occur. Estimation of notch strain during such load drops was not possible. Therefore, a strain-gage extensometer was recently adapted to fit the notch tensile specimen and used to measure notch strain to fracture for alloys N-40, N-60, and 210.

RESULTS

The notch-tensile data for each austenitic stainless steel are listed in Table 1. Also given are tensile yield strength (σ_y), ultimate tensile strength (σ_u), fracture toughness, and the notched-to-unnotched tensile strength ratio. In most cases the data represent averages of at least two measurements taken at 4 K.

183

All the steels tested in this study have a σ_{NTS}/σ_y ratio ranging from 1.07 to 4.15, with most values well above 1.0. Therefore, all the annealed austenitic stainless steels are relatively tough by the conventional notch tensile test criterion.

Usually as the tensile yield strength of austenitic stainless steels increases, their notch tensile strength (σ_{NTS}) also increases, as shown in Fig. 2. This contrasts with the accepted inverse relation between $K_{Ic}(J)$ and σ_y, shown in Fig. 3 for the austenitic steels included in this study. In Fig. 2 there are some glaring exceptions to the $\sigma_{NTS}-\sigma_y$ dependence: In particular, the strong 18/18 alloy has a yield strength of 1780 MPa, and the very tough 413 alloy has a notch tensile strength of 2920 MPa.

The correlation between the notch tensile strength and the J-integral fracture toughness at 4 K is not obvious (see Fig. 4). The 413 and 416 alloys, both of which have very high values of σ_{NTS}, fall outside any trends, however.

We found excellent correlation between the log of the ratio $\sigma_{NTS}/K_{Ic}(J)$ and $K_{Ic}(J)$ (see Fig. 5). Here again, the alloys 413 and 416 deviate from the other alloys, but their deviation is much more modest than that shown in Fig. 4. The best fit equation of data in Fig. 5 is

$$\sigma_{NTS} = 44K_{Ic}(J) \exp{-6.54 \times 10^{-3}K_{Ic}(J)} \qquad (2)$$

where σ_{NTS} has units of MPa and $K_{Ic}(J)$ has units of MPa$\sqrt{m}$. Equation 2, also plotted in Fig. 4, adequately depicts most of the data. Unfortunately, $K_{Ic}(J)$ is not unique for given σ_{NTS} values.

The ratio σ_{NTS}/σ_y is directly proportional to $K_{Ic}(J)$, as shown in Fig. 6. Here Eq. 2 is also included and adequately represents the data. Since all these steels, including the high-strength alloys, have σ_{NTS}/σ_y ratios greater than 1.0, they are all classified as ductile and tough in the macroscopic sense. On the microscopic scale, however, some of the alloys showed significant portions of brittleness. The brittle micromechanisms include slip-band decohesion, twin boundary parting, and intergranular failure, all of which produce smooth reflective facets on the fracture surfaces of the tensile, notch tensile, and fracture toughness test specimens at 4 K. The proportion of ductile and brittle mechanisms varies with metallurgical factors, such as composition and strength.

DISCUSSION

Because multiple values of fracture toughness correspond to single notch tensile strength values (Fig. 4) and because the ratio of notch tensile strength to tensile yield strength is rather insensitive to the value of fracture toughness (Fig. 6), measurement of the notch tensile strength does not provide quantitative fracture toughness information.

The results plotted in Figs. 2-6 are interpreted further: From Fig. 4 it is evident that, under linear elastic fracture mechanics conditions, there is an approximate correlation between σ_{NTS} and $K_{Ic}(J)$ following Eq. 2, when $K_{Ic}(J) \leq 100$ MPa√m. This same trend of direct proportionality between K_{Ic} and σ_{NTS} was demonstrated by linear elastic notch tensile measurements of aluminum alloys by Kaufman et al.[12] At high toughness levels [$K_{Ic}(J) \geq 200$ MPa√m, corresponding to lower yield-strength steels], σ_{NTS} decreases with increasing $K_{Ic}(J)$. The lower yield strength alloys are ductile, and under the notch tensile loading conditions of our specimens, they experienced significant plastic deformation prior to fracture. In the intermediate toughness range of austenitic stainless steels at 4 K [100 MPa√m $\leq K_{Ic}(J)$ ≤ 200 MPa√m], σ_{NTS} is approximately independent of $K_{Ic}(J)$, and there is transition from linear elastic to fully plastic fracture behavior. The tendency toward transition and independence of σ_{NTS} on K_{Ic} was also demonstrated by Kaufman et al.[12] for aluminum alloys at room temperature. Ductile alloys were not included in their study; therefore, they did not detect the entire transition range.

One can approximate the transition by considering the plastic zone size (r_p) under plane strain conditions:[21]

$$r_p = (1/3\pi) (K/\sigma_y)^2 \qquad\qquad (3)$$

where K is the stress intensity factor and r_p is the distance ahead of the crack tip to the edge of the plastic zone. To achieve a plastic zone throughout the cross section, $2r_p$ must be at least equivalent to the diameter of the notched specimen (5.1 mm). Then

$$K/\sigma_y = [(5.1 \text{ mm}/2)(3\pi)]^{1/2} \qquad\qquad (4)$$

Assuming that such conditions are reached when the stress intensity factor reaches $K_{Ic}(J)$, then from Eq. 4:

$$\sigma_y \cong 7K_{Ic}(J) \qquad \text{(metric units)} \qquad\qquad (5)$$

These assumptions may be checked by referral to Figs. 2 through 4. When $K_{Ic}(J)$ is 150 MPa√m, σ_{NTS} is 2430 MPa at the approximate midpoint of the transition from linear elastic to fully plastic behavior (Fig. 4). A yield strength of about 1150 MPa corresponds to these associated $K_{Ic}(J)$ and σ_{NTS} values (Figs. 2 and 3). Or, $\sigma_y = 7.7$ $K_{Ic}(J)$, close to the prediction of Eq. 5. The modest disparity of the ratios implies that plane strain conditions do not quite exist with this specimen configuration: use of plane stress conditions [$r_p = 1/\pi(K/\sigma_y)^2$] would considerably underestimate the ratio σ_y/K_{Ic}.

In cylindrical notch tensile specimens with $K_t = 4.5$, the transition from linear elastic to fully plastic behavior seems to occur when the plastic zone extends throughout the specimen cross section under the notch. Under fully plastic conditions, the notch tensile strength is associated exclusively with material strength, and hence, there is strong correlation with yield strength. To extend the range of one-to-one correlation of σ_{NTS} with K_{Ic} or $K_{Ic}(J)$, the

stress concentration factor at the notch tip must be increased, but decreasing the notch radius requires costly machining or grinding. Increasing specimen diameter precludes the use of the test for plate thicknesses of 12 mm or less and also increases the required cryostat load capacity above that which is normally available.

A possible improvement over the conventional notch tensile test is another technique, which uses an instrumented notch tensile specimen to obtain crack opening displacement (COD) data. COD measurements for notched specimens might be converted to J-integral data for correlation with conventional J-integral fracture toughness measurements. Accordingly, we analyzed the chart recordings of load versus time to estimate the displacement of each notch tensile test. Unfortunately, the correlation between estimated and measured extension was poor, primarily because of the numerous load drops that occur during the tests at 4 K. We are now measuring the notch opening displacement directly with clamp-on strain-gage extensometers, and further analysis of notch tensile COD measurements awaits new data from this approach.

CONCLUSIONS

At present there is no advantage in using notch tensile measurements of austenitic stainless steels to obtain quantitative fracture toughness information.

J-integral fracture toughness, compact-tension specimens, and cylindrical-bar notch tensile measurements have been compared. The notch-tensile-versus-fracture toughness correlation shows three regions:

1. Linear elastic, where σ_{NTS} increases as $K_{Ic}(J)$ increases

2. Elastic-plastic, where σ_{NTS} is essentially independent of $K_{Ic}(J)$

3. Plastic, where σ_{NTS} is directly related to σ_y and inversely related to $K_{Ic}(J)$ [since $K_{Ic}(J)$ is inversely related to σ_y]

The transition region (elastic-plastic) is associated with a plastic zone that extends completely through the notched cross-sectional area.

ACKNOWLEDGMENTS

REFERENCES

1. W. G. Dobson and D. L. Johnson, in: "Advances in Cryogenic Engineering--
   Materials," vol. 30, A. F. Clark and R. P. Reed, eds. Plenum Press,
   New York (1984), pp. 185-192.
2. D. T. Read and R. P. Reed, in: "Advances in Cryogenic Engineering--
   Materials," vol. 26, Plenum Press, New York (1980), pp. 91-101.
3. K. Ishikawa, K. Hiraga, T. Ogata, and K. Nagai, Cryog. Eng. (Tokyo)
   18(1):2-9(1983).
4. C. J. Guntner and R. P. Reed, Trans. Am. Soc. Met. 55:399-419
   (1962).
5. A. Randak, W. Wessling, H. E. Bock, H. Steinmaurer, and L. Faust,
   Stahl Eisen, 91:1255-1269 (1971).
6. A. Hurlich and W. G. Scheck, in: "Advances in the Technology of
   Stainless Steels and Related Alloys," ASTM STP No. 369, American
   Society for Testing and Materials, Philadelphia (1963), pp. 127-143.
7. G. R. Irwin, Report 4763, Naval Research Laboratories, Washington,
   D.C. (1956).
8. J. G. Kaufman and E. W. Johnson, in: "Advances in Cryogenic Engineering,"
   vol. 6, Plenum Press, New York (1960), pp. 637-649.
9. C. M. Carmen, D. F. Armiento, and H. Markus, J. Basic Eng. 87:904-916
   (1965).
10. R. P. Wei and F. J. Lauta, Mater. Res. Stand. 5:305-310 (1965).
11. W. F. Brown, Jr. and J. E. Srawley, "Plane Strain Crack Toughness
    Testing of High Strength Metallic Materials," ASTM STP 410,
    American Society for Testing and Materials, Philadelphia (1966).
12. J. G. Kaufman, G.-T. Sha, R. F. Kohm, and R. J. Bucci, in: "Cracks and
    Fatigue," ASTM STP 601, American Society for Testing and Materi-
    als, Philadelphia (1976), pp. 169-190.
13. P. T. Purtscher and R. P. Reed, in: "Materials Studies for Magnetic
    Fusion Energy Applications at Low Temperatures - VIII," R. P. Reed,
    ed., NBSIR 85-3025, National Bureau of Standards, Boulder, Colorado
    (1985), pp. 123-144.
14. R. L. Tobler, D. T. Read, and R. P. Reed, "Fracture Mechanics:
    Thirteenth Conference," ASTM STP 743, R. Roberts, ed., American
    Society for Testing and Materials, Philadelphia (1981), pp.
    250-268.
15. R. L. Tobler and R. P. Reed, in: "Advances in Cryogenic Engineering--
    Materials," vol. 28, R. P. Reed and A. F. Clark, eds; Plenum
    Press, New York (1982), pp. 83-92.
16. D. T. Read and R. P. Reed, Cryogenics 21:415-417 (1981).
17. D. T. Read and R. P. Reed, in: "The Metal Science of Stainless Steels,"
    E. W. Collings and H. W. King, eds.; Metallurgical Society of the
    AIME, New York (1979), pp. 92-121.
18. R. L. Tobler, "Elastic-Plastic Fracture, Second Symposium; Fracture
    Resistance Curves and Engineering Applications," vol. II, ASTM STP
    803, C. F. Shih and J. P. Gudas, eds., American Society for
    Testing and Materials, Philadelphia (1983), pp. II-763-II-776.

19. R. L. Tobler, R. P. Reed, and P. T. Purtscher, in: "Materials Studies for Magnetic Fusion Energy Applications at Low Temperatures--VIII," R. P. Reed, ed., NBSIR 85-3025 National Bureau of Standards, Boulder, Colorado (1985), pp. 151-165.

20. D. T. Read and R. L. Tobler, in: "Advances in Cryogenic Engineering--Materials," vol. 28, R. P. Reed and A. F. Clark, eds.; Plenum Press, New York (1982), pp. 17-28.

21. J. W. Hutchinson, Trans. ASME 50:1042-1051 (1983).

Table 1. Mechanical Properties of Austenitic Stainless Steels at 4 K.

Specimen Number	σ_{NTS} (MPa)	σ_u (MPa)	σ_y (MPa)	σ_{NTS}/σ_y	$K_{Ic}(J)$ (MPa$\sqrt{m}$)	Reference for Material Characterization
739	1910	1480	460	4.2	273	13
740	2190	1370	720	3.0	244	13
741	2340	1420	870	2.7	254	13
414	2538	1652	950	2.7	143	13
520	1377	1220	960	1.4	87	13
413	2920	1580	1020	2.9	204	13
415	2040	1390	1040	2.0	75	13
416	2690	1630	1160	2.3	238	13
2	1700	1550	440	3.9	--	14
3	1870	1530	530	3.5	337	14
4	2030	1570	740	2.7	266	14
5	2120	1700	880	2.4	230	14
6	2230	1630	900	2.5	235	14
7	2460	1640	1190	2.1	124	14
8	2480	1740	1180	2.1	137	14
9	2390	1700	1290	1.9	124	14
70	2060	1620	660	3.1	192	15
71	2030	1580	720	2.8	215	15
72	2180	1510	760	2.9	243	15
73	2170	1810	880	2.5	117	15
74	2300	1520	960	2.4	121	15
75	2340	1670	990	2.4	149	15
76	2340	1580	1050	2.2	162	15
77	2250	1650	860	2.6	206	15
78	2400	1570	900	2.7	205	15
304L	1880	1680	610	3.1	310	16
304LN	2080	1660	790	2.6	214	16
316	1880	1300	710	2.6	268	16
N-50	2330	1890	1450	1.6	106[a]	17
310	1880	1260	640	2.9	285	18
18/18	1910	2050	1780	1.1	75[a]	19
N-40	2520	1660	1200	2.1	136[a]	19
N-60	1540	1350	990	1.6	91[a]	19
216	2280	1820	1400	1.6	107[a]	19

[a] Data for these steels represent direct K_{Ic} measurements; all other data represent estimates of K_{Ic} from J-integral tests.

63.5 mm
(2.50 in)

26.7 mm
(1.05 in)

61.0 mm
(2.40 in)

Compact Tension

12.7 mm
(0.50 in)

6.30 mm
(0.247 in)

38.1 mm
(1.50 in)

71.4 mm
(2.81 in)

Tensile

76 mm
(3.0 in)

0.130 mm
(0.005 in) R

25 mm
(1.0 in)

12.7 mm (0.50 in)

5.1 mm (0.20 in)

30°
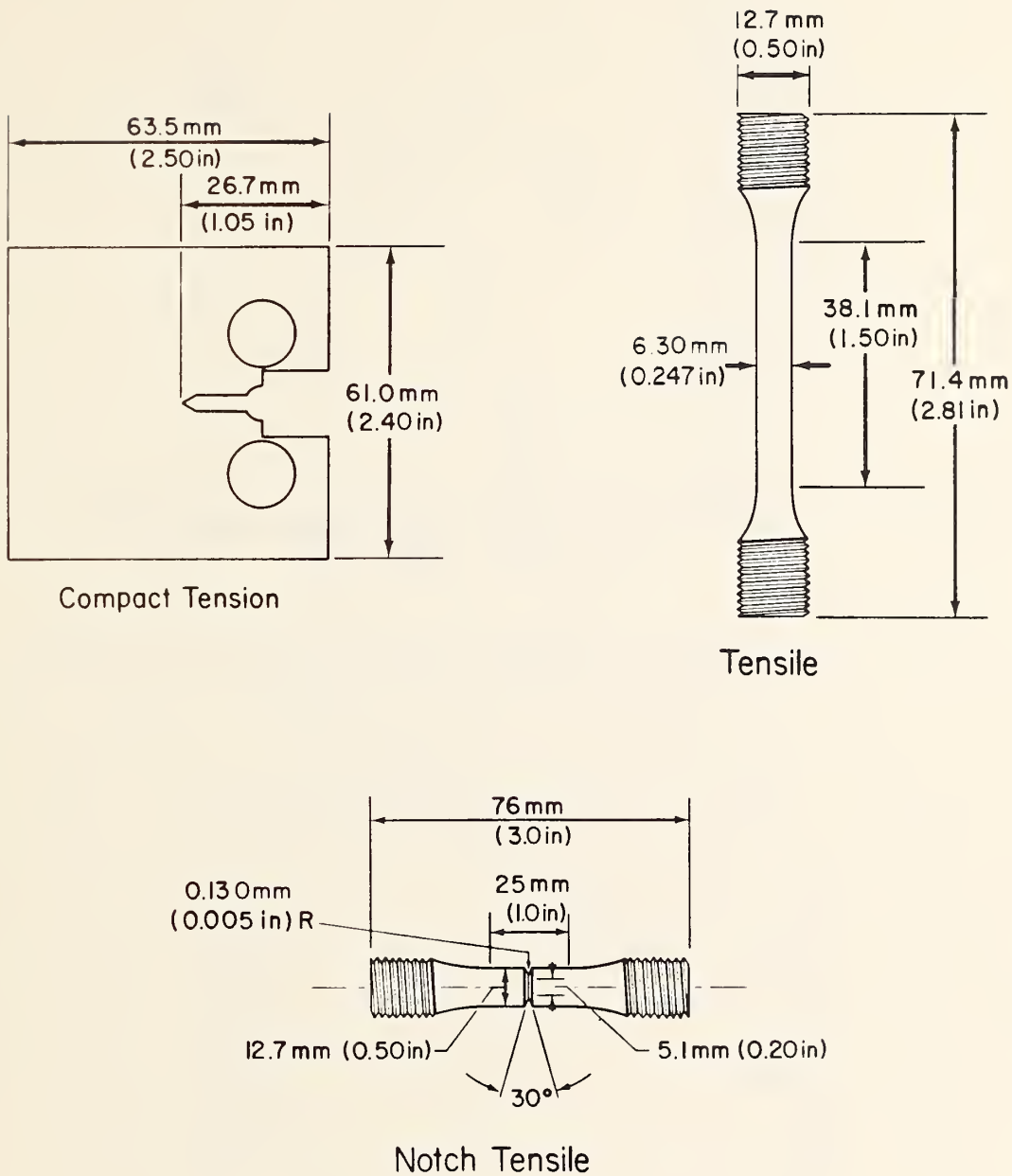
Notch Tensile

Fig. 1.   Tensile, notch tensile, and compact-tension specimens
used in mechanical property measurements.

189
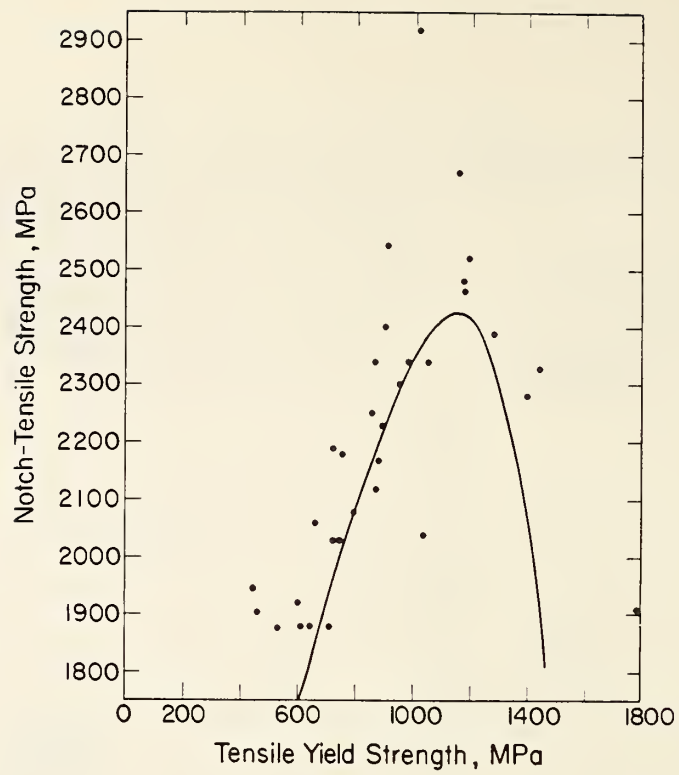
Fig. 2. Notch tensile strength versus tensile yield strength
of annealed austenitic stainless steels at 4 K.
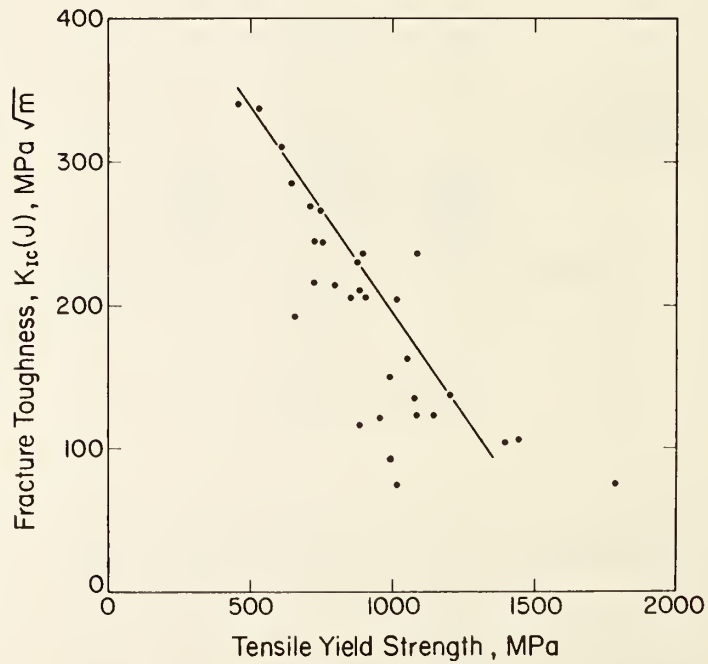
Fig. 3. Tensile yield strength versus fracture toughness of austenitic
stainless steels at 4 K. Solid line is the trend line reported
earlier for austenitic stainless steels at 4 K.[7-11]
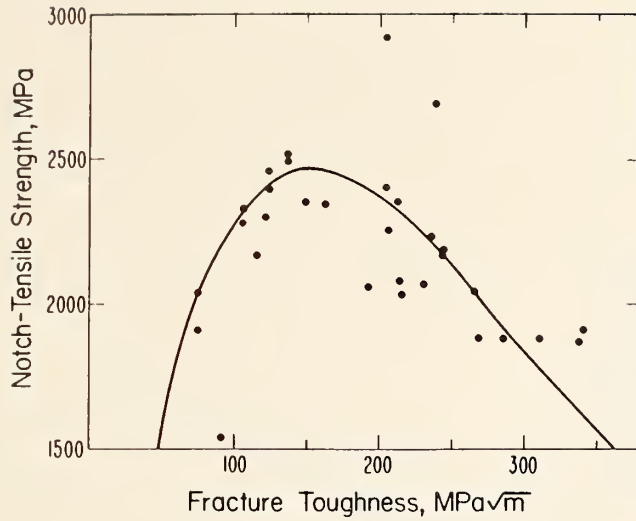
Fig. 4. Notch tensile strength versus fracture toughness of austenitic stainless steels at 4 K. Solid line is Eq. 2.
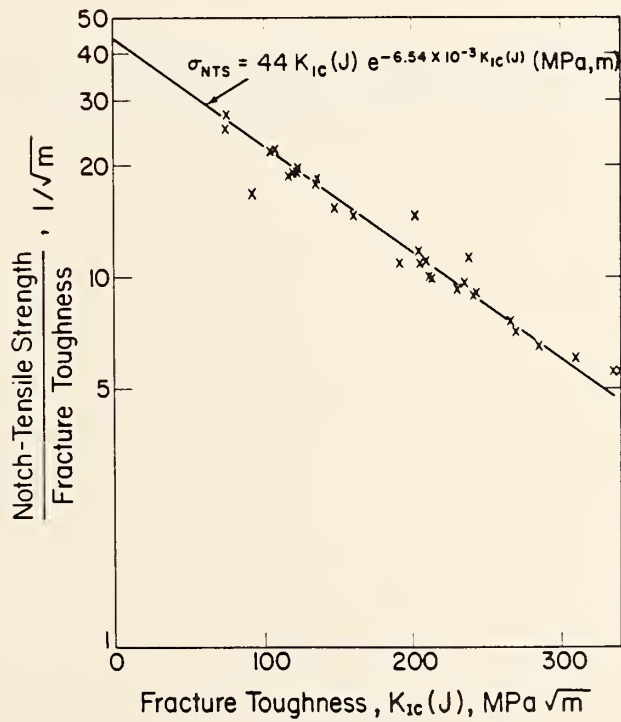
Fig. 5. Ratio of notch tensile strength to fracture toughness plotted against fracture toughness of austenitic stainless steels at 4 K.

191
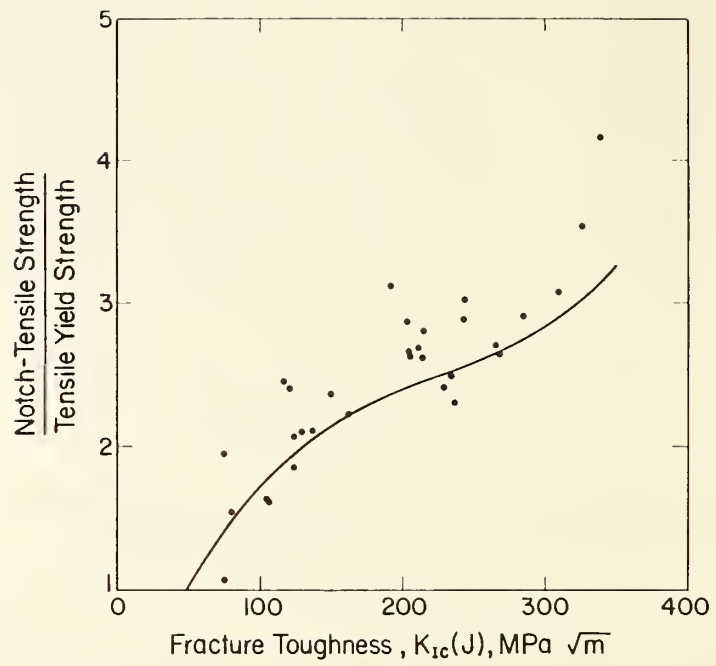
Fig. 6. Ratio of notch tensile strength to tensile yield strength versus fracture toughness of austenitic stainless steels at 4 K.

Elastic constants and instability in face-centered-cubic metals

H. M. Ledbetter
Fracture and Deformation Division, National Bureau of Standards,
Boulder, Colorado 80303, USA

For face-centered-cubic crystals, the single-crystal elastic constants, the C_{ij}'s, reveal not only the well-known tendencies toward mechanical instability, but also another instability, which we call "chemical". Besides considering the fcc elements, we consider also Fe-Ni alloys and Fe-Cr-Ni stainless steels. We suggest an interatomic-force-constant explanation of this instability.

Crystal-structure instability interests both theorists concerned with solid-state cohesion and materials engineers concerned with practical applications of materials. On one hand, we seek to avoid instability. For example, the well-known low-temperature structural transformation in austenitic stainless steels produces a second phase that deteriorates the matrix properties. On another hand, the martensitic transformation in ferritic steels produces desirable high-strength properties. Also, a leading superconductivity specialist remarked recently that to produce higher-T_c materials he would "look for systems that should exist, but won't – unless one can persuade them." In other words, make unstable materials metastable. The better we understand relationships between physical properties and instabilities, the higher our proficiency to control their occurrence, harmful or helpful.

For face-centered-cubic (fcc) metals this note describes a correlation between single-crystal elastic constants and lattice instability, the tendency to transform to either another crystal structure or to another state of order. This is not the well-known mechanical instability discussed by Born and Huang [1], but a "chemical" instability that manifests itself in the elastic constants. By chemical, we mean related to basic interatomic forces. Recently, Nakanishi [2] reviewed thoroughly the elastic-constant/lattice-instability relationships, especially for martensitic phase transformations.

In 1976, Ledbetter and Moment [3] published Fig. 1, a diagram used to describe the unusual elastic behavior of fcc Pu. This figure contains considerable information. For the usual three independent cubic-symmetry Voigt elastic stiffnesses--C_{11}, C_{12}, C_{44}--it plots two dimensionless ratios: $y = C_{12}/C_{11}$ and $x = C_{44}/C_{11}$. The Cauchy relationship, $C_{12}=C_{44}$, is a straight line from (0,0) to (1,1). The point (0.5, 0.5) identifies the prediction of an fcc nearest-neighbor-only central-force model. Most fcc elements occur in

the upper half of the diagram and mostly in the left half. The boundaries x=0 and y=1 correspond to mechanical-stability conditions: $C_{44}>0$ and $(C_{11}-C_{12})>0$. The third mechanical-stability condition, $(C_{11}+2C_{12})>0$, or y>-0.5, does not appear in the diagram; but this is of no consequence because no fcc elements exhibit negative C_{12} values. Straight negative-slope lines emanating from (0,1) correspond to various values of Zener's anisotropy ratio

$$A = 2C_{44}/(C_{11}-C_{12}) \tag{1}$$

All points in the diagram's field correspond to mechanically stable crystal structures.

That Th and Pu occur to the right of x=0.5 provides a crucial basis for this note. All elements to the left of x=0.5 are stable; they exhibit a single crystal structure between T=0 and the melting point. Both Th and Pu are unstable. At high temperatures, Th transforms to a body-centered-cubic crystal structure. Plutonium is notoriously unstable. Between ambient and melting temperatures it exhibits six allotropes: α (monoclinic), β (monoclinic), γ (orthorhombic), δ (fcc), δ' (tetragonal), ε (bcc). (One can conjecture that lower temperatures may reveal further allotropes, perhaps triclinic.) Thus, despite high values of x, representing high elastic rigidity with respect to (100)[001]-type deformation, both Th and, especially, Pu are unstable. It may be significant that elements on the diagram's left tend to be dominated by s-p electrons in their cohesive properties. In Th and Pu the d and f electrons enter strongly into cohesion.

The tendency of Th and Pu toward chemical instability, despite their mechanical stability, encourages one to examine other systems with high x, especially alloys.

Figure 2 shows the variation of x with Ni content for Fe-Ni alloys.

Points for pure fcc iron were determined either by extrapolations or by theory. We see that x is maximum near 30 percent Ni and reaches a relatively high value, 0.8. Of course, this composition region is well known for its instability and the incipient fcc-bcc transformation [4]. That x decreases before the structural transformation occurs suggests a possible magnetic transition that stabilizes the fcc structure for a while. Magnetic-property measurements between 25 and 35 percent Ni would be very useful in understanding this unusual pretransformation behavior.

Figure 3 shows a y-x diagram for austenitic (fcc) stainless steels, which consist mainly of Fe, Cr, Ni, and Mn. These alloys are well known for their instability. At low temperatures they undergo magnetic [5] and/or structural (to bcc) [6] transformations. Plastic deformation of these alloys induces transformations to either bcc or cph (close-packed-hexagonal) structures [7]. This diagram includes points for fcc Fe, Co, and Ni. Iron's allotropy is well known: bcc at low and high temperatures, fcc between [8]. Cobalt, fcc at high temperatures transforms to cph at 603 K. Elastic constants of hypothetical fcc Mn and hypothetical fcc Cr remain, apparently, unestimated. (Recently, Moruzzi et al. [9] estimated the bulk modulus of fcc Mn to be 2.91 GPa, 95 percent of that for bcc Fe. The bulk modulus equals $(C_{11} + 2C_{12})/3$. Thus, unless the C_{44} of fcc Mn behaves abnormally, its elastic constants may resemble Fe's.)

A possible explanation of these instabilities lies in the force constants, which relate more directly to forces between pairs of atoms in solids. Many force-constant models exist [10]. For fcc lattices, Leibfried and Breuer [11] consider a three-force-constant model summarized in Fig. 4. The three parameters consist of a longitudinal spring, f_1, and two different transverse springs, f_2 and f_3, corresponding to bending along [001] and [110], respectively. The

coupling matrix for this model is

$$-\phi_{ij} \overset{[\overset{d}{\wedge}]}{} = \begin{bmatrix} \alpha & \beta & 0 \\ \beta & \alpha & 0 \\ 0 & 0 & \gamma \end{bmatrix} \tag{2}$$

Physically, negative $\phi_{ij}^{[\overset{d}{\wedge}]}$ denotes the force in the i direction on the atom at the origin when the atom at $\overset{d}{\wedge}$ is displaced a unit length in direction j. If the displacement vector corresponds to an eigenvector, then $-\phi_{i\ell}^{[\overset{d}{\wedge}]}$ corresponds to a spring constant. By symmetry $\phi_{11}^{[110]} = \phi_{22}^{[110]}$ and $\phi_{12}^{[110]} = \phi_{21}^{[110]} = \phi_{23}^{[110]} = \phi_{32}^{[110]}$. Components such as $\phi_{13}^{[110]}$ vanish because force and displacement are perpendicular, thus no coupling. Diagonalization of ϕ_{ij} gives three eigenvalues:

$$f_1 = \alpha + \beta \tag{3}$$

$$f_2 = \gamma \tag{4}$$

$$f_3 = \alpha - \beta \tag{5}$$

Leibfried and Breuer relate the f's to the six eigenvalues of the 6x6 Voigt C_{ij} matrix:

$$f_1 = \frac{a}{24}(4\overset{1}{C} + 2\overset{2}{C} + 3\overset{4}{C}) \tag{6}$$

$$f_2 = \frac{a}{12}(-\overset{1}{C} - 2\overset{2}{C} + 3\overset{4}{C}) \tag{7}$$

$$f_3 = \frac{a}{8}(2\overset{2}{C} - \overset{4}{C}) \tag{8}$$

where a denotes cubic unit-cell size.

From the cubic-symmetry invariants,

$$\overset{1}{C} = C_{11} + 2C_{12} \tag{9}$$

$$\overset{2}{C} = \overset{3}{C} = C_{11} - C_{12} \tag{10}$$

$$\overset{4}{C} = \overset{5}{C} = \overset{6}{C} = 2C_{44} \tag{11}$$

the f's relate to the Voigt C_{ij}'s:

$$f_1 = \frac{a}{4} (C_{11} + C_{12} + C_{44}) \tag{12}$$

$$f_2 = \frac{a}{4} (-C_{11} + 2C_{44}) \tag{13}$$

$$f_3 = \frac{a}{4} (C_{11} - C_{12} - C_{44}) \tag{14}$$

and vice versa:

$$C_{11} = \frac{1}{a} (2f_1 + 2f_3) \tag{15}$$

$$C_{12} = \frac{1}{a} (f_1 - 2f_2 - 3f_3) \tag{16}$$

$$C_{44} = \frac{1}{a} (f_1 + 2f_2 + f_3) \tag{17}$$

More-interesting physical C_{ij} combinations are:

$$(C_{11} - C_{12}) = \frac{1}{a} (f_1 + 2f_2 + 5f_3) \tag{17}$$

$$3B = (C_{11} + 2C_{12}) = \frac{1}{a} (4f_1 - 4f_2 - 4f_3) \tag{18}$$

$$(C_{12} - C_{44}) = \frac{1}{a} (-4f_2 - 4f_3) \tag{19}$$

$$A = 2C_{44}/(C_{11} - C_{12}) = (2f_1 + 4f_2 + 2f_3)/(f_1 + 2f_2 + 5f_3) \tag{20}$$

$$(C_{11} - C_{12} - 2C_{44}) = \frac{1}{a} (-f_1 - 2f_2 + 3f_3) \tag{21}$$

$C_{11} - C_{12}$ is the resistance to shear on a [110]-type plane in a [$\bar{1}$10]-type direction. Since this deformation involves both bond stretching (and shortening) and bond bending, not surprisingly it includes f_1, f_2, and f_3. $C_{11} + 2C_{12}$ is three times the bulk modulus (reciprocal compressibility). Since uniform dilatation changes bond lengths but not bond angles, it may seem surprising that the bulk modulus B depends on f_2 and f_3 in addition to f_1. This occurs because the spring constants f_2 and f_3 relate also to many-body forces. (Recall that the third-order perturbation-theory calculation of Axilrod and Teller [12] for interactions between triplets of atoms contained three inter-atomic distances--r_{12}, r_{23}, r_{13}--and three included angles-- γ_1, γ_2, γ_3--with γ_1 being the angle between r_{12} and r_{13}.) $C_{12} - C_{44}$ is the Cauchy (noncentral-

force) discrepancy for cubic crystals. Thus, if accidently $f_2 = -f_3$, then the material will appear to have central forces by the familiar Cauchy criterion $C_{12} = C_{44}$. Thus, this criterion is necessary but not sufficient. The Zener anisotropy ratio, A, depends on all three force constants. For vanishing many-body forces ($f_2 = f_3 = 0$), A = 2. Thus, departures of A from this value also indicate the contribution of many-body forces. In summary, vanishing many-body forces imply that $C_{11} = 2C_{12} = 2C_{44} = 4C'$, where $C' = \frac{1}{2}(C_{11} - C_{12})$. Finally, elastic isotropy demands that $C' = C_{44}$ or that $C_{11} - C_{12} - 2C_{44} = 0$. In terms of force constants, isotropy demands that $f_1 = 3f_3 - 2f_2$, a condition that arises only accidently.

Table 1 contains single-crystal elastic constants and force constants for fcc elements and selected alloys. Except for Th and Pu, all fcc elements exhibit a negative f_2. Both Fe-Ni and Fe-Cr-Ni stainless steels also exhibit a negative f_2.

Consider now a typical metal--copper, where $C_{11}=1.696$, $C_{12}=1.224$, and $C_{44}=0.754 \cdot 10^{11} \text{N/m}^2$. Thus, $f_1/a=0.9185$, $f_2/a=-0.0470$, and $f_3/a=-0.0705$ in the same units. Table 2 shows how the three force constants contribute to various elastic constants and to the elastic anisotropy, A. For both A and C_{12}/C_{11}, we made the very rough approximation that both f_2 and f_3 are small compared with f_1. Except for the Cauchy discrepancy, $C_{12}-C_{44}$, f_1 dominates every elastic constant. As expected, many-body effects show most strongly in $C_{12}-C_{44}$, but also strongly in C', A, and C_{12}/C_{11}. The bulk modulus is least sensitive to many-body terms. In all cases except C_{44}, the f_2 force constant contributes less than the f_3 force constant; bending out of the (100) plane contributes less than bending in the plane. Negative f_2 and f_3 values apparently imply instabilities with respect to bending. But one must remember

that the bending springs represent many-body, not two-body, interactions. Thus, they do not represent simple local effects but, rather, complicated "environmental", long-range effects. Even if all springs are longitudinal and positive, a negative transverse spring can arise quite naturally. Table 2 contains results also for stainless steel. We call this instability "chemical" for two reasons. First, we want to distinguish it from the usual Born-Huang mechanical instability. This does not preclude an eventual mechanical explanation: volume effects, phonon instabilities, higher-order elastic constants, et cetera. Second, we feel the eventual explanation must relate closely to the molecular orbitals, an approach used mainly by chemists [13] but adopted recently by some physicists [14]. Examination of existing single-crystal elastic constants reveals that no other types of materials--ionic, covalent, intermetallic compounds (Nb_3Sn, CuZn)--occur in this region of the y-x elastic-constant diagram. Interestingly, three fcc van der Waals solids-- Ar, Kr, Xe--occur near Th. The instability of these solids is also well known [15]. Another class of materials, the alkali metals (Li, Na, K, Rb, Cs) would also be expected to occur in this instability region [16]. Their fcc elastic constants remain unmeasured, but they were calculated recently by a pseudopotential method [17]. From these results, all five alkali metals cluster in a relatively small region of the y-x diagram. For fcc Na, for example, $C_{11} = 0.0818$, $C_{12} = 0.0651$, $C_{44} = 0.0613 \cdot 10^{11} N/m^2$. Thus, x = 0.941, y = 0.796, well into the instability region, with an x value exceeding even that of Pu. This instability of the fcc alkali metals suggests that d-type wave functions may not be necessary for instability; there is general accept-ance that the cohesive properties of alkali metals are determined completely by s-type (spherical symmetry) wave functions.

We now summarize. Many previous studies recognize that mechanical lattice stability requires the nonvanishing of three elastic constants: C_{44}, $(C_{11} - C_{12})$, and $(C_{11} + 2C_{12})$ as evidence for incipient lattice instability. For fcc metals, the present study suggests a new incipient-instability criterion: $x = C_{12}/C_{11} > 0.5$. For all testable cases, where we know the C_{ij}, the criterion holds. All stable fcc metals--Al, Au, Pb et cetera-- exhibit C_{12}/C_{11} ratios between 0.2 and 0.4. By invoking an interatomic-force-constant model, we see that $C_{12}/C_{11} = 0.5$ corresponds to $f = 0$, where f_2 denotes a transverse spring constant corresponding to a force and a displacement along a [001]-type direction.

Acknowledgment

References

1. M. Born and K. Huang, Dynamical Theory of Crystal Lattices (Oxford, London, 1954), pp. 140-154.

2. N. Nakanishi, Elastic constants as they relate to lattice properties and martensite formation, in Progress in Materials Science, Volume 24 (Pergamon, London, 1980), pp. 143-265.

3. H. M. Ledbetter and R. L. Moment, Elastic properties of face-centered-cubic plutonium, Acta Metall. 24, 891-899 (1976).

4. L. Kaufman and M. Cohen, Thermodynamics and kinetics of martensitic transformations, in Progress in Metal Physics, Volume 7 (Pergamon, London, 1958), pp. 165-246.

5. E. W. Collings and S. C. Hart, Low-temperature magnetic susceptibility and magnetization studies of some commercial austenitic stainless steels, Cryogenics 19, 521-530 (1979).

6. C. M. Wayman, The crystallography of martensitic transformations in alloys of iron, in Advances in Materials Research (Interscience, New York, 1968), pp. 147-304, especially pp. 280-292.

7. R. P. Reed, Martensitic phase transformations, in <u>Materials at Low Temperatures</u> (Amer. Soc. Met., Metals Park, 1983), p. 295.

8. F. Seitz, <u>The Modern Theory of Solids</u> (McGraw-Hill, New York, 1940), pp. 487–488.

9. V. L. Moruzzi, J. F. Janak, and A. R. Williams, <u>Calculated Electronic Properties of Metals</u> (Pergamon, New York, 1978), p. 80.

10. R. A. Moore and J. C. Upadhyaya, Comparison of the major force-constant models for cubic systems using a self-consistency condition, Can. J. Phys. <u>57</u>, 2053–2065 (1979).

11. G. Leibfried and N. Breuer, <u>Point Defects in Metals I</u> (Springer-Verlag, Berlin, 1978), p. 42.

12. B. M. Axilrod and E. Teller, J. Chem. Phys. <u>11</u>, 299–300 (1943).

13. C. A. Coulson, <u>Valence</u> (Oxford, London, 1963).

14. W. A. Harrison, <u>Electronic Structure and the Properties of Solids</u> (Freeman, San Francisco, 1980).

15. M. L. Klein and J. A. Venables (eds.), <u>Rare Gas Solids</u> (Academic, New York, 1977).

16. G. Grimvall and I. Ebbsjö, Polymorphism in metals, Phys. Scripta <u>12</u>, 168–172 (1975).

17. H. M. Ledbetter and T. Suzuki, "Binding energies, elastic constants, and phase transitions in sodium: a pseudopotential study," to be published.

Table 1. Monocrystal elastic constants for fcc elements. Units are $10^{11} N/m^2$, except x, y, A are dimensionless.

Element	C_{11}	C_{12}	C_{44}	B	C'	A	y	x
Al	1.0675	0.6041	0.2834	0.7586	0.2317	1.2231	0.5659	0.2655
Cu	1.6839	1.2142	0.7539	1.3708	0.2349	3.2101	0.7211	0.4477
Au	1.9234	1.6314	0.4195	1.7287	0.1460	2.8733	0.8482	0.2181
Ir	5.800	2.4200	2.5600	3.5467	1.6900	1.5148	0.4172	0.4414
Pb	0.4953	0.4229	0.1490	0.4470	0.0362	4.1160	0.8538	0.3008
Ni	2.5080	1.5000	1.2350	1.8360	0.5040	2.4504	0.5981	0.4924
Pd	2.2710	1.7604	0.7173	1.9306	0.2553	2.8096	0.7752	0.3159
Pt	3.4670	2.5070	0.7650	2.8270	0.4800	1.5938	0.7231	0.2207
Pu	0.3628	0.2673	0.3359	0.2991	0.0478	7.0346	0.7368	0.9259
Rh	4.126	1.935	1.841	2.6653	1.0955	1.6805	0.4690	0.4462
Ag	1.2400	0.9400	0.4650	1.0400	0.1500	3.1000	0.7581	0.3750
Th	0.7530	0.4890	0.4780	0.5770	0.1320	3.6212	0.6494	0.6348

Table 2. For a typical metal, copper, and for stainless steel, relative contributions of three force constants to various elastic constants.

	Copper			Stainless Steel	
	f_1	f_2	f_3	f_2	f_3
C_{11}	1.00	0.00	-0.08	0.00	-0.12
C_{12}	1.00	0.10	0.23	-0.17	0.36
C_{44}	1.00	-0.10	-0.08	0.17	-0.12
C'	1.00	-0.10	-0.38	0.17	-0.59
B	1.00	0.05	0.08	-0.09	0.12
$C_{12} - C_{44}$	0.00	-1.00	-1.00	-1.00	-1.00
$C_{11} - C_{12} - 2C_{44}$	-1.00	-0.10	0.23	0.17	0.36
A	1.00	$(0.0)^a$	(0.31)	(0.00)	(0.47)
C_{12}/C_{11}	1.00	(0.10)	(0.31)	(-0.17)	(0.47)

[a]Parentheses indicate the approximation that both f_2/f_1 and f_3/f_1 are small relative to unity.
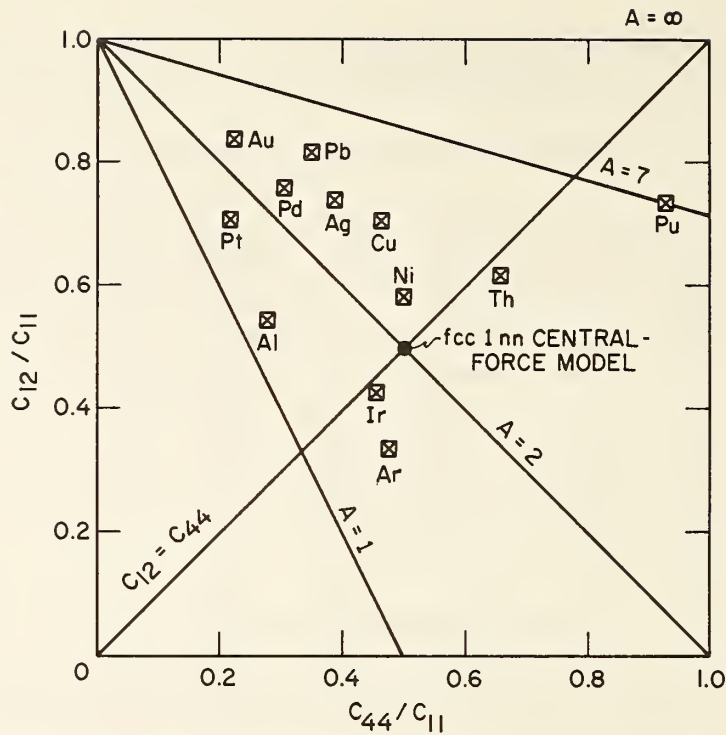
Fig. 1. Reduced elastic stiffnesses for fcc elements. Zener's anisotropy ratio is denoted by A. The Cauchy relationship $C_{12}=C_{44}$ for central forces appears as a line. The center point corresponds to a first-neighbor (1 nn) only central-force model.
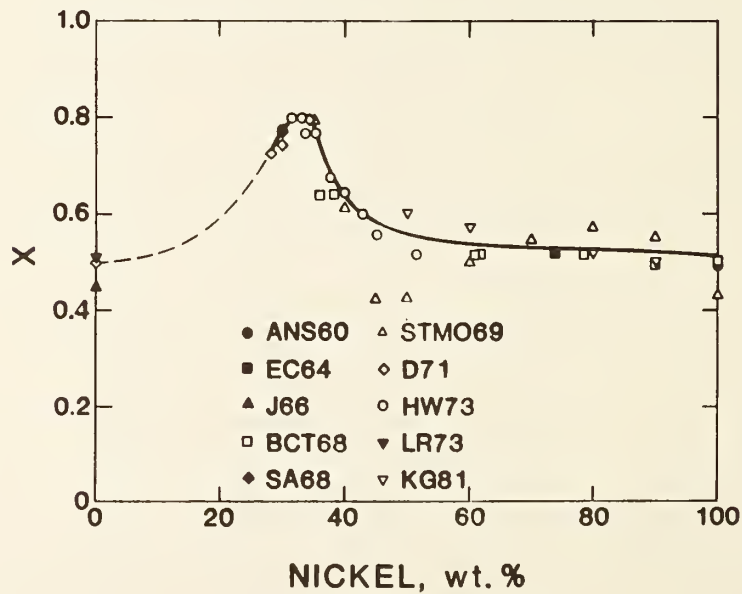
Fig. 2. For fcc Fe-Ni alloys, the variation of $x=C_{44}/C_{11}$ with composition. Maximum near 30 Ni corresponds to an instability.
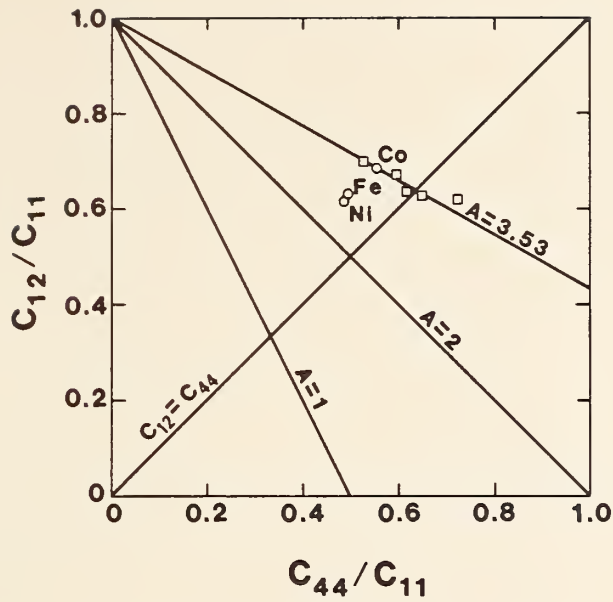
Fig. 3.   Reduced elastic stiffnesses for fcc Fe-Cr-Ni stainless steels.
Compare with Fig. 1.   Face-centered-cubic Fe and Co points were
obtained either from theory or from extrapolation.
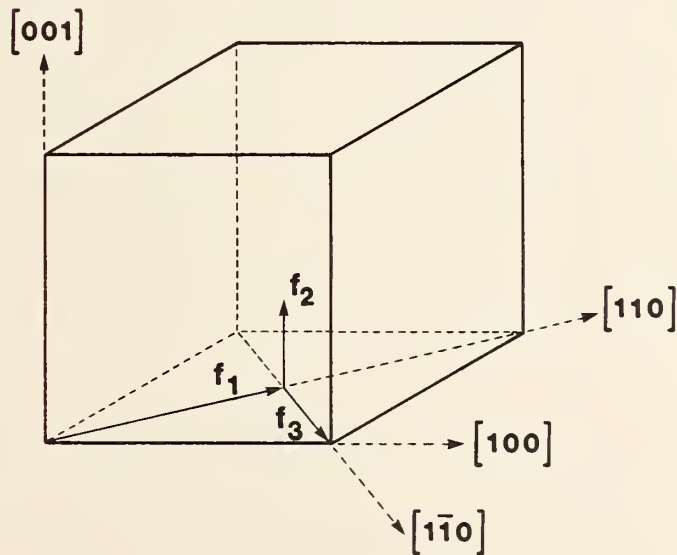
Fig. 4.   Face-centered-cubic unit cell showing eigenvectors and eigenvalues
of the coupling matrices to the nearest-neighbor atoms at
[½ ½ 0]-type positions.

Monocrystal-Polycrystal Elastic Constants of a Stainless Steel

H. M. Ledbetter

Fracture and Deformation Division

Center for Materials Science

National Bureau of Standards

Boulder, Colorado 80303, USA

For a face-centered-cubic steel, we report new measurements of the monocrystal

Voigt elastic-stiffness constants: C_{11}, C_{12}, C_{44}. The monocrystal steel,

Fe-19Cr-10Ni, corresponds closely to the well-known AISI-304 austenitic

stainless steel. Considering seven theories for the monocrystal-polycrystal

elastic constants, we find the Hershey-Kröner-Eshelby theory agrees best with

measurements. It predicts the shear modulus within two percent of observa-

tion, where the Voigt-Reuss first-order bounds differ by forty-nine percent.

We review ten sets of Fe-Cr-Ni C_{ij} results and find that both Zener's elastic

anisotropy and the C_{12}/C_{11} ratio are constant within five percent.

1. Introduction

The relationship between monocrystal physical properties (represented by tensors) and polycrystal physical properties (scalars) remains one of the most intriguing unsolved problems in crystal physics. Tensor 'averages' have been proposed for many physical properties, including dielectric constant, diffusivity, elastic constants, electrical conductivity, magnetic permeability, magnetostriction, piezoelectric constants, and thermal conductivity.

In terms of averaging, elastic constants have received more attention than most other physical properties. Voigt [1] was first to suggest how the fourth-rank elastic-stiffness tensor, C_{ijkl}, could be averaged to obtain the two independent quasi-isotropic elastic constants: the bulk modulus, B, and the shear modulus, G. Forty years later, Reuss [2] showed that Voigt's solution is not unique. Landau and Lifshitz [3] point out that "there is therefore no general relation between the moduli of elasticity of a polycrystal and those of a single crystal of the same substance." Many ingenious approximate averaging methods have been developed, too many to enumerate here. Most of these are either described or referenced in reviews by Hearmon [4], Beran [5], Ledbetter [6], Kröner and Koch [7], and Watt et al.[8].

Until a generally accepted averaging method arises, interest remains high in testing various models against careful measurements. For both ambient and low temperatures, Ledbetter [9,10] recently did this for copper. He considered eight models: Voigt, Hashin-Shtrikman, Hershey-Kröner-Eshelby, Hill (arithmetic), Hill (geometric), Aleksandrov, Ledbetter-Naimon, and Reuss. Among these, the Hershey-Kröner-Eshelby model worked best, predicting the quasi-isotropic polycrystal shear modulus within 1%.

The study reported here tests the various monocrystal-polycrystal models for the elastic constants of an fcc Fe-Cr-Ni alloy. This alloy possesses technological interest because it approximates the chemical composition of AISI-304 stainless steel, probably the best known and most widely used stainless-steel alloy. This study represents the first test of elastic-constant averaging models for a nondilute ternary alloy. While the alloy exhibits macroscopic paramagnetism at ambient temperature, all constituents -- Fe, Cr, Ni -- exhibit ferromagnetism, antiferromagnetism, or both. Thus, local interatomic interactions may be nonparamagnetic. Because the alloy is concentrated, contains magnetic species, and possesses considerable technological interest, we undertook the present study.

2. Experiment

a. Monocrystal

An alloy of nominal weight-percent composition Fe-19Cr-10Ni was vacuum melted and vacuum cast from high-purity metals. Monocrystals were grown by a Bridgman technique, homogenized at 1350°C for 20 h, cut to shape and size with a spark cutter, and annealed at 1100°C for 20 h. Back-reflection Laue x-ray diffraction was used to establish the crystal orientation, which was 2.5° from a [110] axis. (In subsequent measurement and analysis, we ignored this small departure from a [110] axis.) Specimen dimensions were 1.5 x 1.5 x 0.7 cm. Mass density measured by Archimedes's method was 7.937 g/cm^3.

b. Polycrystal

For these, we used the twenty AISI-304-type stainless-steel alloys studied previously by Ledbetter et al. [11] in their as-received wrought-and-annealed conditions. Their average weight-percent chemical composition was 18.6 Cr, 9.3 Ni, 1.3 Mn, with other trace elements. Their average Archimedes-

method mass density was 7.880 g/cm^3. Their average grain size measured 88 μm, ranging from 68 to 105. Figure 1 shows a typical microstructure.

c.   Measurements

We measured sound velocities, longitudinal and transverse, by a pulse-echo-overlap method described previously [11]. For the polycrystals, the percent standard error was 0.3% for v_1 and 0.6% for v_t. This includes all possible error sources: chemical composition, thermal-mechanical treatment, measurement method, and so forth. For the monocrystals, the percent standard error was approximately 0.1%.

3.   Results

Table 1 gives, for both monocrystal and polycrystal, the measured sound velocities together with the derived elastic-stiffness constants calculated from

$$C = \rho v^2 \tag{1}$$

where C denotes elastic stiffness; ρ, mass density; and v, sound velocity. For the polycrystal,

$$C_{11} = C_\ell = \rho v_\ell^2 \tag{2}$$

and

$$C_{44} = G = \rho v_t^2 \tag{3}$$

where C_ℓ denotes longitudinal modulus and G shear modulus. For a monocrystal, along a [110] direction,

$$C_L = \rho v_\ell^2 = (C_{11}+C_{12}+2C_{44})/2 \tag{4}$$

$$C_{t1} = \rho v_{t1}^2 = C_{44} \tag{5}$$

and

$$C_{t2} = \rho v_{t2}^2 = (C_{11}-C_{12})/2 \tag{6}$$

From Eqs. (4) - (6) one obtains the usual three independent Voigt elastic stiffnesses: C_{11}, C_{12}, and C_{44}. For the monocrystal, the bulk modulus is

$$B = (C_{11} + 2C_{12})/3 \tag{7}$$

while for the polycrystal it is

$$B = C_\ell - (4/3)G \tag{8}$$

Based on seven averaging methods, Table 2 gives predicted quasi-isotropic elastic constants. For this table, E denotes Young modulus, G shear modulus, and ν Poisson ratio. All averaging methods predict the same bulk modulus, B = $1.60010^{11}N/m^2$, following Eq. (7). For details of the mathematical relationships associated with the various methods, see Ledbetter [6] or references to the original studies given in [9].

4. Discussion

Results in Table 2 show clearly that, among the seven averaging methods considered, one method agrees best with observation: the Hershey-Kröner-Eshelby method. It predicts the shear modulus within 2%, the Young modulus within 2%, the bulk modulus within 1%, and the Poisson ratio within 2%. Part of the discrepancy may arise from the slightly different chemical compositions of the monocrystal (19Cr - 10Ni) and the average polycrystal (18.6Cr - 9.3Ni - 1.3Mn, plus trace elements). Note also that observation lies much closer to the Hashin-Shtrikman upper bound than to the lower. Especially, this occurs for Poisson's ratio. If real, this suggests that the polycrystal is not perfectly disordered, that it contains texture, characteristic grain shape, or characteristic grain-boundary geometry. But, present results permit no conclusions concerning these matters.

For cubic-symmetry monocrystals where Eq. (7) gives the bulk modulus, the

averaging problem amounts to predicting another elastic constant. Most models predict the shear modulus. The Hershey-Kröner-Eshelby method does this by considering an anisotropic nonhomogeneity embedded in an isotropic matrix. Eshelby [12] gave a relatively simple discussion of this inclusion problem, which leads to a cubic equation for the shear modulus G:

$$G^3 + \alpha G^2 + \beta G + \gamma = 0 \qquad (9)$$

where

$$\alpha = (5C_{11} + 4C_{12})/8 \qquad (10)$$

$$\beta = -C_{44}(7C_{11} - 4C_{12})/8 \qquad (11)$$

and

$$\gamma = -C_{44}(C_{11} - C_{12})(C_{11} + 2C_{12})/8 \qquad (12)$$

An interesting feature of Eq. (9) is that it contains the bulk modulus. In the H-K-E model, the cubic-symmetry shear moduli are not sufficient for predicting G. Other models -- Voigt, Reuss, Hill, Aleksandrov, for example -- do not require B to predict G. The question arises: why does the resistance to shear deformation depend on the resistance to dilation? In isotropic media, we know since Stokes [13] that G and B are the two independent elastic constants representing extreme types of deformation: shape change without volume change and volume change without shape change, respectively. We can factor any general deformation into dilation and shear components. Thus, is this G(B) dependence real or an artifact of the model? Will the final model be of the form $G(C_{44}, C', B)$ or simply $G(C_{44}, C')$?

Recently, Gairola and Kröner [14] derived a simple formula for calculating all the bounds for and the self-consistent (infinite bound) value of the shear modulus of a macroscopically isotropic cubic-symmetry polycrystalline aggregate. The numerical results agree exactly with the Hersey-Kröner-

Eshelby method. The approach differs from the spherical-inclusion problem described above, but it leads to the same results. Using a unified method [15, 16], they derive the result (in their notation):

$$G = \frac{\alpha_2 G_o^2 + \beta_2 G_o + \gamma}{G_o^2 + \alpha_1 G_o + \beta_1} \tag{13}$$

where

$$\alpha_1 = (45\kappa + 24\mu + 36\nu)/40 \tag{14}$$

$$\alpha_2 = (2\nu + 3\mu)/5 \tag{15}$$

$$\beta_1 = 3\kappa(2\mu + 3\nu)/20 \tag{16}$$

$$\beta_2 = 3(6\kappa\nu + 9\kappa\mu + 20\mu\nu)/40 \tag{17}$$

$$\gamma = 3\kappa\mu\nu/4 \tag{18}$$

$$\kappa = (C_{11} + 2C_{12})/3 \tag{19}$$

$$\nu = (C_{11} - C_{12})/2 \tag{20}$$

$$\mu = C_{44} \tag{21}$$

One can easily verify that putting $G_o = \infty$ and $G_o = 0$ leads to the Voigt and Reuss bounds, G_V and G_R, the so-called first-order upper and lower bounds, $G^{(1)}$ and $G_{(1)}$. If instead one puts $G_o = \mu = C_{44}$ and $G_o = \nu = (C_{11} - C_{12})/2$ (μ and ν are the zeroeth-order bounds $G^{(o)}$ and $G_{(o)}$), then one obtains the Hashin-Shtrikman bounds, $G^{(2)}$ and $G_{(2)}$. This self-consistent renormalization scheme yields either the odd-order or the even-order bounds. Either set leads to $G^{(\infty)} = G_{(\infty)} = G$(self-consistent) in exact agreement with Eq. (9). Some authors call the third-order bounds, $G^{(3)}$ and $G_{(3)}$, the Kröner bounds.

Finally, we collect and discuss briefly all previously reported mono-crystal stainless-steel elastic constants. Table 3 contains ten sets of reported elastic constants, converted where necessary to the C_{ij}: C_{11}, C_{12}, and C_{44}. Table 3 contains also B and C' together with the Zener anisotropy:

$$A = C_{44}/C' \tag{22}$$

The table shows also results for fcc Fe, Co, and Ni. The Ni results were measured. The Co results were obtained by extrapolation from measurements on Ni-Co alloys. Diesburg's [23] result for Fe was also obtained by extrapolation, using Fe-Ni alloys. Johnson's [22] result for Fe came from theory based on fitting a two-body central-force interatomic potential to Fe's second-order bcc elastic constants. For the ten Fe-Cr-Ni alloys in Table 3, the Zener anisotropy shows remarkable near-constancy: $A = 3.53 \pm 0.17$, a standard error of 5%. Also nearly constant, we find the ratio $C_{12}/C_{11} = 0.652 \pm 0.025$, a standard error of 4%. These empirical ratios provide an opportunity for calculating the three monocrystal elastic constants from the two quasi-isotropic polycrystal elastic constants. Ledbetter [26] used this approach to estimate the monocrystal elastic constants of 316-type stainless steel. In that study, based on only four Fe-Cr-Ni alloys, he used $A = 3.51$ and $C_{12}/C_{11} = 0.635$.

5. Conclusions

For an austenitic stainless-steel alloy, we considered the monocrystal-polycrystal elastic-constant relationship. Among seven models, the Hershey-Kröner-Eshelby model works best.

214

References

[1]   W. Voigt, Ann. Phys. 38, 573 (1889).

[2]   A. Reuss, Z. Angew. Math. Mech. 9, 49 (1929).

[3]   L. D. Landau and E. M. Lifshitz, Theory of Elasticity, Pergamon, London 1959 (p. 40).

[4]   R. F. S. Hearmon, in Physics of the Solid State, Academic, New York 1969 (p. 401).

[5]   M. J. Beran, Phys. Stat. Solidi (a) 6, 365 (1971).

[6]   H. M. Ledbetter, J. Appl. Phys. 44, 1451 (1973).

[7]   E. Kröner and H. Koch, SM Archives 1, 183 (1976).

[8]   J. P. Watt, G. F. Davies, and R. J. O'Connell, Rev. Geophys. Space Phys. 14, 541 (1976).

[9]   H. M. Ledbetter, J. Phys. D: Appl. Phys. 13, 1879 (1980).

[10]   H. M. Ledbetter, Phys. Stat. Solidi (a) 66, 477 (1981).

[11]   H. M. Ledbetter, N. F. Frederick, and M. W. Austin, J. Appl. Phys. 51, 305 (1980).

[12]   J. D. Eshelby, in Progress in Solid Mechanics, Volume II, North-Holland, New York 1961 (p. 130).

[13]   G. G. Stokes, described in I. Todhunter and K. Pearson, A History of the Theory of Elasticity and of the Strength of Materials, Cambridge U.P., Cambridge 1886.

[14]   B. K. D. Gairola and E. Kröner, Int. J. Eng. Sci. 19, 865 (1981).

[15]   E. Kröner, J. Phys. F: Met. Phys. 8, 2261 (1978).

[16]   B. K. D. Gairola, in Proceedings Continuum Models of Discrete Systems, U. Waterloo P., Waterloo Canada 1980.

[17]   G. Bradfield, J. Iron Steel Inst. 202, 616 (1964).

[18]   K. Salmutter and F. Stangler, Z. Metallkd. 51, 1 (1960).

[19]   M. Kikuchi, Trans. Jap. Inst. Met. 12, 417 (1971).

[20]   M. C. Mangalick and N. F. Fiore, Trans. Metall. Soc. AIME 242, 363 (1968).

[21]   D. S. Kupperman, personal communication (1982). See also D. S.
         Kupperman and K. J. Reimann, IEEE Trans. Sonics Ultrasonics SU-27, 7
         (1980).

[22]   R. A. Johnson, Phys. Rev. 145, 423 (1966).

[23]   D. Diesburg, Ph.D. Thesis, Iowa State University (1971).

[24]   H. J. Leamy and H. Warlimont, Phys. Status Solidi 37, 523 (1970).

[25]   G. A. Alers, J. R. Neighbours, and H. Sato, J. Phys. Chem. Solids
         13, 40 (1960).

[26]   H. M. Ledbetter, Brit. J. NDT 34, 286 (1981).
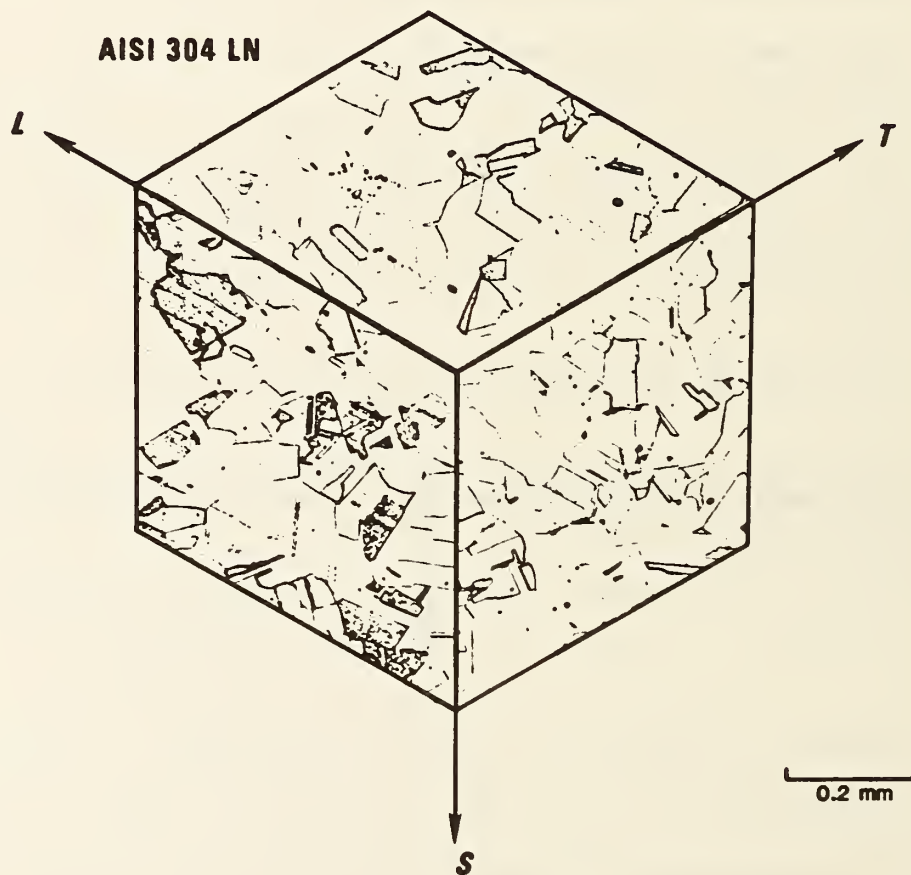
Fig. 1.   Microstructure of a typical polycrystalline 304-type stainless-steel
           alloy in its wrought and annealed condition. LN denotes low carbon
           content and high nitrogen content. The specimen came from a
           commercial plate; L denotes rolling direction; T, transverse in-plate
           direction; and S, through-plate-thickness direction.

216

Table 1

Sound-velocity and elastic-constant results

	Monocrystal	Polycrystal
$\rho\,(g/cm^3)$	7.937	7.880
$v_\ell\,(cm/\mu s)$	0.6121	0.5759
v_{t1}	0.3988	0.3134
v_{t2}	0.2052	-
$C_L\,(10^{11}N/m^2)$	2.974	2.614
$(C_{11}-C_{12})/2$	0.334	0.774
C_{44}	1.262	-
C_{11}	2.046	2.614
C_{12}	1.377	1.066
B	1.600	1.582
E	-	1.996
ν	-	0.290

Table 2

Polycrystalline elastic constants predicted by averaging monocrystal elastic constants

E $(10^{11}N/m^2)$	G $(10^{11}N/m^2)$	ν	Method
2.255	0.891	0.265	Voigt
2.025	0.785	0.289	Hashin-Shtrikman, upper
1.850	0.708	0.307	Hashin-Shtrikman, lower
1.938	0.746	0.298	Hashin-Shtrikman, average
1.960	0.756	0.296	Hershey-Kröner-Eshelby
1.934	0.745	0.299	Hill, arithmetic
1.928	0.742	0.299	Aleksandrov
1.901	0.730	0.302	Hill, geometric
1.596	0.598	0.334	Reuss

Table 3

Monocrystal elastic constants of face-centered-cubic Fe-Cr-Ni alloys; units on elastic constants are $10^{11}N/m^2$, except A, which is dimensionless

Alloy (Cr-Ni)	C_{11}	C_{12}	C_{44}	B	C'	A	Source
12-12	2.109	1.403	1.225	1.638	0.353	3.47	Bradfield [17]
12-18	2.332	1.627	1.226	1.862	0.353	3.48	Salmutter, Stangler [18]
18-12	1.912	1.179	1.386	1.423	0.367	3.78	Kikuchi [19]
18-12	2.159	1.446	1.289	1.684	0.357	3.62	Bradfield [17]
18-14	1.98	1.25	1.22	1.49	0.365	3.34	Mangalick, Fiore [20]
18-19	1.91	1.19	1.24	1.43	0.360	3.44	Mangalick, Fiore [20]
19-10	2.05	1.38	1.26	1.60	0.334	3.78	Present
19-10	2.07	1.32	1.23	1.57	0.375	3.28	Kupperman [21]
19-14	2.05	1.33	1.27	1.57	0.360	3.58	Kupperman [21]
19-19	2.04	1.33	1.26	1.57	0.355	3.55	Kupperman [21]
Fe	2.51	1.57	1.12	1.89	0.470	2.38	Johnson [22]
Fe	2.760	1.735	1.363	2.08	0.513	2.66	Diesburg [23]
Co	2.398	1.634	1.334	1.89	0.382	3.49	Leamy, Warlimont [24]
Ni	2.516	1.544	1.220	1.87	0.486	2.51	Alers, Neighbours, Sato [25]

ELASTIC-CONSTANT ANOMALIES AT THE NEEL TRANSITION IN Fe-18Cr-3Ni-13Mn*

H. M. Ledbetter
Fracture and Deformation Division
Center for Materials Science
National Bureau of Standards
Boulder, Colorado 80303

E. W. Collings
Battelle Columbus Laboratories
Columbus, Ohio 43201

Elastic constants of an 18Cr-3Ni-13Mn austenitic stainless steel were measured ultrasonically between room temperature and liquid-helium temperature. All the elastic constants change anomalously and reversibly near 191 K, which magnetic susceptibility measurements show to be the Néel (paramagnetic-to-antiferromagnetic) transition temperature.

INTRODUCTION

A recent study [1] showed that an Fe-21Cr-6Ni-9Mn stainless steel is elastically anomalous near 130 K. All the elastic stiffnesses -- Young's modulus, shear modulus, and bulk modulus -- decrease anomalously during cooling, and Poisson's ratio increases. It was speculated that these changes reflect a Néel (paramagnetic-to-antiferromagnetic) transition.

A study is reported here for a similar alloy, Fe-18Cr-3Ni-13Mn. Its higher manganese content suggested a possibly higher Neel transition and perhaps a larger elastic anomaly. The previous study [1], which covered the temperature range 76-295 K, left unresolved the question of the very low temperature behavior of the elastic constants. The present study covers the 4-295 K temperature range. More importantly, it includes magnetic-suscepti-bility measurements to detect and characterize any magnetic transitions.

EXPERIMENT

Material

Two 2.5-cm plates from different heats were obtained from a commercial source. The vendor's chemical analysis in weight percent is: 18.09 Cr, 3.26 Ni, 13.22 Mn, 0.37 N, 0.52 Si, 0.12 Mo, 0.038 C, 0.028 P, 0.005 S. In its as-received annealed condition, the Rockwell B hardness is 92 and the grain size is ASTM size 6.

_____

Specimens

For elastic-constant measurements, a rectangular prism 1.4 cm x 1.6 cm x 1.7 cm was prepared with opposite faces flat and parallel within 3 μm.

Absolute Ultrasonic-Velocity Measurements

Room-temperature ultrasonic velocities were measured using a pulse-echo method for both longitudinal and shear waves near 7 and 6 MHz, respectively. Procedures and equipment were described previously [2]. Briefly, a voltage is applied sinusoidally to a quartz piezoelectric transducer bonded to a specimen with phenyl salicylate. The electrical pulse is converted to a mechanical pulse, is transmitted through the specimen, is reflected from the flat specimen surface, and is transmitted back to the transducer that acts as a receiver, partially converting the pulse to an electrical signal that is displayed on a calibrated oscilloscope. From the pulse's transition (round-trip) time, t, the sound velocity is computed from $v = 2\ell/t$, where ℓ is the specimen length. The elastic constants are computed by $C = \rho v^2$, where ρ is the mass density. Different elastic constants are obtained for different types of waves: shear, longitudinal, etc. When the systematic error is neglected, the uncertainty in the reported elastic constants is about 0.1 percent.

Relative Velocity Measurements

The changes in the velocity of sound with temperature were determined by a pulse-superposition method [3]. Briefly, the pulse repetition rate is adjusted so that the time between pulses equals two transit times. This is done by dividing the carrier frequency, f, by a fixed integer, N. Thus, $f/N = 1/2t = v/4\ell$. The oscilloscope display between applied pulses consists of the sum of all odd-numbered echoes, and the carrier frequency is adjusted (as temperature is changed) to maximize the amplitude of the summed-odd-echo envelope. When the dimensional change is neglected, the change in elastic constant is $dC/C = 2dv/v = -2dt/t = 2df/f$, where a typical sensitivity in df/f is 10^{-4} or better.

Magnetic-Susceptibility Measurements

Magnetic susceptibilities were measured at room temperature by the Curie technique using an electronic microbalance and an electromagnet fitted with "constant-force" pole caps 18 cm in diameter. The vertical magnetic force field ($\vec{H}$ x $\partial\vec{H}/\partial z$) at the sample reference position was calibrated using a 486.77 mg piece of high-purity platinum, whose susceptibility (0.977 μemu/g at 293 K) and susceptibility temperature dependence (6.3 x 10^{-10} emu/g·deg from 260 to 300 K) were measured by Budworth, Hoare, and Preston [4]. Further details concerning these measurements are given elsewhere [5].

RESULTS

Table 1 shows the variation with direction of both longitudinal and shear elastic velocities. Since elastic anisotropy is clearly negligible, velocities reported below represent arithmetic averages over three directions. Table 2 shows variations of elastic constants between heats and between heat treatments. Clearly, these variables effect only small changes. Table 3 shows the variations in elastic constants with temperature; Fig. 1 also displays these. Figure 2 shows perhaps the most important result: the correlation between elastic-constant behavior (represented by $C_\ell = \rho v_\ell^2$) and magnetic susceptibility.

DISCUSSION

Magnetic-susceptibility, χ, results shown in Fig. 2 demonstrate conclusively that a Néel (paramagnetic-to-antiferromagnetic) transition occurs at 191 K. A sharp, field-independent maximum in the χ-T curve provides simple, unambiguous evidence for a Néel transition [6].

All the elastic constants behave anomalously around the Néel temperature, T_N, as shown in Fig. 1, that is, both dilatation-type (B) and shear-type (G) elastic constants behave anomalously. Regular (paramagnetic) materials show smoothly increasing E, G, and B and decreasing ν with decreasing temperature. Poisson's ratio, which is usually affected only slightly by most metallurgical variables [7], changes particularly abruptly for the present alloy and provides a good indicator of the magnetic transition. Except for Poisson's ratio, all the elastic constants exhibit regular behavior at temperatures sufficiently separated from T_N. The bulk-modulus softening well above T_N indicates either that compressibility increases premonitorily to the Néel transition or that a second transition (of unknown character) precedes the Néel transition during cooling.

Elastic constants, C_{ijkl}, change at any phase transition because they relate intimately to the interatomic potential, $\Phi(r)$. Thus, the elastic constants are [8]:

$$C_{ijkl} = \frac{\partial^2 U}{\partial n_{ij} \partial n_{kl}}$$

where U is the thermodynamic internal energy

$$U = 1/(2V°) \sum \Phi(r)$$

which is summed over all ion pairs; n_{ij} denotes the Brugger strain and V° denotes atomic volume. Clearly, any strain-dependent contribution to the energy contributes also to the elastic constants. Thus, either changes in $\Phi(r)$ or changes in ionic arrangement affect the C_{ijkl}.

In the present case $\Phi(r)$ is affected by antiferromagnetic ordering, the energetics of which parallels ferromagnetic ordering in many ways. In several studies [9,10] relationships between ferromagnetic ordering and changes in elastic constants have been discussed and in a few studies the antiferromagnetic case has been considered [11-14]. The authors discuss this topic in detail elsewhere [15].

Other thermodynamic properties related to $\Phi(r)$, e.g., thermal expansivity and specific heat, should also behave anomalously near T_N. Existing thermal expansivity data on these alloys are insufficiently precise ($\Delta\ell/\ell$ about 10^{-5}) to detect the transition. Specific-heat measurements on this alloy were made at low temperatures, but not near T_N [16]. If no specific-heat anomaly occurs near T_N, then sound velocities or elastic constants may provide the most sensitive indicator of the transition.

In summary, all elastic constants of Fe-18Cr-3Ni-13Mn behave anomalously near 191 K, which magnetic-susceptibility measurements show to be the temperature of a Néel (paramagnetic-to-antiferromagnetic) transition. Such anomalies in the physical properties are expected at a magnetic transition, consistent with their dependence on the interatomic potential. These findings agree with those reported previously for Fe-21Cr-6Ni-9Mn, whose lower Néel temperature reflects its lower manganese content.

ACKNOWLEDGMENTS

REFERENCES

1. H. M. Ledbetter, Mater. Sci. Eng. 29, 255-260 (1977).

2. E. R. Naimon, W. F. Weston, and H. M. Ledbetter, Cryogenics 14, 246-249 (1974).

3. H. J. McSkimin, J. Acoust. Soc. Amer. 33, 12-16 (1961).

4. D. W. Budworth, F. E. Hoare, and J. Preston, Proc. R. Soc. Lond. A 257, 250 (1960).

5. E. W. Collings and R. D. Smith, J. Less Common Met. 48, 187-198 (1976).

6. A. H. Morrish, Physical Principles of Magnetism (Wiley, New York, 1965), p. 452.

7. W. Kƍter and H. Franz, Metall. Rev. 6, 1-55 (1961).

8. D. C. Wallace, Thermodynamics of Crystals (Wiley, New York, 1972), p. 19.

9. G. A. Alers, J. R. Neighbours, and H. Sato, J. Phys. Chem. Solids 13, 40-55 (1960).

10. G. Hausch, Phys. Stat. Solidi (A) 15, 501-510 (1973).

11. W. P. Mason, Phys. Rev. 82, 715-723 (1951).

12. D. E. Eastman, J. Appl. Phys. 37, 996-997 (1966).

13. P. Makhurane and P. Gaunt, J. Phys. C 2, 959-965 (1969).

14. K. Kawasaki and A. Ikushima, Phys. Rev. B 1, 3143-3151 (1970).

15. H. M. Ledbetter and E. W. Collings, in Metal Physics of Stainless Steels (TMS-AIME, New York, 1979, 22-40).

16. E. W. Collings and R. D. Smith, Advances in Cryogenic Engineering, vol. 24 (Plenum, New York, 1978, 214-223).

Table 1. Elastic wave velocities in Fe-18Cr-3Ni-13Mn at T = 295 K.

Propagation Direction	Longitudinal Velocity (cm/μs)	Shear Velocity (cm/μs)
x = through thickness	0.5701	0.3161
y = transverse direction	0.5698	0.3153
z = rolling direction	0.5697	0.3161
Mean value	0.5699	0.3158
Std. deviation	0.0002	0.0005

Table 2. Room-temperature (T = 293 K) sound velocities and elastic constants for Fe-18Cr-3Ni-13Mn.

	Heat 1 Solution Treated, Furnace Cooled	Heat 1 Solution Treated, Water Quenched	Heat 2 Hot Rolled, Annealed
Mass density (g/cm^3)	7.830	7.817	7.835
Long. velocity $(cm/\mu s)$	0.5699	0.5633	0.5697
Shear velocity $(cm/\mu s)$	0.3163	0.3104	0.3143
Long. modulus $(10^{11} N/m^2)$	2.543	2.481	2.543
Shear modulus $(10^{11} N/m^2)$	0.783	0.753	0.774
Bulk modulus $(10^{11} N/m^2)$	1.499	1.477	1.511
Young's modulus $(10^{11} N/m^2)$	2.001	1.931	1.983
Poisson's ratio	0.277	0.282	0.281
Std. deviation of v_ℓ	0.0003	0.0003	0.0009
Std. deviation of v_t	0.0002	0.0005	0.0013

Table 3. Elastic constants of Fe-18Cr-3Ni-13Mn at selected temperatures.

Temp. (K)	Longitudinal Modulus (10^{11} N/m^2)	Young's Modulus (10^{11} N/m^2)	Shear Modulus (10^{11} N/m^2)	Bulk Modulus (10^{11} N/m^2)	Poisson's Ratio
300	2.493	1.949	0.761	1.478	0.280
280	2.502	1.962	0.767	1.479	0.279
260	2.510	1.975	0.773	1.479	0.278
240	2.517	1.986	0.778	1.480	0.276
220	2.522	1.995	0.782	1.479	0.275
200	2.524	2.002	0.786	1.476	0.274
180	2.484	1.953	0.764	1.465	0.278
160	2.467	1.941	0.760	1.454	0.277
140	2.470	1.944	0.761	1.456	0.278
120	2.477	1.949	0.763	1.460	0.278
100	2.487	1.957	0.766	1.466	0.278
80	2.492	1.961	0.768	1.468	0.277
60			0.768		
40			0.771		
20			0.773		
4			0.773		
Estimated Uncertainty	0.025	0.022	0.005	0.010	0.004
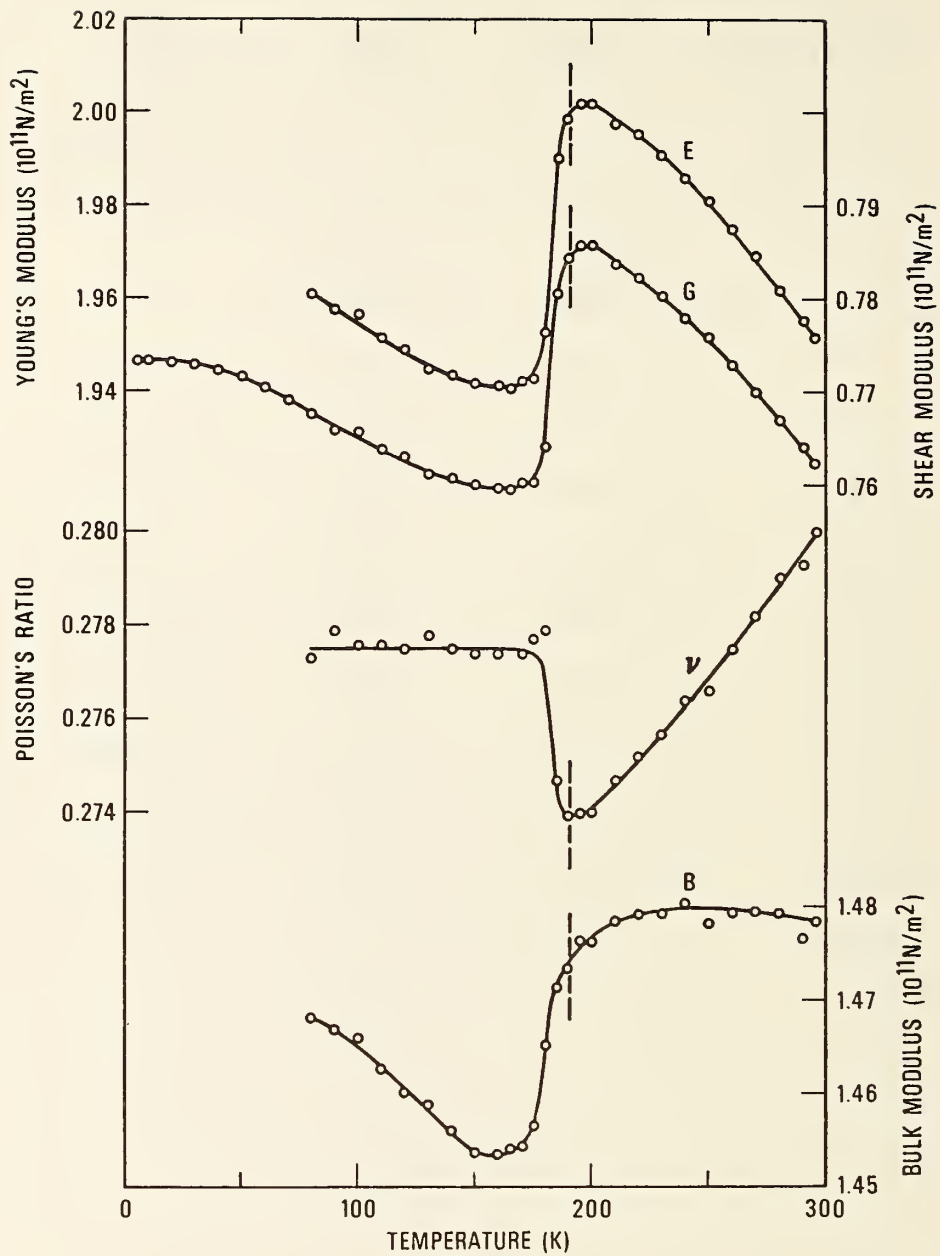
Fig. 1.   Temperature dependence of four elastic constants: E,
          Young's modulus; G, shear modulus; B, bulk modulus
          (reciprocal compressibility); and ν, Poisson's ratio.
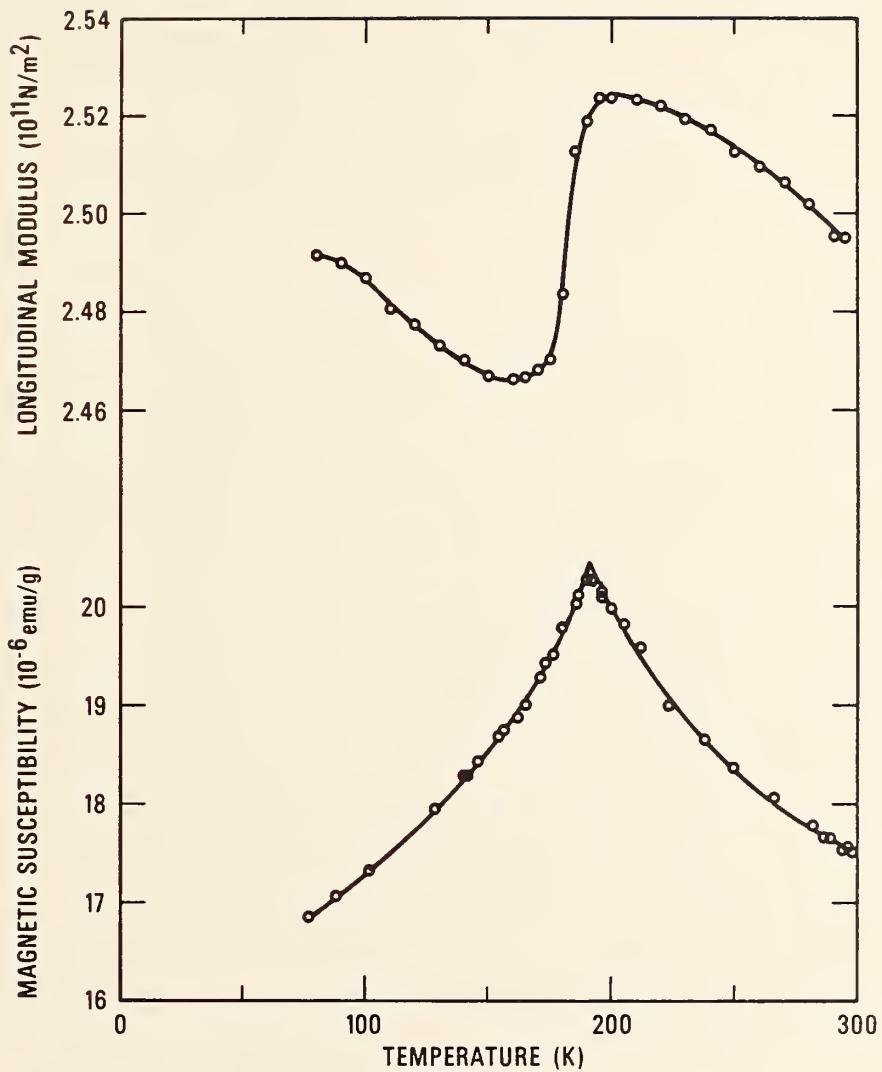
Fig. 2. Temperature dependence of longitudinal modulus $C_\ell = \rho v_\ell^2$ and magnetic susceptibility. As discussed in the text, these results evidence a Néel transition at 191 K.

AUTOMATIC NEAR-THRESHOLD FATIGUE-CRACK
GROWTH-RATE MEASUREMENTS AT LIQUID HELIUM TEMPERATURE[†]

R.L. Tobler and Y.W. Cheng

Fracture and Deformation Division

National Bureau of Standards

Boulder, Colorado 80303

The development of a fully automated test apparatus for near-threshold fatigue crack growth rate measurements in a liquid helium environment is described, and some initial results for AISI 300 series stainless steels are presented. The experimental apparatus consists of a servohydraulic test machine and a cryostat, complete with minicomputer, programmable arbitrary waveform generator, programmable digital oscilloscope, and fully automatic liquid helium refill system. The technique uses 6.4-mm-thick compact specimens subjected to systematically decreasing loads, with 24-h operation at 40 Hz, the crack growth being continuously monitored by specimen compliance measurements. The results presented in this study include da/dN-versus-ΔK curves and threshold fatigue stress intensity factors, ΔK_{th}, at 4 K for AISI 304L, 304LN, and 316 stainless steels. The near-threshold fatigue behaviors of these materials are similar, and the fatigue crack growth rate trends at intermediate ΔK levels nearly agree with published results.

Key words: austenitic stainless steels; computer-automated test systems; cryogenic properties of materials; fatigue of materials; fatigue crack growth rates; threshold stress intensity factors.

[†]Contribution of NBS; not subject to copyright.

INTRODUCTION

Recent workshop presentations [1,2] indicated that fatigue properties are essential to the design of some magnetic fusion energy structures. Of special interest are the near-threshold fatigue crack growth rates (da/dN) and threshold stress intensity factors (ΔK_{th}) of austenitic stainless steels. These parameters relate to alloy development and structural design analyses since they lead to the identification of conditions below which existing cracks can not grow in fatigue. Experimental determinations of these parameters are needed because few cryogenic measurements exist, and there are no reliable prediction schemes.

Hooper [1] showed that near-threshold fatigue crack growth data at rates as low as 10^{-10} m/cycle would permit more accurate life predictions in the toroidal field coil cases of tokamak-type superconducting magnets. Tokamak machines operate in pulsed mode and could accumulate hundreds of thousands of cycles (N) during a lifetime at 4 K. The potential savings from efficient alloy selection and design would more than compensate for the expense of threshold fatigue measurements at 4 K.

Previous threshold fatigue studies [3-5] dealt primarily with ferritic steel behavior at ambient temperature. For these materials it is known that the da/dN-versus-ΔK curves on log-log coordinates typically have a sigmoidal shape, and that metallurgical effects are relatively strong in the near-threshold region. The applicability of fatigue crack growth thresholds to very high-cycle rotating machinery such as steam turbine rotors has become well established; load ratio, environment, and alloy microstructure have been identified as major factors affecting material performance.

At cryogenic temperatures, the available threshold fatigue data for austenitic stainless steels suitable for engineering applications are limited to AISI-304 type (i.e., Fe-18Cr-10Ni) steels and JBK-75 (i.e., Fe-14Cr-29Ni)

base metal and welds. The data for JBK-75 [6,7] were obtained at 295, 77, and 4 K at stress ratios of 0.1 and 0.8. The data for AISI 304 [8,9] do not extend below 77 K and were obtained for R ratios of 0.05 and -1. Our purpose is to expand this data base to include other materials and test variables. In this paper we describe a fully automatic threshold fatigue test apparatus and present our first measurements for AISI 300 series austenitic stainless steels tested in liquid helium at a stress ratio (R) = 0.1.

TEST METHODOLOGIES

Threshold fatigue testing is notoriously difficult and time-consuming, and the additional requirement of maintaining a liquid helium environment significantly increases the cost of testing. Therefore, the choice of test methodology is important. At least two approaches are possible for cryogenic studies: the ultrasonic technique and the automated closed-loop servohydraulic technique.

The ultrasonic technique was successfully used by Stanzl and coworkers [9-11] at test temperatures down to 77 K. This method offers the advantage of high frequencies (e.g., 20 kHz), which greatly reduces the test duration (the frequency is typically 100 Hz or less for closed-loop servohydraulic apparatus). We rejected this method for liquid helium testing, however, reasoning that adiabatic heating is bound to occur in the crack tip plastic zones causing problems of temperature control.

The alternative pursued here is an automated test system that allows continuous testing, data collection, and load adjustments to be performed by computer in the absence of an operator. Automation minimizes testing time and operator attention while reducing data scatter, owing to higher precision in crack length measurement and better control of data point spacing. The automatic procedure is also relatively easy to implement with minimal operator

training, and it eliminates subjective interpretation and operator bias. In designing a cryogenic system we referred to the work of Liaw et al. [7], Williams et al. [12], and Cheng and Read [13] and incorporated additional modifications, consistent whenever possible with proposed and existing standards [14-16].

EXPERIMENTAL APPARATUS

The experimental apparatus consists of a 100-kN servohydraulic test machine and cryostat, a programmable digital oscilloscope, a programmable arbitrary waveform generator, a minicomputer, and an automatic liquid helium refill system. The complete apparatus is shown in figure 1.

The servohydraulic machine has an inverted stage with its actuator above a cantilevered cryostat load frame. The specimen is pinned at the bottom of the load frame and enclosed during cryogenic tests in a vacuum-insulated stainless steel Dewar. The frame columns are fiberglass-reinforced plastic tubes and the loading rod is plastic-impregnated wood. Nonmetallic materials of low thermal conductivity were employed to reduce the steady-state heat leak into the Dewar. The cryostat design and associated instrumentation are described in detail elsewhere [17-19].

The servohydraulic machine includes a servo control system with two dc conditioners, a valve drive, a signal amplifier, and a load cell. A conventional function generator and electrical cycle counter are also provided in the machine console but these are not used in automatic threshold fatigue testing. Instead, the fatigue cycle counts are calculated by computer from the test frequency and elapsed time, and a programmable arbitrary waveform generator is used since the applied load levels vary with time.

The programmable digital oscilloscope contains two 15-bit 100 kHz digitizers and serves as an analog-to-digital (A/D) converter. The problems en-

countered with slower A/D converters (interruptions during the testing and low test frequencies) are eliminated because of the high-speed A/D conversion rate and the freeze-and-hold memory capability of this oscilloscope. This unit also provides a continuous display of the load-versus-displacement relationship from which crack closure effects can be monitored.

The minicomputer includes a cathode ray tube (CRT) terminal, a line printer, a dual floppy disc storage unit, and a digital plotter. The minicomputer uses 16-bit words and has 128-K words of memory. The minicomputer also contains an internal clock that reads to 1/60 s. The IEEE-488/GPIB instrument interconnection bus is used for the interface between the computer and the programmable digital oscilloscope, and between the computer and the programmable arbitrary waveform generator. The sequence of operation and interactions between the various components is represented by a flow diagram in figure 2.

To keep the specimen fully submerged in liquid helium for continuous 24-h operation at 4 K, an automatic refill system was incorporated (figure 3). The system consists of a 30.5-cm superconducting liquid-level detector, a level controller, a conventional three-way solenoid valve, a pressurized helium gas cylinder, and a 500-ℓ liquid helium supply Dewar. A vacuum-jacketed flexible copper transfer line connects the supply Dewar to the cryostat. Except for this custom-built transfer line, all components of the liquid helium refill system were obtained commercially.

The liquid helium in the cryostat is monitored by the level detector, which is attached to one of the load frame columns. The desired minimum and maximum level limits are set on the controller, and these limits trigger the solenoid valve that regulates liquid helium transfer.

Operation is as follows: First, the supply Dewar is pressurized and liquid helium transfers into the cryostat. When the liquid reaches the

maximum limit, the solenoid switch vents the pressure in the supply Dewar to the atmosphere and the liquid helium transfer stops. As the fatigue test proceeds, the steady state boil-off gradually causes the liquid in the cryostat to fall to the minimum level. At this point the vent closes, the supply Dewar is repressurized, and liquid helium again transfers into the cryostat. When the maximum level is reached, the process repeats.

Tests at 4 K consume one standard K-cylinder of helium gas per day and 4.5 ℓ of helium per hour. The evaporated helium is released to the atmosphere and not recovered because the installation of a gaseous helium recovery and liquefaction system is too expensive at this time. Tests at other temperatures are also possible. For example, tests in liquid nitrogen at 76 K use a system similar to that shown in figure 3, but nitrogen is substituted for helium and a nitrogen level detector and controller are used.

SPECIMEN GEOMETRY AND CLIP GAGE

The compact specimen geometry chosen for this study is shown in figure 4. The specimen width (W) is 76.2 mm and the thickness (B) is 6.4 mm. The relatively large W/B ratio of 12 provides a sizable ligament for crack growth while minimizing the fatigue load requirements. The initial machined notch is 22.7-mm long (a/W ≅ 0.3) and the notch tip radius is 0.127 ± 0.05 mm. Specifications for grips, fixtures, and specimen preparation are detailed in ASTM E 647-83 and other relevant documents [14-16].

The clip gage used in threshold fatigue tests is a variant of the ring gage previously described [19]. We modified it to use very short beams which enable the gage to be tightly mounted close to the specimen. This stabilizes the gage against vibration and reduces the signal noise. Calibrations at 295, 76, and 4 K indicated that the gage calibration factors are independent of temperature to within 2 percent.

Crack length (a) is measured by the compliance technique with a clip gage mounted at the specimen edge. Compliance is defined as the specimen deflection per unit load, which depends on crack length for a given material and specimen geometry. The load cell and clip gage signals were interfaced to the computer, enabling the crack length to be inferred once per minute and displayed on the CRT terminal.

A flow chart for the automated near-threshold fatigue crack growth test is shown in figure 5. At the beginning of a test, the input parameters are typed into the computer through the CRT terminal. These parameters include specimen identification, specimen dimensions, Young's modulus, selected time interval for measuring crack length, intermediate load level for compliance measurement, initial ΔK_{max}, stress ratio, C' (defined below) and test frequency. The time interval for measuring crack length is short enough that the crack growth increments will not exceed the recommended values in ASTM E 647-83. The intermediate load level for compliance measurement is used to avoid errors due to crack closure effects [7,12].

As the specimen is fatigued under the prescribed loading conditions and cyclic frequency, a crack initiates and begins to grow. When the preselected time interval (1 min) for crack length measurement is reached, the computer requests the compliance data from the oscilloscope, which instantaneously freezes the load-versus-displacement signals in memory and transmits them to the computer. It correlates the data to a straight line using a linear least-squares fit. A linear correlation coefficient of 0.995 or better is usually obtained. From the resulting compliance, the instantaneous crack length is computed using Saxena and Hudak's [20] calibration function. The precision of the computed crack length is typically within 0.04 mm.

Only a portion of the load-versus-displacement curve is used for the compliance calculation (i.e., the part from a specified intermediate load level to a value corresponding to 95 percent of the maximum fatigue load). The specified intermediate load is typically the mean load, because this is usually larger than the crack closure loads. The upper 5 percent of the load is excluded to eliminate any noise in the signals at maximum load during high-frequency tests.

As the crack grows, the difference between the current-measured crack length and the last recorded crack length is checked against a specified value (0.5 mm), which is within the recommended values of ASTM E 647-83. If the increment of crack growth is equal to or greater than the specified value, the computer calculates N, ΔK, and da/dN. The line printer also prints the calculated compliance, the linear least-squares correlation coefficient, and the values a, N, da/dN, and ΔK. All these data are stored on floppy disks for use in post-test analyses.

In near-threshold fatigue tests, the loads are progressively decreased in the decreasing-ΔK technique. The load levels are calculated from the following equations [15]:

$$\Delta K = \Delta K_0 \exp[C'(a - a_0)] \tag{1}$$

$$\Delta P = BW^{\frac{1}{2}} \Delta K / f(a/W) \qquad \text{for the compact specimen} \tag{2}$$

$$P_{max} = \Delta P/(1 - R); \qquad P_{min} = P_{max} R \tag{3}$$

where

P_{max} = maximum load

P_{min} = minimum load

R = P_{min}/P_{max}

B = specimen thickness

W = specimen width

a = the current crack length

a_0 = the crack length at the beginning of the test

$f(a/W) = [2 + (a/W)][0.886 + 4.64(a/W) - 13.32(a/W)^2 + 14.72(a/W)^3$

$- 5.6(a/W)^4]/[1 - (a/W)]^{3/2}$

ΔK = current crack-tip stress-intensity range

ΔK_0 = crack-tip stress-intensity range at the beginning of the test

C' = a constant

For a typical decreasing-ΔK technique, C' (Eq. 1) is assigned a small, negative number such as -0.08. Other types of tests can also be performed, depending on the choice of the value of C'. For example: C' is set at a small positive value for an increasing-ΔK technique, or C' is set equal to zero for a constant-ΔK technique.

The sequence of operations is as follows (see figure 5): after each crack length measurement, the crack length is compared with the last stored crack length to ensure that a specified measurable amount of crack growth has occurred. If this is not done, then some unnecessary load level adjustments will take place because of scatter in the crack length measurement. After the crack grows a certain amount (e.g., 0.13 mm), the new ΔK is calculated from equation (1) and the new crack length is stored. The load levels are then adjusted using equations (2) and (3).

At the relatively high frequencies desired in near-threshold fatigue testing, hydraulic lag can occur. Then, the specimen is not actually subjected to the load range commanded by the computer (or waveform generator). Overprogramming is sometimes necessary to overcome the problem. Automatic overprogramming is a trial-and-error process whereby the computer monitors the values of P_{max} and P_{min} through the programmable digital oscilloscope and makes necessary changes to achieve the commanded values of P_{max} and P_{min}.

During the test, point-to-point data reduction is used to calculate ΔK and da/dN from a and N. If the results of ΔK versus da/dN scatter excessively, the seven-point incremental polynomial method can be used to smooth the results after the test is completed.

The computer programs for post-test analyses include the following capabilities:

1. Reducing a-versus-N data to ΔK-versus-da/dN by the seven-point incremental polynomial method;

2. Converting units;

3. Plotting data in desired units;

4. Plotting data in desired coordinate ranges;

5. Plotting data for several different specimens on one graph (for comparison);

6. Calculating the material constants C and n in the Paris equation da/dN = $C(\Delta K)^n$ [15] and drawing the regression line through the data.

It was observed in preliminary tests that crack closure, a common cause of nonlinear compliance behavior, became more pronounced at lower loads as the crack grew longer and the threshold region was approached. To minimize the influence of crack closure, ΔK_{th} determinations at relatively short a/W values were desired. For this reason the da/dN-versus-ΔK curves in this study were obtained in two steps. The rates from about 10^{-8} to 10^{-10} m/cycle were first measured by the decreasing-ΔK technique starting at ΔK = 15 MPa$\cdot$m$^{\frac{1}{2}}$ with C' = -0.08 and f = 40 Hz. After reaching ΔK_{th} at 10^{-10} m/cycle, the test was stopped. The second data set was then measured by the increasing-ΔK technique, starting again at about ΔK = 15 MPa$\cdot$m$^{\frac{1}{2}}$ but with C' = 0.10 and f = 10 or 20 Hz. This second data set provided the rates above 10^{-8} m/cycle and approaching 10^{-6} m/cycle.

For simplicity in this study, the da/dN-versus-ΔK curves and ΔK_{th} results are presented on the basis of the applied ΔK values with no corrections for crack closure. Since there are no accepted "standard" values for da/dN-versus-ΔK or ΔK_{th} for these materials, no meaningful statements can be made about the accuracy of results. The measurement precision is commensurate with current practice as discussed in the appropriate standards [14-16].

MATERIALS

The tested materials were plates of AISI 304L, 304LN, and 316 stainless steels in the as-received annealed condition. The AISI 304L and 304LN plates were 25-mm thick, whereas the AISI 316 plate was 50.8-mm thick. Tables 1 and 2 list the alloy compositions and 4-K mechanical properties. The near-threshold fatigue test specimens were machined in the TL orientation.

RESULTS AND DISCUSSION

The da/dN-versus-ΔK curves at R = 0.1 for the AISI 300 series austenitic stainless steels tested in this study are shown in figures 6 through 8. The fatigue crack growth rates extend four orders of magnitude, from 10^{-6} to 10^{-10} m/cycle, and are two orders of magnitude lower than any rates previously published for this alloy at cryogenic temperatures. At their lowest values (10^{-10} m/cycle) the rates correspond to 1 Angstrom per load cycle, or less than one lattice spacing per load cycle. The ΔK_{th} values (operationally de-fined at 10^{-10} m/cycle) for AISI 304L, 304LN, and 316 are 7.4, 8.3, and 8.5 MPa·m$^{\frac{1}{2}}$, respectively, at 4 K.

The data trend for AISI 304L (figure 6) is sigmoidal, as expected, but the rates for this heat at intermediate ΔK values are higher than rates re-ported for other AISI 304L heats. The alloy tested in this study has signif-icantly higher nitrogen and lower nickel content than previous heats [21], and these compositional variations likely contribute to the 4-K rate differences.

239

The data for AISI 304LN are compared with a trend for previous measurements [21] on the same plate of steel at higher ΔK levels in figure 7. The previous data represent tests of 25.4-mm-thick compact specimens (W/B = 2) of similar orientation and at frequencies from 20 to 25 Hz; the present data represent 6.4-mm-thick specimens (W/B = 12) at 20 Hz. The two independently determined trends are in reasonable agreement, although the previous measurements are slightly higher for unknown reasons. A similar observation is made for the AISI 316 stainless steel in figure 8, where comparison is again made with previous data [22] from 25.4-mm-thick specimens (W/B = 2) of the same plate of steel.

When the three steels are compared (figure 9) we see that the AISI 304L steel exhibits the lowest ΔK_{th} value while the values for AISI 304LN and 316 are nearly identical. A correction for crack closure might affect this comparison. Nevertheless, it appears that the differences in the near-threshold fatigue behaviors of these AISI 300 series steels at 4 K are not very great.

SUMMARY

A fully automatic computer-controlled apparatus was designed and assembled to conduct near-threshold fatigue crack growth rate tests at liquid helium temperature, 4 K. In response to crack growth as monitored by compliance measurements in 6.4-mm-thick compact specimens, the fatigue loads are systematically decreased until the operationally defined threshold for fatigue crack growth is reached at 10^{-10} m/cycle.

At present, a near-threshold test lasts 4 days with 24-h operation and is performed at a frequency of 40 Hz. Typically, thirteen million fatigue cycles are applied to a given specimen. The liquid helium consumption rate is

4.5 ℓ/h, and the total liquid helium cost is about $1500 per threshold measurement. Modifications continue to be made to improve the accuracy of the measurements and to reduce costs.

The present test system was used in a preliminary study of AISI 300 series stainless steels at 4 K and at a stress ratio of 0.1. The results consist of da/dN-versus-ΔK curves and threshold stress intensity factors, ΔK_{th}. The ΔK_{th} values for AISI 304L, 304LN, and 316 stainless steels are 7.4, 8.3, and 8.5, respectively. The scope of future testing will be expanded to include temperature, stress ratio, and frequency effects for these steels.

ACKNOWLEDGMENT

REFERENCES

1. R.J. Hooper, Use of crack propagation rate test data in establishing design allowable stresses, presented at the NBS/DOE Workshop on Materials at Low Temperatures, October 17-19, 1983, Vail, Colorado.

2. P. Komarek, Structural material investigation in conjunction with superconducting magnet projects, presented at the NBS/DOE Workshop on Materials at Low Temperatures, October 14-17, 1984, Vail, Colorado.

3. "Fatigue Crack Growth Threshold Concepts," D.L. Davidson and S. Suresh, Eds., Metallurgical Society of the AIME, Warrendale, Pennsylvania (1984), p. 565.

4. "Fatigue Thresholds - Fundamentals and Engineering Applications," Vols. I and II, J. Bäcklund, A.F. Blom, and C.J. Beevers, Eds., Engineering Materials Advisory Services, Ltd., Chameleon Press, London (1982), p. 1174.

5. R.O. Ritchie, Near-threshold fatigue-crack propagation in steels, Int. Met. Rev., Rev. 245, Nos. 5 and 6: 205-230 (1979).

6. P.K. Liaw, W.A. Logsdon, and M.H. Attaar, Computerized near-threshold fatigue crack growth rate testing at cryogenic temperatures: technique and results, in: "Fatigue at Low Temperatures," ASTM STP 859, R.I. Stephens, Ed., American Society for Testing and Materials, Philadelphia, Pennsylvania (1985).

7. P.K. Liaw, W.A. Logsdon, and M.H. Attaar, Automated near-threshold fatigue crack growth rate testing of JBK-75 stainless steel at cryogenic temperatures, in: "Austenitic Steels at Low Temperatures," R.P. Reed and T. Horiuchi, Eds., Plenum Press, New York (1983), pp. 171-185.

8. Y. Katz, A. Bussiba, and H. Matthias, Transitions in fatigue processes at low temperatures, in: "Advances in Cryogenic Engineering -- Materials," Vol. 30, A.F. Clark and R.P. Reed, Eds., Plenum Press, New York (1984), pp. 339-347.

9. E.K. Tschegg and S.E. Stanzl, Fatigue crack propagation and threshold in bcc and fcc metals at 77 and 293 K, Acta Metall. 29:33-40 (1981).

10. S. Stanzl and R. Mitsche, High frequency fatigue of metals, crack initiation and propagation, in: "Fracture 1977," Vol. 2, D.M.R. Taplin, Ed., University of Waterloo Press, Waterloo, Ontario, Canada (1977), pp. 749-753.

11. E.K. Tschegg, R.O. Ritchie, and S.E. Stanzl, Ultrasonic methods for determination of near-threshold fatigue crack growth rates in "Fatigue Thresholds - Fundamentals and Engineering Applications," Vol. I, J. Bäcklund, A.F. Blom, and C.J. Beevers, Eds., Engineering Materials Advisory Services, Ltd., Chameleon Press, London (1982), pp. 99-112.

12. R.S. Williams, P.K. Liaw, M.G. Peck, and T.R. Leax, Computer-controlled decreasing ΔK fatigue threshold test, Eng. Fract. Mech. 18:953-964 (1983).

13. Y.W. Cheng and D.T. Read, An automated fatigue crack growth rate test system, in: "Automated Test Methods for Fracture and Fatigue Crack Growth," ASTM STP 877, American Society for Testing and Materials, Philadelphia, Pennsylvania, to be published.

14. Standard test method for constant amplitude fatigue crack growth rates above 10^{-8} m/cycle, ASTM Designation E 647-83, in: "1984 Annual Book of ASTM Standards, Metals - Mechanical Testing; Elevated and Low-Temperature Tests," Section 3, Vol. 03.02, American Society for Testing and Materials, Philadelphia, Pennsylvania (1984), pp. 711-731.

15. Proposed ASTM test method for measurement of fatigue crack growth rates, Appendix II in: "Fatigue Crack Growth Measurement and Data Analysis," ASTM STP 738, S.J. Hudak, Jr. and R.J. Bucci, Eds., American Society for Testing and Materials, Philadelphia, Pennsylvania (1981), pp. 340-356.

16. R.J. Bucci, Development of a proposed ASTM standard test method for near-threshold fatigue crack growth rate measurement, in: "Fatigue Crack Growth Measurement and Data Analysis," ASTM STP 738, S.J. Hudak, Jr. and R.J. Bucci, Eds., American Society for Testing and Materials, Philadelphia, Pennsylvania (1981), pp. 5-28.

17. C.W. Fowlkes and R.L. Tobler, Fracture testing and results for a Ti-6Al-4V alloy at liquid helium temperature, Eng. Fract. Mech. 8:487-500 (1976).

18. D.T. Read and R.L. Tobler, Mechanical property measurements at low temperatures, in: "Advances in Cryogenic Engineering--Materials," Vol. 28, R.P. Reed and A.F. Clark, Eds., Plenum Press, New York (1982), pp. 17-28.

19. R.L. Tobler and J.A. Shepic, Design and performance of a ring-shaped clip gage for fracture mechanics testing, submitted to J. Test. Eval.

20. A. Saxena and S.J. Hudak, Jr., Review and extension of compliance information for common crack growth specimens, Int. J. Fract. 14:453-468 (1978).

21. R.L. Tobler and R.P. Reed, Interstitial carbon and nitrogen effects on the cryogenic fatigue crack growth of AISI 304 type stainless steels, J. Test. Eval. 12:364-370 (1984).

22. D.T. Read and R.P. Reed, Fracture and strength properties of selected austenitic stainless steels at cryogenic temperatures," in: "Materials Studies for Magnetic Fusion Energy Applications at Low Temperatures -- II," NBSIR 79-1609, National Bureau of Standards, Boulder, Colorado (1979), pp. 81-122.

Table 1. Composition of test materials (wt. %).

Material	Fe	C	Mn	P	S	Si	Cr	Ni	Cu	Mo	Co	N
AISI 304L	bal.	0.020	1.73	0.024	0.005	0.62	18.20	8.56	0.24	0.40	0.16	0.082
AISI 304LN	bal.	0.037	1.50	0.022	0.017	0.57	18.0	9.91	0.197	0.205	----	0.120
AISI 316	bal.	0.057	1.86	0.024	0.019	0.58	17.25	13.48	----	2.34	----	0.030

Table 2. Measured mechanical properties of test materials.

Material	Test Temp. (K)	Yield Strength (MPa)	Ultimate Strength (MPa)	Elongation (%)	Reduction of Area (%)	Rockwell Hardness (R_B)
AISI 304L	295	245	642	66	77	82
	4	610	1678	35	48	--
AISI 304LN	295	279	612	68	62	79
	4	745	1570	34	42	--
AISI 316	295	228	576	56	73	79
	4	711	1301	48	57	--
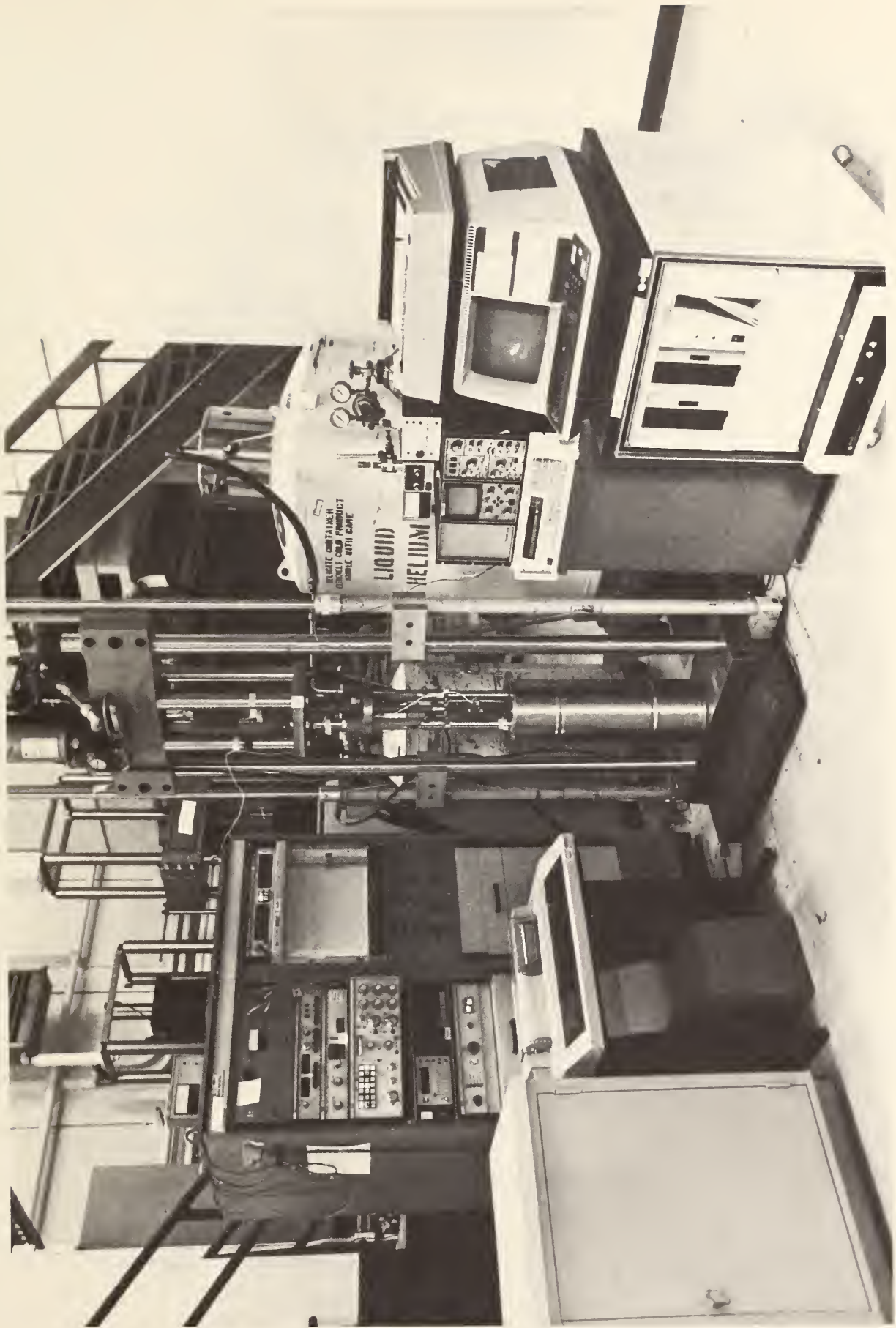
Figure 1 Fully automatic cryogenic near-threshold fatigue crack growth rate test apparatus used in this study.

245
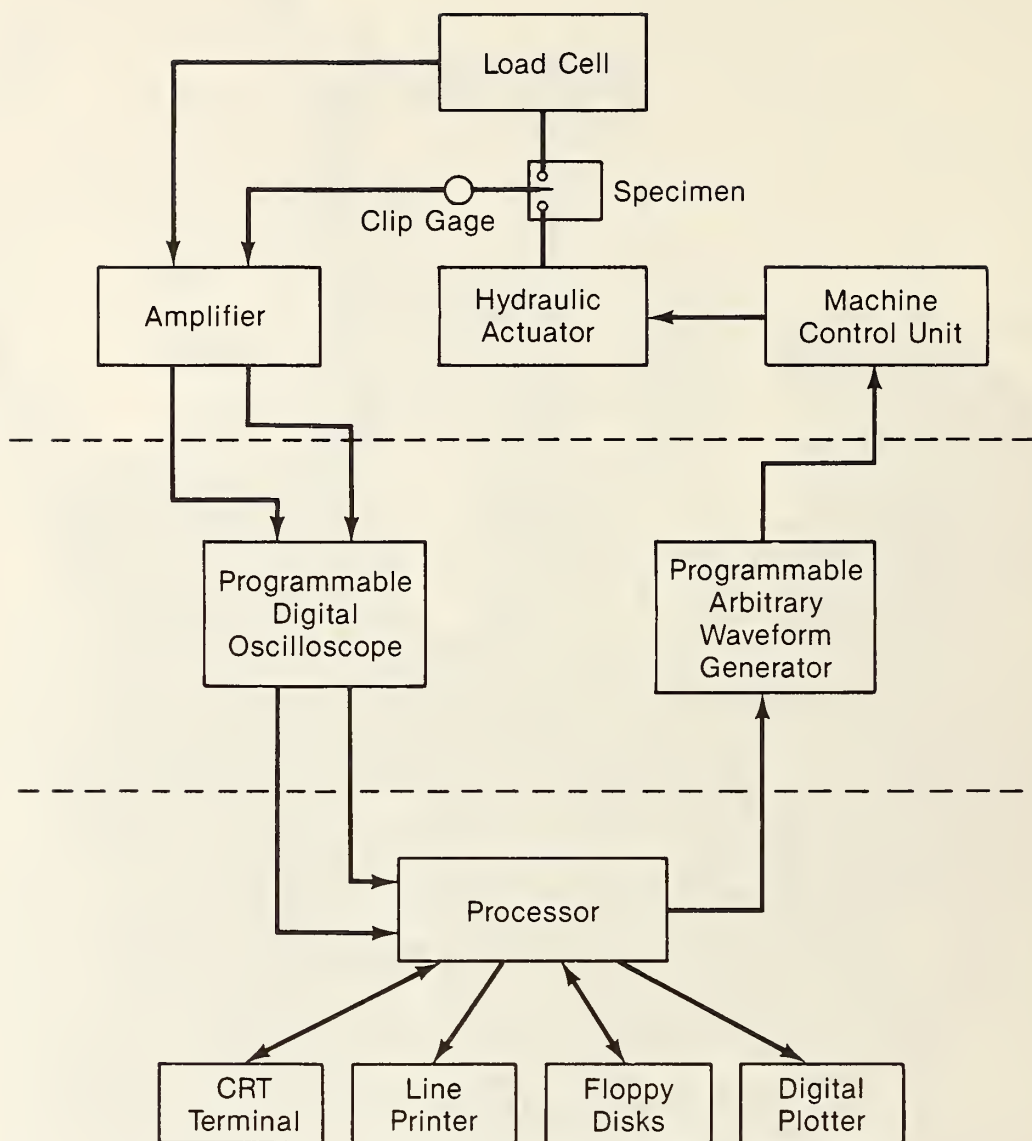
Figure 2 A flow chart of the automatic fatigue crack growth rate test system.
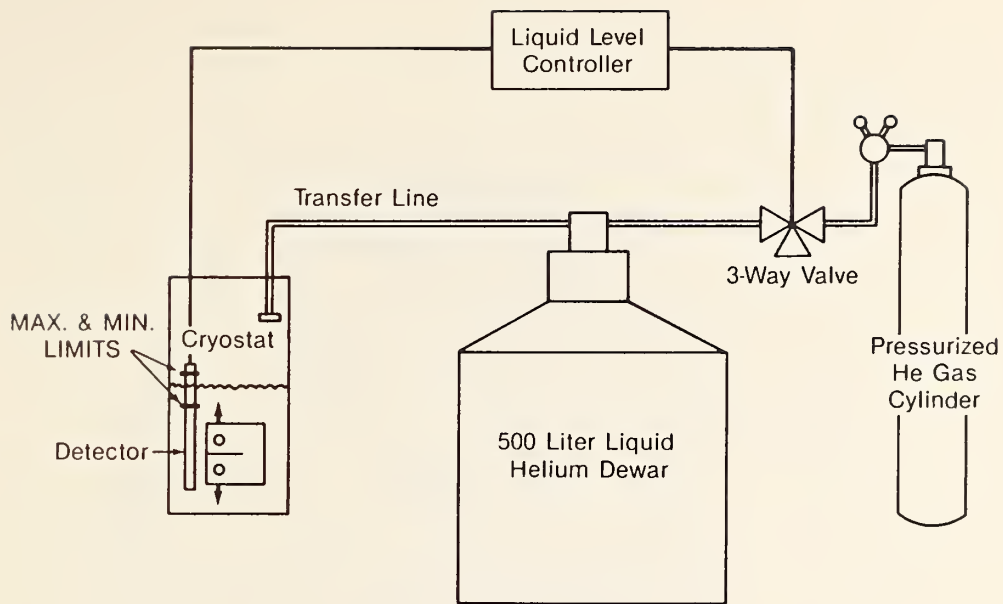
Figure 3   A schematic of the automatic liquid helium refill system.
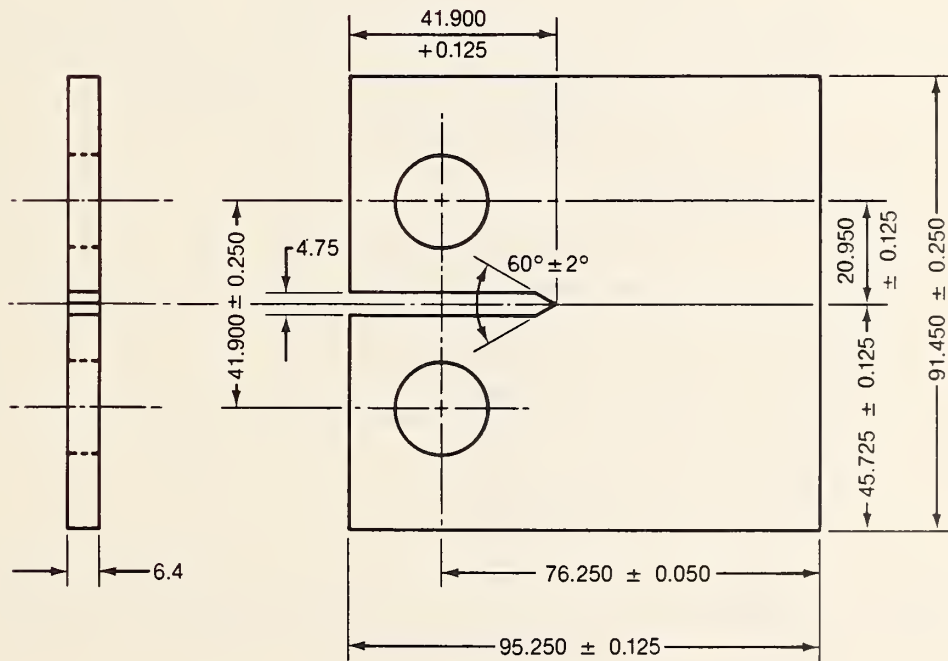
Finish $\overset{32}{\vee}$, except holes, as noted.
(Dimensions in millimeters)

Figure 4   The compact-type test specimen used in this study.
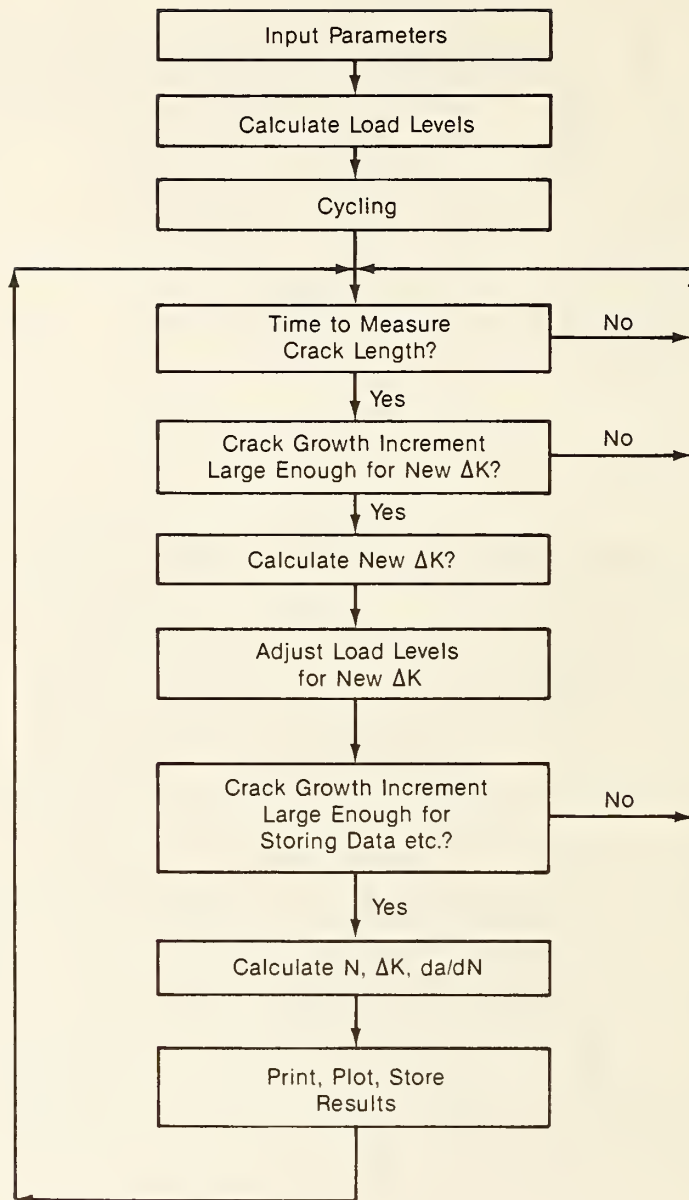
Figure 5   A summary flow chart of the automated near-threshold
fatigue crack growth rate test.
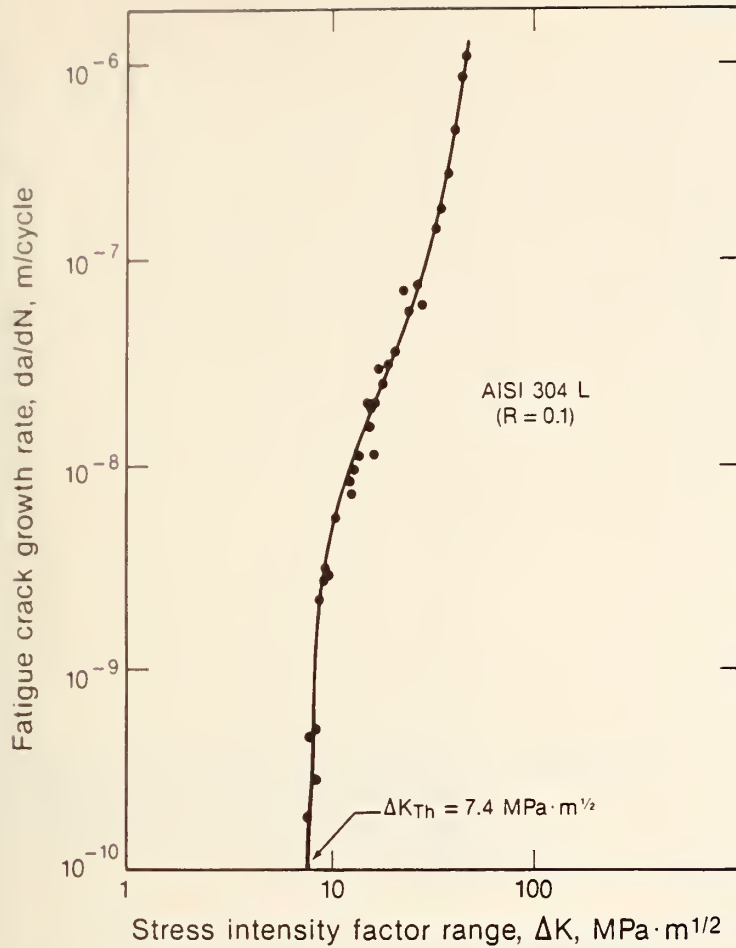
Figure 6   Fatigue crack growth rate data and threshold stress intensity factor for AISI 304L stainless steel at 4 K.
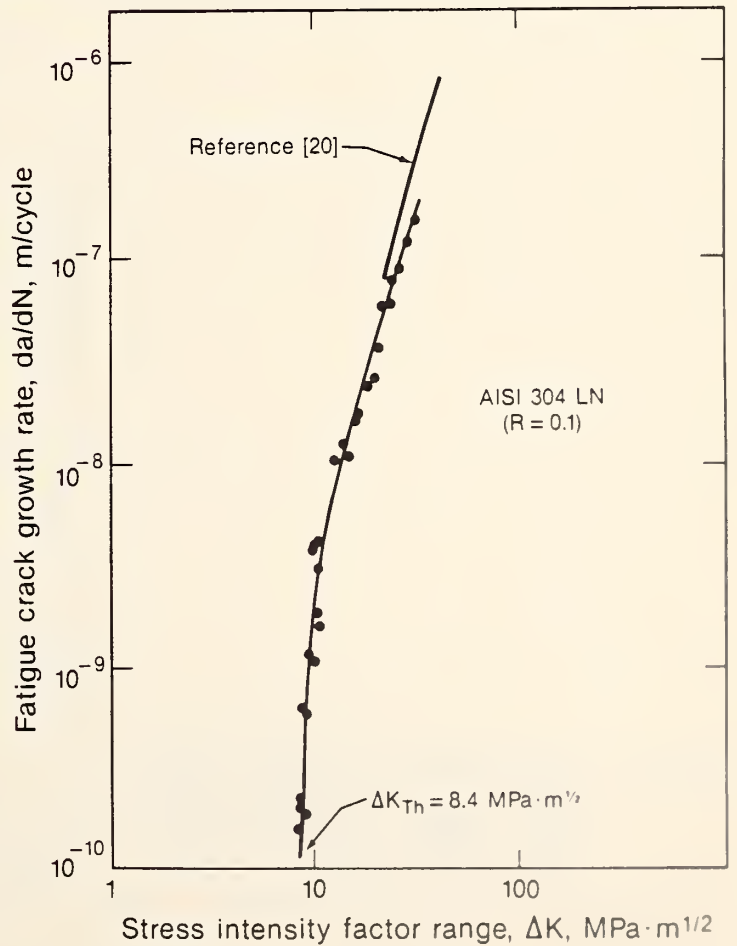
Figure 7   Fatigue crack growth rate data and threshold stress intensity factor for AISI 304LN stainless steel at 4 K.
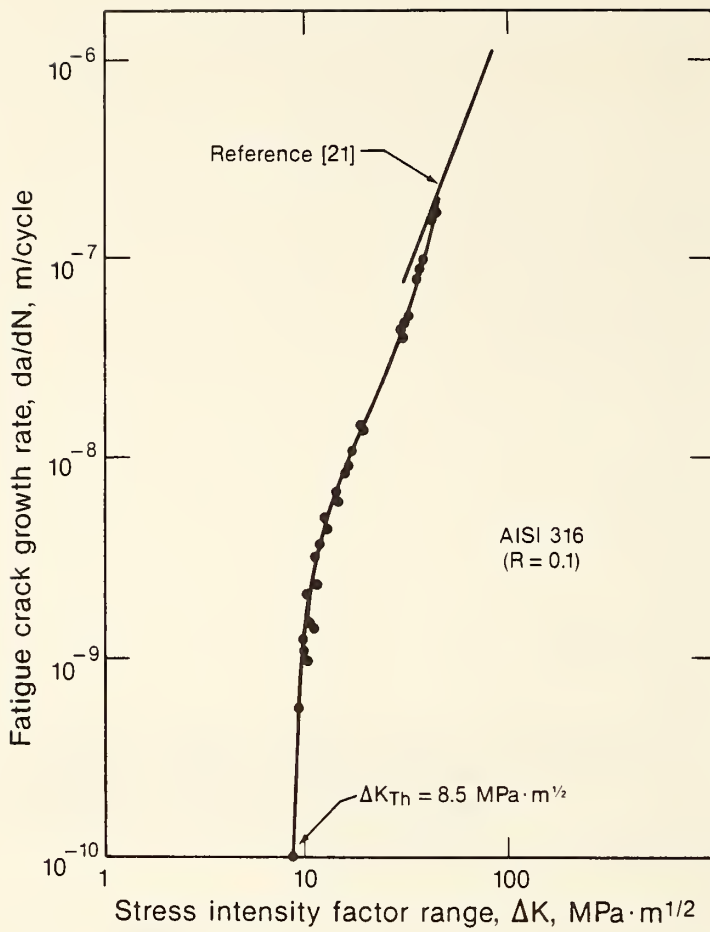
Figure 8   Fatigue crack growth rate data
and threshold stress intensity
factor for AISI 316 stainless
steel at 4 K.
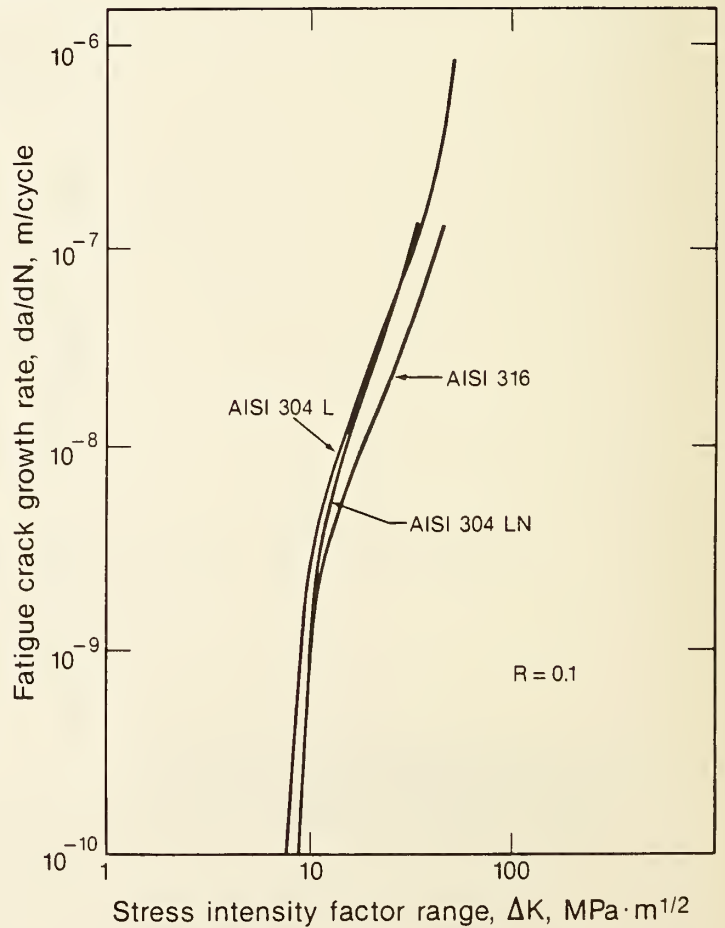
Figure 9   Comparison of fatigue crack
growth rate curves for AISI
304L, 304LN, and 316 stain-
less steels at 4 K.

FATIGUE CRACK INITIATION FROM NOTCHES
IN AUSTENITIC STAINLESS STEELS†

R. L. Tobler and Q. S. Shu*

Fracture and Deformation Division

National Bureau of Standards

Boulder, Colorado

Fatigue crack initiation from notches in austenitic stainless steels was studied for the first time using compact specimens of two common cryogenic alloys: AISI 316 and AISI 304L. The procedure is based on a fracture mechanics technique whereby $\Delta K \cdot \rho^{-1/2}$, a parameter proportional to the change in maximum elastic stress at the notch root, is correlated with the cycles to initiate a 0.254-mm crack. The effects of some experimental variables including notch radius, stress level, specimen size, and test temperature (295, 76, and 4 K) are presented, and the fatigue crack initiation resistances of the AISI 316 and 304L austenitic steels are compared with martensitic and ferritic/pearlitic steel data at room temperature.

Key words: austenitic stainless steels; cryogenic properties; fatigue; fatigue crack initiation; fracture mechanics; notch tip radius effect.

---

*Visiting scholar on leave from Zhejiang University, Hangzhou, People's Republic of China.

INTRODUCTION

Fatigue crack initiation, long neglected in fatigue studies of structural alloys at cryogenic temperatures, is explored in this paper using the fracture mechanics approach promoted by Jack and Price [1]. This approach assumes that the crack initiation life of a notched specimen correlates with the maximum elastic stress, S_{max}, in the material ahead of the notch, and that S_{max} is proportional to the parameter $K \cdot \rho^{-1/2}$, where K is the applied nominal stress intensity factor range and ρ is the notch tip radius. Thus:

$$2K \cdot (\pi\rho)^{-1/2} = S_{max} = k_t S \qquad (1)$$

where k_t is an elastic stress concentration factor and S is the nominal stress.

In Eq. 1, the nominal K is obtained from standard stress intensity expressions where the notch length, ℓ, is used as if it were equivalent to a sharp crack of length a. Justification for this derives from analysis showing that the elastic stress field distribution ahead of a blunt crack is similar in many respects to that ahead of a sharp crack [2]. If the notch length is much larger than ρ, Eq. 1 is accurate to within 10% [3,4]; if not, another method must be used because the notch is no longer crack-like in form.

Further rationale for the use of $K \cdot \rho^{-1/2}$ or S_{max} for the characterization of fatigue crack initiation at notches is set forth by Rolfe and Barsom [5] and also by Dowling [6]. Previous studies have considered only martensitic and ferritic/pearlitic steels at room temperature [7-16]. This paper represents the first application to austenitic stainless steels at 295, 76, and 4 K. Several variables influencing the results for austenitic stainless steels are examined: notch radius, stress level, test temperature, and specimen size. Fatigue crack initiation threshold behavior is also considered, and it is concluded that the performance of austenitic stainless steels can not be predicted from the established trends for nonaustenitic steels at room temperature.

MATERIALS

Commercial grade AISI 316 and AISI 304L austenitic stainless steel plates were tested in their as-received (annealed) conditions. These steels are microstructurally stable at 295 K, but they exhibit partial martensitic phase transformations during tests at 76 and 4 K. The mill chemical compositions of these steels in weight percent are listed in Table 1. The conventional mechanical properties are listed in Table 2.

SPECIMENS

The majority of tests used 6.4-mm-thick compact specimens, as shown in Fig. 1. These specimens were 76-mm wide and had notch radii of 0.127 ± 0.051 mm. A series of 25.4-mm-thick, 50.8-mm-wide specimens was also prepared to demonstrate the specimen size effect. The notches were machined such that the normal to the notch plane was in the transverse direction of the plate, and the direction of crack propagation was in the longitudinal direction of the plate (TL orientation [17]). To study the notch radius effect, variations of ρ ranging from 0.076 to 1.27 mm were created by grinding ($\rho \leq 0.9$ mm) or drilling ($\rho \geq 0.9$ mm). The notch radii were measured from profile photographs on both faces of the specimen and the minimum ρ was used. There were no subsequent notch tip preparations, such as annealing or polishing.

TEST PROCEDURE

Crack initiation was detected by compliance measurements (deflection per unit load) using a clip gage mounted at the specimen edge. The specimens were cycled at a stress ratio of 0.1 and at frequencies up to 20 Hz, with periodic interruptions for single-cycle loadings at 0.02 Hz. During single-cycle loadings, the load cell and clip gage signals were fed into a minicomputer for

real-time data reduction, and a standard compliance function was used to infer crack lengths. The computer-assisted technique was developed by Cheng and Read [18].

Plots of crack length versus cycles (a versus N) were recorded and analyzed for the crack initiation data. Crack initiation was defined at N_i as the number of cycles to achieve a 0.254-mm increment of growth, Δa_i. The values of N_i were then plotted versus $\Delta K \cdot \rho^{-1/2}$ or $\Delta K \cdot \rho_o^{-1/2}$, where ρ_o is a critical radius defined below, and $\Delta K = K_{max} - K_{min}$ for the fatigue load cycle. Finally, a threshold for fatigue crack initiation was defined as the value of $\Delta K \cdot \rho_o^{-1/2}$ at $N_i = 10^6$ cycles. The threshold corresponds to a level of stress for which fatigue cracks do not initiate below 10^6 cycles, and its significance for nonaustenitic steels is discussed by Rolfe and Barsom [5].

During each test the fatigue loads were constant, and ΔK increased with Δa. However, the ΔK increase for $\Delta a_i = 0.254$ mm at constant load was negligible, less than 5%. Progressively deeper notches were machined after each crack initiation measurement so that each specimen could be used three times.

COMPLIANCE ANOMALY AND DEFINITION OF CRACK INITIATION

A typical a-versus-N curve is shown in Fig. 2. Shortly after the test began there was an apparent decrease of crack length owing to an anomalous compliance decrease. With continued cycling the compliance gradually increased as a consequence of true crack initiation and growth, the net result being a shallow minimum in the a-versus-N curves at each temperature. Possible explanations for this anomaly are offered later in discussion.

Various definitions of crack initiation have been used since the choice is arbitrary and dependent on test procedure. In previous studies at 295 K, N_i was most often defined as the number of cycles needed to initiate a

0.254-mm crack, as determined by visual observation of the notch tip with a traveling microscope. In this study using the compliance technique, N_i was taken a full 0.254-mm increment beyond the true starting notch length. Increasing Δa_i would shift N_i to higher cycles (see Fig. 3), but this would only slightly increase the measured threshold for crack initiation as indicated in Fig. 4.

RESULTS

Notch Radius Dependence

The effect of notch radius on fatigue crack initiation was studied at 76 K for three material/ΔK combinations. In each case, ρ was varied while ΔK was held constant. The resulting plots of ρ-versus-N_i, shown in Figs. 3 and 5, have two regions. In the first region, N_i apparently is independent of ρ, and in the second region N_i increases with ρ, according to a nonlinear function. The critical radius, ρ_0, is found at the intersection of the two trends, and it represents a radius below which further increases in notch acuity have no effect on crack initiation life.

To determine ρ_0, several polynomial expressions were fit to the ρ-versus-N curves, but the results were strongly biased by the number of terms in the polynomial. Instead, Fig. 6 presents plots of $\Delta K \cdot \rho^{-1/2}$ versus N_i on natural logarithmic coordinates. Such plots facilitate the determination of ρ_0 since the data are then subject to linear least squares fits. The values of ρ_0 deduced from the intersection points of Fig. 6 are:

AISI 316 (T = 76 K, ΔK = 46 MPa·m$^{1/2}$): ρ_0 = 0.255 mm

AISI 316 (T = 76 K, ΔK = 23 MPa·m$^{1/2}$): ρ_0 = 0.175 mm

AISI 304L (T = 76 K, ΔK = 46 MPa·m$^{1/2}$): ρ_0 = 0.290 mm

The ρ_0 values for AISI 316 and AISI 304L at 76 K and ΔK = 46 MPa·m$^{1/2}$ are nearly equivalent. These results are also equivalent to the result for mild

steel where ρ_o = 0.25 mm at 295 K [1]. The AISI 316 results suggest a possible ρ_o dependence on ΔK, but this point is uncertain owing to sizable data scatter.

Material Dependence

The fatigue crack initiation resistances of the two austenitic stainless steels at 76 K are compared in Fig. 7. These data were obtained using specimens of constant radius, ρ = 0.127 ± 0.050 mm. Since this radius is lower than ρ_o, the data are plotted in terms of $\Delta K \cdot \rho_o^{-1/2}$. This provides a more meaningful correlation since any radius lower than ρ_o would not affect the crack initiation life.

As shown in Fig. 7, the data for the two steels at 76 K appear to be grouped relatively close together over most of the range of N, but the threshold is 25% higher for AISI 304L than for AISI 316. The ultimate tensile strength, σ_u, for AISI 304L is also about 22% higher than that of AISI 316 at 76 K (see Table 2). The threshold, therefore, appears to be material dependent and correlates to σ_u, as brought out further in discussion.

Temperature Dependence

Figures 8 and 9 show the effects of test temperature on crack initiation resistance. The curves at all three temperatures (295, 76, and 4 K) were constructed using the ρ_o values measured at 76 K (0.255 for AISI 316 and 0.290 for AISI 304L). This approximation introduces uncertainty in the 295- and 4-K results but was tolerated because the precise temperature dependence of ρ_o is unknown and would be costly to determine. For AISI 316, Fig. 8 indicates that the crack initiation resistance increases monotonically with temperature reductions from 295 to 76 to 4 K. The 76 and 4 K data converge at high N, so that the thresholds at 76 and 4 K are nearly equivalent and higher than at 295 K.

For AISI 304L, Fig. 9 indicates somewhat different behavior: Again, the crack initiation resistance is higher at 76 and 4 K than at 295 K. However, the 76- and 4-K curves crossover at $N_i = 2 \times 10^5$ cycles. Consequently, for N_i less than 2×10^5, the fatigue crack initiation resistance is lower at 4 K than at 76 K, whereas for N_i greater than 2×10^5, the 4-K resistance is equivalent or slightly higher than that at 76 K.

Specimen Size

Figure 10 compares 76-K crack-initiation data of 6.4- and 25.4-mm-thick specimens taken from the same heat of AISI 316 steel. The width-to-thickness ratios for these specimens are 12 and 2, respectively. A specimen size effect is demonstrated, in that crack initiation occurs sooner in the 25.4-mm-thick specimens for all values of $\Delta K \cdot \rho_0^{-1/2}$. The threshold is also 20% lower for the thicker specimens.

There are two possible explanations for the size effect. First, a plastic constraint effect may be operative such that the crack initiation resistance is actually lower for the 25.4-mm-thick × 50.8-mm-wide specimens than for the 6.4-mm × 76-mm specimens. Otherwise the size effect may reflect a limitation owing to the use of a nominal ΔK, as mentioned in the discussion below.

DISCUSSION

The use of a nominal ΔK value to describe notch conditions has been criticized, since early crack growth is controlled by the notch tip plastic strain, and since linear elastic fracture mechanics loses significance for small cracks [19,20]. However, the notch tip strains responsible for fatigue should correlate with $\Delta K \cdot \rho^{-1/2}$ if the notch tip stresses are relatively small [6,13], and the $\Delta K \cdot \rho^{-1/2}$-versus-$N_i$ correlations should still be tenable,

assuming that the notch tip plasticity is similar for specimens having similar values of $\Delta K \cdot \rho^{-1/2}$ [6]. Recently, several models were derived in support of the $\Delta K \cdot \rho^{-1/2}$-versus-$N_i$ correlations [21,22]. Therefore, additional experimental work is required to verify the useful limits of these correlations.

Several practical problems of this method became evident in this study. First, the definition of fatigue crack initiation at $\Delta a_i = 0.254$ mm is arbitrary, and its measurement is affected by the compliance anomaly (Fig. 2). An apparent decrease of crack length with fatigue cycling was also observed in the work of Heubaum and Fine [23]. They attribute the anomaly to the influence of residual compressive stresses induced during the development of the notch tip plastic zone, or else to an increase in the amount of out-of-plane displacement. Another possible explanation from Nicholas et al. [24] involves a change in the three-dimensional stress state with cycling such that there is a stiffening of the effective modulus of the material in the direction normal to the notch plane.

Another problem arose in connection with the critical radius, ρ_0. Our findings suggest that ρ_0 may be mildly dependent on the ΔK level. Also, ρ_0 might be temperature dependent, because these austenitic steels are microstructurally stable at 295 K but unstable (i.e., transforming to martensite) at 76 and 4 K. To determine ρ_0 precisely for each set of experimental conditions would require considerable effort and expense. On the other hand, assuming that ρ_0 is constant at 295, 76, and 4 K increased the uncertainty of results in Figs. 8 and 9. Future tests should use notches with ρ greater than ρ_0 to avoid this problem.

Despite these problems, the fracture mechanics method of this study provided useful information on fatigue crack initiation resistance. Qualitative agreement is evident between present results and expectations from conventional S-N fatigue tests. Conventional S-N tests involve both crack initiation and

crack propagation, but crack initiation strongly predominates in the high-cycle range. For $N \cong 10^6$, the crack initiation stage may account for up to 90% of the total fatigue life. Therefore, some correlation is expected between fatigue crack initiation test results and S-N test data in the high-cycle range.

In general, conventional S-N data for metals at constant temperature show a trend of increasing fatigue life with increasing σ_u. Also, a metal's fatigue resistance typically increases at low temperatures owing to an increase of σ_u. Thus, the thresholds for crack initiation for both alloys in this study increased at cryogenic temperatures (Figs. 8 and 9). Also, in Fig. 7, the ~25% higher threshold for AISI 304L relative to that of AISI 316 at 76 K ranks in proportion to the 22% difference in σ_u for these alloys.

As noted earlier, fatigue crack initiation from notches in nonaustenitic steels has been extensively studied at 295 K, and excellent correlations have been established between the threshold and tensile properties (σ_y or σ_u). Generally, the threshold increases with increasing strength, until at sufficiently high strengths ($\sigma_y \cong 965$ MPa or $\sigma_u \cong 1035$ MPa) there is no longer any effect [5]. In Fig. 11, the data trends for martensitic and ferritic/pearlitic steels at 295 K are represented and compared with the austenitic stainless steel data from this paper at 295, 76, and 4 K.

The thresholds for the two austenitic steels increase with σ_y or σ_u at low temperatures owing to higher strengths, but otherwise there appears to be no similarity between the austenitic and nonaustenitic steel behaviors. The correlation of thresholds with σ_y (Fig. 11) for austenitic steels is especially poor. Several plausible reasons for this difference in material dependence can be given. Under stable conditions (295 K) the austenitic steels workharden according to significantly different stress-strain laws, whereas under metastable conditions (76 or 4 K) the austenitic steels transform partially to

martensitic phases with very high work-hardening capacities. Moreover, conventional S-N fatigue data for ferritic steels show a true fatigue limit near 10^6 cycles, whereas austenitic steels do not. Instead, austenitic steels are characterized by an endurance limit that continues to decrease in the high-cycle range between 10^6 and 10^9 cycles. In this study, a fatigue crack initiation threshold was arbitrarily defined at $N_i = 10^6$ cycles. Tests continuing to 10^9 cycles may have given different results, but such tests are time consuming and costly at 4 K, and are therefore beyond the scope of present study.

SUMMARY AND CONCLUSIONS

A fracture mechanics approach to the characterization of fatigue crack initiation at notches was applied for the first time to AISI 316 and 304L austenitic stainless steels at 295, 76, and 4 K. The data presented here are potentially useful for estimating the crack initiation life of components and for correlating with other mechanical properties, including conventional tensile or S-N fatigue data. The following conclusions emerged:

1) The a-versus-N curves inferred by specimen compliance measurements reveal an anomalous effect whereby the system stiffens and the crack length apparently decreases by several percent. This anomaly occurs just after fatigue cycling begins and, apparently, prior to crack initiation.

2) The fatigue crack initiation resistance of austenitic stainless steels tends to decrease with decreasing notch tip radius until a critical radius is reached, below which there is no further effect.

3) The fatigue crack initiation resistance of AISI 316 and AISI 304L austenitic stainless steels increases at cryogenic temperatures, and the increase at $N_i = 10^6$ cycles approximately correlates with the increase in ultimate tensile strength.

4) The fatigue crack initiation resistance of AISI 316 and AISI 304L austenitic stainless steels is subject to a specimen size effect at 76 K.

5) The fatigue crack initiation threshold behavior of austenitic stainless steels is dissimilar to and can not be predicted from the established correlations for martensitic and ferritic/pearlitic steels at 295 K.

ACKNOWLEDGMENT

REFERENCES

1. A.R. Jack and A.T. Price, The initiation of fatigue cracks from notches in mild steel plates, Int. J. Fract. Mech. 6, 401-409 (1970).

2. M. Creager and P.C. Paris, Elastic field equations for blunt cracks with reference to stress corrosion cracking, Int. J. Fract. Mech. 3, 247-252 (1968).

3. T.D. Dudderar and E.M. Doerries, A study of effective crack length using holographic interferometry, Exp. Mech. 16, 300-304 (1976).

4. K. Heckel and R. Wagner, The tensile fatigue behavior of CT specimens with small notch root radius, Int. J. Fract. 11, 135-140 (1975).

5. S.R. Rolfe and J.M. Barsom, Fracture and Fatigue Control in Structures, Applications of Fracture Mechanics, Prentice Hall, Englewood Cliffs, New Jersey, 208-231 (1977).

6. N.E. Dowling, Fatigue at notches and the local strain and fracture mechanics approaches, Fracture Mechanics, ASTM STP 677, American Society for Testing and Materials, Philadelphia, 247-273 (1979).

7. R.G. Forman, Study of fatigue crack initiation from flaws using fracture mechanics theory, Eng. Fract. Mech. 4, 333-345 (1972).

8. M.B.P. Allery and G. Birbeck, Effect of notch root radius of the initiation and propagation of fatigue cracks, Eng. Fract. Mech. 4, 325-331 (1972).

9.   J.M. Barsom and R.C. McNicol, Effect of stress concentration on fatigue crack initiation in HY-130 steel, Fracture Toughness and Slow Stable Cracking, ASTM STP 559, American Society for Testing and Materials, Philadelphia, 183-204 (1974).

10. W.G. Clark, Jr., Evaluation of the fatigue crack initiation properties of type 403 stainless steel in air and steam environments, Fracture Toughness and Slow Stable Cracking, ASTM STP 559, American Society for Testing and Materials, Philadelphia, 205-224 (1974).

11. J.T. Barnby and R. Holder, Fatigue properties of a cast steel, Int. J. Fract. 12, 631-637 (1976).

12. A. Baus, H.P. Lieurade, G. Sanz, and M. Truchon, Correlation between the fatigue crack initiation at the root of a notch and low-cycle fatigue data, Flaw Growth and Fracture, ASTM STP 631, American Society for Testing and Materials, Philadelphia, 96-111 (1977).

13. W.G. Clark, Jr., Stress-corrosion crack initiation in high strength type 4340 steel, Flaw Growth and Fracture, ASTM STP 631, American Society for Testing and Materials, Philadelphia, 121-138 (1977).

14. Y.H. Kim, T. Mura, and M.E. Fine, Fatigue crack initiation and microcrack growth in 4140 steel, Metall. Trans. 9A, 1679-1683 (1978).

15. B.L. Braglia, R.W. Hertzberg, and R. Roberts, Crack-initiation in a high-strength low alloy steel, Fracture Mechanics, ASTM STP 677, American Society for Testing and Materials, Philadelphia, 290-302 (1979).

16. R. Brook, A. Cadman, and C.E. Nicholson, Initiation of short cracks at notches by fatigue, Proceedings of ICF International Symposium on Fracture Mechanics, Science Press, Beijing, China, 624-628 (1983).

17. Standard terminology relating to fracture testing, ASTM designation: E 616-82, 1984 Annual Book of ASTM Standards, American Society for Testing and Materials, Philadelphia, 671-684 (1984).

18. Y.W. Cheng, and D.T. Read, An automated fatigue crack growth rate test system, Automated Test Methods for Fracture and Fatigue Crack Growth, ASTM STP 877, American Society for Testing and Materials, Philadelphia, to be published.

19. R.A. Smith, A simplified method of predicting the rates of growth of cracks initiated at notches, Fracture Mechanics in Engineering Practice, Applied Science Publications, London, 173-182 (1977).

20. R.A. Smith and K.J. Miller, Prediction of fatigue regimes in notched components, Int. J. Mech. Sci. 20, 201-206 (1978).

21. K. Tanaka, Y. Nakai, and R. Kawashima, Fracture mechanics approach to fatigue crack initiation from deep notches, Eng. Fract. Mech. 18, 1011-1023 (1983).

22. K. Tanaka and T. Mura, A micromechanical theory of crack initiation from notches, Mech. Mater. 1, 63-73 (1981).

23. F. Heubaum and M.E. Fine, Short fatigue crack growth behavior in a high strength low alloy steel, Scripta Metall. <u>18</u>, 1235-1240 (1984).

24. T. Nicholas, N.E. Ashbaugh, and T. Weerasooriya, On the Use of Compliance for Determining Crack Length in the Inelastic Range, <u>Fracture Mechanics</u>, ASTM STP 833, R.J. Sanford, Ed., American Society for Testing and Materials, Philadelphia, 682-698 (1984).

Table 1.   Composition of test materials (wt.%).

Material	Fe	C	Mn	P	S	Si	Cr	Ni	Cu	Mo	Co	N
AISI 304L	bal.	0.020	1.73	0.024	0.005	0.62	18.20	8.56	0.24	0.40	0.16	0.082
AISI 316	bal.	0.057	1.86	0.024	0.019	0.58	17.25	13.48	--	2.34	--	0.030

Table 2.   Mechanical properties of test materials.

Material	Test Temperature (K)	Yield Strength (MPa)	Ultimate Strength (MPa)	Elongation (%)	Reduction of Area (%)	Rockwell Hardness (R_B)
AISI 304L	295	245	642	66	76	82
	76	441	1516	44	61	--
	4	610	1678	34	48	--
AISI 316	295	228	576	56	73	79
	76	608	1243	62	70	--
	4	711	1301	48	57	--
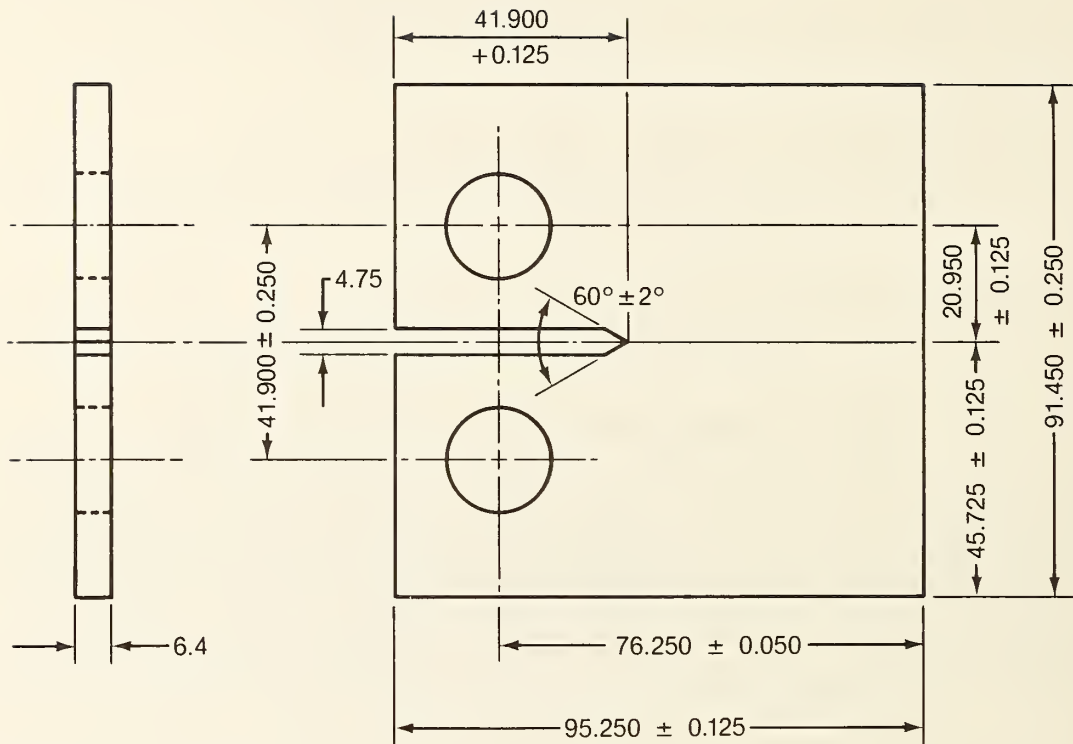
Finish $\overset{32}{\sqrt{}}$, except holes, as noted.
(Dimensions in millimeters)

Figure 1. Compact fatigue crack initiation specimen.
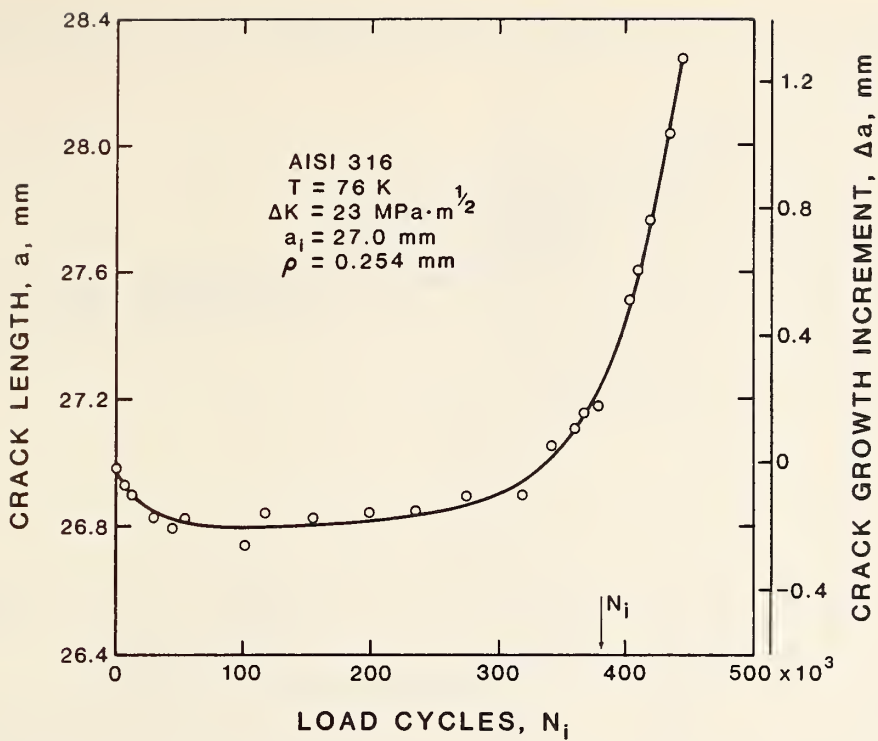
Figure 2.   Typical a-versus-N curve, where a is inferred by the compliance method.
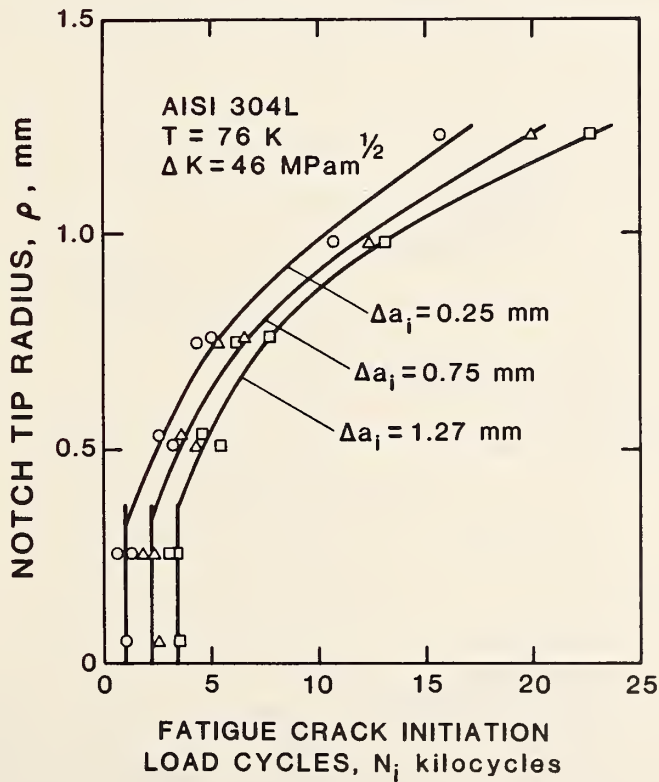
Figure 3.   Effect of notch tip radius on crack initiation life for several Δa_i increments: AISI 304L at 76 K and $\Delta K = 46$ MPa·m$^{1/2}$
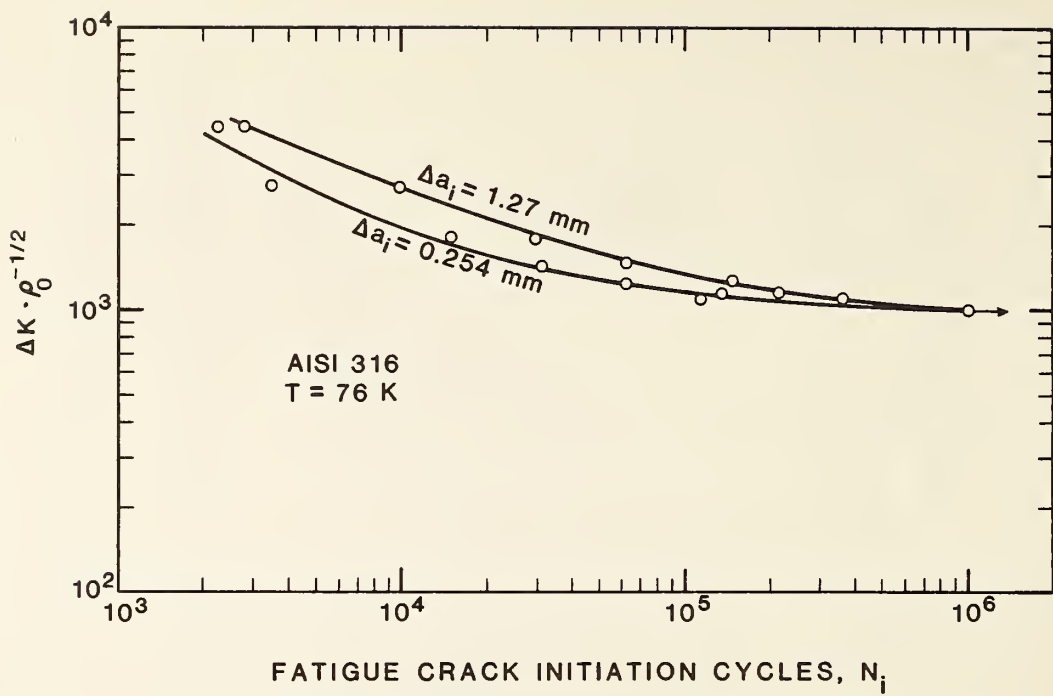
Figure 4. The $\Delta K \cdot \rho_0^{-1/2}$-versus-$N_i$ correlations for alternative definitions of crack initiation.
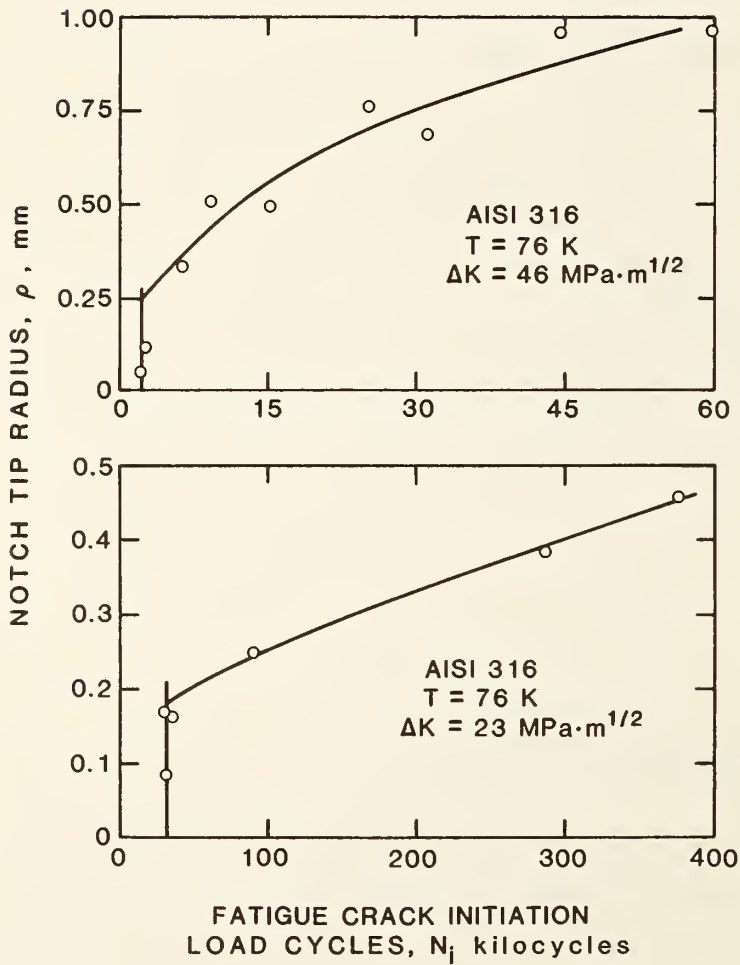
Figure 5. Effect of notch tip radius on crack initiation life: AISI 316 at 76 K and at two ΔK levels.
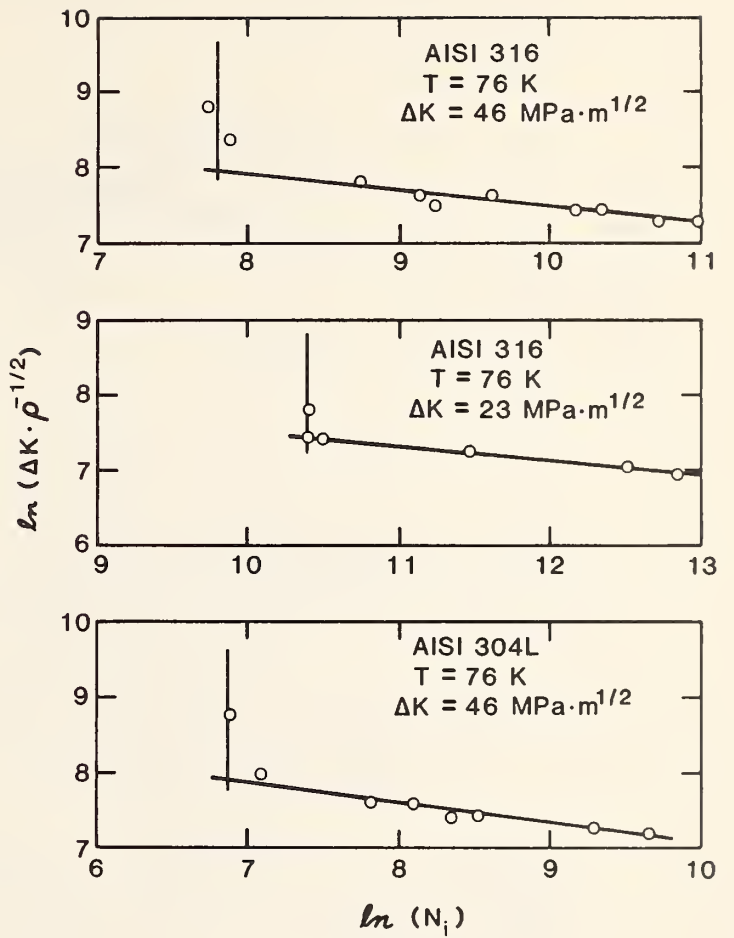
Figure 6. Plots of $\ln(\Delta K \cdot \rho^{-1/2})$-versus-$\ln(N_i)$ for tests where ΔK is held constant, ρ is varied, and ρ_0 is determined from the $\Delta K \cdot \rho^{-1/2}$ value at the intersection of two straight lines.
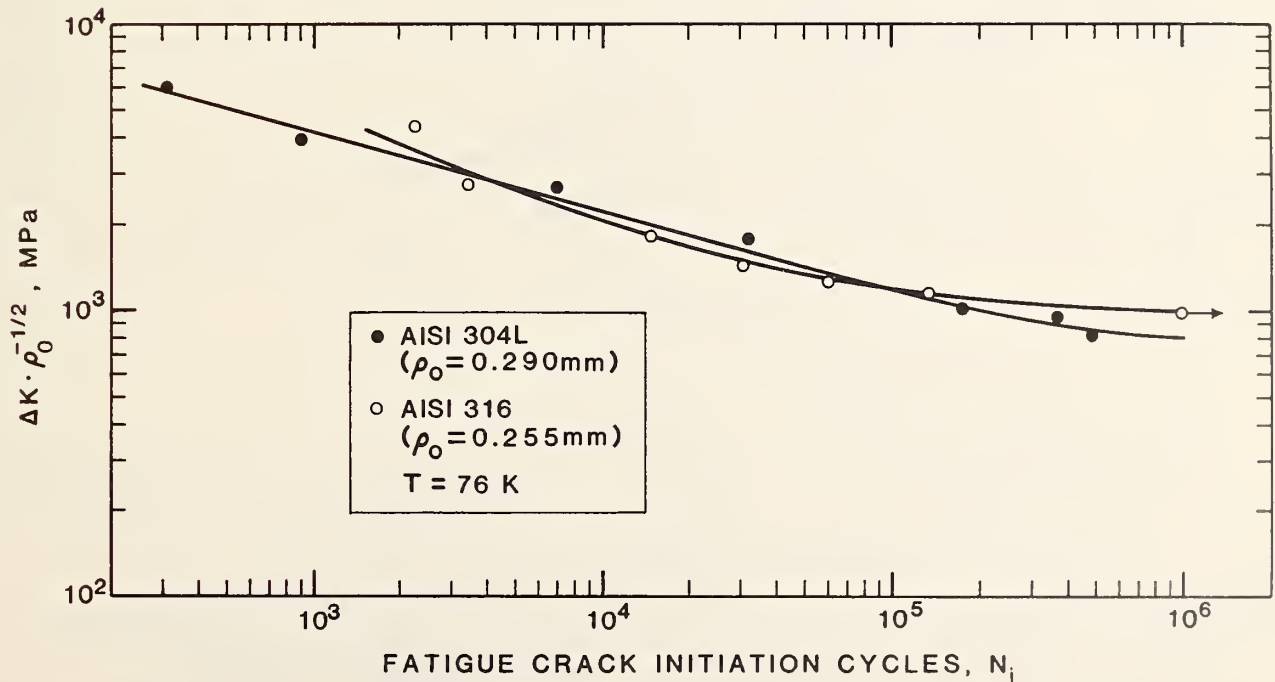
Figure 7. The $\Delta K \cdot \rho_0^{-1/2}$-versus-$N_i$ curves for AISI 316 and AISI 304L at 76 K. (Arrow indicates runout.)

267
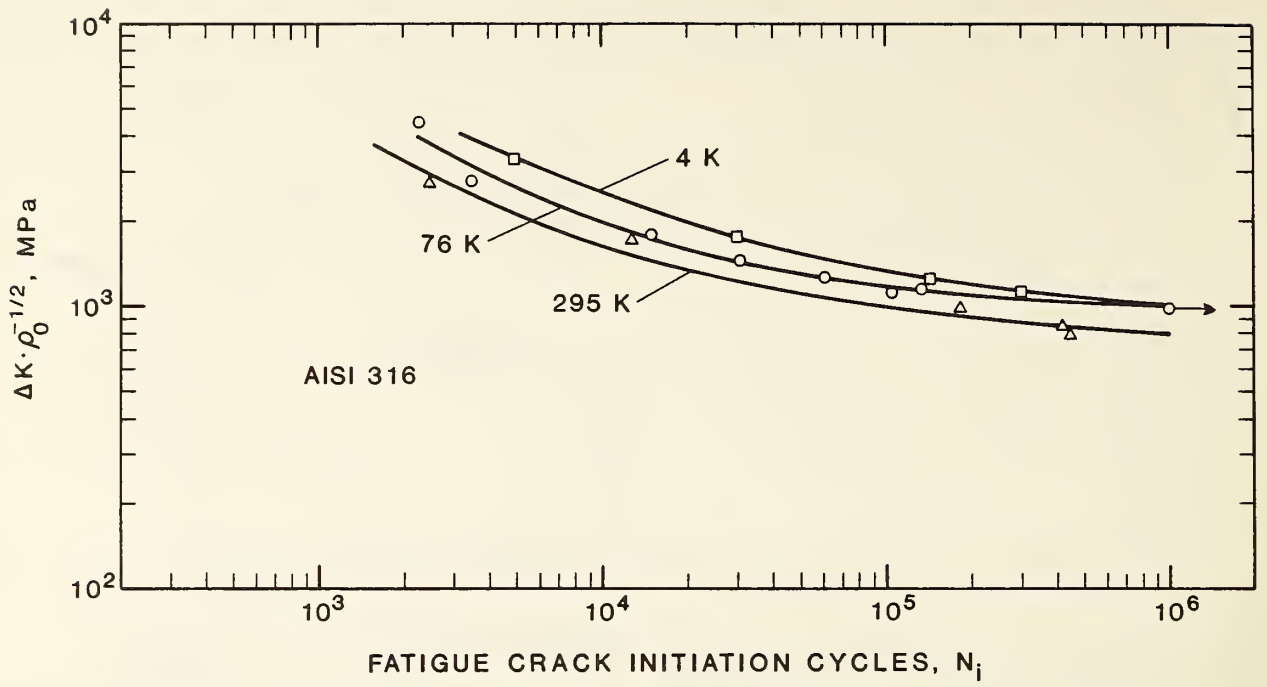
Figure 8. Effect of temperature on the $\Delta K \cdot \rho_o^{-1/2}$-versus-$N_i$ correlation for AISI 316 stainless steel. (Arrow indicates runout.)
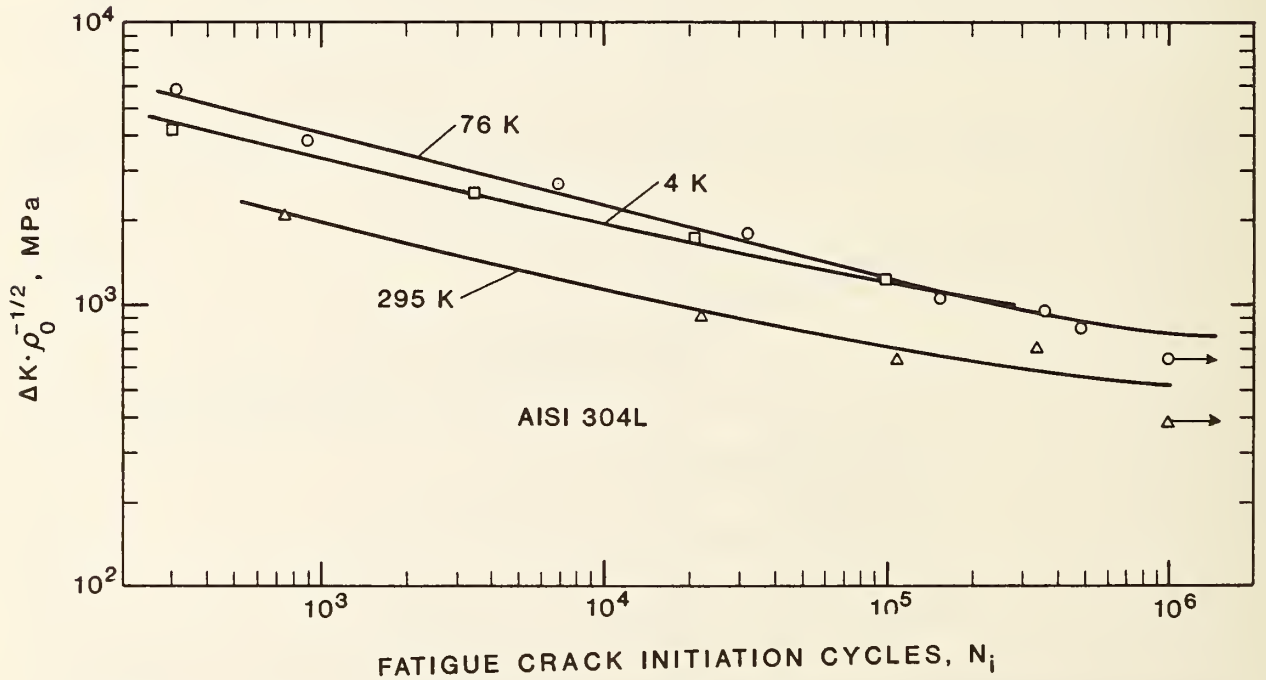
Figure 9. Effect of temperature on the $\Delta K \cdot \rho_o^{-1/2}$-versus-$N_i$ correlation for AISI 304L stainless steel. (Arrow indicates runout.)
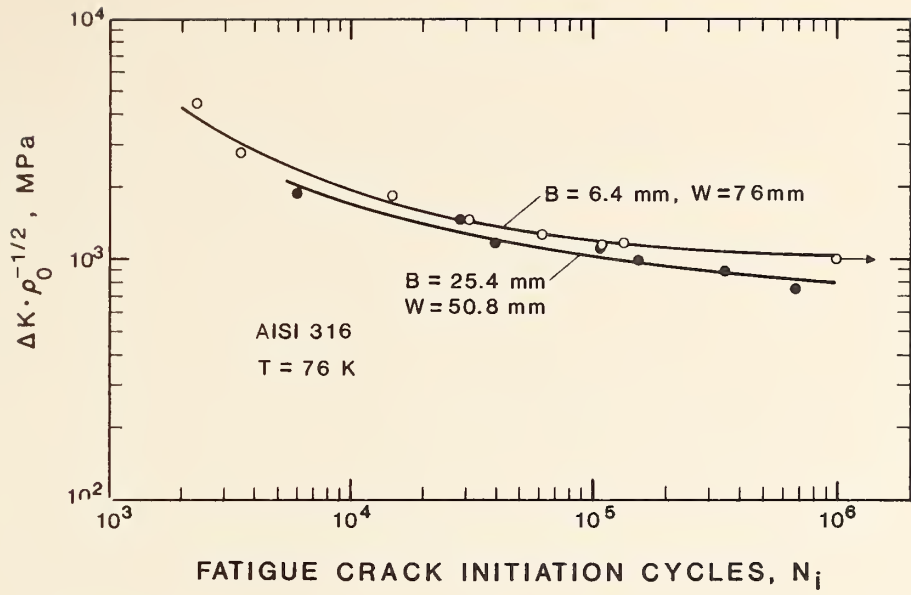
Figure 10. Effect of compact specimen size on the fatigue crack initiation
resistance of AISI 316 stainless steel at 76 K.   (Arrow indicates
runout.)
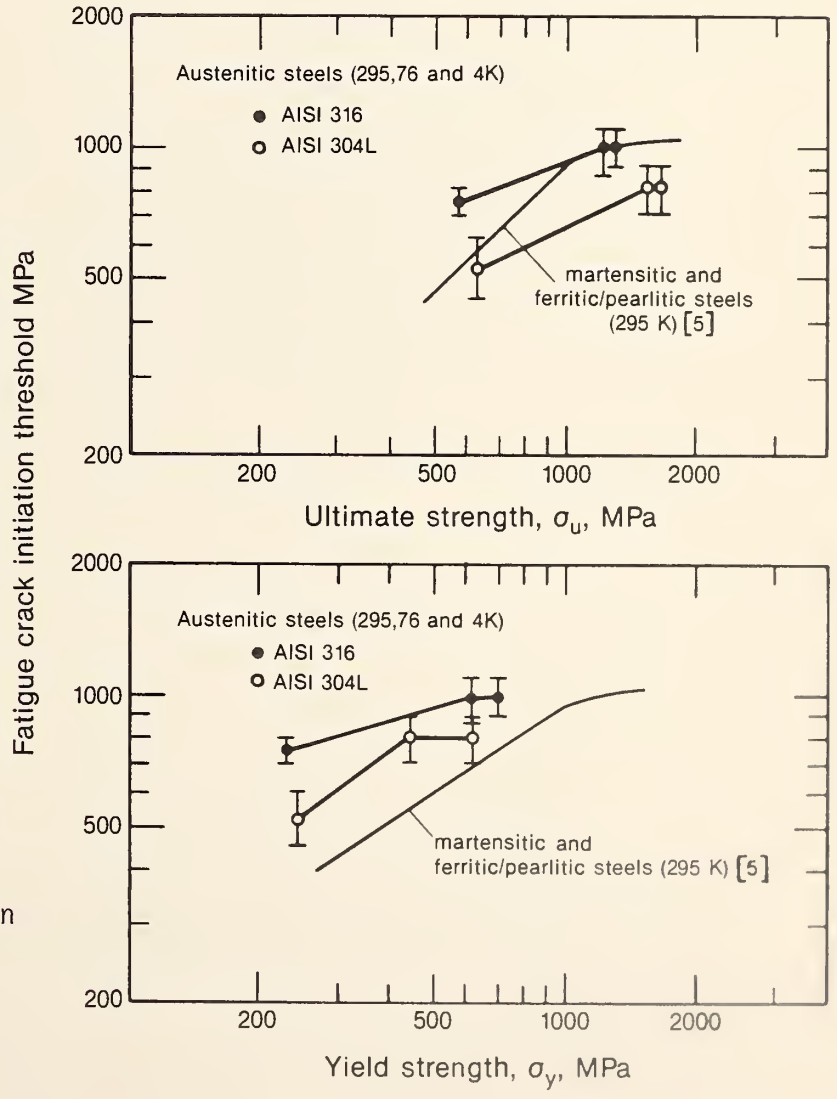
Figure 11. Correlation of fatigue-
crack initiation threshold
with tensile properties,
showing differences between
austenitic steels and
martensitic or ferritic/
pearlitic steels.

269

STACKING-FAULT ENERGIES IN 304-TYPE STAINLESS STEELS:
EFFECTS OF INTERSTITIAL CARBON AND NITROGEN*

H. M. Ledbetter and M. W. Austin[†]

By measurement, we studied the problem of stacking-fault probability and stacking-fault energy in nine 304-type stainless-steel alloys where C-plus-N content varied from 0.3 to 1.3 atomic percent. In one formulation of the problem, stacking-fault energy depends on four variables: stacking-fault probability, unit-cell size, <111>-direction Young's modulus, and dislocation density (or root-mean-square distortion strain). From powders, we determined stacking-fault probability by x-ray diffraction; we measured shifts of (111) and (200) diffraction peaks in both annealed-recrystallized and heavily deformed specimens. This analysis also yielded the unit-cell size. Obtaining the <111> Young modulus requires knowing the monocrystalline elastic constants, C_{ij}, which we estimated from the polycrystalline elastic constants with a reverse Kröner method and an assumption about the C_{12}/C_{11} ratio. We determined the distortion strain from the relative deformation-induced broadening of the (111) and (222) diffraction peaks. With C-plus-N alloying, unit-cell size increases approximately 0.3 percent, the <111> Young modulus decreases approximately 0.5 percent, stacking-fault probability decreases approximately 6 percent, and distortion strain increases approximately 2 percent. The combined effects of these variable changes predict that stacking-fault energy increases approximately 10 percent per percent interstitial C-plus-N content. Of the four variables, stacking-fault probability contributes most to the increase; for the zero-interstitial-content intercept, we found 0.016. For stacking-fault energy, we found a zero-solute intercept of 18 mJ/m^2. No difference appeared between effects of interstitial C and N. Peak-broadening showed that the effective size of the coherently diffracting domain decreased approximately 30 percent per percent solute; the zero-solute intercept was 450 A.

Key words: alloying effect; austenitic steel; face-centered-cubic alloy;
            interstitial; iron-base alloy; stacking-fault energy; stainless
            steel; x-ray diffraction.

INTRODUCTION

Close-packed crystal structures often contain defects in the stacking sequence of close-packed (octahedral) planes. We call this defect a <u>stacking fault</u>. In a face-centered-cubic (fcc) crystal structure, a stacking fault converts the perfect abcabc stacking to either abcbca (intrinsic fault) or to abcbabc (extrinsic fault). Clearly, deformation faults must be intrinsic. Stacking-fault geometry has received considerable attention. For example, Hirth and Lothe [1] devoted 48 pages of their dislocation-theory textbook to a description of fcc stacking faults, which relate intimately to partial dislocations. Several authors reviewed the subject of stacking faults: Seeger [2,3], Christian and Swann [4], and Christian and Vitek [5].

Stacking-fault energy (sfe), γ, is what we call the extra energy associated with the stacking defect. Apparently, Heidenreich and Shockley [6] first estimated this energy; for cobalt they obtained 20 mJ/m^2. Hirth and Lothe [1] gave a table of sfe for thirteen close-packed metals; values range from 16 mJ/m^2 for Ag to 750 mJ/m^2 for Rh. For common metals, they reported 166 for Al, 45 for Cu, 125 for Ni, 125 for Mg, and 140 for Zn. Because we can represent a stacking fault as two coherent-twin boundaries, we expect the stacking fault energy to be approximately twice the energy of a coherent-twin boundary.

Stacking-fault energy interests both theorists and experimentalists because it relates closely to various solid-state phenomena. These phenomena include relative phase stability [7]; cross-slip [3]; and dislocation jogs, which influence plastic deformation [8]. Rhodes and Thompson [9] mentioned that sfe affects such metallurgical phenomena as work hardening, stress-corrosion cracking, and hydrogen embrittlement. Adler and Wagner [10] added to this list several other phenomena: recrystallization, texture, microstructure, and low-temperature creep.

EXPERIMENTAL APPROACHES

Many methods exist for determining sfe experimentally. A review by Gallagher in 1970 [11] gave twelve methods:

- creep measurements (microstrain)
- coherent-twin energy
- deformation twinning
- extended dislocation nodes
- faulted dipoles
- grain-boundary energy
- fault probability, x-ray, normalized
- loop annealing
- rolling texture
- tau-three
- tetrahedra

Although incomplete, this list suggests many approaches to measuring sfe and shows that sfe relates to many solid-state phenomena.

Reported experimental values vary considerably. For Cu, for example, Gallagher [11] gave twenty-four values with a range of 24 to 165 mJ/m^2 and a recommended value of 55 mJ/m^2.

THEORETICAL APPROACHES

With a few caveats, we can equate the stacking-fault energy to the energy difference between cph (close-packed-hexagonal) and fcc phases. Then sfe connects closely with the panoply of relative-lattice-stability theory. For nontransition metals, theory gives reasonable agreement with observation. Theory gives the correct sign, correct magnitude, and correct structural trends. For transition metals, the theory of sfe requires further improvement.

To date, no one has calculated the sfe of an Fe-Cr-Ni alloy or of fcc Fe, where an accepted interatomic potential exists [12]. However, existing calculations for other systems give some insights for Fe. Especially, calculations for Cu assume special importance. Despite Cu possessing a filled 3d shell, its cohesive properties reflect a strong d-electron contribution. Thus Cu differs from Fe principally in the number of d electrons.

Blandin, Friedel, and Saada [13,14] considered, in the approximation of pair interactions, the stability of fcc crystal structures against twinning and faulting. Because faults do not affect the number and spacing of nearest-neighbor atoms, Blandin et al. represented the interatomic potential by its large-r asymptotic form involving Friedel oscillations. These authors concluded that the electron-to-atom ratio controls the cph-fcc relative stability.

Using a pairwise central-force approximation and a Morse interatomic-potential function, Cotterill and Doyama [15] calculated for Cu a sfe of 30 mJ/m^2. Using a Harrison pseudopotential for Al, they calculated 250 mJ/m^2. By considering a series of interatomic potentials, they concluded that the sfe depends strongly on the chosen potential.

In his book on pseudopotentials in metals, Harrison [16] gave a second-order-perturbation pseudopotential model for sfe. Although, they did not calculate sfe, Suzuki and Ledbetter [17] showed that the usual pseudopotential calculation for sfe includes four terms: Born-Mayer energy (or some equivalent energy to allow for the d-electron interaction); the Madelung-Fuchs (electron-ion electrostatic) energy; and the first-order and second-order perturbation-theory band-structure terms.

Hodges [18,19] reported two sfe studies. The first follows the approach of Blandin et al. [13]. In the second, for four non-3d-band metals with sp-electron bonding, Hodges used a Heine-Abarenkov pseudopotential to estimate the sfe. Also, Hodges established a relationship between sfe and the difference between cph and fcc crystal-structure energies.

For Pb, Hodges obtained a negative sfe. Bonsignori et al. [20] attributed this failure to Hodges's local approximation. Using a nonlocal model, approximated by a phenomenological energy-wavenumber characteristic, Bonsignori et al. predicted a positive, low sfe.

By a pseudopotential method that one would expect to yield a negative sfe, Krasko et al. [21] predicted a remarkably accurate value for Cu: 40 mJ/m^2.

Using a two-resonance-parameter one-electron band-structure approach, Pettifor [22] considered the equilibrium crystal structures of the 3d-transition metals and found that the energy difference, $\Delta E = E(cph) - E(fcc)$, varies cyclically with N, the number of d-plus-outer-s electrons per atom. Pettifor found fcc stable in the ranges $11 > N > 8.6$ and $6.7 > N > 4.5$. This model predicts that fcc Fe possesses a negative sfe. Pettifor gave possible reasons why the model gives the wrong sign for ΔE.

In studying Al, Wilkes and Sargent [23] used a pair potential, calculated 142 mJ/m^2, and verified that the energy of an intrinsic stacking fault equals twice the energy of a twin. These authors pointed out that calculating the sfe provides a good test of a proposed interatomic potential because the fault does not change the near-neighbor distance. If this distance changed, it might invalidate the perturbation-theory basis of the interatomic potential.

Using the Blandin et al. [13] method, Beissner [24] calculated the sfe of six metals, including Cu, for which he obtained 45 mJ/m^2. Beissner concluded that a first-order perturbation method succeeds, that exchange and correlation effects do not contribute, and that one can treat the important and difficult nonlocal effects approximately by an empirical energy-wavenumber characteristic. For noble metals, this characteristic strongly affects the calculation. Thus, for 3d-electron metals, Beissner finds little hope for a successful simple model. Beissner used an up-to-date pseudopotential to construct a real-space potential that was summed over atomic planes.

To calculate sfe, Vitek [25] used three types of interatomic potentials: Johnson, Morse, and an oscillation, such as the Harrison-Pick pseudopotential. For central-force interactions, he found the predictions agreed with a hard-sphere model.

Using a wavenumber-space calculation, Devlin [26] sought to improve Beissner's results. For six metals, including Cu, he found good agreement between calculation and observation. For Cu, for which he obtained 71 mJ/m^2, Devlin found that the band-structure term accounted for 95 percent of the sfe. Thus, electrostatic and d-electron-overlap terms are small.

Focusing on transition metals, Beissner [27] improved the previous calculations of Beissner and of Devlin. In his second study, Beissner introduced the third-order term in the perturbation expansion of the total energy. This term sums the three-ion interaction energies. Beissner went beyond Pettifor's model [22] by considering nonresonant scattering. His results

depend strongly on valence, especially for valences lower than that of Fe. In transition metals, Beissner found that sfe depends mainly on two effects: resonant scattering and three-ion interactions.

A recent study by Esterling et al. [28] considered Cu and obtained 73 mJ/m^2 for the sfe. These authors considered many different interatomic potentials and concluded that sfe does not provide a good fitting parameter for empirical potentials.

DEFORMATION FAULTS AND X-RAY DIFFRACTION

Proof that metals contain stacking faults originated with Edwards and Lipson [29], who studied Co. Their x-ray diffraction patterns showed a remarkable systematic mixture of sharp and diffuse lines. These authors reasoned that some lines remain unaffected by faults, whereas others change both position and intensity. In a companion paper, using reciprocal-lattice concepts, Wilson [30] modeled the Co case. His model predicts the linewidths, that ℓ-even lines broaden more than ℓ-odd lines, and that total line intensity changes only slightly.

Cobalt's faults probably originate in a martensitic transformation, which contains a shear deformation in its mechanism.

Barrett [31] suggested that mechanical stress should cause stacking faults. He reasoned that such deformation-induced faults must arise frequently because gliding atomic planes do not know where to stop. For atoms gliding over an "a" plane, both "b" and "c" sites offer the same number of near neighbors and the same interatomic forces. Each wrong stop produces a fault. Barrett [32] pointed out that deformation faults could account for many observations: strain markings, increased x-ray reflection near slip bands, deformation-induced disappearance of Kikuchi lines, and hardening of latent slip planes. Barrett also emphasized that faulting involves low interfacial energy and small volume-free-energy increase. Later, Barrett [33] produced the first direct proof of mechanically induced faults in metals. He detected stacking disorders in deformed Cu-Si alloys by analyzing x-ray diffraction patterns from oscillating polycrystals. For non-Laue diffraction streaks, he noted direction, length, and intensity. Barrett relied on the predictions by Wilson [34] and Zachariasen [35,36] that faults do not widen (11·0) rhombohedral-hexagonal spots because they belong to the class h-k = 3n, where n denotes any integer, including zero. Barrett also invoked Zachariasen's derivation of the intensity distribution along a diffraction streak. In another study, Barrett [37] measured the (200) K_α line widths in several plastically deformed fcc metals. He concluded that faults contribute significantly to line broadening.

The subject advanced markedly when Paterson [38] derived explicit expressions for fault density, which is given either by the breadth or displacement of the reciprocal-lattice streak. In the x-ray diffraction pattern, faults cause line broadenings and line shifts. For {111} planes, for example, two lines remain sharp and unshifted, whereas six become diffuse and shift to a higher Bragg diffraction angle, theta, the usual diffraction angle in Bragg's law. For {200} planes, all six become diffuse and move to

lower theta. Paterson says "the intensity distribution, the displacements of peaks, and the integral breadths ... are determined completely in terms of α." (Alpha denotes stacking-fault probability, the probability that a given plane is faulted.) To obtain quantitative details of the x-ray diffraction pattern, one must convert from the reciprocal lattice to real space and sum the various contributions using Warren and Averbach [39] multiplying factors.

Paterson's model contains several assumptions that deserve mention: faults are distributed randomly, exist solely in one set of planes within a monocrystal, and occur in small numbers (small alpha). Also, application of Paterson's broadening relationship assumes no broadening from sources other than faults. But we know that lines broaden from other factors: small coherently diffracting domains and distortions within these domains.

In a remarkable review on the Fourier analysis of line profiles, Warren [40] effected the above-mentioned reciprocal-space-to-real-space transformation and gave an expression for alpha based on line shifts:

$$\Delta(2\theta°) = \frac{90\sqrt{3}}{\pi^2} \ \alpha \ \tan\theta \left[\frac{\sum_b (\pm)L_o}{(u+b)h_o^2} \right] \tag{1}$$

where the reader should see Warren's Eq. (48) for definitions of terms. For various hkℓ, Warren tabulated the term within brackets which arises because the basic equations hold only for one point in reciprocal space. X-ray diffraction lines represent superpositions (sums) from many reciprocal points. This summation involves averaging. For the first two fcc diffraction lines, Eq. (1) gives

$$\Delta(2\theta°_{111}) = \frac{45\sqrt{3}}{2\pi^2} \ \alpha\tan\theta_{111} \tag{2}$$

and

$$\Delta(2\theta°_{200}) = - \frac{45\sqrt{3}}{\pi^2} \ \alpha\tan\theta_{200} \tag{3}$$

Thus,

$$\Delta(2\theta°_{200} - 2\theta°_{111}) = - \frac{45\sqrt{3}\alpha}{\pi^2} \ [\tan\theta_{200} + (1/2)\tan\theta_{111}] \tag{4}$$

Warren gave four advantages for using a measurement suggested by this relationship: (1) the two $\Delta2\theta°$ displacements add because they differ in sign; (2) sample-position error is compensated partially; (3) error arising from deformation-induced lattice-constant change is compensated partially; (4) no need arises to measure accurately a single reflection. This relationship provides a direct determination of alpha, independent of line broadening caused by particle size and lattice distortion.

For a typical metal (unit-cell size = a = 3.60 Å) examined with Cu $K_{\alpha 1}$ radiation (wavelength = λ = 1.54 Å), Eq. (4) becomes

$$\Lambda(2\theta^\circ_{200} - 2\theta^\circ_{111}) = -5.31\alpha \tag{5}$$

Thus, to measure an alpha of 0.001, one needs a peak-position inaccuracy in 2θ of approximately 0.005 degrees, perhaps the practical limit of existing commercial diffractometers.

When stress occurs in the diffracting particles, one must correct Eq. (4) to allow for the elastic strain. Wagner et al. [41] give this correction in a relationship written in terms of the lattice constant, a:

$$\frac{\Delta a_{111} - \Delta a_{200}}{a} = -K\alpha + Z\sigma \tag{6}$$

where σ denotes stress and

$$Z = (S_1)_{111} - (S_1)_{200} \tag{7}$$

where, for an elastically isotropic material,

$$S_1 = -\nu/E \tag{8}$$

where ν denotes Poisson ratio and E, Young modulus. For anisotropic materials

$$S_1 = -\nu_{hk\ell}/E_{hk\ell} \tag{9}$$

Determining $\nu_{hk\ell}$ and $E_{hk\ell}$ from the monocrystal elastic constants remains an unsolved problem. Many studies used the average of the Voigt (constant strain) and Reuss (constant stress) models. More recently, some studies used a Kröner average.

Several notable reviews exist on the relationship between plastic deformation and x-ray diffraction. Greenough [42] reviewed the early studies and gave 114 references. Warren's [40] review, emphasizing Fourier analysis of line profiles, lists 43 references. Welch and Otte's [43] brief, insightful literature evaluation contains 60 references. Vasilev and Smirnov [44] covered a broad field, emphasized Soviet studies, and gave 335 references. Wagner [45] published an excellent mathematical overview, invaluable to the practitioner, that includes 91 references.

Relationship between stacking-fault probability and stacking-fault energy

Consider stacking faults to arise from the separation of an fcc slip dislocation into two partial, or so-called half, dislocations of the Heidenreich-Shockley type:

$$\frac{a}{2}[10\bar{1}] = \frac{a}{6}[2\bar{1}\bar{1}] + \frac{a}{6}[11\bar{2}] \tag{10}$$

Then one can derive the following relationship

$$\gamma = (1/24\sqrt{3}\pi)a^3 G(111)\rho/\alpha \qquad (11)$$

where γ denotes stacking-fault energy; a, unit-cell size; ρ, dislocation density (cm/cm^3); α, stacking-fault probability, and

$$G(111) = (C_{11} - C_{12} + C_{44})/3 \qquad (12)$$

is the elastic shear modulus for any direction on a (111) plane, where C_{ij} denote the three independent cubic (Voigt) elastic stiffnesses.

Many studies get information about sfe by measuring its probability and making some assumption about density. G(111) tends to vary slowly with composition, is known for common alloys, and can often be estimated for others. As described below, this approach to sfe sometimes fails, as for the present alloys.

One often writes Eq. (11) with mean-square strain substituted for dislocation density. Whether dissociated or not, dislocations distort the lattice and cause a strain $\sqrt{(\bar{\varepsilon}^2)}$. Williamson and Smallman [46] showed that dislocation density and dislocation-induced strain relate according to

$$\rho = 2k\varepsilon^2/a^2 \qquad (13)$$

where the constant k depends on the model and ranges between 2 and 28. For a screw dislocation, Wilson [47] gave an exact peak-broadening calculation; for a face-centered-cubic lattice with Burgers vector $b = [110]$, Wilson's model predicts $k = 16.1$. Rounding this to 16, Eq. (13) becomes

$$\rho = (32/a^2)\varepsilon^2 \qquad (14)$$

and Eq. (11) becomes

$$\gamma = (4/3\sqrt{3}\pi)aG(111)\varepsilon^2/\alpha \qquad (15)$$

Some risk exists in applying the above relationships to highly mechanically deformed materials. These relationships apply to the equilibrium case where the partial dislocations separate by an equilibrium spacing, the equilibrium stacking-fault width, established by a balance between dislocation elastic repulsive force and the fault's surface tension. Highly deformed materials do not represent equilibrium. Stacking faults, which contribute to the mechanical deformation by relieving the applied stress, may grow wider than the equilibrium size. Perhaps they extend across the entire crystal. Taking $\gamma = 20$ mJ/m^2, the equilibrium size for stainless steel is [48]

$$\eta = G(111)(b_1 \cdot b_2)/2\pi\gamma = (1/24\pi) G(111)a^2/\gamma = 57 \text{ Å} \qquad (16)$$

By considering elastic stored energy, Adler et al. [49] rewrote Eq. (15):

$$\gamma = (2/5\sqrt{3})aE(hk\ell)\varepsilon^2/\alpha \qquad (17)$$

where E(hkℓ) becomes E(111) for (111)-type diffraction peaks, where E denotes the Young modulus perpendicular to the diffracting crystallographic plane. The factor of 5 in the denominator arises from a study by Adler and Otte [50]. The present study adopts Eq. (17) as the basic relationship among stacking-fault energy (γ), unit-cell size (a), <111>-direction Young modulus [E(111)], microstrain (ϵ), and stacking-fault probability (α).

STUDIES ON Fe-Cr-Ni ALLOYS

Otte [51] reported perhaps the first x-ray diffraction, although qualitative, study of stacking-fault formation in Fe-Cr-Ni-type alloys. He concluded that both Cr and Mn lower the stacking-fault energy, Ni lowers it less, and C produces a small effect, probably raising the stacking-fault energy. Quantitatively studying three alloys--Fe-16Cr-15Ni, Fe-16Cr-12Ni, and Fe-30Ni--Goldman and Wagner [52] concluded that Ni increases the austenite stacking-fault energy, and Cr decreases it.

The present study used x-ray diffraction methods to study the effect of interstitial C plus N on the stacking-fault energy of 304-type austenitic steel. On this subject, from analysis of published results, Schramm and Reed [53] reported the surprising chemical-composition dependence:

$$\gamma = 4 + 1.8\ W(Ni) - 0.2\ W(Cr) + 410\ W(C) \tag{18}$$

and

$$\gamma = 34 + 1.4\ W(Ni) - 1.1\ W(Cr) - 77\ W(N) \tag{19}$$

where γ has units of mJ/m^2 and W denotes weight percent. By surprising we mean that the C coefficient is so large and opposite in sign to the N coefficient. Re-examination of the C effect by Brofman and Ansell [54], using transmission electron microscopy, led to the conclusion

$$\gamma = 16.7 + 2.1\ W(Ni) - 0.9\ W(Cr) + 26\ W(C) \tag{20}$$

with the C coefficient lower by a factor of 16 than the Schramm-Reed result. Brofman and Ansell found that their result "concurs with the literature in finding that γ is relatively insensitive to small changes in carbon content for this ... alloy ...."

EXPERIMENT

Materials

Nine stainless-steel plates were purchased from the research laboratory of a U.S. steel manufacturer. All plates had nearly the same base composition, which fell within the limits of ASTM specification A240 for AISI-304 stainless steel, nominally Fe-18Cr-10Ni-1.5Mn-0.01P-0.02S-0.55Si-0.2Mo-0.2Cu weight percent. The C-and-N contents varied, as shown in the mill chemical analyses in Table I. The nine plates were produced from three 136-kg vacuum-induction-melted heats, split with respect to C level, and teemed into

7.6-cm x 20-cm x 36-cm hot-topped cast-iron ingot molds. The ingots were reheated and soaked at 1561 K (2350°F), hot-rolled into 2.54-cm plates, and air cooled. The plates were finally annealed at 1332 ± 7 K (1937 ± 13°F) for 1 h and water quenched. Hardness and grain size are also listed in Table I.

Specimens

We obtained powders by filing bulk material at ambient temperature. We sieved these powders through a No. 100 screen with a 150-μm opening size. On the basis of a grain size of 78 to 105 μm, deformed powder particles contained one to seven crystals. Annealing consisted of heating powders in evacuated capsules for 30 min at 1000°C. We obtained x-ray diffraction specimens by sprinkling powders into a viscous grease in a recess in a flat plate and pressing them lightly to achieve flatness.

In the alloys containing lower C plus N, high mechanical deformation caused by filing induced fcc-to-bcc (gamma-to-alpha) phase transition. This martensitic phase evidenced itself principally as a (110)-bcc diffraction peak at a slightly higher 2θ than the (111)-fcc diffraction peak. Annealing the powders reduced, but did not eliminate, this peak. Because the two peaks show a 2θ separation of approximately one degree, the (110)-bcc peak was removed readily using a deconvolution procedure. For the cph (epsilon) phase, we found no evidence. If this phase occurred, one would expect a (0002)-cph diffraction peak at exactly the (111)-fcc 2θ value and a (10$\bar{1}$1)-cph diffraction peak at 2θ near 46.7 degree.

Equipment

The measuring apparatus consisted of a commercial horizontal Bragg-Brentano-focusing, computer-automated diffractometer with a 22-cm diffracto-meter radius. The diffractometer contained a scintillation counter and a monochromator, a curved-graphite (Johann) type, located between the specimen and the counter.

Measurements

Using diffracted-beam monochromatic Cu-K_α radiation at an exciting potential of 45 kV, we step-scanned at 0.02-degree increments in 2θ for either 90 s or 1500 counts, whichever occurred first. The wider deformed (111) peak corresponded to approximately 100 measurements. We stored the measurements in a computer for later processing. We removed $K_{\alpha 2}$ radiation by Rachinger's method and obtained peak positions by fitting to a Pearson type-7 function

$$y = I_{max} \left[1 + \frac{(\theta - \theta_{max})^2}{2W^2} \right]^{-2} \tag{21}$$

where I_{max} denotes maximum intensity; θ, diffraction angle; and W, full peak width at half-maximum intensity.

In both the incident beam and the diffracted beam, we used 1-mm horizontal Soller-slit packs with 4.0-degree vertical divergence slits and 0.05-degree receiving slits.

The uncontrolled temperature in the diffractometer chamber varied from 26 to 29°C. Typically, all three (111), (200), and (222) peaks were scanned in 12 h.

We corrected the peaks for both Lorentz scattering factor and for polarization.

Storing deformed powders at ambient temperatures showed some small so-called self-annealing after approximately 20 days. Both peak breadth and peak position relaxed measurably toward the annealed values.

Peak Broadening

Aqua [55] established that one can determine x-ray diffraction peak-broadening by three methods: Fourier analysis, integral breadth, and variance. For the present study, we took the line breadth, B, as the width at half-maximum intensity fitted to the Pearson function, Eq. (21).

Several methods exist to correct for instrumental peak broadening. For a Cauchy peak shape, a linear relationship applies:

$$B_d = B_{obs} - B_a \tag{22}$$

where subscript d denotes deformed; obs, observed; and a, annealed. For a Gaussian peak shape, the correction is quadratic:

$$B_d^2 = B_{obs}^2 - B_a^2 \tag{23}$$

Wagner and Aqua [56] showed that a better relationship lies between these two limits and is parabolic:

$$B_d = B_{obs} - B_a^2/B_{obs} \tag{24}$$

For the present study, we adopted Eq. (24) to correct for instrumental peak broadening and obtain the widths of diffraction peaks for the deformed case. Wagner and Aqua cite several other studies that support Eq. (24).

Apparently, Dehlinger and Kochendörfer [57] were first to suggest (in 1939) that diffraction-peak breadth arises from two principal sources: particle size, where

$$B_p = \lambda/D \cos\theta \tag{25a}$$

and strain, where

$$B_s = k \tan\theta \tag{25b}$$

In these relationships, D denotes particle size; θ, diffraction angle; λ, x-ray wavelength; and k, a constant. Note that only B_p depends on λ. This permits separating the two terms. Thus,

$$B = B_p + B_s \tag{26}$$

or

$$\frac{B \cos\theta}{\lambda} = \frac{1}{D} + \frac{4\varepsilon \sin\theta}{\lambda} \tag{27}$$

Here, we use the result that $k = 4\varepsilon$ [56], where ε denotes the microstrain in Eq. (17). Thus, a graph of $(B \cos\theta)/\lambda$ versus $(\sin\theta)/\lambda$ gives D as the inverse intercept and 4ε as the slope. To obtain D and ε, we did this analysis for the (111) and (222) diffraction peaks. As discussed by Wagner and Aqua [56], using another set, such as (200) and (400), leads usually to different results for D and ε, especially ε, because Young modulus, $E(hk\ell)$, depends strongly on direction.

Estimation of G(111) and E(111)

Because the appropriate-composition monocrystals do not exist, one can not determine G(111) or E(111) directly. But, the polycrystal elastic constants were reported [58]. From these, one can estimate the C_{ij} by the following method.

Especially for cubic crystal symmetry, the problem of relating the mono-crystal elastic constants (C_{11}, C_{12}, C_{44}) to the quasi-isotropic polycrystal-line elastic constants (B, G) has been studied extensively, both theoretically [59] and experimentally [60]. The bulk modulus, B, because it is a rotational invariant of the elastic-stiffness tensor, is always given by

$$B = (C_{11} + 2C_{12})/3 \tag{28}$$

even for a highly textured material. The expression for the shear modulus, G, depends on the assumptions of the model. Considering the self-consistent problem of an anisotropic monocrystal inclusion embedded in a corresponding isotropic matrix and assuming stress equilibrium at the interface, Kröner [61] showed that

$$G^3 + \alpha G^2 + \beta G + \gamma = 0 \tag{29}$$

where

$$\alpha = (5C_{11} + 4C_{12})/8 \tag{30}$$

$$\beta = -C_{44}(7C_{11} - 4C_{12})/8 \tag{31}$$

and

$$\gamma = -C_{44}(C_{11} - C_{12})(C_{11} + 2C_{12})/8 \tag{32}$$

In the forward case, these relationships permit the calculation of B and G from the C_{ij}, the isotropic from the anisotropic, two elastic constants from three.

With one additional piece of information, from either theory or observation, from some single relationship among the C_{ij}, one can compute the reverse case also. The C_{ij} can be computed from B and G. This additional piece of information comes from the existing C_{ij} values for fcc Fe-Cr-Ni alloys. Recently, Ledbetter [62] reviewed these. Among these alloys, he found a surprising near constancy of both

$$C_{12}/C_{11} = 0.652 \pm 0.025 \qquad (33)$$

and Zener's anisotropy index

$$A = 2C_{44}/(C_{11} - C_{12}) = 3.53 \pm 0.17 \qquad (34)$$

Using the first relationship and Kröner's method, one obtains the elastic constants shown in Table II. We see that within a standard deviation of one-half percent G(111) does not vary from the value 66.8 ± 0.3 GPa. Similarly, E(111) does not vary from the value 304 ± 2 GPa. Thus, neither elastic constant accounts for any measurable variation of sfe with composition. One obtains the shear modulus on the (111) plane from Eq. (12) and the <111>-direction Young modulus from

$$E(111)^{-1} = S_{11}(2S_{11} - 2S_{12} - S_{44})/3 \qquad (35)$$

where the S_{ij} elastic compliances relate inversely to the C_{ij} elastic stiffness:

$$[C_{ij}] \cdot [S_{ij}] = I_{6x6} \qquad (36)$$

where I denotes the 6x6 identity matrix. We estimate the uncertainty in both G(111) and E(111) as 2 percent.

Unit-Cell Size

We obtained the unit-cell size, a, from annealed powders. Figure 1 shows a typical case. This figure shows a for various hkℓ diffraction peaks plotted versus $\cos\theta \cdot \cot\theta$, which equals zero when $2\theta = 180°$. Thus, the intercept gives the best unit-cell size. The line represents a linear least-squares fit. The double points represent the $K_{\alpha 1}$ and $K_{\alpha 2}$ reflections. For the present study, we estimate the uncertainty in a as ± 0.0002 A.

RESULTS

Table III contains the study's principal results for the nine alloys: unit-cell size, stacking-fault probability, root-mean-square distortion strain, size of the coherent-diffracting domain, and finally, the stacking-fault energy. Measured polycrystal and calculated monocrystal elastic constants occur in Table II. Figure 2 shows these results together with linear-least-squares trend lines.

For the stacking-fault energy the best-fit line is

$$\gamma(mJ/m^2) = 18.3 + 1.9 \ A(C + N) \qquad (37)$$

or

$$\gamma(mJ/m^2) = 18.3 + 8.2 \ W(C + N) \qquad (38)$$

where A and W denote atomic and weight percentages of C plus N. Attempts failed to separate the C and N effects.

Concerning imprecision and uncertainty, Fig. 2 reflects the first. Above, we give uncertainties for E(111) and for a. Often, authors estimate uncertainty in sfe as plus-or-minus 50 percent. Our experience suggests no stronger statement for the present study.

DISCUSSION

Can we understand the study's most important result: interstitial C and N atoms increase the stacking-fault energy of an fcc Fe-18Cr-10Ni alloy? For this discussion, we sometimes ignore the alloy and focus on unalloyed Fe. Also, we assume that stacking-fault energy varies as $\Delta E = E(cph) - E(fcc)$, where E denotes energy.

The energy difference between Fe's cph and fcc forms provides a focus of several studies: Kaufman et al. [63], Andersen et al. [64,65], Grimvall [66], Pettifor [22], and Hasegawa and Pettifor [67]. Among these studies, both different approaches and sometimes contradictory conclusions arise.

For Fe's three crystalline structures—bcc, fcc, cph, Andersen et al. [64,65] calculated the dependence of magnetic properties on crystal structure and on atomic volume. Their model involves self-consistent, spin-polarized band calculations. For transition metals, their results contain many implications: (1) The 3d-band structure determines crystal structure and magnetic moments. (2) Under compression, "kinetic" energy overcomes "exchange" energy with a resulting reduction of magnetic moment. (3) The sp-d hybridization is significant, but less so than s-p hybridization. (4) The number of d electrons and the Stoner parameters are constant, independent of crystal structure and independent of atomic volume. (5) For a given atomic volume, paramagnetic potential parameters are independent of crystal structure. (6) For the bcc crystal structure, paramagnetic fermi level, E_f, occurs at a peak in the density-of-states curve, and not at a peak for the cph crystal structures. (7) The sp electron energy should not affect crystal structure because the sp band is nearly isotropic. (8) A ferromagnetic-bcc to paramagnetic-cph phase transition occurs when the bcc atomic radius is reduced 4 percent. (9) The Fe is ferromagnetic at all volumes exceeding 0.92 of the bcc equilibrium volume.

Using an itinerant-electron-model spin-fluctuation theory, Hasegawa and Pettifor [67] calculated the free energy of the bcc (α, δ), fcc (γ), and cph (ϵ) phases of Fe. They considered effects of both temperature and pressure. They focused on magnetic band-structure contributions and ignored both lattice vibrations and short-range magnetic order. They found the following

results: (1) At zero temperature, the nonmagnetic energy favors ε. This agrees with the observation that the isovalent 4d and 5d nonmagnetic elements Ru and Os show a cph crystal structure. (2) At zero temperature, the magnetic energy stabilizes the α phase. (3) The bcc density-of-states curve shows a strong peak near the fermi level, E_f, where the cph and fcc phases show no peak. Thus, only bcc Fe satisfies the Stoner criterion for ferromagnetism. (4) Pressure (lower volume) decreases the magnetic energy and favors the cph phase. (5) A cph-fcc phase transition occurs at T = 340 K because the cph-phase entropy decreases less rapidly because of a lower density-of-states near the fermi level. (6) Magnetic interactions dominate the α-γ-δ phase interrelationships. No need exists to invoke phonon contributions.

The above studies show that increasing volume favors the fcc phase over the cph phase. Thus, higher atomic volume increases stacking-fault energy in fcc Fe. By x-ray diffraction Ledbetter and Austin [68] showed that alloying interstitial C plus N into Fe-18Cr-10Ni increases volume by 0.7V(Fe) per interstitial atom, where V(Fe) denotes the atomic volume of Fe.

If effective atomic volume determines the C-plus-N effects on stacking-fault energy, it may contribute also to effects of substitutional elements: Cr, Ni, and Mn. For the alloys, the effective atomic volumes equal 11.53 A^3. For the principal elements, the atomic volumes equal 11.71 for Fe, 11.94 for Cr, 10.87 for Ni, and 12.21 for α-Mn and 14.41 for γ-Mn. Thus, atomic-volume considerations suggest that Cr and Mn increase sfe and Ni decreases sfe. Except for Ni, no experimental consensus exists concerning alloying effects on sfe in Fe-Cr-Ni alloys. Almost everyone agrees that Ni produces a small increase; if included in Eq. 38, the coefficient for Ni would take a value of approximately two.

The failure of atomic volume to explain Ni's effect on sfe suggests other factors: the electronic density of states--N(E) versus E--and the electron-to-atom ratio (e/a). Considering only Fe, Cr, and Ni, these alloys possess an e/a ratio of 6.8 (Fe = 7, Cr = 5, Ni = 9, Mn = 6). Using a two-parameter d-resonance model, Pettifor [22] calculated the N(E) curves for bcc, fcc, and cph phases by a hybridized near-free-electron scheme. Pettifor found that the N(E) curves for fcc and cph are practically identical for e/a ≥ 4, except that cph does not possess a peak near e/a = 7.5, which favors fcc at higher e/a. This extra fcc N(E) peak assumes importance for sfe considerations. Nickel added to Fe-Cr-Ni would raise the fermi energy more for the cph case than for the fcc case, thus increasing ΔE(cph-fcc), and thus increasing the sfe. Conversely, added to Fe-Cr-Ni, both Cr and Mn would lower e/a, decrease ΔE(cph-fcc), and lower the sfe. Therefore, considering both atomic volume and e/a, both factors suggest that Mn decreases sfe. For Cr and Ni, the two factors suggest opposing effects. From observation for Ni, the e/a effect dominates the volume effect.

Not considered by Pettifor [22], another factor enters: magnetic interactions. Much more difficult to consider theoretically, these electron spin-spin interactions received attention by Andersen et al. [63,64] and by Hasegawa and Pettifor [67]. As described above, contrary to previous studies, the latter concluded that "phase transitions in iron are driven by the

magnetic contributions to the free energy." Although fcc Fe-Cr-Ni-Mn alloys exhibit no macroscopic magnetism, effective local magnetic moments must occur because all four atomic species exhibit either ferromagnetism or antiferromagnetism.

All three of these factors--atomic volume, density of states, and magnetic interactions--interrelate. Strictly, one can not consider them separately. Calculations by Andersen et al. [63,64] show that local magnetic moment increases with increasing atomic volume. And we know that increased volume decreases bandwidth and increases N(E). The study by Madsen et al. [64] shows relationships among volume, d-state density, and local magnetic moment.

Although we see how interstitial C and N increase volume, their effect on electron-to-atomic and on magnetic interactions remains unclear. Using sound velocity, Ledbetter [69] showed for Fe-Cr-Ni alloys that C and N increase volume, reduce the magnetic interaction, and suppress the paramagnetic-antiferromagnetic phase transition that occurs in these alloys at low temperatures. Magnetic-susceptibility-versus-temperature measurements confirm the sound-velocity results [70]. We do not know whether C and N contribute electrons to the free-electron band structure or whether C and N form local, covalent bonds and local intermetallic compounds such as Fe_4C and FeC.*

CONCLUSIONS

From this study, six conclusions emerge:

1. Interstitial C plus N increase the stacking-fault energy (sfe) of 304-type stainless steel. The increase amounts to approximately 10 percent per atomic percent solute. The intercept (zero-C-plus-N) value of sfe equals 18 mJ/m^2.

2. Behaviors C and N do not differ significantly.

3. Among four variables, stacking-fault probability (sfp) produces the largest change in sfe. The sfp decreases approximately 6 percent per atomic percent solute. The intercept sfp equals 0.016.

4. Considering the other three variables, distortion strain increases approximately 2 percent, unit-cell size approximately 0.3 percent and both G(111) and E(111) decrease approximately 0.5 percent. Thus, the unit-cell size and elastic-constant variables nearly offset.

---

* Before finally publishing this manuscript, the authors intend to add several topics to the discussion section. These include: the low sfe of Fe-Cr-Ni alloys compared with fcc Ni, the element adjacent to Fe in the periodic table; the relationship between microstrain and plastic deformation, especially the yield strength; the decrease in coherently diffracting domain size; and, perhaps, dislocation density.

5. The coherent-diffracting-domain size decreases approximately 30 percent. The intercept value equals 450 Å.

6. Not yet do we understand why C and N increase sfe. Possible factors in the final understanding include atomic volume, electron-to-atom ratio, and magnetic interactions.

ACKNOWLEDGMENTS

REFERENCES

1. J. P. Hirth and J. Lothe: Theory of Dislocations, pp. 306-353, Wiley-Interscience, New York, 1982.

2. A. Seeger: in Defects in Crystalline Solids (Bristol Conference), pp. 328-339, The Physical Society, London, 1954.

3. A. Seeger: in Dislocations and Mechanical Properties of Crystals, pp. 243-329, General Electric Co., 1957.

4. J. S. Christian and P. R. Swann, in Alloying Behavior and Effects in Concentrated Solid Solutions, pp. 105-269, Gordon and Breach, 1965.

5. J. W. Christian and V. Vitek: Rep. Prog. Phys., 1970, vol. 33, pp. 307-411.

6. R. D. Heidenreich and W. Shockley: Strength of Solids, pp. 57-75, Physical Society, London, 1947.

7. V. Heine and D. Weaire: Solid State Phys., 1970, vol. 24, pp. 249-463.

8. A. Seeger: in Defects in Crystalline Solids (Bristol Conference), pp. 391-401, The Physical Society, London, 1954.

9. C. G. Rhodes and A. W. Thompson: Metall. Trans. A, 1977, vol. 8A pp. 1901-1906.

10. R. P. I. Adler and C. N. J. Wagner: J. Appl. Phys., 1962, vol. 33, pp. 3451-3458.

11. P. C. J. Gallagher: Metall. Trans., 1970, vol. 1, pp. 2429-2461.

12. R. A. Johnson: Phys. Rev., 1966, vol. 145, pp. 423-433.

13. A. Blandin, J. Friedel, and G. Saada: J. Phys. (Paris), 1966, vol. 27, pp. C3-128-C3-136.

14. A. P. Blandin: Phase Stability in Metals and Alloys, pp. 115-124, McGraw-Hill, New York, 1967.

15. R. M. J. Cotterill and M. Doyama: Phys. Rev., 1966, vol. 145, pp. 465-478.

16. W. A. Harrison, Pseudopotentials in the Theory of Metals, pp. 207-209. Benjamin, New York, 1966.

17. T. Suzuki and H. M. Ledbetter: Philos. Mag., 1983, vol. 48, pp. 83-94.

18. C. H. Hodges: Acta Metall., 1967, vol. 15, pp. 1787-1784.

19. C. H. Hodges: Philos. Mag., 1967, vol. 15, pp. 371-392.

20. F. Bonsignori, V. Bortolani, and G. Velo: Nuovo Cimento, 1968, vol. 57, pp. 194-207.

21. G. L. Krasko, V. N. Teliyants, R. T. Pozvonkova, and Y. 1. Zaslavskii: Sov. Phys. - Solid State, 1968, vol. 9, pp. 2414-2416.

22. D. G. Pettifor: J. Phys. C, 1970, vol. 3, pp. 367-377.

23. P. Wilkes and C. M. Sargent: Met. Sci. J., 1972, vol. 6, pp. 216-219.

24. R. E. Beissner: Phys. Rev. B, 1973, vol. 8, pp. 5432-5442.

25. V. Vitek: Philos. Mag., 1973, vol. 18, pp. 773-786.

26. J. F. Devlin: J. Phys. F, 1974, vol. 4, pp. 1865-1882.

27. R. E. Beissner: Phys. Rev. B, 1976, vol. 13, pp. 5131-5135.

28. D. M. Esterling, A. R. McGurn, I. M. Boswarva, and R. J. Arsenault: Mater. Sci. Eng., 1984, vol. 68, pp. 97-106.

29. O. S. Edwards and H. Lipson: Proc. Roy. Soc. Lond., 1942, vol. 180, pp 268-277.

30. A. J. C. Wilson: Proc. Roy. Soc. Lond., 1942, vol. 180, pp. 277-285.

31. C. S. Barrett: in Cold Working of Metals, pp. 65-112, American Society for Metals, Metals Park, Ohio, 1948.

32. C. S. Barrett: in Imperfections in Nearly Perfect Crystals, pp. 97-128, Wiley, New York, 1952.

33. C. S. Barrett: Trans. AIME, 1950, vol. 188, pp. 123-135.

34. A. J. C. Wilson: Acta Crystall., 1952, vol. 5, pp. 318-322.

35. W. H. Zachariasen: Phys. Rev., 1947, vol. 71, pp. 715-717.

36. W. H. Zachariasen: Acta Crystall., 1948, vol. 1, pp. 277-281.

37. C. S. Barrett and M. A. Barrett: Phys. Rev., 1951, vol. 81, p. 311.

38. M. S. Paterson: J. Appl. Phys., 1952, vol. 23, pp. 805-811.

39. B. E. Warren and B. L. Averbach: J. Appl. Phys., 1950, vol. 21, pp. 595-599; J. Appl. Phys., 1952, vol. 23, pp. 497-500.

40. B. E. Warren: Prog. Metal Phys., 1959 vol. 8, pp. 147-202.

41. C. N. J. Wagner, J. P. Boisseau, and E. N. Aqua: Trans. Metall. Soc. AIME, 1965, vol. 233, pp. 1280-1286.

42. G. B. Greenough: Prog. Metal Phys., 1952, vol. 3, pp. 176-219.

43. D. O. Welch and H. M. Otte: Adv. X-Ray Analy., 1963, vol. 6, pp. 96-120.

44. D. M. Vasilev and B. J. Smirnov: Sov. Phys. Usp., 1961, vol. 4, pp. 226-259.

45. C. N. J. Wagner: in Local Atomic Arrangements Studied by X-Ray Diffraction, pp. 219-269, Gordon and Breach, New York, 1965.

46. G. K. Williamson and R. E. Smallman: Proc. Phys. Soc., 1955, vol. B68, pp. 577-585.

47. A. J. C. Wilson: Research, 1949, vol. 2, pp. 541-542.

48. L. F. Vassamillet: J. Appl. Phys., 1961, vol. 32, pp. 778-782.

49. R. P. I. Adler, H. M. Otte, and C. N. J. Wagner: Metall. Trans., 1970, vol. 1, pp. 2375-2382.

50. R. P. I. Adler and H. M. Otte: Mater. Sci. Eng., 1966, vol. 1, pp. 222-238.

51. H. M. Otte: Acta Metall., 1957, vol. 5, pp. 614-627.

52. A. J. Goldman and C. N. J. Wagner: Acta Metall., 1963, vol. 11, pp. 405-413.

53. R. E. Schramm and R. P. Reed: Metall. Trans. A, 1975, vol. 6A, pp. 1345-1351.

54. P. J. Brofman and G. S. Ansell: Metall. Trans. A, 1978, vol. 9A, pp. 879-880.

55. E. N. Aqua: Acta Crystall., 1966, vol. 20, pp. 560-563.

56. C. N. J. Wagner and E. N. Aqua: Adv. X-ray Anal., 1964, vol. 7, pp. 46-65.

57. U. Dehlinger and A. Kochendörfer: Z. Krist. Miner. Petrol., 1939, vol. 101, p. 134.

58. H. M. Ledbetter and M. W. Austin: Mater. Sci. Eng., in press.

59. H. M. Ledbetter: J. Appl. Phys., 1973, vol. 44, pp. 1451-1454.

60. H. M. Ledbetter: J. Phys. D., 1980, vol. 13, pp. 1879-1884.

61. E. Kröner: Z. Phys., 1958, vol. 151, pp. 504-518.

62. H. M. Ledbetter: Phys. Stat. Solidi (a), 1984, vol. 85, pp. 89-96.

63. L. Kaufman, E. V. Clougherty, and R. J. Weiss: Acta Metall., 1963, vol. 11, pp. 323-335.

64. J. Madsen, O. K. Andersen, U. K. Poulsen, and O. Jepsen: in Magnetism and Magnetic Materials, AIP Conference Proceedings 29, pp. 327-328, American Institute of Physics, New York, 1976.

65. O. K. Andersen, J. Madsen, U. K, Poulsen, O. Jepsen, and J. Kollar: Physica, 1977, vol. 86-88B, pp. 249-256.

66. G. Grimvall: Phys. Scr., 1976, vol. 13, pp. 59-64.

67. H. Hasegawa and D. G. Pettifor: Phys. Rev. Lett., 1983, vol. 50, pp. 130-133.

68. H. M. Ledbetter and M. W. Austin; National Bureau of Standards, Boulder, Colorado, unpublished research, 1984.

69. H. M. Ledbetter, Res Mech., forthcoming.

70. T. Datta, U. South Carolina, Columbia, unpublished research, 1985.

Table I. Chemical Composition (weight percent), Hardness, and Grain Size.

	Cr	Ni	Mn	P	S	Si	Mo	Cu	C	N	C + N	Hardness (Rockwell B)	Grain Size (μm)
1	18.3	10.1	1.57	0.021	0.019	0.50	0.20	0.210	0.028	0.039	0.067	73.4	85
2									0.058	0.039	0.097	74.1	78
3									0.089	0.039	0.128	78.5	90
4	18.0	9.91	1.50	0.022	0.017	0.57	0.205	0.197	0.037	0.120	0.157	81.9	105
5									0.067	0.120	0.187	83.5	85
6									0.094	0.120	0.214	84.2	78
7	20.3	9.97	1.42	0.024	0.016	0.55	0.195	0.200	0.030	0.240	0.270	87.3	98
8									0.057	0.240	0.297	88.0	82
9									0.085	0.240	0.325	88.5	90

Table II. Measured Polycrystal and Estimated Monocrystal Elastic Constants.
(Except for dimensionless A, all units are GPa.)

Alloy	B	G	C_{11}	C_{12}	C_{44}	G(111)	E(111)	A
1	158.8	78.5	206.8	134.8	128.4	66.8	303.4	3.567
2	159.7	78.8	207.9	135.6	128.9	67.1	304.8	3.567
3	158.5	78.6	206.4	134.6	128.9	66.9	304.2	3.591
4	160.0	78.4	208.3	135.8	127.6	66.7	302.4	3.520
5	157.4	78.9	204.9	133.6	130.2	67.2	306.16	3.652
6	157.8	78.5	205.5	134.0	128.9	66.8	304.0	3.606
7	158.7	78.2	206.6	134.7	127.7	66.5	302.1	3.552
8	156.2	78.9	203.4	132.6	130.8	67.2	306.8	3.695
9	159.2	77.8	207.3	135.2	126.4	66.2	299.9	3.506

Table III. Principal Results

C + N (at. pct.)	a (Å)	α	ϵ (10^{-3})	D (Å)	γ (mJ/m^2)
0.28	3.5914	0.013	3.05	447	18.8
0.42	3.5915	0.017	3.13	364	14.8
0.56	3.5918	0.017	4.01	450	24.4
0.64	3.5939	0.017	3.61	342	19.5
0.78	3.5951	0.013	3.28	295	21.6
0.91	3.5945	0.017	3.32	295	16.7
1.09	3.5988	0.014	3.67	323	23.7
1.21	3.5996	0.017	3.64	376	20.3
1.34	3.5990	0.012	3.00	260	19.2
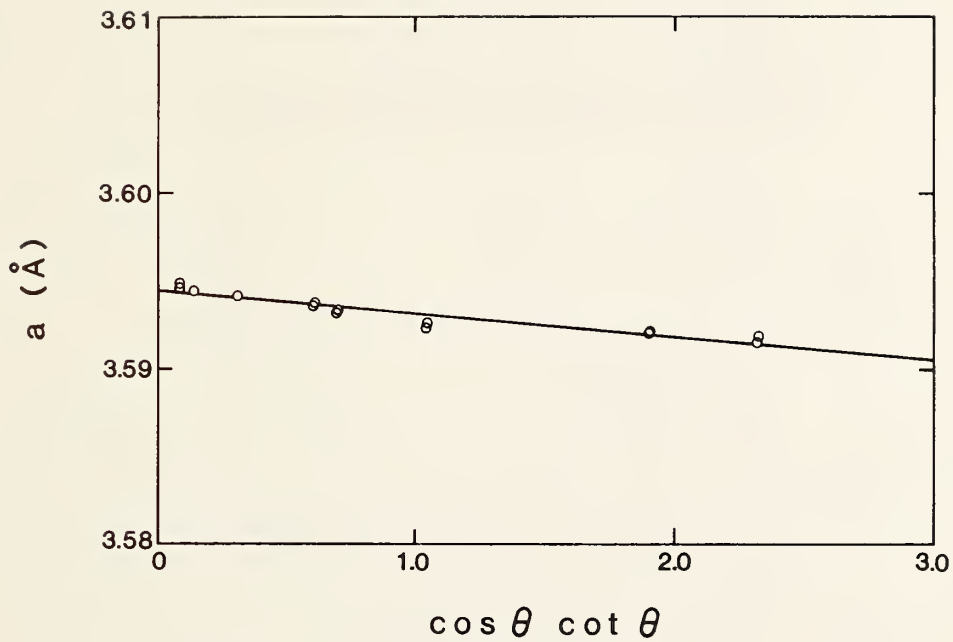
Fig. 1. For alloy 6, unit-cell size versus cosθ cotθ, where θ denotes Bragg angle. Intercept gives unit-cell size, 3.5945 Å, based on a linear-least-squares fit. Double points represent $K_{\alpha 1}$ and $K_{\alpha 2}$ diffraction peaks.
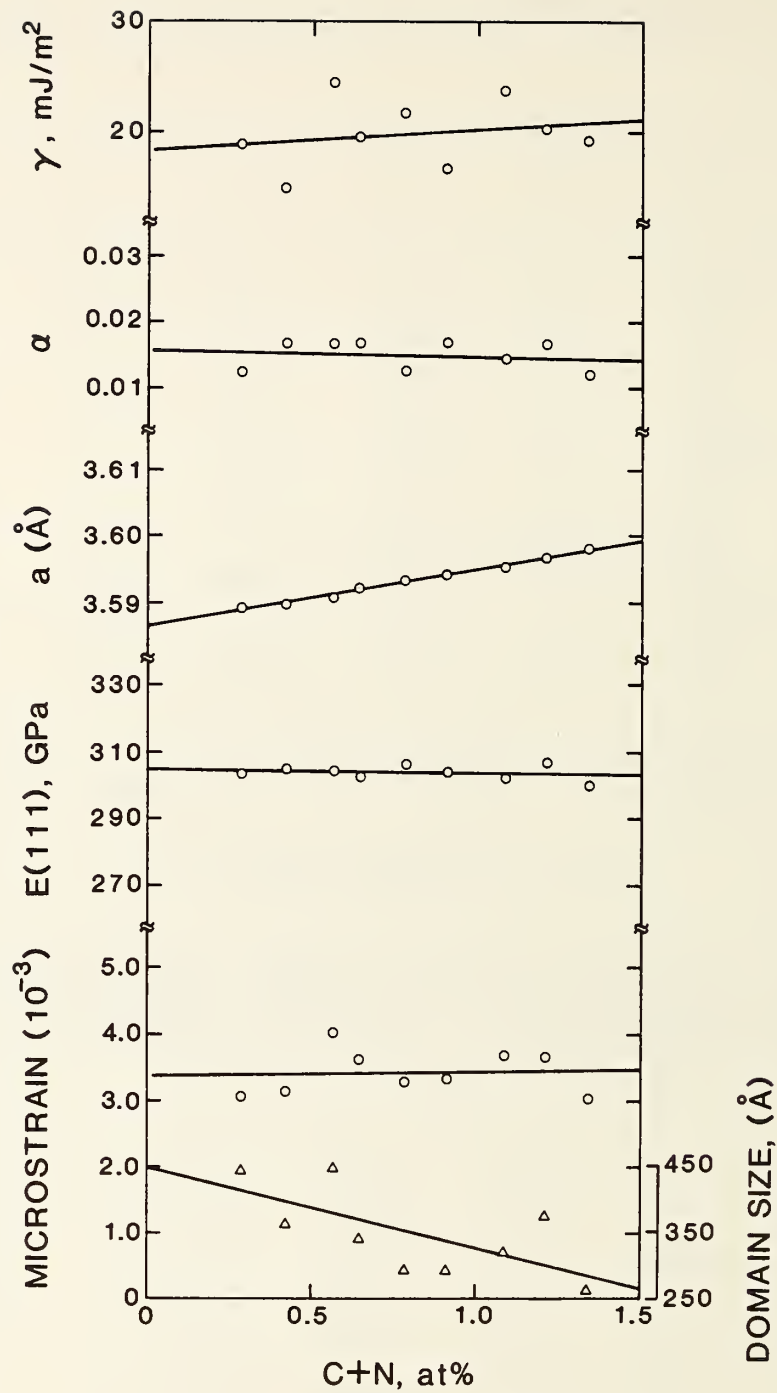
Fig. 2. Versus atomic percent carbon plus nitrogen, the variation of six
quantities: stacking-fault energy, stacking-fault probability,
unit-cell size, Young modulus in <111> direction, root-mean-square
strain, and size of coherently diffracting domain.

294

TECHNOLOGY TRANSFER

TECHNOLOGY TRANSFER PROGRAM

LEADER: N. J. Simon, NBS

OBJECTIVES:

1. Organization of workshops to promote interaction between designers and material specialists. Major topics include issues related to low-temperature material needs of the fusion energy program and reviews and new low-temperature data on structural alloys, composites, and weldments.
2. Production and distribution of an annual report as well as monthly highlight reports to OFE/DOE.
3. Preparation of handbook pages and supporting documentation on low-temperature mechanical and physical properties of structural materials for superconducting magnets. The pages are to be distributed to workshop attendees and others in the low-temperature materials applications community. The pages will also be presented for inclusion in the "Materials Handbook for Fusion Energy Systems."

RESEARCH PAST YEAR (1984):

1. "Materials Studies for Magnetic fusion Energy Applications--VII," (NBSIR 84-3000, 448 pages, May 1984, editors R. P. Reed and N. J. Simon) has been sent to the Technology Information Center, ORNL, and to a number of interested persons who have requested copies.
2. Handbook pages and supporting documentation covering mechanical properties of AISI 304 (N, LN, HN, LHN) have been prepared. These pages will be submitted to the "Materials Handbook for Fusion Energy Systems." Analysis of the correlation of AISI 304 (N, LN, HN, LHN) mechanical properties with interstitial nitrogen and carbon content is included. Preliminary work was completed in preparation for development of handbook pages on AISI 316 and AISI 304 weldments.
3. International cooperation was established in research to develop radiation-resistant laminates to meet requirements for the fusion energy program.

RESEARCH THIS YEAR (1985)

1. Tentative plans are to hold the low-temperature materials workshop again, in October 1985.
2. "Materials Studies for Magnetic fusion Energy Applications--VIII," (NBSIR 85-3025, 341 pages, 1985, editor R. P. Reed) is the current edition of the annual report.
3. The AISI 316 handbook pages and the Fe-21Cr-6Ni-9Mn handbook pages are currently in the review process for "Materials Handbook for Fusion Energy Systems," and the AISI 304 (N, LN, HN, LHN) handbook pages will enter the review process later this year.
4. Preparation of AISI 304 (N, LN, HN, LHN) handbook pages will be completed this year. Preparation of handbook pages on AISI 304 weldments will be completed.
5. Efforts promoting international cooperation in research to develop radiation-resistant laminates will continue. Interaction between the United States and Japan on structural materials research will be explored.

NBS-DOE WORKSHOP: MATERIALS AT LOW TEMPERATURES

October 14-17, 1984; Vail, Colorado

Fracture and Deformation Division
National Bureau of Standards
Boulder, Colorado

The annual NBS-DOE workshop provided the opportunity for dis-
cussion of problems, advances, and goals in the development of mate-
rials for low temperature superconducting magnet systems for magnetic
fusion energy. Formal and informal discussions centered on welding,
magnet systems, radiation-resistant organic insulators, and structural
alloys.

PROGRAM

NBS-DOE Workshop: Materials at Low Temperatures
October 14-17, 1984
Vail, Colorado

Sunday, October 14

   Registration (5:00-8:00 p.m.)   Complimentary cocktails
                                          and hors d'oeuvres

Monday, October 15

   Registration (7:30-9:00 a.m.)

      SESSION 1 (8:30 a.m.-12:00 m.)   MAGNET SYSTEMS
                                           V. K. Der, Chairman

   Introduction   R. P. Reed, NBS
   Need for Establishing Design Allowables and   V. K. Der, OFE
      Guidelines for Magnet Systems
   Materials Aspects of the Large Coil Program   M. Lubell, ORNL
   Status of Fabrication of Superconducting   J. Zbasnik, LLNL
      Magnets for MFTF-B
   Structural Materials Research in Japan   H. I. McHenry, NBS
   Quantitative Materials Research   R. P. Reed, NBS
      Objectives: The JAERI Box

      SESSION 2 (1:30-5:00 p.m.)   WELDING FOR LOW TEMPERATURE SERVICE
                                           T. A. Siewert, Chairman

   Welding Structures for Liquid Helium Service: E. N. C. Dalder, LLNL
      Past, Present, Future
   The Effect of Weld Microstructures on the   J. C. Lippold, Sandia
      Fracture Behavior of 316L Weldments at 4 K
   Fracture Toughness of Austenitic Stainless   G. M. Goodwin, ORNL
      Steel Weld Metal at 4 K
   Stainless Steel Heavy Vessel Fabrication   H. Helmbrecht, B & W
   Fully Austenitic - Fissure Resistant Filler   R. A. Bushey, Alloy Rods
      Material
   Stainless Steel Welding Research   T. A. Siewert, NBS

      DISCUSSION SESSION 1 (7:30-9:00 p.m.)   RESEARCH OBJECTIVES IN WELDING
                                              E. N. C. Dalder, Leader

Tuesday, October 16

   Registration (8:00-9:00 a.m.)

301

Tuesday, October 16 (continued)

SESSION 3 (8:30-11:00 a.m.)   RADIATION RESISTANT ORGANIC INSULATOR
                                        DEVELOPMENT, M. B. Kasen, Chairman

The ORNL Cryogenic Neutron Irradiation Facility   R. Coltman, ORNL
Nonmetallic Materials Radiation Studies at NBS   M. B. Kasen, NBS
Neutron Irradiation Studies of Polymers at LANL   D. Tucker, LANL
Nonmetallic Materials Radiation Research at MIT   H. Becker, MIT
Damage Types in Woven Composites at Low Temperatures R. D. Kriz, NBS

DISCUSSION SESSION 2 (11:00 a.m.-   RESEARCH OBJECTIVES IN NONMETALLICS
                     12:30 p.m.)   R. R. Coltman, Leader

SESSION 4 (1:30-5:00 p.m.)   STRUCTURAL ALLOYS
                                         J. W. Morris, Chairman

Structural Material Investigation in Conjunction   P. Komarek, KFK
   with S.C. Magnet Projects at KFK
Low Temperature Mechanical Properties   R. P. Reed, NBS
Phase Transformations in Fe-Mn Alloys   J. W. Morris, Jr.,
                                                         Univ. of California
Effect of Molybdenum on Metallurgical Character-   P. J. Grobner,
   istics of Austenitic Stainless Steels   Climax Molybdenum
Near Threshold Fatigue Crack Growth in   R. L. Tobler, NBS
   Austenitic Stainless Steels
Summary of Strain Rate Effects in Austenitic Steels   W. Dobson, Binary Assoc.
Magneto-Mechanical Effects in 304 Stainless Steels   B. Fultz, Univ. of Calif.
Materials Handbook for Fusion Energy Systems -   N. J. Simon, NBS
   304N, LN, HN Cryogenic Properties
Martensitic Transformation Temperatures in   J. Self, CSM
   Austenitic Steels

DISCUSSION SESSION 3 (7:30-9:00 p.m.)   "JAERI BOX," STRUCTURAL ALLOY RESEARCH
                                         OBJECTIVES, H. I. McHenry, Leader

Wednesday, October 17

SESSION 5 (8:30-9:30 a.m.)   REPORTS FROM DISCUSSION SESSIONS
                                         R. P. Reed, Chairman

SESSION 6 (9:30 a.m.-12:00 m.)   CODES AND STANDARDS--TASK GROUP ON
           (1:30-5:00 p.m.)   CRYOGENIC MATERIALS (Metal Properties
                                         Council), H. C. Rogers, Chairman

DISCUSSION SESSION 4 (1:30-5:30 p.m.)   TASK GROUP ON CONDUCTOR SHEATH ALLOYS
                                         E. N. C. Dalder, Leader

FOREWORD

The annual 1984 workshop promoted interaction between those involved in development of low temperature superconducting magnet systems for magnetic fusion energy and the structural materials research community serving this effort. There were four formal sessions on Monday, October 15 and Tuesday, October 16:

- Magnet Systems: Design Concepts, Materials Requirements, Progress Reports
- Welding for Low Temperature Service
- Radiation Resistant Organic Insulator Development
- Austenitic Steels: Properties and Low Temperature Behavior

Each session included a number of short technical presentations by representatives of NBS, universities, national laboratories, fabricators, and other organizations involved in the fusion program. In addition, informal sessions were held to review FY85 research objectives; in particular, to discuss the advisability of setting national quantitative materials research objectives, similar to those set by the Japan Atomic Energy Research Institute with respect to strength and toughness for austenitic steels at 4 K. Objectives for structural alloys, welding, and nonmetallics were discussed in three separate sessions. Other issues that were discussed included magnet design philosophy with respect to allowable stress levels, the establishment of material and property priorities for data compilation and review, and techniques of assessment of the available low temperature data base for design use. A special task group discussed issues related to the use of conductor sheath alloys.

Reports from the informal discussion sessions were presented Wednesday morning, October 17. Those assisting in the preparation of this report included Victor Der (Office of Fusion Energy), Ed Dalder (Lawrence Livermore National Laboratory), Harry McHenry (NBS), Nancy Simon (NBS), Ralph Tobler (NBS), and Ron Kriz (NBS).

Workshop participants representing many companies and laboratories discussed their research. Therefore, the summary contains company names and trade names that were integral to the discussions. Such identification does not imply recommendation or endorsement by the National Bureau of Standards, nor does it imply that the materials, equipment, or source identified are necessarily the best available for the purpose.

Richard P. Reed
National Bureau of Standards

LOW TEMPERATURE MATERIALS WORKSHOP
FOR MAGNETIC FUSION ENERGY - AN INFORMAL SUMMARY

Magnet Systems

The theme of this session was materials research objectives to support design of magnet systems. A permeating issue throughout the workshop was whether or not the U.S. structural materials research program should focus on quantitative objectives, e.g., target values for strength fracture toughness and for magnet structures. In this session five presentations were given on design and materials aspects of magnet systems.

Victor Der (OFE DOE) proposed a need for establishing design allowables and criteria/guidelines for magnet systems. The need for design allowables was identified for structural alloys and weldments, insulators, conductors, and cryogenic coolants. An example of allowables and criteria needs for structural design was used as an illustration. The objective of this proposal was to begin a program over the next two years to address the need for allowables and criteria/guidelines by establishing working groups to produce an updatable magnet design handbook. Interfaces and details of the types of working groups were presented. Feedback from the session audience on this idea was generally positive, i.e., there appeared to be a consensus that such an activity was needed. However, there were suggestions that the schedule may be rather ambitious in light of a general lack of data to support the determination of design allowables. Another suggestion was that inspection guidelines should also be included. There was a concern that it may be difficult to convince scientists to abide by these guidelines because of a desire to push experiments to their limits. At the very least, however, this approach should be pursued to drive the design process for magnet systems.

Martin Lubell (ORNL) reported on the materials aspects of the Large Coil Program (LCP) at ORNL. An overview of the Large Coil Test Facility (LCTF) included a description of the fabrication and installation of the vacuum tank, the stainless steel bucking post, and the spider-frame base. The LCP involves international collaborative testing of an array of six 8-tesla coils, three from the U.S. and one each from Japan, Euratom, and Switzerland. A detailed discussion was given on the variety of approaches to the design, fabrication, and assembly of all six coils of a D-shape profile. These coils are heavily instrumented and therefore their costs are not representative of that for production coils. Acoustic emission (AE) monitoring during an intermediate three-coil test indicated that noises from the winding and from the coil structure were distinguishable. However, because the signals are still not fully understood, additional work in this area will be required before AE monitoring could be used as a means of coil protection. It was also suggested that perhaps oval-shaped coils may better withstand bending moments in magnet structures than D-shaped coils. Also, oval-shaped coils are likely to be easier and cheaper to construct. Finally, it was pointed out that structural analyses of the LCTF is continuing, and that structural analyses of the coils will be compared with data to be obtained from the six-coil test.

Jon Zbasnik (LLNL) reported on the status of fabrication of superconducting magnets for MFTF-B. A strong point was made that each piece of material used in the magnets and welds was tested at 4 K, and that considerable time was devoted to X-ray inspections of welds for defects. The magnet system is comprised of solenoids, Nb-Ti axicells, Nb_3Sn axicell inserts, transition coils, trim coils, and Yin-Yang coils. The solenoids, 12 of about 12,000 kg (27,000 lb) each, are encased in 304LN. The casing, acting as a structural containment, must also be leak tight for liquid helium. The solenoids were shipped to LLNL in August 1983. The Nb-Ti axicells, of about 24,000 kg (54,000 lb) each, are "layer cake" wound. The first axicells are expected to be delivered in November 1984 and installed in April-May 1985. The Nb_3Sn axicell inserts see the most severe radiation environment in the MFTF-B. The conductor was manufactured by Furukawa who was the only supplier to meet the delivery schedule. Completion of the first coil is scheduled for November 1984 and the second, for February 1985. The transition coils, "baseball" in shape, are of two different sizes, one weighing 41,000 kg (45 tons) and the other 23,000 kg (25 tons). The coil casing is fabricated from 10-cm (4-in)-thick 304LN-SS. All four coils are scheduled for delivery between January and April 1985. The trim coils, 16 in all, are used as correction coils to fine tune alignments with the transition coils. Trim coil casing is 1.9-cm (0.75-in) thick 304LN. Winding is complete, close out welding is about 40% complete, and assembly and installation are targeted for December 1984 through April 1985. The Yin-Yang coils weigh about 330,000 kg (360 tons). Both Yin-Yang coils are complete and LLNL is now attaching the LN_2 panels which require a total of 10,000 joints. Installation of the Yin-Yang coils is scheduled for December 1984. The MFTF-B project attempted to qualify all the magnet materials used in the magnet system. Although there will be no opportunity to test the Nb_3Sn axicell insert coils before operation in MFTF-B, a substantial design margin has been built into these coils.

Harry McHenry (NBS), who just completed a year's assignment for the Office of Naval Research in Tokyo, reviewed current low temperature structural materials research in Japan. The Japan Atomic Energy Research Institute (JAERI) initiated a program in 1982 to develop a structural steel alloy for the large superconducting magnets planned for the Fusion Experimental Reactor (FER). A set of target properties was established for the new alloy on the basis of the design requirements for the FER coil system. The responsibility for developing an alloy with these properties was assumed by three Japanese steel companies working in conjunction with JAERI: Japan Steel Works, Ltd.; Kobe Steel, Ltd.; and Nippon Steel Corp. At first, tensile and Charpy impact tests were conducted at 4 K on 68 candidate alloys.

Five alloys were selected from this group for additional research:

		Content (wt.%)					
Alloy	Developer	C	Cr	Ni	Mn	N	Other
1	Nippon	0.02	25	13	--	0.35	
2	Nippon	0.02	27	18	--	0.35	
3	Japan Steel	0.02	12	12	10	0.2	5 Mo
4	Kobe	0.05	13	5	22	0.2	
5	Nippon	0.05	15	1	25	0.2	1 Cu, Nb

Development activities since mid-1983 included further characterization using fracture toughness and fatigue crack growth rate tests, primary processing studies for scaling up to commercial practice, and the development of welding materials and procedures for use with these new alloys. It is expected that final determination on these five alloys will be made in late 1984.

The research objectives of the JAERI structural alloy program, described by McHenry, were formulated from design considerations of the toroidal field (TF) coils for their proposed Fusion Experimental Reactor. Dick Reed (NBS) reviewed these. From assessment of the finite element stress analysis of the proposed coil case and windings, it was concluded that the maximum design stress would be 500 MPa. Analyses of Nb_3Sn superconductor critical current as a function of strain found that a maximum strain of 0.005 was permissible. Design conditions for both the conductor sheath and coil case were:

$$\text{design stress, } \sigma_d \leq 1/3 \; \sigma_u, \text{ tensile ultimate}$$
$$\sigma_d \leq 2/3 \; \sigma_u, \text{ tensile yield stress}$$
$$\sigma_d \leq 1/2 \; \sigma_u, \text{ stress at 0.005 strain}$$

A yield strength at 4 K of 1200 MPa was formulated. This was based on maximum allowable strain for the sheath material of TF coils using Nb_3Sn superconductor. The conductor sheath strain limitation of 0.005 corresponded to an elastic limit of 1000 MPa, which corresponds to a yield strength of 1200 MPa.

A fracture toughness of 200 MPa√m was proposed based on the minimum stress to grow a 1-mm surface crack through the 100-mm-thick TF coil-case under 500 MPa stress in fatigue loading.

Reed pointed out concern for the lack of ultimate tensile strength (σ_u) research objectives if one design criterion is that the design stress must be less than 1/3 σ_u. Typical ultimate strengths of high-strength austenitic steels ($\sigma_y \cong 1200$ MPa) are about 1.6 σ_y. Thus, considering that 1/3 σ_u equals about 640 MPa and that 2/3 σ_y equals about 800 MPa, it is obvious that σ_u, rather than σ_y would be restrictive on the maximum allowed design stress.

Welding for Low Temperature Service

This session consisted of six presentations on the welding of austenitic stainless steels and the properties of stainless steel welds at 4 K. The first presentation was an overview by Ed Dalder (LLNL) that traced the development of stainless steel welding practices from the mid-70's to the present and outlined research and development needed for the next five years. He emphasized the importance of 316L as the principal weld metal for magnet construction. Early studies provided basic data on strength, toughness, fatigue crack growth and the influence of metallurgical variables on these properties. Presently procedures are developed for SMA and FCA welding, and a suitable data base exists for using these processes for magnet construction. Further work is needed to understand the importance of nitrogen, ferrite, and microfissures on mechanical properties; to develop a larger data base for design; and to develop more efficient and reliable welding practices, particularly for out-of-position welding.

John Lippold (Sandia National Labs) addressed the dichotomy of the weld ferrite effect on the properties of 316L weld deposits, i.e., ferrite reduces the incidence of microfissures, but also reduces fracture toughness. Two approaches to future metal formulation that minimize microfissures in low ferrite welds were discussed: a Mn-modified 316L and a controlled ferrite number (CFN) 316L. Tests on weld deposits of these filler metals indicated that at similar strength levels and ferrite contents (<2%), the toughness of the CFN welds was substantially better than the Mn-modified welds. A model was proposed to account for these differences in terms of microstructural inhomogeneity resulting from elemental partitioning during solidification.

Gene Goodwin (Oak Ridge National Labs) described the selection of welding processes and weld filler metals for the fabricating of a large toroidal superconducting magnet. Published toughness values were collected and compared with SMA, GTA, and FCAW values generated in this study. All three processes were found to be suitable for the intended service, with the GTA welds having the highest toughness. The fabrication, including special fixturing, was also reviewed.

Methods for fabricating heavy section austenitic stainless steel structures were reviewed by Herb Helmbrecht (Babcock-Wilcox). Emphasis was placed on the strict controls necessary to insure satisfactory properties in stainless steel welds intended for low temperature service. Using conventional welding practices, property variability may result because of

variations in the welding conditions introduced by changes in the welding environment, differences in base metal dilution and procedural differences associated with manual and semiautomatic welding.

The use of fully automatic GMA welding procedures with adaptive controls was advocated to provide the consistency needed to meet weld metal property requirements.

Roger Bushey (Alloy Rods) reviewed the substantial reduction in fissuring tendency possible through trace element control. A standard 320-type stainless steel was compared with a similar composition with strict controls on the trace element (particularly phosphorus and sulfur). Fissure bend test photographs illustrated the lack of fissures in the controlled composition. The slag system was also shown to affect the fissure tendency. Further work was recommended to control the merits of low residual contents on the fissure tendencies of other filler metals for cryogenic service.

Tom Siewert (NBS) reviewed four projects performed in the preceding year at the Boulder Laboratory in support of the DOE program. These projects included three evaluations of weld properties and a fatigue crack growth study of CF8M castings. The tensile properties and fracture behavior of a Fe-15Mn-8Ni-1Mo-0.7C fully austenitic weld metal at 4 K were presented. The 4 K properties of a Fe-25Mn-5Cr-1Ni composition were compared for three different welding processes: GTA, SA, and SMAW. Improvements in pre-dictive equations for 76 K Charpy V-Notch tests were explained. The fatigue crack growths of CF8M castings were compared for various ferrite levels. These reports are published in more detail in the 1984 and 1985 NBSIR publications.

Nonmetallics

Ralph Coltman (ORNL) reported that work continues on constructing the National Low Temperature Neutron Irradiation Facility (NLTNIF). This facility, which is designed to approximate the fluence seen by an MFE superconducting magnet, will be available to all U.S. researchers inter-ested in studying material behavior in an irradiated environment at temperatures from 3.5 K to 300 K. It is a moveable open core reactor operating at 2 MW with a Zircalloy gamma-ray shield. Radiation characteristics are:

Fast Neutron Flux:	2.2×10^{17} n/m^2/s
Thermal Neutron Flux:	1.4×10^{17} n/m^2/s
Routine Fluence:	2×10^{23} n/m^2
Energy Deposition (in Al):	3×10^{10} rads

The fixed sample chamber is 4 cm in diameter and 25 cm long. Gradients in neutron flux vary no more than 10% along the length of the chamber. Specimens may be removed from the chamber and transferred to a storage cryostat without warmup. On-line data acquisition will be available to

monitor property changes in situ. Other spectra of radiation can be implemented by changing the shielding. In situ testing while under irradiation can be performed with appropriate fixtures. The facility is expected to become operational in late 1985.

Bud Kasen (NBS) described a new simplified specimen configuration and test procedure that is being investigated to optimize data obtained when testing nonmetallic organic insulators in a cryogenic irradiation environment. This work is being done cooperatively with laboratories in Japan (Osaka University) and in England (Rutherford Laboratory). A major objective is to reduce the cost vs. rads of allowable radiation for insulation materials in MFE superconducting magnets.

Some goals for the proposed test specimens are: small size, no edge effects, inexpensive, characterizable, defect free, easily produced, adaptable to a variety of test methods.

The test technique involves pulling a fiber bundle from a resin bath into a tubular teflon tube of about 3 mm i.d. followed by in situ curing. Much effort was given to developing methods required for producing high quality specimens. Several new techniques are required: vacuum degassing of resins while mixing, vacuum preimpregnation of fibers, and curing under nitrogen gas pressure.

A new technique using ultrasonic energy for resin mixing is under study. This techique, developed by William (Todd) Hodges (NASA Langley Research Center), eliminates the use of solvents and extends the range of polymer systems that can be used with the specimen production system.

Tests have shown that the basic production techniques can produce specimens 3 mm in diameter with less than 0.3% variation in diameter.

Initial mechanical tests were conducted by subjecting 15-mm-long specimens to longitudinal shear a modified short beam shear test. Sequential load drops in the stress-strain curve were found to correspond to sequential formation of interlaminar shear failure. With the first load drop taken as the shear strength criterion, experiments demonstrated an increase in interlaminar strength from 9.4 MPa at 295 K to 23.3 MPa at 76 K. Development of this and other test methods are continuing.

Dennis Tucker (LANL) reported on cryogenic irradiation studies of G-10CR, G-11CR Kapton, Bisphenol A epoxy, NP-530* (polyimide), and Spaulrad (polyimide). Specimens were irradiated in liquid helium at:
1.5×10^{21} n/m^2 E>0.1 Mev
2.6×10^{21} n/m^2 E>0.1 Mev
4.1×10^{21} n/m^2 E>0.1 Mev
Electrical tests:
dielectric constants and loss tangents
dc resistivity
dielectric breakdown strength

Mechanical tests at 75 K:
        flexural strength (three point bend)
        compressive strength
        flexural modulus

Experimental results showed some decrease in mechanical strength with increasing neutron fluence for all test materials; however, only G-10CR exhibited serious degradation. G-11CR had the highest retained strength values. G-10CR degradation was the highest of all materials tested. A comparison of these results with ORNL results on the same materials under gamma irradiation indicated that the boron content in type E glass reinforcement may accelerate degradation in a neutron environment.

Future work includes:
        irradiation at higher doses
        comparison of neutron vs. gamma for polyimide
        synthesis, irradiation, and testing of model resin systems

Herb Becker (MIT) presented a short progress report of ongoing efforts at MIT in which thin sheets of S2-glass/polyimide laminates are being tested in cyclic compression. Both irradiation and testing were performed at 295 K. Mechanical failure was defined as total breakdown of material into a powder. Results showed significant losses in resistivity; however, the lowest obtained resistivity was judged satisfactory for fusion magnets.

Ronald Kriz (NBS) and Walter Muster (EMPA, Switzerland) explained by analysis and experiment how fiber breaks and fiber bundle cracks can influence the mechanical response of G-10CR and G-11CR thin laminates at low loads. Analysis also showed a trade-off between stiffness and fill crack arrest at low temperatures. Experiment showed a strong correlation between fill cracks and "knees" in the stress-strain curves. Except for G-10CR at 77 K, fill cracks and fiber cracks in the warp bundles occur at the same mechanical load. Except for G-11CR and 77 K, fiber breaks and fill cracks are not related. Future studies will measure influence of damage at low loads on thermal physical properties.

Structural Alloys

Peter Komarek's (KFZ, Karlsruhe) talk on structural material investigations in conjunction with superconducting magnet projects in Germany covered three areas: selection of coil case materials, design approaches to failure prevention, and methods of NDT inspection of thick austenitic steel welds.

Candidate materials were characterized by fracture toughness and fatigue crack growth rate tests including threshold measurements at 300, 77 and 4 K. Electroslag remelted stainless steel demonstrated enhanced toughness, and an alloy equivalent to AISI 316LN was selected, having K_{Ic} values of 200 MPa√m for the weldment at 4 K. Based on the improved properties, critical flaw size calculations showed that a flaw size of ≤3.5 mm (as

compared with a previous ≤ 2mm) was acceptable, and this reduced the stringency of previous inspection requirements. Methods of NDT inspection were then considered and it was shown that ultrasonics was applicable to thick section welds, assuming use of longitudinal waves, angular transmitters, and reduced sensitivity volumes.

In summary, this work shows that structural materials investigations properly carried out with the establishment of a specific data base can significantly reduce the conservative requirements which otherwise limit materials use.

Dick Reed followed with an overview of progress in several areas of NBS research on austenitic stainless steels, OFHC copper, and 1100 aluminum. Fundamental research is ongoing in areas of tensile, notch tensile, creep, fatigue, fractography, and physical property investigation. Efforts in tensile testing have been directed at strain rate effects and temperature dependence of flow strength. It was noted that the strain rate effects were found to be proportionately less at 4 K than at higher temperatures. Notch tensile data failed to provide useful correlations with quantitative fracture toughness measurement and so are falling from serious consideration as a possible substitute for J-integral test characterization. For the J-integral results, fractographic investigations suggest that a very fine precipitate or inclusion of a so-far undefined composition nature may account for scatter in low toughness alloys.

Primary creep at 4 K occurs in AISI 310 stainless steel at the yield point, and additional testing is being pursued to define the relevance of creep to design at 4 K. Collaborative efforts with Colorado School of Mines, Climax Molybdenum, Carpenter Technology, and welding consumable suppliers are also being pursued to develop less expensive and stronger austenitic stainless steels.

Bill Morris's (U. of California) talk provided an intense description of three types of Fe-Mn alloys, their characteristic phase transformation tendencies, and the effects of these transformations on mechanical property behavior. Three representative types were considered: Fe-16 or -17Mn ($\alpha \rightarrow \epsilon \rightarrow \alpha'$), Fe-20 or -25Mn ($\alpha \rightarrow \epsilon$) and Fe-31 or -36Mn (relatively stable). Changes in work-hardening rates with strain and anomalies in yield strength ordering owing to phase transformations were described and the relationships between strength, test temperature, and volume fraction of phases after deformation and fracture were given with consideration of the relevant mechanisms of alloy softening and hardening.

The fundamental understanding of these binary alloys is important because it can lead to suggestions for the improvement of high-Mn alloy steels, and because analogies to the mechanical behaviors of AISI 304 alloys exist.

Paul Grobner (Climax Molybdenum) reviewed the effects of Mo on the (1) microstructure, (2) mechanical properties and (3) corrosion resistance of austenitic stainless steels. Molybdenum encourages the formation of ferrite and sigma phases and stabilizes carbides and austenite. Molybdenum is also an effective solid solution strengthener and (compared in terms of weight percent) only the interstitial elements have a stronger effect on strength. Molybdenum improves pitting and crevice corrosion resistances and also improves intergranular corrosion resistance in nonoxidizing environments. This information is relevant to the consideration of possible austenitic stainless steel alloy development or modification.

Ralph Tobler (NBS) presented new data describing the near-threshold fatigue crack growth rates and threshold stress intensity factor parameters of AISI 316, 304L, and 304LN stainless steels at 4 K. Experimental data of this kind are needed because few data are available and there are no reliable data prediction schemes. To obtain these data, a fully automated computer-controlled test apparatus was designed and assembled. This apparatus reduces testing time and cryogen costs and will be used to establish a sizable 4 K data base to meet the emerging needs of designers.

Brent Fultz (U. of California) described the results of a study that confirms that magnetic fields influence the mechanical properties of metastable austenitic steels. In fact, the imposition of a magnetic field on these alloys affects the amount of phase transformation independent of other variables so that the effects of phase transformation and alloy stability can be separated and studied for the first time.

Changes in σ-ε behavior were noted for AISI 304L and 304LN steels as a function of increasing field strengths of 8, 12, and 18 tesla. The magneto-mechanical effects were more pronounced at higher fields and more pronounced for AISI 304L than for AISI 304LN. It was confirmed that softening in the early part of the σ-ε curve was due to the window mechanism, and that later hardening was due to martensitic phase transformation.

Nancy Simon (NBS) reviewed the results of efforts to correlate mechanical property data for AISI 304 type stainless steels. These studies were based on data compiled from a wide variety of sources in support of handbook publications. Correlations were sought for conventional tensile properties, fracture toughness, Charpy impact energies, fatigue crack growth rates, and Young's modulus, with respect to interstitial content or temperature. Despite the relatively high variability attending these interlaboratory results, significant correlations were discovered for σ_y vs [C+N] at 300, 77, and 4 K; for ultimate strength vs [C+N] at 300 K, and for $K_{Ic}(J)$ vs [N] at 4 K. All other correlations were completely obscured by scatter from uncontrolled variables in the data spliced from different sources. In these latter cases, weak property dependences on interstitial contents or temperature were often revealed by data taken from individual laboratories representing a controlled alloy series.

313

Joel Self (Colorado School of Mines) developed a new constitution diagram and equation for the martensitic transformations of high-alloy steel welds. The previous equations of Schaeffler and Andrews applied to narrow compositional limits and consisted entirely of linear terms. The new equation is far more general and is based on consideration of data available for iron binaries and ternaries, low-alloy steels, manganese steels, austenitic, ferritic, and martensitic stainless steels, and tool steels. Interactive terms were incorporated in the constitutive equation, and the importance of such terms in allowing a more general correlation of composition and microstructure in a wide variety of alloys was demonstrated.

Research Objectives in Nonmetallic Materials

(1) The presently available commercial insulating laminates (G-10CR, G-11CR, and the polyimide variants) should be further evaluated for cryogenic radiation degradation at high neutron fluence in the ORNL reactor when it becomes operational in 1985.

(2) Organic insulator materials presently available and their characterization state appear to meet the requirements of the designers for construction of magnets that will not be subjected to radiation. However, materials having substantially improved radiation resistance will be required when designs incorporate magnets subjected to radiation. It was commented that, in the short run, the radiation tolerance requirements will be higher than in the future, since the initial designs may not have the extensive blanketing that would be used in a commercial reactor. Requirements may be for a tolerance equivalent to 10^{11} rads during this developmental period. This consideration should be factored into the materials research program.

(3) Meaningful criteria for laminate failure are required. The present criteria of a 50% decrease in strength accompanied by visible material damage were considered questionable.

(4) Improved dissemination of insulator radiation effects data is needed.

(5) Research on degradation of potting resins is required.

(6) Carbon insulators should be investigated because they are presently used on some magnet systems and should be very radiation resistant. An example is colloidal carbon carried in a volatile solvent. The influence of residual solvent on radiation resistance should be examined.

(7) Research on developing improved insulators at lower cost should be continued. Although insulator cost is a small fraction of the total cost of an MFE reactor, the potential for cost savings on the order of many millions of dollars exists for a relatively small research funding cost. Development of insulators less costly to fabricate is a desirable objective.

(8) There was a consensus that establishment of specific nonmetallic material performance objectives (the JAERI Box principle) did not have ready application at the present stage of insulator development.

(9) The use of glass-filled phenolics has good advantages for fabrication, but radiation tolerance is uncertain and should be determined.

(10) From a list of property change information needed as a function of irradiation dose, mechanical properties have first priority. Dimensional stability and creep were given high priority while gas evolution and electrical properties were felt to be less important.

Research Objectives in Welding

From intense discussions, several research objectives evolved:

(1) Develop a welding consumable, capable of being deposited by at least two fusion-welding processes, with following 4-K properties:

$$1.0 \text{ GPa (150 ksi) } \sigma_y: \quad 160 \text{ MPa}\sqrt{m} \text{ (150 ksi}\sqrt{in}) \ K_{Ic}(J)$$
$$1.2 \text{ GPa (180 ksi) } \sigma_y: \quad 200 \text{ MPa}\sqrt{m} \text{ (180 ksi}\sqrt{in}) \ K_{Ic}(J)$$

(2) Using type 316L welding consumable as a MODEL, determine effects of residual elements (P,Si,C,O,Nb, etc.) and the purity of the weld deposit on 4-K $K_{Ic}(J)$. Currently, a very large scatter exists in the 4-K K_{Ic} data on 0 ferrite number welds.

(3) Starting with GTA or/and GMA processes, develop appropriate artificial intelligence for a fully automated welding process. Because of the extreme sensitivity of the weld deposit to minor variations in deposit conditions, industry representatives recommended automation as the only way to insure uniformity and reliable fracture toughness.

(4) Use available technology to develop fully automated ultrasonic techniques of nondestructive evaluation of thick stainless steel welds. A review of inspection techniques in nonfusion projects using thick sections will facilitate this effort.

(5) Review current weld-metal data bases to develop interim design allowables and other recommendations for additional work. A data base has been accumulated on 316L and similar filler materials using several weld processes, but the information has not yet been collected and critically evaluated.

Research Objectives for Structural Alloys

(1) Fe-Cr-Ni austenitic stainless steels should be improved through the
following studies:
     Grain size control
     Inclusion control/melting practices
     Control of residual elements
     Thermomechanical processing
     Weldability/HAZ studies

Because of the wide range of experience with the Cr-Ni austenitic stain-
less steels at 4 K and the many advantages of these steels such as commer-
cial availability, weldability and acceptable 4-K properties, the
consensus was that these stainless steels would continue to be used in
fusion magnet projects. However, significant problems encountered the
low-temperature use of these stainless steels need to be addressed.
Rejection rates of up to 50% have been reported for thick 304LN plates
(8-15 cm; 3-6 in) that failed to meet specifications due to very large
grain sizes, ASTM 00 (~ 2.5 cm; ~ 1 in). At present, the technology to
produce these plates consistently is not available; therefore, the areas
listed above were proposed for investigation.

(2) Alloy Development
     Research areas to focus for development of new alloys include:
     High-manganese austenitic steels
     Reduced-cost/high-strength stainless steels
     High-nickel ferritic alloys

New alloy development was seen as important in reaching the long-range
goals of the fusion energy program, but this effort should be subordinate
to improvement of the present Cr-Ni austenitic stainless steels. There
appear to be advantages to high-manganese alloys in regard to thermo-
mechanical processing and decreased sensitivity to impurities and grain
size variation, but there are also aspects of processing that are rela-
tively expensive. A high level of concern was expressed regarding the
weldability of these alloys. No published information on welding has come
from the Japanese developers of these alloys, and it was felt that the
Japanese research program had not given sufficient emphasis to the
weldability problems expected for alloys of these compositions.

(3) Quantitative Goals
In contrast to the Japanese situation, where properties recommendations
were developed as a response to a specific tokamak design, the Fusion Ex-
perimental Reactor, the United States does not currently have budgetary
approval for a specific machine. Japanese magnet designers are all
members in one institute, JAERI, whereas United States designers are
associated with a variety of institutions and often propose competitive
approaches to fusion design problems. Thus, a uniform viewpoint is
lacking in the United States. However, it was recognized that quantita-
tive goals could serve as a yardstick for progress of materials research

programs in developing new alloys. Also, the JAERI effort represented far greater allocation of resources than is appropriate now in the United States toward this goal.

(4) Corrosion Resistance
This was not considered a prime requirement because stainless steel magnet cases also have to undergo a cleaning cycle.

(5) Ferromagnetic Alloys
It was felt that ferritic alloys should not be eliminated from consideration, but that better calculation of the expected increases in applied stress should be made.

Executive Summary of Sessions on Research Objectives

It was realized that the "JAERI box" formulation followed from design considerations for the proposed Fusion Experimental Reactor and from the concern of JAERI designers. On the other hand, there are no planned large projects in the United States at present, and the session discussion did not produce strong support from designers for quantitative research objectives. However, it was apparent that quantitative research objectives would be of assistance in guiding fundamental research programs and in providing a yardstick for the assessment of these programs. In the future it is quite possible that quantitative research objectives will be derived from fracture-mechanics (fitness-for-service) assessment, since it will be necessary to establish maximum allowable weldment flaw sizes and minimum structural alloy and weldment toughness levels based on maximum service stress or strain.

The research from the three discussion sessions can be represented in three principal categories:

    (1) For current structural materials, such as 304LN with 316L weld-
    ments and G-10 and G-11 insulators, there was strong support for data
    collection and evaluation, property measurements, assessment of
    variables such as creep and fatigue, and improvement through better
    processing.

    (2) Support to begin establishment of design properties was recog-
    nized. Effort to begin assignment of design allowables was advocated.
    Unfortunately, in most cases this must be initiated with a relatively
    sparse data base.

    (3) It was realized that for the future a new generation of struc-
    tural materials must be developed. For these new materials, radiation
    must be considered. This includes consideration of lower-cost
    higher-strength austenitic stainless steels, high-manganese steels,
    ferritic steels, and movement toward more radiation-resistent insula-
    tors, such as polyimides. It is in this category that quantitative
    research objectives may be set to guide materials research and alloy
    producers.

Possible quantitative research objectives are:

Structural Material	Research Objectives		
	Yield Strength (MPa)	Toughness (MPa$\sqrt{m}$)	Others
Alloy Steel	1100	200	Equivalent to 304LN in fatigue, creep, physical properties, cost
Conductor Sheath	700	100	Thermal expansion, $\alpha \cong 10 \cdot 10^{-6}$ K^{-1} at 293 K, equivalent to Nb$_3$Sn/Cu-bronze
Welding Consumable	1000	200	1 welding process
	1000	150	2 welding processes

Conductor Sheath Alloy Development Task Group

The problem addressed by this task group is the following: The superconductor of a forced-flow superconducting magnet is subject to large strain due to the difference in thermal expansion between the conductor and conductor sheath alloy. The Nb$_3$Sn conductor used in these applications is particularly sensitive to strain, with strains of the amount expected from differential thermal contraction causing sizeable degradation of the critical current. Because the extensive heat treatment required for reaction of the superconductor/stabilizer complex caused deterioration in the mechanical properties of some conductor sheath alloy welds, JBK-75 was selected for this application due to better ductility retention after heat treatment. However, the large mismatch in thermal expansion between JBK-75 and the Nb$_3$Sn/Cu conductor has led to suggestions that Incoloy alloys such as 903 and 905 be used as the sheath material since their thermal contraction coefficients more closely match that of Nb$_3$Sn. Discussion by members of the task group confirmed that critical current density of Nb$_3$Sn could be enhanced by minimizing the thermal contraction difference between conductor and sheath during cooling from the Nb$_3$Sn reaction temperature to 4 K (Martin Lubell, MIT; Peter Komarek, Karlsruhe).

Considerations raised with regard to the use of an Incoloy alloy included the following:

(1) Heat treatment of the Incoloy series alloys is similar to that done to react the superconductor/stabilizer complex, but the time period would be of the order of 100 hours as compared to the 1 or 2 hour reanneal at 950°C followed by a water quench used after rolling Incoloy plate. There is a need to make tests to determine whether ductility is retained after such heat treatment. Not much work has been done in this area, and a complicated behavior involving both softening and embrittlement has been reported.

(2) Work in progress at LLNL to evaluate the responses of JBK-75 and Incoloy 9XX (903, 905, 909) iron-based superalloys to possible Nb_3Sn reaction heat treatments shows that: a. JBK-75 - autogeneous (made without filler-addition) GTA welds show formation of cellular η phase at weld-metal grain boundaries. No η was seen in unwelded material. b. Incoloy 9XX (903, 905, 909) autogeneous GTA welds, weld HAZs (heat-affected zones), and unwelded materials show continuous grain-boundary phases after 24 hour exposure at 700-800°C. Identification of phases is under way.

(3) The void fraction has been found to have a substantial effect upon the magnitude of the compressive forces transmitted to the superconductor. Whether or not a connected path exists for a void fraction greater than about 17% was considered controversial. Considered as a percolation problem, such a path should not exist, but M. Hoenig (MIT) has evidently found or calculated effects for a void fraction of around 30-40%. It was recommended that a finite-element analysis of the strain transmitted to the conductor be done, as this would show how J_c (strained)/J_c(unstrained) varies as a function of void fraction. Herb Becker (MIT) will make available to LLNL results of finite-element stress-analysis of an I.C.C.S. conduction-sheath, operating under ALCATOR DCT conditions, so the effects of 4 K mechanical properties on integrity of sheath alloys may be evaluated.

(4) A suggestion was made that if no suitable sheath alloy could be found considering both thermal and mechanical properties, the possibility of reinforcing a sheath with a U-section for sufficient mechanical strength be considered. However, it was pointed out that this solution would have the effect of decreasing the gross current density in the magnet because so much space would be occupied by non-current-carrying material or empty space.

(5) Crack initiation and growth is an important factor in the selection of a conductor sheath alloy. Sufficient helium to degrade the 4-K vacuum insulation can leak through a very small crack. Data on da/dN are evidently available for JBK-75 in a recent article in Cryogenics, but da/dN data need to be acquired on Incoloy alloys.

(6) L. Summers (LLNL) will do mechanical testing of the new alloys under consideration. His preliminary metallographic studies indicate that a complicated metallurgical structure is present after thermal treatment, implying that toughness and strength at 4 K may be degraded. Since this testing should take place before the next meeting and will require at least three months, the next meeting of the task force was set for March 8, 1985 at LLNL following the Topical Meeting on Controlled Nuclear Fusion in San Francisco. The schedule for work at LLNL before this meeting includes: (a) completion of heat-treatment studies by January 31, 1985 and (b) determination of 4-K tensile and fracture toughness response of unwelded and autogeneous GTA welds in all four alloys by February 28, 1985.

(7) Possible alternatives to Incoloy alloys include the high manganese alloys developed in Japan. These alloys also have lower thermal contraction, about 1/2 that of 304. It was suggested that conductor sheath alloy development be included in the items that the United States wishes to include in the proposed joint United States/Japan structural alloys exchange program.

Ken Agarwal
General Dynamics
San Diego, California

John Arvidson
NBS
Boulder, Colorado

Frank Babish
Sandvik Steel Co.
Scranton, Pennsylvania

Ken Banks
Teledyne McKay
York, Pennsylvania

Herb Becker
MIT
Cambridge, Massachusetts

Jim Bialek
Princeton Plasma Physics
Princeton, New Jersey

Roger Bushey
Alloy Rods
Hanover, Pennsylvania

Bernie Carpenter
Colorado School of Mines
Golden, Colorado

Ralph Coltman
ORNL
Oak Ridge, Tennessee

Edward Dalder
LLNL
Livermore, California

Victor Der
Office of Fusion Energy
Washington, D.C.

Jack Ekin
NBS
Boulder, Colorado

Brent Fultz
LBL
Berkeley, California

Gene Goodwin
ORNL
Oak Ridge, Tennessee

Paul Grobner
AMAX Materials Res. Center
Ann Arbor, Michigan

Drew Hazelton
Intermagnetics General Corp.
Guilderland, New York

Philip Heitzenroeder
Princeton Plasma Physics
Princeton, New Jersey

Herb Helmbrecht
Babcock-Wilcox
Barberton, Ohio

Thomas Hordubay
Westinghouse Electric Corp.
Pittsburgh, Pennsylvania

M. B. Kasen
NBS
Boulder, Colorado

Peter Komarek
Nuclear Research Center
Karlsruhe, F. R. Germany

Ronald Kriz
NBS
Boulder, Colorado

John Lippold
SNLL
Livermore, California

Martin Lubell
ORNL
Oak Ridge, Tennessee

Harry McHenry
NBS
Boulder, Colorado

J. W. Morris, Jr.
University of California
Berkeley, California

Walter Muster
Federal Labs for Materials
    Testing
Dubendorf, Switzerland

Lew Myers
Carpenter Tech.
Reading, Pennsylvania

Carl Osgood
Cranbury, New Jersey

Craig Peters
LBL
Berkeley, California

Pat Purtscher
NBS
Boulder, Colorado

Richard Reed
NBS
Boulder, Colorado

Harry Rogers
Drexel University
Philadelphia, Pennsylvania

Joel Self
Colorado School of Mines
Golden, Colorado

Oscar Seth
CBI
Houston, Texas

Tom Siewert
NBS
Boulder, Colorado

Nancy Simon
NBS
Boulder, Colorado

Leonard Summers
LLNL
Livermore, California

Ralph Tobler
NBS
Boulder, Colorado

Dennis Tucker
LANL
Los Alamos, New Mexico

Robert Walsh
NBS
Boulder, Colorado

Jon Zbasnik
LLNL
Livermore, California

CRYOGENIC STEELS FOR SUPERCONDUCTING MAGNETS:
DEVELOPMENTS IN JAPAN

Harry I. McHenry

Fracture and Deformation Division
National Bureau of Standards
Boulder, Colorado

The Japan Atomic Energy Research Institute initiated a program in 1982 to develop cryogenic steels for use in the large superconducting magnets planned for the Fusion Experimental Reactor. The target properties for the cryogenic steels are a yield strength of 1200 MPa at 4 K and a fracture toughness of 200 MPa√m at 4 K. Progress on developing these steels was reviewed at a U.S./Japan workshop in December 1984. Five Japanese steel companies have developed candidate alloys that met or nearly met the property goals. The new steels include 25Cr-14Ni-4Mn, 12Ni-12Cr-10Mn-5Mo, 13Cr-5Ni-22Mn and 15Cr-1Ni-25Mn. All of the alloys are nonmagnetic, stainless steels that are alloyed with nitrogen (0.2 to 0.35%). Following the workshop, the participating steel companies were visited. This report summarizes the information about these new steels obtained at the workshop and during the visits.

INTRODUCTION

Superconductivity is one of the high technologies that Japan has targeted for concerted development. There are national programs to use superconductivity to enhance the efficiency of generating, storing, and transmitting electrical power. Superconducting magnets are being developed for fusion power devices, magneto-hydrodynamic (MHD) power generators and high energy physics experiments. Numerous research and development programs are being conducted to develop these applications and to develop improved superconducting materials.

The scope of this report is limited to recent developments in cryogenic steels for structural applications in superconducting magnets. The main source of information was the United States/Japan Joint Planning Workshop on Low Temperature Structural Materials and Standards (Tokyo; December 17 to 21, 1984), which was held to initiate a program of cooperative research in the area of materials and structures technology for superconducting magnets for fusion energy systems. The workshop was cosponsored by the U.S. Department of Energy (DOE) and the Japan Atomic Energy Research Institute (JAERI) and organized by Dr. Susumu Shimamoto of JAERI and Dr. Victor Der of DOE, Office of Fusion Energy. A summary of the workshop topics outside the scope of this report is given in Appendix A. The thirty Japanese participants represented the various organizations involved in Japan's effort to develop superconducting magnets for fusion energy: JAERI, National Research Institute for Metals, universities (Tohoku, Osaka, Tokyo), steel companies (Nippon Steel, Kawasaki Steel, Japan Steel Works, Kobe Steel, and Nippon Kokan), and electrical manufacturers (Hitachi, Toshiba, and Mitsubishi Electric). The six U.S. participants represented organizations in the DOE fusion energy program: Lawrence Berkeley Laboratory, Lawrence Livermore National Laboratory, Massachusetts Institute of Technology, National Bureau of Standards, and Princeton Plasma Physics Laboratory. A list of attendees is given in Appendix B.

REQUIREMENTS ON THE CRYOGENIC STEELS

Cryogenic steels will be used for the main structural members of the superconducting magnets of the Fusion Engineering Reactor (FER), a tokamak device being designed by JAERI to demonstrate the technical feasibility of electrical power generation by fusion energy. Currently in the design stage, the FER will take ten years to build and is not expected to go into operation until about the year 2000. Even then, it will only be an experimental reactor, to be followed in the development plan by a prototype reactor and a demonstration reaction. Thus, the market for the steels discussed in this report will not develop fully until well into the twenty-first century, a good example of the long-term outlook of Japanese industry. In the meantime, these steels may be useful for other superconductivity projects.

The superconducting magnets being designed for FER are truly enormous structures. Current designs call for 10-m diameter coils in 12 T field at currents of 20 kA. The stored energy is 30 GJ. A dozen or so of these magnets will be used to confine the hot plasma within a donut-shaped vacuum

vessel. A schematic of the conceptual design is shown in Figure 1. The principal design features governing alloy selection are the enormous size and stored energy of the magnets, the extremely high forces exerted by the magnets, and the limited space available for the structure. These features result in the need for steels with sufficient strength to perform the required structural functions within the space available, sufficient fatigue and fracture resistance to operate safely, and sufficient fabricability to be practical. The choice of materials is further restricted by the adverse operating environment of the magnet system: a design temperature of 4 K, magnetic fields up to 12 T, and moderate levels of neutron irradiation.

The Superconducting Magnet Laboratory at JAERI's new Fusion R & D Center in Nakamachi, Ibaraki-ken, is responsible for the FER magnet design. In 1981, a program was initiated to develop a steel that meets the FER design requirements prior to the start of construction, about 1988. The approach was to establish a set of target properties and then work together with the Japanese steel industry to develop a suitable steel. The target properties, first announced in 1982, are:

- yield strength   1200 MPa at 4 K
- fracture toughness   200 MPa$\sqrt{m}$ at 4 K
- fatigue strength   ~316 stainless steel
- permeability $\mu \leq 1.02$
- corrosion resistance   rust resistance
- fabricability   weldability and machinability
- plate thickness   up to 200 mm

For initial screening, Charpy V-notch impact tests at 4 K are used in lieu of the fracture toughness tests; the property target is 100 J.

THE JAERI/INDUSTRY DEVELOPMENT PROGRAM

The task of developing an alloy with these properties has been undertaken by three steel companies working in conjunction with JAERI: Japan Steel Works, Kobe Steel, and Nippon Steel. In addition, Nippon Kokan is working independently to develop an alloy with the same property goals. Kawasaki Steel is working with JAERI to develop a sheet material with the same property goals after exposure to the thermal cycle required for the superconductor sheath material. The contracts between JAERI and the participating companies were vaguely described to me as simply the responsibilities of each party in the mutual development program; apparently JAERI doesn't pay the companies for their developmental efforts.

The yield strength and toughness targets have served as go-no go screening requirements. The magnetic permeability requirement has limited the consideration of steels to those that are fully austenitic and nonmagnetic. The corrosion resistance target has led to use of a minimum of 12% Cr. The remaining targets have not yet had an apparent influence on the alloy development efforts.

The development schedule is shown in Figure 2. For initial screening, tensile and Charpy impact tests were conducted at 4 K on 89 candidate alloys in four general alloy classes:

- stainless steel (SS)   31 steels
- high-Mn stainless steel (HMSS)   40 steels
- high-Mn steel (HMS)   14 steels
- ferritic steel (FS)   4 steels

A total of 18 stainless steels (9 SS and 9 HMSS) met the yield strength (> 1200 MPa) and Charpy impact (> 100 J) screening goals. Two high-Mn steels met the goals but were dropped from further consideration because of insufficient Cr to be stainless steels. One ferritic steel met the goals, but was dropped because of the preference for nonmagnetic steels. Of these, some were of similar chemistry, thereby reducing the number of alloys included in the second stage of screening (fracture toughness tests at 4 K) to 11 (4 SS and 7 HMSS); the candidate alloys are shown in Table 1. As shown in Figure 3, the two high-Mn stainless steels did not meet the strength and toughness goals; however, the results were judged to be close enough to keep the steels in the program.

The five alloys developed in the JAERI industry program have excellent combinations of strength and toughness at 4 K. Thus, the alloy development phase of the JAERI program has been completed. These alloys also have satisfactory corrosion resistance and the physical properties are assumed to be suitable, i.e., low magnetic permeability and acceptable electrical resistance and thermal expansivity. The remaining tasks for the steel industry participants are (1) to conduct primary processing studies for scaling up to commercial practice, (2) to verify that the properties can be met in the large plates required for the FER, and (3) to develop the welding materials and procedures for use with these new alloys. The latter task is, perhaps, the most challenging. It has been undertaken primarily by Nippon Steel and Kobe Steel, the two major suppliers of welding consummables in Japan. In addition, JAERI will be conducting fatigue crack growth studies during 1985 to verify that the new steels have fatigue properties at 4 K that are comparable to those of 316 stainless steel.

VISITS TO PARTICIPATING STEEL COMPANIES

Following the workshop, the U.S. delegates had the opportunity to visit the Tokyo-area facilities of the four participating steel companies, and in my case, Nippon Kokan. The facilities visited were as follows:

Japan Steel Works	Head Office	Tokyo
Kawaski Steel Company	Research Laboratories Chiba Works	Chiba
Kobe Steel	Welding Division	Fujisawa
Nippon Steel Corporation	Research Laboratories II	Sagamihara
Nippon Kokan K.K.	Technical Research Center	Kawasaki

These visits plus additional details regarding each company's research on cryogenic steels are summarized below.